A Study of Protoplanetary Disk Structure around Herbig Ae Stars through Millimeter and Sub-millimeter Observations

Eiji Akiyama

Department of Astrophysics
College of Science
Ibaraki University

March 2012

博士学位論文

ミリ波サブミリ波観測によるHerbig Ae型星に付随する原始惑星系円盤の構造に関する研究

平成24年3月

茨城大学大学院理工学研究科
宇宙地球システム科学専攻

秋山　永治

Study of Protoplanetary Disk Structure around Herbig Ae Stars through Millimeter and Sub-millimeter Observations

Eiji Akiyama

In Partial Fulfillment of the Requirements for the Degree of Doctor of Philosophy
in the Subject of Astrophysics

Department of Astrophysics
College of Science
Ibaraki University

Defended February 2nd, 2012

Acknowledgments

There are countless people involved in my research and the substantial contributions of all collaborators are represented in this thesis. The accomplishment of this thesis definitely stands on top of their dedicated cooperation and invisible efforts.

I can not find any words describing my gratitude enough to Munetake Momose, as my thesis advisor, for the guidance and support. His attitude and approach to research have inspired me the most and serves as a good role model for me. I am grateful for valuable support from Yoshimi Kitamura and Kazuya Saigo in helping me work with model fitting. They provided model codes and instructed programing skills. My research would not have been successful if it were not for the support of disk group meeting members and radio astronomy group in Nagoya University, particularly Masahiko Hayashi and Hideko Nomura who have provided me a lot of best advices about physical and chemical disk structure analysis, observational method and instrument settings, and line selection based on astrochemistry. I also feel deep gratitude to Catherine Walsh for providing ionization fraction data through amazingly complex model codes.

Special thanks also go to all Nobeyama radio observatory staff for providing lessons and supports in the fundamentals of radio astronomy observations and opportunities to observe over the years. I received practical guidances in manipulating telescope and setting and adjusting receivers and spectrometers. The valuable know-how and helpful tricks that I could cultivate there will have been surely of benefit in conducting observation in the future. I am particularly grateful to Takashi Tsukagoshi, Yoshito Shimajiri, and Hiroyuki Kaneko for assisting my observation and data reduction at the sacrifice their own works and sharing knowledge ideas and skills. They are always welcome any questions and on-the-spot consultation during observation. I would also like to thank all students including other universities and institutes, particularly Tomonobu Inayama, Kazumi Sakai, Takashi Matoba, Yuki Nakagawa, Nanako Murakami, and Hiroyuki Hoshi. They have made my research more productive and provided spiritual support all the time.

I am always grateful to my family for their understanding, support, patience, and encouragement. They let me do whatever I want to do all the time. I absolutely could not have done this without them. I am very fortunate to be part of the family. I never forget contribution of my late uncle. He was very understanding and guided me toward the field of science and and prepare the environment for me to work hard. I have a great esteem for him not just as my uncle but as a scientist and a businessperson. I always thought that I wanted to be like him since I was a child. His words always helped me when I passed through the hard time and will remain unchanged in the future.

This research would not have been possible without all persons concerned.

Abstract

Since the first exo-planet was discovered by Mayor and Queloz in 1995, more than 600 exo-planet candidates has been discovered by September 2011 and although unofficial, the Kepler Science Team announced 1235 exo-planet candidates on February 1, 2011. It has become evident that the presence of extrasolar planetary system is ubiquitous in our galaxy as search for exo-planets progresses. However, a number of fundamental problems still remain regarding the planet formation process and comprehensive understanding has not yet been achieved. The accretion process from dust to planetisimals and from planetisimals to planets takes place in a protoplanetary disk, which simultaneously evolves with the central star, and the evolutionary process completely depends on disk temperature and density distributions. The location at which dust coagulation occurs in protoplanetary disks can be examined once the temperature distribution in the disk is given because the temperature critically determine the location of the snowline. This is thought to be essential for determining where Jovian planets are born in planetary system. The density distribution provides initial conditions for core accretion process and the time scale of the planetary disk evolution. This thesis provides the millimeter and sub-millimeter observational data toward three protoplanetary disks around intermediate mass pre-main-sequence stars (Herbig Ae stars), HD 163296, HD 31648, and HD 169142, demonstrates a verification strategy for disk structure by applying multiple molecular emission data, and finally derives the two dimensional temperature and surface density distributions of the disks.

Emission that originates from a disk can be identified by a single-dish telescope. The disk emission can be differentiated from the emission from surroundings by a close mapping toward the central star and its neighbor. This detection method has been well established by previous studies as well as interferometric observations. As a result of mapping the star+disk system and its vicinity with a grid of 2000 - 3000 AU squares by ^{12}CO (J=1–0) and ^{12}CO (J=3–2) lines, a double-peaked profile, which is a decisive characteristic for a disk emission in rotational motion, is successfully obtained only at the direction of the star+disk system. A number of disk models to reproduce observational emission profiles have been developed and the temperature and density distributions of the disk can be derived by making radiative transfer calculations. Taking advantage of different optical depth for each CO line, the author found the different fitting temperature for each CO line and estimate the vertical location from which an emission caused by rotational transition of a linear rigid rotor molecule, such as CO, originates. It was found that there exist at least two different temperature layers in the disk 100 AU away from the central star; 10 - 20 K in the interior and 30 - 40 K in the upper surface of the disk. This kind of picture is consistent with the passive disk characteristic predicted by the disk theory.

Although the radial density distribution is not fully understood in both observational and theoretical works, it is empirically supported that the power-law disk model with distribution in density shows a good agreement with the observational results. With the recent advent of improved observational equipment and facilities, the observational census for diffused gas near outer edge of the disk that used to be very difficult to observe has recently become possible. The optically thick line that reflects the emission from the tenuous gas in outer disk makes a peak to peak width narrower, whereas the optically thin line that reflects mostly the emission from the dense inner disk makes the width wider. This effect can be well explained if the disk is assumed to be in Keplerian rotation and makes it possible to study the viscous disk evolution in protoplanetary disk from observational approach. However, once the outer radius is given to the traditional power-law density model, the density become zero exactly at the given radius, or the disk is truncated at the outer edge. Similarity solution disk model that make the density decrease gradually at the outer region of the disk was introduced to model fitting and recently it was successful to explain two different results of disk radius obtained by dust continuum and molecular emission line but no attempt to introduce model fitting with observational results

obtained by only molecular emission lines. As a result of comparison between both disk models, the best fitting model is different from the objects; the emission profile of HD 31648 shows a good agreement with the one derived by the similarity solution disk model, whereas the emission profile of more evolved disk around HD 163296 shows a better fit with the one derived by traditional power-law disk model. The exponential tail is not simply detected due to sensitivity limitation of the detectors. Although it requires further validation in the case of HD 163296, the gradual reduction of density near the outer edge is not detected because the disk is so evolved that its density as a whole is not sufficiently high. In the case of HD 169142 having nearly face-on configuration, the size of disk does not affect to the observed line profile, and the velocity widths of each CO profile are almost identical. Thus, it is difficult to confine the radial density distribution and evolutionary stage.

The presence of the magneto-rotational instability (MRI) is expected in the protoplanetary disks. The MRI is one of the strong candidate that triggers gas dispersion of the disk as it induces turbulence in the disk. The presence of MRI can be concluded if the ionization fraction of the disk is determined since all of the other physical properties, such as temperature, sound speed, and magnetic pressure can be calculated or given by observations. The author selected the J=1–0 line emitted by HCO^+ molecules, which is a main source for electron. As a result of determining ionization through HCO^+ (J=1–0) line, the ionization fraction was found to be nearly 10^{-9} and sufficiently high enough to drive MRI (10^{-10} - 10^{-12}). In spite of a plenty of unknown factors for gas dispersion mechanism, our observational results suggest that the turbulence driven by MRI may occur at a distance of 100 AU from the central star.

The diversity of planetary system is thought to be determined by the diversity of protoplanetary disk in early stage of evolution. It is possible to correlate density structure with evolutionary stage by increasing the number of samples. The results in this thesis provide constrains or new information for constructing the formation scenario of star and planetary system and are expected to contribute to further development of future study in both observation and theory.

概要

1995 年、Mayor と Queloz によって初めて系外惑星が発見されて以来、2011 年 9 月までに 600 以上の系外惑星候補天体が発見されている。また、2011 年 2 月 1 日には非公式ではあるが Kepler 宇宙望遠鏡によって 1235 個の惑星候補天体が報告されている。このように太陽系のような惑星系は普遍的な存在であることが徐々に明らかになってきたが、惑星系の形成過程について根本的な問題が数多く残されており、依然として統一的な理解が得られていない。ダストから微惑星、微惑星から惑星への集積過程は中心星と同時に形成される原始惑星系円盤内で進行するが、その過程は円盤の温度や密度分布に大きく依存する。円盤の温度分布はスノーラインの位置を決定するので氷ダストの凝集場所が特定できる。これは木星のような巨大ガス惑星が惑星系のどこに形成されるかについて本質的な役割を果たす。また円盤の質量分布は惑星集積課程の初期条件や進化のタイムスケールを与えることになる。本論文は、中質量星 (Herbig Ae 型星) に付随する原始惑星系円盤 3 天体、HD163296、HD31648、HD169142 の観測データと分子輝線による円盤構造の観測的検証法を提供し、最終的に円盤の温度及び密度の 2 次元構造を示す。

単一鏡による円盤放射の検出は高密度マッピングにより円盤と周囲の成分を切り分けることで可能であり、干渉計観測と同様に実績のある検出法である。全ターゲット天体に対して ^{12}CO (J=1–0) 及び ^{12}CO (J=3–2) を用いて 2000 から 3000 AU の空間グリッドでマッピングを行った結果、天体が存在する方向のみから回転円盤の決定的特徴であるダブルピークプロファイルの取得に成功した。現在では観測結果を再現する円盤モデルが多数開発されており放射輸送計算を駆使することにより円盤の温度や密度構造を導くことができる。我々は複数の異なる CO 放射の光学的厚みの違いを利用し、理論モデルとの整合温度と各々の CO 同位体分子の回転遷移線に対する鉛直方向に沿った放射層の位置を見積もることで円盤の鉛直方向の温度分布を算出した。その結果、少なくとも 2 つの異なる温度層が円盤内に存在し中心星から 100 AU 離れた低温側の温度は約 10 - 20 K、高温側の温度は 30 - 40 K となった。そして上空ほど高温で赤道面近傍では低温であることが判明した。この結果は理論的に予測されるパッシブディスクの描像とよく一致する。

円盤の動径方向の密度構造は理論的にも良く理解されていないが、半径に対してべき乗分布を仮定すると理論モデル計算と観測結果が良く一致する事が経験的に知られている。近年の著しい観測装置の発展のおかげで、これまで観測が困難であった円盤外縁部の希薄なガス成分に対して観測が可能となってきた。我々が進めてきた高感度の CO マルチライン観測でも、密度が低い円盤外縁部を反映する光学的に厚いラインではピーク間隔が狭く、密度が高い円盤内縁部を反映する光学的に薄いラインでは広くなる結果が得られた。これは円盤がケプラー回転していると考えれば自然に説明ができ、円盤の粘性進化について観測的事実からアプローチが可能となってきた。しかしこれまで適用されてきたべき乗則モデルの場合、円盤の外径を決定するとその場所を境界として密度がゼロとなりカットオフを伴った構造となる。最近では円盤外縁部で緩やかな密度減少を組み込んだ相似解モデルが導入され、ダスト連続波の観測で良い成果が報告されているがガス観測での導入例はない。そこで、相似解モデルと従来のべき乗則モデルを比較した結果、天体によって最適なモデルが異なることが判明した。HD31648 の円盤に対しては相似解モデルの方が観測結果と良く一致するが、より進化の進んだ HD163296 の円盤に対してはべき乗則モデルの方が観測結果と一致する。更なる検証が必要であるが、これは HD163296 の円盤では進化が進みガスが散逸しつつあり全体的に密度が低いため、外縁部で生じていると推測される緩やかな密度減少がそもそも検出されないためと考えられる。尚、HD169142 の円盤は face-on 天体であり、それぞれの CO のプロファイルのピーク間隔がほぼ同じであるため、円盤のサイズを明確に反映することができない。そのため、観測結果が双方のモデルで再現するので密度構造や進化段階について制限することができていない。

原始惑星系円盤では磁気流体不安定 (MRI) の発生が理論的に予測されている。MRI は円盤内で乱流を引き起こすのでガスの散逸原因の有力候補となる。MRI は温度や磁気圧等の物理量に依存するが、そのほとんどが他の観測で見積もられているので、基本的には円盤の電離度が分かれば MRI の存在が分かる。よって、主な電子の供給源である HCO^+ 分子を選択し J=1–0 輝線で観測を行った。その結果、MRI を引き起こすのに必要な電離度 (約 10^{-10} - 10^{-12}) 以上である 10^{-9} が達成しており、MRI が発生している可能性が示された。円盤ガスの散

逸機構には不明な点が多いが少なくとも中心星から数 100 AU 離れた場所で乱流が起こっている可能性が示されたこととなる。

惑星系の多様性は進化の初期段階の原始惑星系円盤の多様性によって決定されると考えられている。天体数を増やすことによって、円盤の密度構造と進化段階を関係づける事が可能である。本論文の結果は星・惑星系形成シナリオを構築するための新たな情報を提供するとともに、観測及び理論の面で今後の更なる研究の発展に寄与すると期待される。

Contents

Chapter 1

Introduction

1 Star Formation

1.1 Star Formation Scenario for Low Mass Stars

The formation of low-mass star, like our Sun, is one of the most fascinating topics of the modern astronomy. The understanding of the origin of the solar system has now been tremendously progressed and the star formation scenario has refined and improved based on observational verifications. While star is forming, the remaining gas and dust material forms what is frequently referred to by astronomers as a protoplanetary disk surrounding the star. Observations toward the solar system and exoplanetary systems indicate that planets form in such a protoplanetary disk. The central star and the disk surrounding it evolve together and construct a star+disk system bounded gravitationally, so it is first necessary to consider when and how the star formation begins.

Star formation begins in dark clouds and giant molecular clouds (GMCs) that are made of molecular gas and dust in a mass ratio of approximately 100 : 1. Molecular clouds are typically 10 - 100 pc in size, 10^3 - 10^5 $M_\odot$ in mass, 10^2 - 10^5 cm^{-3} in density, and $\simeq$ 10 K in temperature. High density portion in molecular clouds, a molecular cloud core, contracts by a factor of a million in size to form a star. A molecular cloud core as a whole are known to have angular momentum and its rotation becomes faster and increase centrifugal force as it contracts. The core continues contracting in an early stage of contraction since the inward gravitational force exceeds the outward centrifugal force. Then, the centrifugal force counteracts the action of contraction after the core achieves compact enough and the contraction finally stops. However, the infall motion continues in the direction of rotational axis because the centrifugal force does not act in the direction. The molecular cloud core in spherical shape, therefore, eventually becomes disk-like geometry. It is thought that the disk with nearly 100 AU in radius and $\simeq$ 0.01 - 0.02 $M_\odot$ in mass is formed in the case of an object with solar mass scale.

The disk is known to be protoplanetary disk that mainly consists of molecular gas. A small amount of dust, which is responsible for characterizing disk thermal structure, settles toward the mid-plane of the disk. As further dust settlement onto the mid-plane of the disk, the disk becomes gravitationally unstable and finally splits into a number of small celestial bodies with $\sim$ 10 km in size, so called planetesimals, are formed. The planetesimals that rotate around the central star experience a series of collisions with each other, leading the formation of several precursors of planets, i.e. protoplanets. The effect of gravitational attraction between planetesimals located near central star is small due to significant gravitational force acting from central star. As a result, the planetesimals encounter a collision with others orbiting only near site and can accumulate less material in the inner disk than the outer disk, therefore, the protoplanets form in smaller size. In addition, the protoplanets are formed quickly because collisions occur with greater frequency due to higher number density of protoplanets and with high rotational velocity motion around the central star. In the region distant from gravitational effect from the central star, on the other hand, the protoplanets rotate in low Keplerian velocity and the orbital spacing between protoplanets become wider and, as results, protoplanets grow slowly in interplanetary wide-open space. Since dust including ice is in abundant supply in low temperature environment, protoplanets with larger mass than terrestrial planets can be formed with comparative ease. A rapid gas accretion starts after the mass of the cores exceeds $\sim 10\ M_\oplus$ if the gas still sufficiently remains in the disk. Thick-layered atmosphere is formed and covers the cores. The continuation of disk gas accretion is facilitated as the mass of the protoplanets increases and a giant gas planet, such as Jupiter, eventually forms. In the region more distant from the central star, low number density of planetesimals and low orbital velocity cause less collision and it takes time longer for the formation of protoplanets. A small amount of gas is supplied to protoplanets because most of gas is already dispersed before the core grows large enough to capture the gas. Hence, an icy giant planet (Neptunian planet), such as Uranus or Neptune, has a thin layer of atmosphere. It is estimated that the gas disk of the solar system disappears in $\sim 10^7$ years and it took $\sim 10^8$ years until the planetary system in present day had formed.

The central star gains mass from the disk during the period of disk formation. The temperature rises as the central star contracts and finally reaches $\simeq 10^7$ K that is capable of nuclear fusion of hydrogen in the center of the star. The central star evolves forward to a so-called main sequence star. It is recognized that most of the material of typical star is provided through the disk and a small amount of mass left from the accretion leads to form a planetary system. The theoretical study of a star formation process has improved and now verified the correctness of our understanding based on observational evidence. The observational studies in multi-wavelength are essential to look overall structure and physical properties of the protoplanetary disk in each evolutionary phase.

1.2 Classification of Spectral Energy Distributions

The infrared (IR) spectral energy distribution (SED) is measured through broad-band photometry and classified by its shape. The SED classification that is based on the IR spectral index ($\alpha_{\rm IR}$) first proposed by Lada (1987) and subsequently refined several times. $\alpha_{\rm IR}$ is defined by

$$\alpha_{\rm IR} = \frac{d{\rm log}\lambda F_\lambda}{d{\rm log}\lambda} \tag{1.1}$$

and usually measured by two fixed wavelengths: 2.2 μm (K-band) and 10 μm was used before, but in recent studies 2.2 μm and 24 μm, which is one of the Spitzer bands for the long wavelength, are widely used. Photons emitted from the central star is absorbed by circumstellar dust and re-emitted at longer wavelengths. This reprocessing effect by the material in the circumstellar environment is characteristic of an earlier evolutionary phase. Therefore, the significance of the reprocessing provides a good measure of how evolved a star+disk system. Figure 1.1 shows four SEDs for each class with corresponding density map and schematic illustrations. The prevailing SED classification is as follows:

- Class 0

  It is deeply embedded and obscured by the dense circumsteller gas and dust that resides in the infall envelope and thus its emission hardly comes from deep inside of the core. The SED of the class 0 objects shows that of a cold black body with temperature less than 30 K (André et al. 1993). As a result, SED has a peak in the far-IR or sub-mm and no measurable flux emitted in the near or mid-IR (André et al.

1993). The luminosity of class 0 objects is produced by gravitational energy released by infalling the gas and dust in the molecular cloud core. It typically lasts for $\sim 10^4$ years, which is one oder of magnitude shorter than the free-fall time ($\tau_{ff} \sim 1/\sqrt{G\rho}$) of the molecular cloud core. Class 0 objects are typically interpreted as protostars that accompany highly active jet and outflow. Historically, the Class 0 source was introduced by André et al. (1993) and was added to the classification scheme originally proposed by Lada (1987).

- Class I
  SED has peak in the mid- or far-IR and a positive slope ($\alpha_{\rm IR} \gtrsim 0$) in the near-IR range. Class I objects are the most luminous at far-IR around 100 μm (Lada 1987). They are inferred to be embedded protoplanetary disks in substantial circumstellar envelopes. The SED of class I is hotter than that of class 0 since the amount of circumstellar material is smaller and therefore, more emission from the core can be detected even though mass infall is still on-going. The outflow is still in active and bipolar cavities or shells are found by near-IR and radio observations (Tamura et al. 1991; Fuente et al. 1998). Disk-like structure with a size of $\sim$ 100 - 1000 AU is formed around the central star. Class I phase continues for $\sim 10^5$ years, corresponding to the free-fall time.

- Class II
  SED has a negative slope ($-1.5 \lesssim \alpha_{\rm IR} \lesssim 0$) in the near and mid-IR range, but still shows a significant IR excess emission between mid-IR and millimeter ranges. This excess is due to an accretion disk around the central star. Class II objects are referred to as classical T Tauri stars (CTTS) whose Hα equivalent width is greater than 10 Å. These are optically visible pre-main-sequence stars with a disk, but little or no remaining envelope. Therefore, mass accretion onto the central star has stopped as well as outflow. The objects between Class I and II eventually appears on a curve known as the birthline in the Hertzsprung-Russell (HR) diagram. The class II objects are thought to have an age of $\sim 10^6$ years.

- Class III
  SED shows almost identical to that of a stellar photosphere and $\alpha_{\rm IR}$ is $\simeq$ -1.5. Class III objects, which is often referred as Weak-line T Tauri stars (WTTS) are the most evolved pre-main-sequence stars with very thin or no disks. The life time of class III objects is $\sim 10^7$ years, i.e., the Kelvin-Helmholtz timescale ($\tau_{KH} \sim GM^2/rL_*$, where G is the gravitational constant and M, r, and L_* is the mass, the radius, and the luminosity of the object) for solar mass object is $\simeq 3 \times 10^7$ years.

An additional sub-class characterized by a significant deficit of flux in the near-IR and a substantial IR excess in the mid- and far-IR has been proposed after new spectra obtained by Spitzer Space Telescope (SST) with highly improved resolution in the IR. It had revealed stars with inner disks that are mostly devoid of small dust grains. These objects are referred to as "transitional disks" and thought to be the bridge between class II and class III objects; CoKu Tau/4 (D'Alessio et al. 2005), TW Hya (Calvet et al. 2002), GM Aur and DM Tau (Calvet et al. 2005), CS Cha (Espaillat et al. 2007a). More recently, disk gaps in optically thick protoplanetary disks in early evolutionary phase has been found by Espaillat et al. (2007b). Significant near-IR excesses when compared to the well-known median SED of T Tauri stars and previously studied transitional disks suggest the incipient development of disk gaps. As a result, "a pre-transitional disk", which is speculated to be a precursor of transitional disk, is newly proposed as a new sub-class between class II and transitional disk stage.

Observations of dust continuum emission provide a lot of protoplanetary disks' properties and a large number of objects over a broad range of wavelengths are amassed as many as statistical analysis can be safely made. Near- and mid-IR emission comes from the inner disk within 1 AU, where the disk is optically thick at

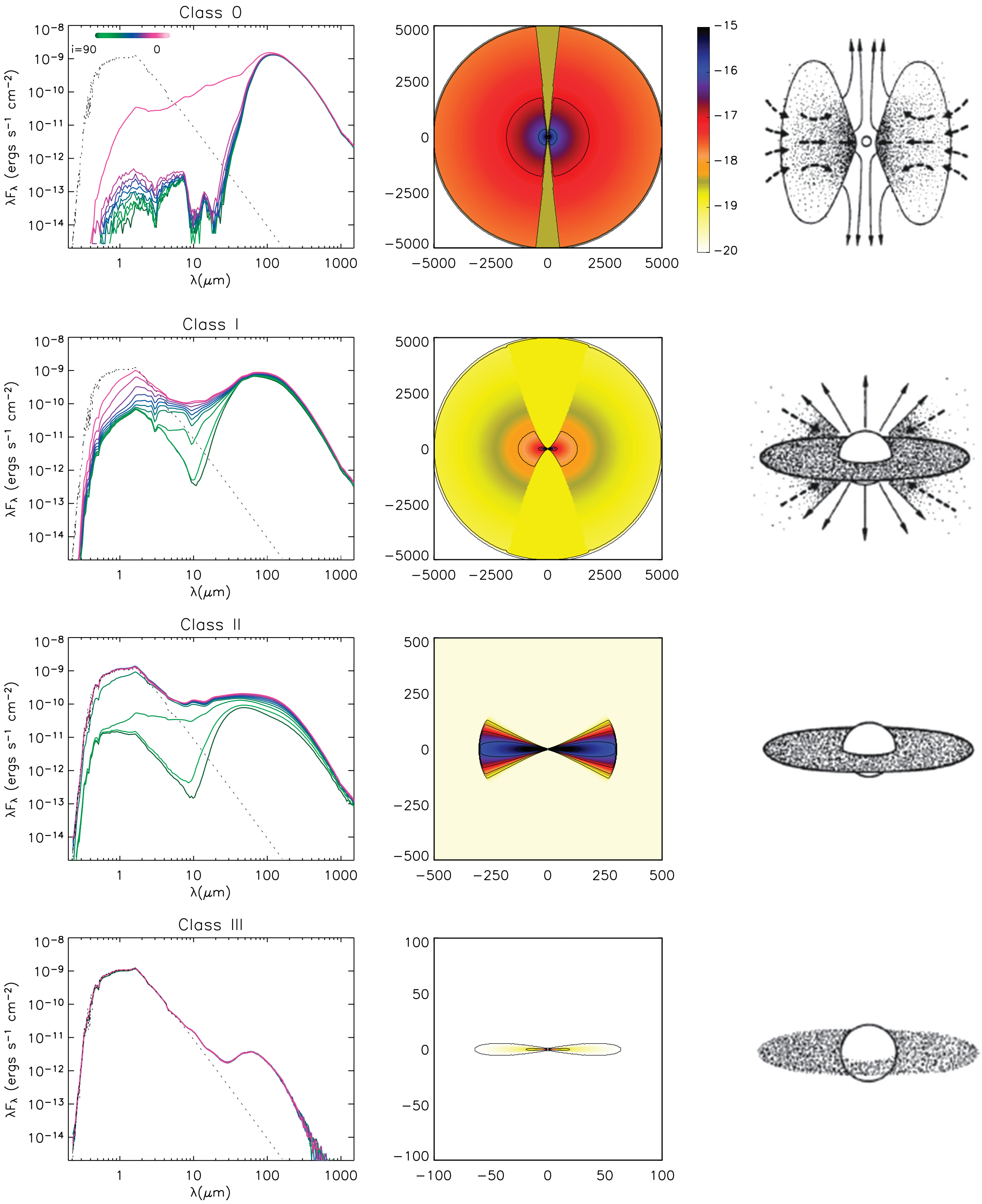

Figure 1.1 Young Stellar Object (YSO) classification for solar-mass stars. (Left): SEDs of star+disk system in each class are provided. (Middle): Corresponding density distribution map to the SEDs on the left panels are calculated by Whitney et al. (2003). (Right): The general geometrical views corresponding to each class are also provided as a reference (Lada 1987; André 1994).

these wavelength in most cases, while longer wavelength emission primarily comes from the outer disk in low temperature. The total dust mass (gas + dust) in the disk can be derived form the dust continuum emission at mm wavelengths and therefore the total disk mass can be estimated despite significant uncertainties in gas-to-dust ratio. Disk masses derived from standard assumptions range between 0.1 - 0.001 $M_{\odot}$ and the median disk mass is approximately 1 % of the stellar mass in class I and Class II stages.

1.3 Solar System Formation Scenario

Ever since an exo-planet around 51 Pegasi was first discovered (Mayor & Queloz 1995), more than 600 of exo-planet candidates were reported by September 24, 2011 (see Figure 1.2). Although it is an unofficial report, Kepler Space Telescope (KST) discovered 1235 exo-planets candidates by February 1, 2011. Therefore, planetary systems like our solar system ubiquitously exist and their structures and diversity including the variety of sizes, masses, densities, orbital sizes, and reflectivity of these planets, how many planets there are in multiple-star systems, the distribution of sizes and shapes of the orbits, and the abundance of terrestrial and larger planets in or near the habitable zone of a wide variety of stars, have now become next main scientific objectives.

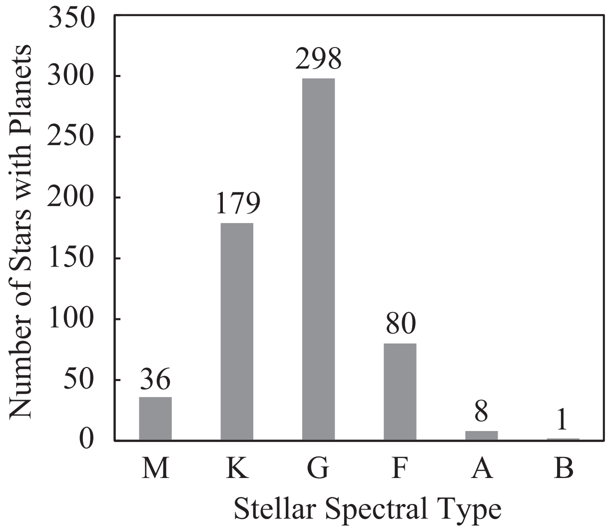

Figure 1.2 The number of stars with planets. The graph is made based on the information provided by the Extrasolar Planets Encyclopedia (http://exoplanet.eu) in September 2011.

The solar system is thought to be evolved from a "premordial solar nebula" like a protoplanetary disk around a young star. Therefore, it is instructive to study the formation process of protoplanetary disk for understanding solar system formation process. A general groundwork of solar system formation scenario was laid by Safronov (1969) and Hayashi (1981). The difference between Safronov model and the Hayashi model (Kyoto model) is how terrestrial planets evolve from planetesimals, terrestrial planets evolve in the absence of gas in the disk in the Safronov model while terrestrial planets evolve in the disk gas and they capture the gas during their formation in Kyoto model. Kyoto model has developed to core-accretion disk model which is widely accepted as a standard theory for planet formation (Kokubo & Ida 2002). The following important hypotheses form as a base for the standard model.

(1) Disk Hypothesis

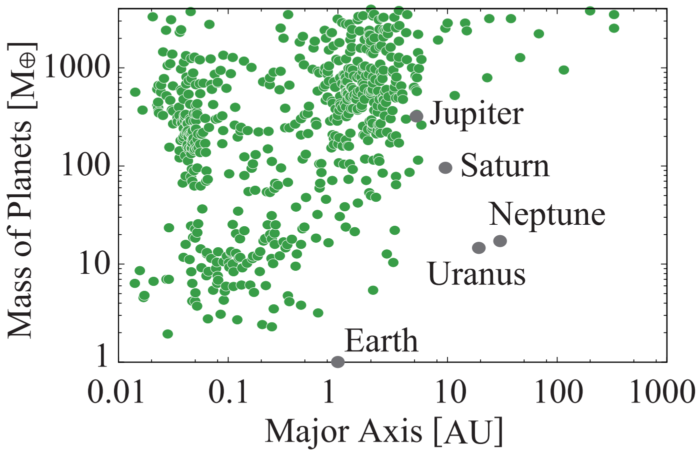

Figure 1.3 The relation between exoplanets' orbit and mass. The solar planets are plotted on the diagram as a reference (ref. http://exoplanet.eu).

- A planetary system forms from a low-mass protoplanetary disk that is a by-product of star formation.
- A protoplanetary disk consists of gas and dust.

(2) Planetesimal Hypothesis

- Planetesimals with a few kilometers in size are formed from dust.
- Solid planets are formed by gravitational aggregation of planetesimals that are revolved around the Sun.

It is still unsolved how the dust grains grow in a protoplanetary disk to kilometer size objects. There is a controversial issue if the dust can grow in turbulent gas in the disk. Dust diffuse out of the disk with the gas if the dust remains in small size (0.1 - 1 μm). Furthermore, dust is known to be negatively charged by electrons in the stellar wind. Dust must overcome Coulomb's repulsive force somehow. The inward orbital drift due to drag force by the disk gas acting on meter-sized bodies is significant and they fall onto the central star in a few hundred years. The standard model for formation of the solar system is based on the "minimum mass" solar nebulae model, in which the disk has minimum mass to reproduce terrestrial and giant gas planets in present-day solar system. The general formation scenario of solar system based on the standard model is as follows:

(1) A protoplanetary disk with $\simeq$ 0.01 - 0.02 $M_\odot$ in disk mass forms.

(2) Planetesimals form after dust sedimentation on the mid-plane of the disk.

(3) Solid cores of terrestrial and jovian planets are formed by gravitational aggregation of planetesimals.

(4) Planetary atmosphere collapses after the mass of core reaches to $\simeq$ 10 $M_\oplus$. If the disk gas still remains around the core, the gas flows onto the planet. Jupiter and Saturn are thought to be formed in this manner.

(5) The gas in the disk disperses into the interstellar space and finally disappears.

(6) Uranus and Neptune can not have a thick atmosphere because most of gas already dissipated when their cores grow to a sufficiently large size.

The formation of giant gas planets is well explained by the core accretion model (Kokubo & Ida e.g. 2002). When the mass of the core grows to $\simeq 10\ M_\oplus$, the gas flows onto the planet if it still remains in the disk. Since the more massive planets can take the more gas in and progress faster, giant gas planets are formed through the gas accumulation process at an accelerated rate. The planets continue to gain mass until gaps in the disk are created around the their orbits or the gas in the disk dissipates. The more massive cores can generally form far from the Sun where the surface density of dust component is high. In the region beyond the snow line at 2.7 AU from the Sun (see Figure 1.4), the dust surface density increases by more than three times due to an aggregation of H_2O ice. Therefore, giant gas planets are easily formed beyond the snow line. Note that giant planets can form even inside the snow line if the natal disk is sufficiently massive.

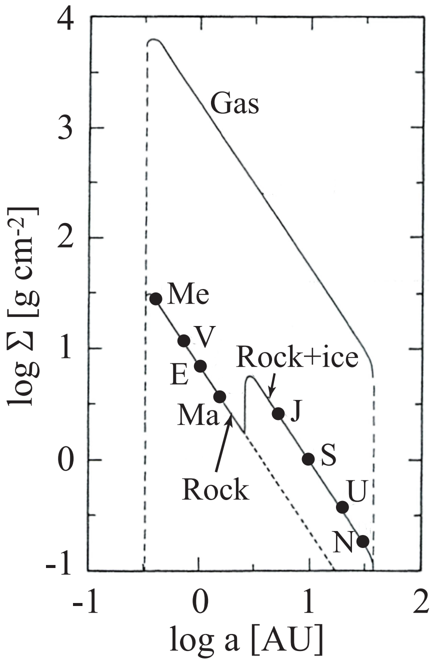

Figure 1.4 Radial surface density distribution of dust and gas for the solar system. Positions of the planets are plotted on the diagram and denoted by an initial letter of each planet, Me, V, E, Ma, J, S, U, and N, respectively (Hayashi 1981).

The core formation takes for a long time at a location far more distant from the Sun. The gas in the disk had been dissipated when a core outside the Saturn's orbit grew as large as critical mass and, as a result, no giant gas planet could form beyond 10 AU in distance. Sice the protoplanetary disk around TTSs have insufficient gas to form even Neptunian mass planets and thus giant planets must be formed at least within a few million year lifetime of protoplanetary disk. Furthermore, the disk fraction in the youngest (1 Myr) star clusters is close to 100 % but the number of disks drops rapidly with time and almost no disks remain in 10 million year-old clusters (Beckwith et al. 1990). This observational result implies that typical disk lifetime is a few million years. This in turn sets a strict limit on the timescale of the formation of giant gas planets.

In the core accretion model, surface density distributions for dust and gas are expressed by

$$\Sigma_{\rm d}(r) = 7 \times f_{\rm d}\eta_{\rm ice}\left(\frac{r}{1{\rm AU}}\right)^{-3/2} \quad [{\rm g\ cm^{-2}}] \tag{1.2}$$

$$\Sigma_{\rm g}(r) = 2400 \times f_{\rm g}\left(\frac{r}{1{\rm AU}}\right)^{-3/2} \quad [{\rm g\ cm^{-2}}] \tag{1.3}$$

where f_d and f_g are scaling factors. If the gas-to-dust ratio is the same as the Sun,

$$f_d = f_g. \tag{1.4}$$

$f_d = f_g = 0.7$ for minimum mass solar nebulae model. Note that if the radial surface density of the disk decreases as a function of r with a power of $-3/2$, f_d and f_g should be $\sim$ 0.1 - 10 from total disk mass obtained by millimeter observation (see also Figure 1.4). $\eta_{\rm ice}$ is an augmentation factor of the surface density due to H_2O condensation and given by

$$\eta_{ice} = \begin{cases} 1 & \text{for } r < r_{\rm ice} \\ 4.2 & \text{for } r > r_{\rm ice} \end{cases} \tag{1.5}$$

where $r_{\rm ice}$ is the distance to the snow line. If the disk is optically thin, the radial temperature distribution derived by equating a stellar radiation with black body radiation from a particle is

$$T \simeq 280 \left(\frac{r}{1\mathrm{AU}}\right)^{-1/2} \left(\frac{L_*}{L_\odot}\right)^{1/4} \quad [\mathrm{K}], \tag{1.6}$$

where L_* is the stellar luminosity and normalized by solar luminosity ($L_\odot$). H_2O condenses at 150 - 170 K and therefore $r_{\rm ice}$ at 170 K for a star of 0.5 - 3 $M_\odot$ in stellar mass (M_*) will be

$$r_{\rm ice} = 2.7 \left(\frac{L_*}{L_\odot}\right)^{1/2} \simeq 2.7 \left(\frac{M_*}{M_\odot}\right)^2 \quad [\mathrm{AU}]. \tag{1.7}$$

The snow line of the solar system is located at 2.7 AU from the Sun, corresponding to the location between Mars and Jupiter. It is consistent with the boundary between terrestrial and giant gas planets in our solar system. The density at the mid-plane of the disk (ρ_0) for solar system is

$$\rho_0 = \frac{\Sigma_{\rm g}}{\sqrt{\pi} h} \simeq 2 \times 10^{-9} f_g \left(\frac{r}{1\mathrm{AU}}\right)^{-11/4} \quad [\mathrm{g\ cm^{-3}}], \tag{1.8}$$

where h is the scale height and expressed by

$$h = \frac{\sqrt{2} c_s}{\Omega_{kep}} \simeq 4.7 \times 10^{-2} \left(\frac{r}{1\mathrm{AU}}\right)^{-5/4} \quad [\mathrm{AU}], \tag{1.9}$$

where c_s is the sound of speed and estimated to be

$$c_s \simeq 1 \times 10^5 \left(\frac{T}{300K}\right)^{1/2} = 1.1 \times 10^5 \left(\frac{r}{1\mathrm{AU}}\right)^{-1/4} \left(\frac{L_*}{L_\odot}\right)^{1/8} \quad [\mathrm{cm\ s^{-1}}] \tag{1.10}$$

It is also important to overview disk formation by considering angular momentum. Molecular cloud cores maintained in hydrostatic equilibrium in star-forming molecular clouds are observed to have angular velocities (Ω_c) of order $\sim 10^{13}$ - 10^{14} rad s^{-1} (Goodmann et al. 1993; Zuckerman & Matthew 1996; Caselli et al. 2002). The sound of speed (c_s) in molecular cloud at temperature $T \simeq 10$ K is $\simeq 0.2$ km s^{-1}. The star-forming density (ρ) for low mass Sun-like stars induced by Jeans collapse can be estimated by

$$M_J \simeq \frac{{c_s}^3}{G^{3/2} \rho^{1/2}} \tag{1.11}$$

and exceeds $\sim 10^{-19}$ g cm^{-2}. The sizescale that surrounding materials fall inward (R_J) obtained by

$$R_\mathrm{J} \simeq \frac{c_\mathrm{s}}{\sqrt{G\rho}} \tag{1.12}$$

and calculated to be $\simeq 0.1$ pc. The specific angular momentum of the collapsing core (J_c) is thus

$$J_\mathrm{c} \simeq \Omega_\mathrm{c} R_\mathrm{J}^2 \simeq 10^{21-22}\ [\mathrm{cm}^2\ \mathrm{s}^{-1}]. \tag{1.13}$$

The maximum angular velocity at which the core can rotate without breaking (Ω_break) can be calculated by equating centrifugal acceleration with gravity and expressed by

$$\Omega_\mathrm{break} = \sqrt{\frac{GM_*}{r_c^3}}, \tag{1.14}$$

where r_c is the radius of the core. Ω_break for a star like the Sun therefore will be $\sim 10^{-3}$ s^{-1}. A maximum specific angular momentum to keep the core gravitationally bound (J_break) is thus

$$J_\mathrm{break} = \Omega_\mathrm{break} r_*^2 \simeq 10^{18-19}\ \mathrm{cm}^2\ \mathrm{s}^{-1}, \tag{1.15}$$

where r_* is the radius of the central star. According to the estimation from equation 1.13, it is clear that $J_\mathrm{break} \ll J_\mathrm{c}$ and young stars have much lower angular momenta than the gas clouds. The angular momentum of order $\sim 10^{-2}$ – 10^{-4} cm^2 s^{-1} needs to be lost during the star formation. Due to rapid reduction in size during collapse continuing for nearly 10^5 years, the star-forming cloud with small amount of initial rotation drastically gains angular velocity and forms into geometrically thin shape, as known as a disk at the end of gravitational collapse. Typical disk size of 100 - 1000 AU corresponds to the radius that is expected from J_c. Primordial solar nebula must also have such a radius.

2 What are Herbig Ae/Be Stars?

Herbig Ae/Be (HAeBe) stars, named after Herbig (1960) who works first in a systematic way, are widely recognized as intermediate mass counterparts of low mass T Tauri stars (Waters & Waelkens TTSs, 1998). About 300 HAeBe stars with 1.5 - 8 $M_\odot$ in stellar mass, 1 - 10^4 $L_\odot$ in stellar luminosity, 8000 - 30000 K in effective temperature, and 10^5 - 10^7 years in stellar age are summarized in a catalog (Thé et al. 1994). In the past 20 years or so, the formation of intermediate mass stars between 1.5 and 3 $M_\odot$ and between 3 and 8 $M_\odot$ has become a great of interest. The lower limit of mass corresponds to the mass that stars are relatively stable during their quasi-static contraction. The upper limit of mass corresponds to the mass that hydrogen burning begins in the inner core of stars. The stars with more than 8 $M_\odot$ do not experience pre-main-sequence stage which both HAeBe stars TTSs do and hydrogen burning and infall occurs at the same time. The characteristics among TTSs, HAeBe stars, and high mass stars have become clear and therefore it has been capable of making their distinction possible. Pre-main-sequence stars with more than 2 $M_\odot$ are expected to follow a radiative track, so-called Henyey track that low mass stars less than 0.5 $M_\odot$ do not follow, after the end of Hayashi track. Stars more than 8 $M_\odot$ do not experience pre-main-sequence star time and exist as obscured objects. Therefore, the evolution process of intermediate mass pre-main-sequence stars is qualitatively different form those of low mass TTSs and high mass stars. The formation of low mass TTSs can take place in giant molecular cloud, as well as in less massive dark cloud, while massive stars form only in giant molecular clouds[1]. HAeBe stars can be regarded as an interface between low mass and high mass star formation (Appenzeller 1994).

As introduced in Section 1.3 in this chapter, an enormous number of exo-planets have been discovered so far around not only low-mass Sun-like stars but stars more massive than the Sun. β Pictoris (β Pic) is a $\sim$ 20 million year old main-sequence star with A in spectral type, a little smaller than Vega and thought to have planets (Barrado y Navascués et al. 1999). The Infrared Astronomical Satellite (IRAS) detected remarkable excesses at $\lambda \gtrsim 12$ μm and subsequent optical imaging detected the dust disk stretching out up to 1400 AU (Smith & Terrile 1984; Crifo et al. 1997). Mid-infrared observation revealed disk structure more detail and the observed sub-μm amorphous silicate peaks indicated the presence of three ring-like distributions of planetesimals at 6, 16, and 30 AU from the central star (Okamoto et al. 2004). Finally, a giant gas planet orbiting 8 to 15 AU from a central star was directly imaged (Lagrange et al. 1997). Star+disk system like β Pic or Vega must experienced pre-main sequence stage before become a main-sequence star. Possible precursors of such stars can be intermediate mass pre-main-sequence HAeBe stars.

In comparison with TTSs, there are advantages and disadvantages in observing HAeBe stars and they are summarized as below,

(1) Advantages

- HAeBe stars are brighter than TTSs and typically it is easier to be observed.
- The disks around HAeBe stars are sufficiently warm so that depletion of gas species by freezing hardly occurs.

(2) Disadvantages

- Statistical analysis is difficult because only small number of nearby HAeBe stars are available for observations.
- HAeBe stars have more unknown factors than TTSs do.

The targets should be carefully selected based on the observational purposes. The initial mass function (IMF) induces a fact that the more massive the stars are, the fewer the number of stars exists. Statistical analysis on HAeBe stars definitely need TTSs' data to compensate for their deficiencies in sample quantity.

2.1 Definition of Herbig Ae/Be Stars

The definition of HAeBe stars was modified since Herbig (1960) first proposed. The following definitions summarized by Waters & Waelkens (1998) are now widely accepted.

(1) Pre-main sequence emission stars with A or B in spectral type.

(2) Infrared excess due to circumstellar dust must be seen.

(3) The luminosity class must be between Ⅲ and V.

Criterion (1) indicates that the disk is geometrically thin because the stellar radiation is visible as an emission line. Criterion (2) excludes the objects with IR excess due to free-free emission from ionized gas in a circumstellar disk. Criterion (3) excludes the $B_{[e]}$-supergiants, which are massive post-main-sequence stars (Zickgraf

[1]It is recently suggested that high mass stars can be formed through collision between molecular clouds by radio observations and approximately 10 % of high mass stars might be created through the cloud - cloud collisional process (Y. Fukui 2012, workshop at Ibaraki University)

et al. 1986). The other definitions and suggestions are made by Davies et al. (1990) and van den Ancker et al. (1997a) and theirs are similar to the ones provided above. Note that early F-type pre-main-sequence stars are also recently included. HD 142527, for example, is recognized as a Herbig F star. The objects can be recognized as HAeBe stars if and only if all of the above criteria are met.

2.2 Basic Observed Properties and SED Classification of Herbig Ae/Be Stars

Stellar winds, bipolar outflows, accretion, circumstellar disks, and envelopes associated with HAeBe stars have been found by observation from radio to X ray (Mundt & Ray 1994; Fuente et al. 1998; Edwards et al. 1993; Brooke et al. 1993; Cantó et al. 1984). The mass loss rate from stellar wind obtained by the IR HI recombination line is in the range 10^{-6} - 10^{-8} $M_{\odot}$ yr^{-1}, generally consistent with the radio data (Nisini et al. 1995). Physical properties for a number of HAeBe stars, such as effective temperature, luminosity, and mass, were derived from the observational results obtained by Hipparcos project. Then the observed HAeBe stars are plotted on the Hertzsprung-Russell (HR) diagram with the pre-main-sequence evolutionary tracks and the birthline calculated by Palla & Stahler (1993), as shown in Figure 1.5 (van den Ancker et al. 1998).

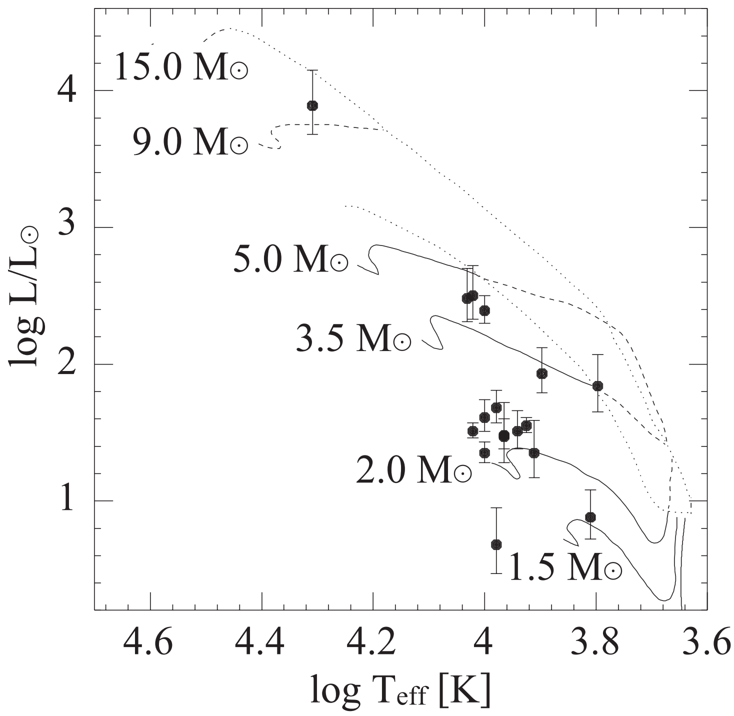

Figure 1.5 Hertzsprung-Russel (HR) diagram of HAeBe stars based on Hipparcos distance measurement taken from van den Ancker et al. (1998). Solid and dashed lines indicate the theoretical evolutionary tracks of pre-main-sequence stars. The upper and lower dotted lines are the birthlines for accretion rate of 10^{-4} and 10^{-5} $M_{\odot}$ year^{-1}, respectively by Palla & Stahler (1993).

The presence of circumstellar material around HAeBe stars is characterized by remarkable IR excess in the SED. The IR excesses that are observed in HAeBe stars originate from circumstellar accretion disks, as has been suggested for TTSs (Hillenbrand et al. 1992). Since the UV continuum, which can be attributed to hot gas directly irradiated by the central star, is also detected from the circumstellar gas disk in many HAeBe stars, the circumstellar disks around HAeBe stars have a wide range in temperature, significantly higher than the stellar effective temperature (Meeus et al. 1998). Subsequently, a number of HAeBe stars have been studied by Meeus et al. (2001). The observations present ISO spectra combined with IR and sub-millimeter photometry

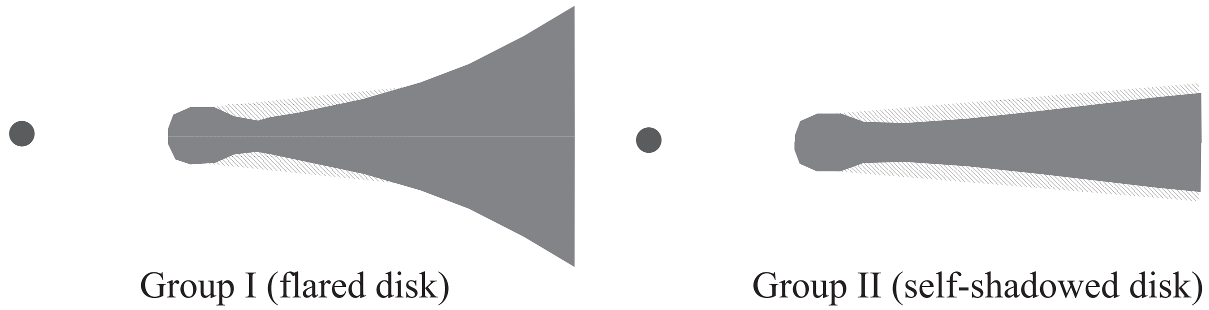

Figure 1.6 Schematic cross-sectional view of geometrical structure of disks in group I (left) and group II (right). Group I disk is frequently called flared disk while group II disk is called non–flared, self-shadowed disk, or sometimes flat disk.

by ground-based telescopes towards 14 HAeBe stars. After comparing the SED features of each object, the observed HAeBe stars can be classified into two main groups on the basis of the overall SED shape; group I and group II. Group I sources have a relatively strong far-IR flux, which is energetically comparable with the flux in the near-IR. Group II sources show a similar near-IR excess as group I sources, but their flux drastically falls off towards the far-IR. In addition to the characteristics in near- and far-IR excess in the SED, the groups can be further subdivided into two more subgroups under the condition whether 10 μm silicate feature appears or not (Meeus et al. 2001). Group Ia and IIa sources have the solid state band, while group Ib and IIb sources do not. Similar approach was conducted before and classified 47 HAeBe stars in three groups based on the slope of the IR continuum (Hillenbrand et al. 1992). These three groups were though to be created by different geometries of the circumstellar objects, i.e. only disks as group I and disks plus envelopes as group II. However, in order to explain the shape and intensity of the SED at far-IR in group II, the central object must be redder than the central star and as a result, group II should be composed of star and disk system (Natta et al. 1993a). Note that a low mass companion also accounts for the IR excess and possibly photometric amplitude variability in some degree. Spatially resolved map in subsequent observations also shows a central star and a disk surrounding it.

The difference of SED features of the two groups proposed by Meeus et al. (2001) were described by disk geometry (Dullemond & Dominik 2004, see also Dullemond et al. 2001; Dullemond 2002; Dominik et al. 2003). The distinction between group I and group II sources was examined quantitatively by the disk having a flaring geometry or not, as shown in Figure 1.6. The fraction of energy reprocessed by circumstellar dust is typically 30 - 50% in group I sources and about 15 - 30% in group II sources. A flaring disk captures and reprocesses more stellar radiation at large radii than self-shadowed disks do, and therefore naturally has a stronger far-infrared excess. However, it remained unclear what physical mechanism could cause some disks to be flaring and others to be flat. In fact, most of passive disk models (Chiang & Goldreich 1997; Dullemond et al. 2001) have a flaring geometry. A possible mechanism that could flatten a disk is dust settling. Due to the gravity by the central star, dust grains can slowly drift towards the mid-plane of the disk while the gas remains behind. Since the stellar radiation is absorbed almost exclusively by dust, the photosphere of the disk flattens as dust settling proceeds (Chiang et al. 2001). Chiang et al. (2001) also mention that the SEDs of these sources could only be fitted with the disk proposed by Chiang & Goldreich (1997) if the vertical geometric thickness was artificially reduced by a factor of about 3 to 5. They argue that this suggests that dust settling is a key mechanism for the group II type SEDs.

Photometric time variability in the emission profiles is also observed among HAeBe stars. The variability occurred in AB Aurigae (AB Aur), for example, was detected in optical and UV spectra with a period of 32±4 hours, corresponding to the estimated stellar rotation (Böhm et al. 1996). HD 163296 is the most extensively

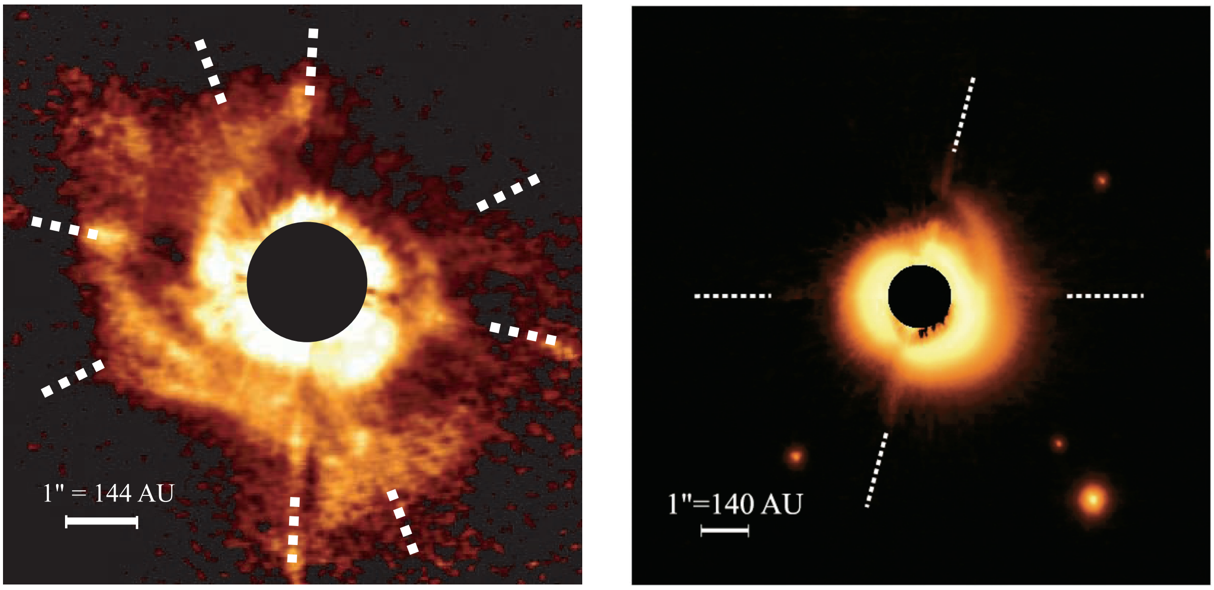

Figure 1.7 (Left): Direct H-band image of the circumstellar structure around AB Aur. The directions of the spider patterns are indicated by dashed lines. The inner area of 1.7" diameter filled by a dark circle (r < 120 AU) is photometrically unusable and is masked (Fukagawa et al. 2004). (Right): Same as the left figure configuration for HD 142523. The central mask radius is 0.66", corresponding to ∼ 90 AU (Fukagawa et al. 2006).

monitored star and the time variability of the scattered light from the disk arises probably because the scale height of inner disk wall changes within a few years. This phenomenon can induce variable self-shadowing of the outer disk. The azimuthal asymmetric disk structure is also responsible for producing an azimuthally asymmetric shadow on the outer disk (Wisniewski et al. 2008).

2.3 Disk Morphology and Structure

The morphology of the circumstellar disk has been a major subject of disk studies since direct images of the protoplanetary disks in the Orion nebula were first taken by Hubble Space Telescope (HST, McCaughrean & O'dell 1996). Infrared telescopes and millimeter and sub-millimeter interferometers have provided detailed information of disks around both TTSs and HAeBe stars, yielding information on the non-axisymmetric structure. Thanks to the recent instrumental improvements, a clear spiral arms in AB Aur and a banana split shape in HD 142527 shown in Figure 1.7 indicates that these disks should have complex structure and dynamical motion.

Recent millimeter and sub-millimeter interferometric observations have revealed two dimensional disk structure of HAeBe stars (Piétu et al. 2007; Isella et al. 2007). Temperature distribution along the vertical direction of the disk should also be taken into account when one examines how the gas and dust inside the disk evolve. Theoretical studies predict that flared circumstellar disks should have two or more layers with distinct temperature in vertical direction that are formed by diffusion of stellar radiation scattered at the disk surface (Chiang & Goldreich 1997; D'Alessio et al. 1999; Inoue et al. 2009). To examine vertical structure of the disks based on observations, it requires examples as many as possible, though several studies have already tried to make vertical temperature or density distributions unveiled (Panić et al. 2008; Dartois et al. 2003; Piétu et al. 2007; Akiyama et al. 2011). HAe stars, HD 163296, HD 169142, and HD 31648, are the best targets for this purpose because it exhibits strong emission from the disk in many CO isotopologue lines.

In the last few decades, it has been revealed that HAeBe stars are commonly accompanied by a circumstellar disk like TTSs by direct imaging at infrared and radio wavelengths (Fukagawa et al. 2004; Wisniewski et al. 2008; Mannings & Sargent 1997b; Mannings et al. 1997a; Piétu et al. 2003). These disks are believed to be the precursors of planetary systems around HAe stars, and are the important targets to study the formation process of a planetary system around an intermediate-mass star. Recent advanced instruments have revealed their physical properties, such as the disk mass, the radial temperature and surface density distributions, the outer radius of the disk, and the velocity field. The mass of individual planets at each orbit and time scale of planet formation can be estimated once the mass of the protoplanetary disk (or radial surface density distribution) is determined. The gas disks around HAe stars are suitable for structural analysis based on temperature or surface density with high accuracy, since HAe stars are brighter than TTSs and have little effect of CO depletion occurred at temperature below 20 K as described before. For instance, Panić et al. (2008) estimated the disk mass that is below 20 K in temperature in HAe star HD 169142 system. The CO freeze-out could be efficient only at the mid-plane in the outer disk region that contains about 8 % of the total disk mass. This small fraction is caused by the higher luminosity of HD 169142 than the typical luminosity of T Tauri stars. The number of well-studied disks around HAe stars, however, is still insufficient to establish a firm understanding of their physical conditions and their statistics; only a few of limited examples of their structure have deeply been analyzed (Panić et al. e.g., 2008; Piétu et al. e.g., 2007).

2.4 Evolution Process of Herbig Ae/Be Stars

The development of a theory for the stellar evolution of intermediate mass was performed and led to the establishment of the evolutionary tracks (Palla & Stahler 1993; D'Antona & Mazzitelli 1994). It revealed that intermediate mass stars have shorter lifetime in the pre-main-sequence stage. This kind of study also introduced a new concept of the birthline at which stars become optically visible. The location of birthline shows a good agreement with the observed locations of HAeBe stars in the HR diagram (Palla & Stahler 1990). The angular momentum evolution is also a great interest of HAeBe stars (ref. Section 1.3 in this chapter). The main sequence A and B stars tends to rotate rapidly but low mass stars, as a whole, rotate slowly. Therefore, measurements of the rotation velocity, v sin$i$, for HAeBe stars can provide a clue for answering the angular momentum evolution of intermediate stars (Böhm & Catala 1995).

The mass range in pre-main sequence stars has been examined in young open clusters and associations, such as M42 or NGC1333. As results from the studies, it was found that HAeBe stars are relatively rare in some clusters. The population of HAeBe stars is relatively high in M42 ($<$ 1 Myrs in mean stellar age) and NGG1333 ($\leq$ 1 - 2 Myrs in age), while only $\sim$ 10 % have IR excesses and no IR excess is present in at least 60 % of the objects in the 2 - 4 Myr old cluster NGC2244 (Bruhweiler et al. 2010; Hensberge et al. 2000; Pérez et al. 1987). The fraction of IR excesses seems to be larger in younger clusters (Hillenbrand 1997; Lada et al. 1996). Therefore, it is speculated that the lifetime of the HAeBe stars is typically the order of a few million years.

Dullemond & Dominik (2004) proposed an evolutionary scenario in which a protoplanetary disk evolve from a flared disk (group I) to self-shadowed disk (group II). They demonstrated a clear correlation among the SED slope, disk mass, and grain size through model simulations as shown in Figure 1.8. The remarkable results they obtained are as follows:

(1) The flaring disk models with 10^{-1} - 10^{-3} $M_{\odot}$ in disk mass have a strong far-IR excess, while the self-shadowed disk models, which are constructed by reducing disk mass of the flaring disk model to 10^{-4} - 10^{-6} $M_{\odot}$, have a weak far-IR.

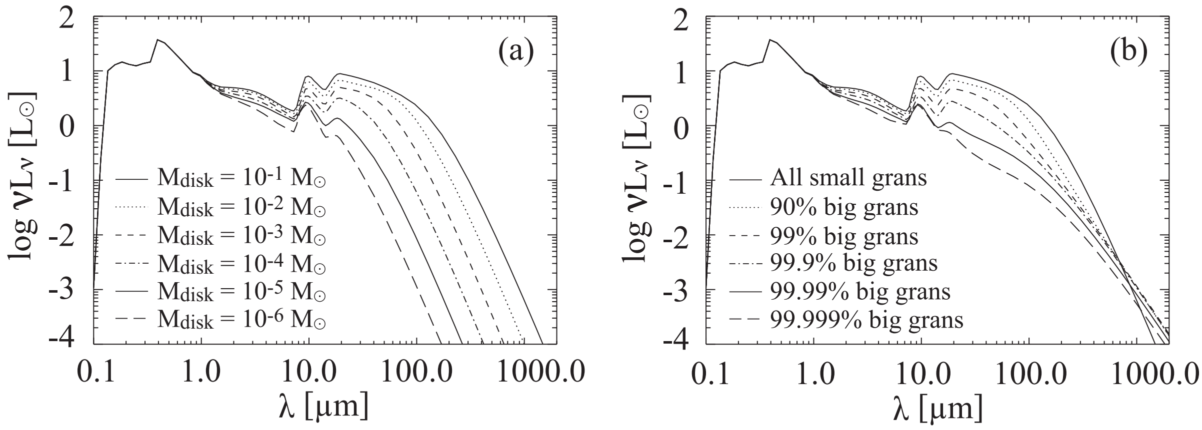

Figure 1.8 SED computed by Dullemond & Dominik (2004) model. Panel (a) shows SEDs of the disks with varying disk mass from 10^{-1} $M_\odot$ up to 10^{-6} $M_\odot$. Panel (b) shows the SED of panel (a) with reducing the amount of mass of small grains (0.1 μm in size). The total disk mass is maintained the same with the amount of mass adapted to the model described in panel (a)

(2) The SED curve in millimeter to sub-millimeter range changes from steep curve to Rayleigh-Jeans-like flat slope as the grains grow form 0.1 μm to 2 μm in the early stage of class II disks.

The consequences listed above seems to be consistent with the group I and II distinction. Since it is considered that the disk reduces their mass and grains grow larger as the disks evolve in core accretion disk model, the disks experience group I stage first and shifts to group II stage[2].

3 Single-Dish Telescopes vs Interferometers

The observations of protoplanetary disks in radio frequency are made by either single-dish telescopes or interferometers. The major characteristics of the both single-dish telescopes and interferometers are summarized below:

1. Single-Dish Telescopes

(1) Strength

- Higher sensitivity can be achieved in observation. No missing flux effect occurs (see interferometers characteristic below).
- Absolute flux scale can easily be determined.
- Data reduction is relatively simple.

(2) Weakness

- Less spacial resolution can be achieved. It is impossible to spatially resolve a disk.
- The observation can be greatly affected by the atmospheric emission, especially the observation in continuum.
- The antenna gain can fluctuate during observations for large diameter telescopes.
- It is not suitable for the image with large dynamic range.

[2]The disk evolution have recently been reconsidered among astronomers since several transitional disks with a large inner hole were discovered (details in Section 1.2 in this chapter). This observational evidence suggests that disk may evolve form group II to group I.

2. Interferometers

(1) Strength

- The highly resolved image can be obtained. The nearby disks ($d = \sim 100$ AU) can be spatially resolved.
- The observations are less affected by atmospheric emission because of uncorrelated component.
- The contamination from side lobes (confusion signal) can be eliminated by the phase rotation.
- The image with large dynamic range can be obtained.

(2) Weakness

- It is difficult to observe the diffuse gas component due to the spacial filtering.
- Data reduction is complex and usually takes long time to get a final image.

In principle, interferometers may lose the emission originated from the diffused gas in the outer region of the disk. Single-dish telescope is expected to have a higher sensitivity and can make up for deficiencies in detection of the uniformly distributed gas. Thus, interferometers are good at identifying the morphology of the disk in detail, whereas single-dish telescopes are suitable for obtaining the weak emission. Hence, observations such as a survey are often made by a single-dish telescope first, then interferometric observations aimed at detail and intensive research for particular objects of interest will be performed as a follow-up observation. The both single-dish telescopes and interferometers have a mutually complementary relationship.

4 Ionization Fraction of the Protoplanetary Disks

The evolution theory of an accretion disk (Lynden-Bell & Pringle 1974; Hartmann et al. 1998) is well explained in view of the viscous transportation of angular momentum and makes calculation of the amount of material, the location, and the timescale of planet formation possible. However, the observed timescale of the disk evolution, 1 – 10 Myr, is much shorter than the expected evolution timescale simply derived by the viscous transport of angular momentum due to only molecular viscosity. The framework of viscosity due to turbulence in accretion disks was developed by Shakura & Sunyaev (1973) and they successfully explained the timescale of the disk evolution by observations.

Several ideas about the cause of turbulence, such as gravitational instability including Kelvin-Helmholtz instability (Gammie (2001); Mann et al. (2009)), shear instability (Youdin & Shu 2002; Ishitsu & Sekiya 2003), and thermal convective instability (Lin & Papaloizou 1980; Cabot et al. 1987; Nomura 2002) have been proposed and the most compelling theory among them now is the magneto-rotational instability (Balbus & Hawley MRI, 1991; Sano et al. MRI, 2000). The fundamental principle of the MRI is fairly simple. In the effect of perturbing a weak vertical magnetic field penetrating an uniform disk, some fluid slightly moves inward and some slightly moves outward due to gas freezing to magnetic field lines. Because of differential rotation of Keplerian disk, perturbed magnetic field line will be sheared by the differential rotation of the disk. Since the magnetic field is too weak to maintain the original magnetic field configuration in the disk by magnetic tension, magnetic field line will snap and charged particles such as protons, electrons, and ionized gas molecules trapped and winded around the magnetic field line will be released in bursts. This effect causes a turbulence in the gas disk. The broken magnetic field line connects with the adjacent ones in the disk and recover to the original magnetic field configuration that threads vertically the disk. The magnetic field tension acts to reduce the angular momentum of the inner fluid element and accelerate that of outer fluid element. The transfer of angular momentum increases the separation more and more, and finally results in an instability (Armitage

2010). The cyclic process of connection and disconnection of magnetic field lines makes the instability invoke continuously.

It is essential to induce MRI that magnetic tension ($\sim B^2/4\pi$, where B is magnetic field) must be weaker than the pressure of the gas that is subject to frozen onto the magnetic field lines. Generally, MRI does not occur at the region higher than the scale height (h) because the gas pressure becomes lower at $z \gg h$ while B^2 remains the same. Thus, the magnetic field line little fluctuates and the magnetic field in the disk remains stable. MRI also needs sufficient time to carry on until the magnetic field lines dissipate from the fluid element. That is, the dissipation timescale of magnetic field line can be given by

$$\frac{h^2}{\eta_B} > \frac{h}{v_A}. \tag{1.16}$$

where v_A is Alfvén velocity ($B/\sqrt{4\pi\rho}$) and η_B is magnetic diffusivity and defined as

$$\eta_B = \frac{c^2}{4\pi\sigma_c}. \tag{1.17}$$

where c is the speed of light and σ_c is the electric conductivity. σ_c is directly proportional to the ionization fraction. The magnetic dissipation time directly depends on magnetic diffusivity. The ionization fraction of protoplanetary disk is typically low but it is estimated that MRI can be induced in the ionization fraction of 10^{-10} (Sano et al. 2000), depending on the physical conditions.

The source to ionize the gas would be the thermal dissociation by the radiation from the central star, UV or X-ray from the central star, and the external cosmic ray. The thermal dissociation is effective only at the region near the central star. The photo-dissociation by the UV and X-ray is also significant only at the region near the central star or disk surface because they can not penetrate into the dense gas region in the disk. The cosmic ray, however, can reach to the region of $\sim$ 100 g cm^{-2}, and thus it works effectively as a source of ionizing gas at the outer disk. MRI therefore can occur near the the central star ($r \lesssim 0.1$ AU), near disk surface, and at the outer disk ($r \gtrsim 10$ AU) and invokes MHD turbulence. However, the ionization fraction near the mid-plane of the disk at 1 AU $\lesssim r \lesssim$ 10 AU where it is important for planet formation is extremely low, and therefore there is expected to be no MRI, leading to no MHD turbulence. This annular “dead zone” is predicted and commonly accepted (Gammie 1996).

MRI strongly depends on the amount of ionized gas and magnetic field. Sano & Stone (2002) shows the evolution of the MRI in weakly ionized accretion disks and introduces the magnetic Reynolds number ($Re_{\rm M}$) as a criterion that determines MRI emergence. The definition of $Re_{\rm M}$ is possible in several ways and they define as

$$Re_{\rm M} \equiv \frac{v_{Az}^2}{\eta_B \Omega}, \tag{1.18}$$

where v_{Az} is the Alfvén speed only along the vertical component of the magnetic field, Ω is the angular frequency of the Kepler rotation of the disk. The condition for turbulence is given by

$$\frac{v_{Az}^2}{\eta_B \Omega} \gtrsim 1. \tag{1.19}$$

Note that this critical value is not affected by the strength and geometry of magnetic field in this definition and thus ionization degree is an important parameter for considering turbulence occurred in protoplanetary disks. If the $Re_{\rm M}$ is defined by

$$Re_{\rm M} \equiv \frac{v_A^2}{\eta_B \Omega}, \tag{1.20}$$

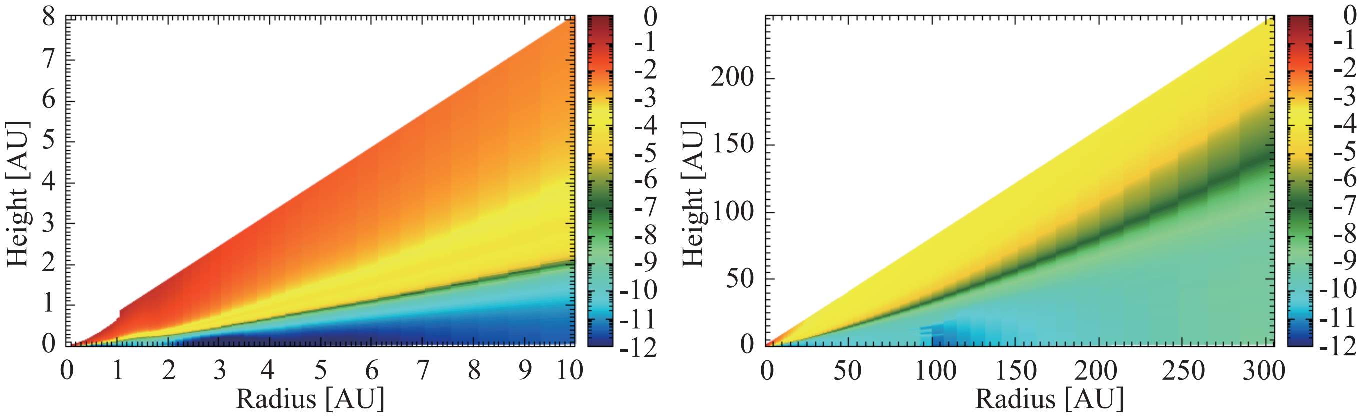

Figure 1.9 Fractional abundance of electrons as a function of disk radius and height up to maximum radii of 10 AU (left) and 305 AU (right) (Walsh et al. 2010).

the condition for MRI driven turbulence is $v_A^2/\eta_B\Omega \gtrsim 30$. Note, however, that $Re_{\rm M}$ depends on the magnetic field strength in this definition and therefore magnetic field strength needs to be estimated observationally.

The electric abundance in an axisymmetric disk surrounding a typical T Tauri star with stellar mass of 0.5 $M_\odot$, temperature of 4000 K, a mass accretion rate of 10^{-8} $M_\odot$ yr^{-1}, and a viscous parameter (α) of 0.01 is calculated through chemical network processes including thermal desorption, cosmic-ray-induced desorption, and photodesorption (Walsh et al. 2010). Figure 1.9 shows the electron fractional abundance as a function of disk radius and height within a radius of 10 AU and 305 AU. The ionization fraction varies between a minimum value of 10^{-12} in the densest region of the disk up to a value of ~ 0.1 in the hottest, the most irradiated surface region closest to the star. The ionization fraction of the disk obtained by their simulation implies that it is sufficiently possible to induce MRI throughout the disk around the scale height.

The emergence of MRI critically depends on the ionization fraction according to equation (1.20) and this fraction can be estimated empirically (Stahler & Palla 2004). Since electrons are the dominant negatively charged species, the relative density of free electrons need to be defined as

$$[{\rm e}^-] \equiv \frac{n_{e^-}}{n_{\rm H}}, \tag{1.21}$$

where n_{e^-} and $n_{\rm H}$ are the number densities of free electron and hydrogen, respectively. Note that $[{\rm e}^-]$ is also often defined as $n_{{\rm e}^-}/(n_{\rm H} + n_{\rm H_2})$ and the number densities of both atomic and molecular hydrogen are considered in the ionization fraction in Walsh et al. (2010) calculation shown in Figure 1.9 and 1.10. It is impossible to directly obtain $[{\rm e}^-]$ by observation but a relatively abundant molecule in protoplanetary disks, HCO^+, can be detected through its rotational transitions, along with CO. It is capable that the ionization fraction is indirectly derived by HCO^+ observation, preferably $H^{13}CO^+$ observation because of a optically thin line. The ionization fraction can be estimated by the following equation and the derivation is given in Appendix B.

$$[{\rm e}^-]^2 = \frac{k_2\zeta({\rm H_2})}{k_{\rm dr}({\rm H_3^+})k_{\rm dr}({\rm HCO^+})}\frac{[{\rm CO}]}{[{\rm HCO^+}]}\frac{1}{n_{\rm H}} \tag{1.22}$$

where k_2 is the dissociation rate of H_3^+, $\zeta({\rm H_2})$ is the volumetric impact rate with cosmic ray, $k_{\rm dr}({\rm H_3^+})$ is the reaction rate of H_3^+, $k_{\rm dr}({\rm HCO^+})$ is the reaction rate of HCO^+, [CO] and $[{\rm HCO^+}]$ are number density of CO and HCO^+ with respect to hydrogen, and $n_{\rm H}$ is the number density of hydrogen. These rate are obtained by laboratory experiments, $k_2 = 2 \times 10^{-9}$ cm^3 s^{-1}, $\zeta({\rm H_2}) = 5 \times 10^{-17}$ s^{-1}, $k_{\rm dr}({\rm H_3^+}) = 4 \times 10^{-6}$ cm^3 s^{-1},

$k_{dr}(HCO^+) = 3 \times 10^{-6}$ cm^3 s^{-1}, $[CO]/[HCO^+] = 10^4$, and $n_H = 10^4$ cm^{-3}, and equation (1.22) yields $\sim 10^{-7}$. The value is consistent with the result of model calculation based on chemical network process in the disk and achieved slightly above the scale height where ^{13}CO (J=1–0) line traces. Figure 1.10 shows the HCO^+ fractional abundance and number density of HCO^+ molecules in the case of HAe stars (ref. Walsh et al. 2012, 2010). They quantitatively shows that HCO^+ molecule is the most abundant ionized molecule near scale height in the disk and thus has the most suitable line as an ionization tracer. The abundance of HCO^+ with respect to CO ($[CO]/[HCO^+]$) can be determined by HCO^+ (J=1–0) or preferably $H^{13}CO^+$ (J=1–0) line observations and model fitting and should be provided for estimating the ionization fraction. The estimation based on the observational results may reduce the uncertainty in the calculation and become more persuasive.

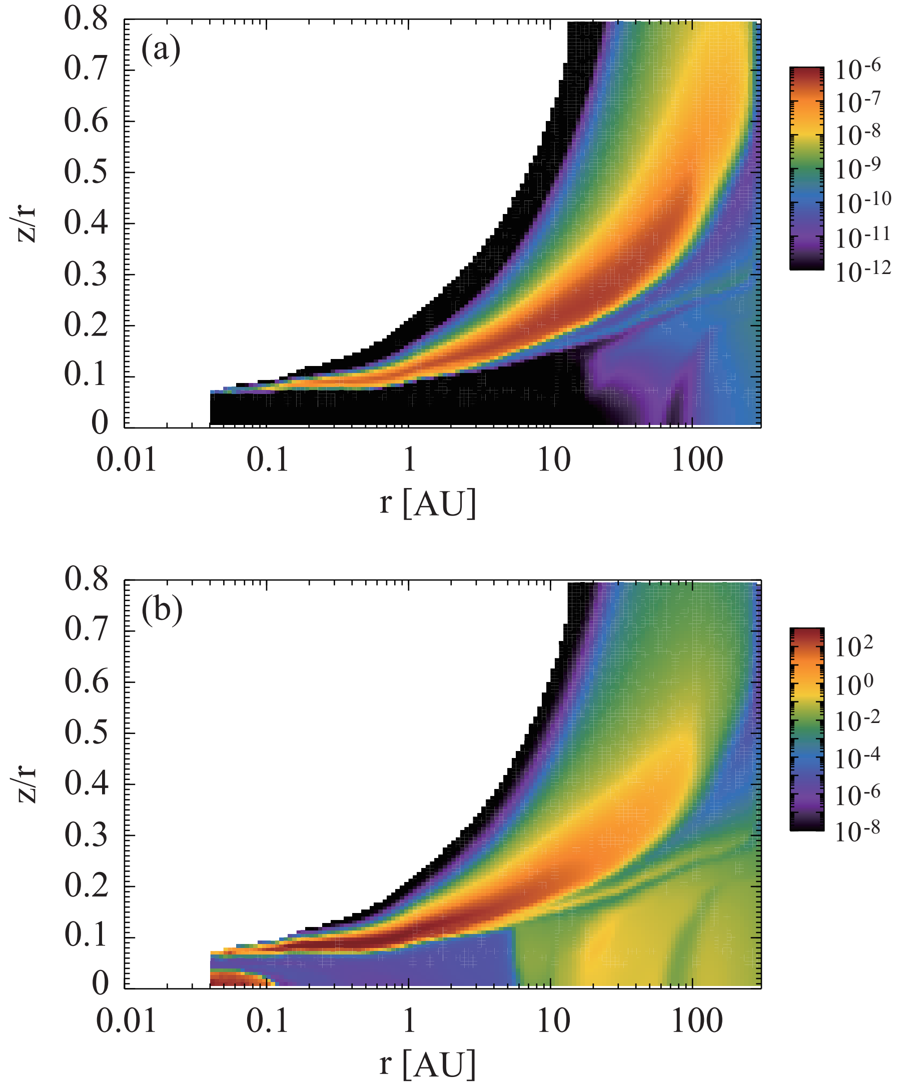

Figure 1.10 (Top): Diagram of HCO^+ abundance as a function of the disk radius (r) in two dimensional view. r is plotted on the abscissa while vertical distance normalized by r from the mid-plane of the disk is plotted on the ordinate. (Bottom): two dimensional diagram of HCO^+ column density distribution in the disk. Both the abscissa and the ordinate indicates the same as the those in the top diagram. These two diagrams are provided with the dedicated efforts of Catherine Walsh in Queens University as a favor in advance of publishing paper (Walsh et al. 2012, 2010).

5 The Aims of This Study and Outline

The study of the star and planetary system formation consists of many fields of studies. Figure 1.11 shows the overview of primarily on-going protoplanetary disk studies, including structural analysis, time evolution, and chemical composition, as well as astrobiology. Above all, two dimensional axisymmetric structure is mainly covered in this thesis.

	Entire Disk	Radial Distribution	2 Dimensional Distribution	3 Dimentional Distribution
Structure (r, z, φ)	M, R	$[\rho_g, T](t)$ $[\rho_d, T](t)$ exponential tail	$[\rho_g, \rho_d, T](r, z)$ $[\rho_g, \rho_d, T](r, \varphi)$	$[\rho_g, \rho_d, T](r, z, \varphi)$
Evolution (t)	[M, R](t)	$[\rho, T](t)$ ring transitional disks	$[\rho, T](r, t, \varphi)$	$[\rho, T](r, z, \varphi, t)$
Chemical Composition (X_i)	X_i	$X_i(t)$	$X_i(r, \varphi, t)$	$X_i(r, z, \varphi, t)$

Figure 1.11 Major classified topics in the study of protoplanetary disk formation. This study dealt in this thesis is placed at the topic designated by a red box.

Temperature and density structure of protoplanetary disks derived by observation is desired for establishing a general planet formation scenario and observations have now become to respond to the expectations of the theorists. The temperature and density distributions of the protoplanetary disk are responsible for the evolutionary process of planetary systems and the root of the diversity seen in planetary systems discovered until today can be traced back to them. The location at which dust coagulation occurs in protoplanetary disks can be examined in detail once the location of snowline, which is most critically affected by the temperature distribution in the disk, is determined. This is thought to play an essential role for determining where Jovian planets are born in planetary system. The density distribution provides initial conditions for the core accretion process and the time scale of the planetary disk evolution.

This thesis provides the millimeter and sub-millimeter observational data toward three protoplanetary disks around intermediate mass pre-main-sequence stars (Herbig Ae stars), HD 163296 (Chapter 3), HD 31648 (Chapter 4), and HD 169142 (Chapter 5). It demonstrates a verification strategy for disk structure by applying multiple CO isotopologues' emission data, and finally derives the two dimensional temperature and surface density distributions of the disk. The observational studies of the thesis have been performed by the following aims:

(1) To determine physical properies of the the protoplanetary disks.

(2) To derive radial and vertical temperature and density distributions in the protoplanetary disks.

(3) To reveal whether the magneto-rotational instability exist or not.

The author tried to achieve the aims mentioned above by following approaches:

(1) Observations of the emissions from protoplanetary disks by multi-CO isotopologue lines ^{12}CO (J=1–0), ^{13}CO (J=1–0), C^{18}O (J=1–0), ^{12}CO (J=3–2), and ^{13}CO (J=3–2) (Chapter 3, 4, and 5).

(2) Model fitting by two types of disk models, the traditional power-law disk model and the similarity solution disk model (Chapter 2, 3, 4, and 5).

(3) The derivation of the ionization fraction of the protoplanetary disk (Chapter 3, 4, and 5).

(4) The comparison among the disks focusing on diversity of temperature and density structure and evolutionary age (Chapter 6).

The most remarkable features of the study are as follows:

(1) Additional new CO emission line data and systematic structural analysis of protoplanetary disks by using five CO isotopologue emission line data.

(2) The first attempt to introduce a fitting by the similarity solution disk model only with molecular gas emission line profiles.

(3) The correlation between density structure and evolutionary stage.

The results in this thesis provide constrains or new information for constructing the formation scenario of planetary systems.

Chapter 2

Disk Model

1 Disk Thermal Structure

Stellar radiation is a main heating source for dust in protoplanetary disks. The dust particles re-radiate after absorbing the stellar radiation and subsequently heat others hovering around them. Therefore, the temperature of the dust near surface directly irradiated by stellar emission tends to be high and the temperature heated by re-radiation from the dust in the disk interior becomes low. Such a kind of vertical temperature distribution can be inferred from the detection of the silicate line in 10 μm band as an emission, not as an absorption. Gas temperature can be greatly affected by the stellar radiation like dust temperature. Several observations have revealed that young stars, such as T Tauri stars, have strong radiation in UV and X-ray. UV photons induce photo-electric effect on the dust surface and X-ray ionizes hydrogen or other atoms. The high energy electrons released through these processes collide with atomic or molecular gas and, shortly afterwards, raise gas temperature. The temperature near disk surface is controlled by balancing between these heating effects and cooling by emission from hydrogen, oxygen, or ionic carbon atoms.

As photo-dissociation region around high mass stars, gas temperature remains high in upper low density region of the disk due to inefficient energy exchange process caused by less frequent collision between gas and dust particles. The hot molecular gas emission observed in near-IR thought to be originated from the high temperature region in upper surface of the disk where heated by UV and X-ray from the central star. In high density region near the disk mid-plane, energy exchange between gas and dust efficiently works and therefore gas and dust are of equal temperature. Gas density distribution along vertical direction can be determined by hydrostatic equilibrium, which is achieved by balancing stellar gravitation in vertical direction with pressure gradient. Hence, gas temperature distribution affects gas density distribution. Conversely, gas density affects gas temperature through several types of heating and cooling processes. It is important to comprehensively deal with both distributions when a disk model is constructed.

2 Protoplanetary Disk Models

Study of protoplanetary disk models to reproduce observational results has developed since a number of protoplanetary disks had been detected and their physical properties had been derived. An extensive research capability attained by Infrared Astronomical Satellite (IRAS) in 1983 and statistical analysis about dust emission from protoplanetary disks became possible (Kenyon & Hartmann 1987; Adams et al. 1990). Protoplanetary disk models that are explicitly considered temperature and density structure developed before the disks were actually confirmed by observations. It is possible to derive some basic physical properties of the disks, such as size and inclination, from fitting the spectral profile obtainable by optically thick tracers (Omodaka et al. 1992; Acke & van den Ancker 1993; Kitamura et al. 1993).

Using the the three disk systems data obtained by NRO 45 m and ASTE telescope, Two kinds of disk models were compared, the classical power-law disk model and the similarity solution disk model. In the former, both temperature and the surface density are described by power-law distributions as functions of the radial distance from a central star (details in Section 2.1 in this chapter), whereas in the latter, only temperature is described by a power-law function and the surface density described by a combination of power-law and exponential decay functions (details in Section 2.2 in this chapter). The similarity solution model has recently attracted a renewed attention because of better fitting accuracy (Hughes et al. 2008). The fitting results toward HD 163296, HD 31648, and HD 169142 by both models and their comparisons are described in chapter 3, 4, and 5, respectively.

2.1 Power-Law Disk Model

The classical power-law disk model has been utilized for characterizing the temperature and the surface density distributions in the protoplanetary disk around young stars (Hayashi et al. 1985; Safronov 1969; Weidenschilling 1988). The temperature and surface density distribution is important for understanding the formation of planetary system (see Section 1.3 in Chapter 1). The power-law distributions in temperature and surface density have been applied for model fitting and successful to estimate physical properties of the disk, such as the outer radius, temperature and surface density at an arbitrary distance, or inclination (Kitamura et al. 1993; Piétu et al. 2003; Dent et al. 2005; Raman et al. 2006; Isella et al. 2007; Panić et al. 2008; Hughes et al. 2008; Akiyama et al. 2011) and therefore it has been recognized as the most common model for a long time.

Several assumptions for the disk structure and parameters are applied in the model fitting. First, the disk is assumed to have Keplerian rotation, as was observationally proven to be the cases in other HAe stars, such as HD 169142 and HD 31648 (Panić et al. 2008; Mannings et al. 1997a). Isella et al. (2007) pointed out the existence of a Keplerian rotating disk around HD 163296 from “a butterfly shape” seen in its position velocity diagram. Secondly, the temperature distribution over the disk, $T(r)$, is assumed to follow a power-law form of the radius with an index of -0.5, as described by the following equation (see also equation (1.6)):

$$T(r) = T_{100} \left(\frac{r}{100\text{AU}} \right)^{-0.5}, \tag{2.1}$$

where r is the radius in cylindrical coordinate system centered on the star and T_{100} is the temperature at $r = 100$ AU (Beckwith et al. 1990). This assumption implies that the temperature is constant along the vertical direction (z) at a certain r. In reality, a circumstellar disk should have a temperature distribution along the vertical direction. An elaborate disk model (e.g., Chiang & Goldreich 1997; Tanaka et al. 2005) predicts that the surface regions where the stellar radiation can penetrate and heat directly will have higher temperature than that in the interior regions, forming 2-layer temperature structure. A single-layer temperature model, however, can still be applicable because an optically thick line should have a “photosphere” at each r, and its characteristic temperature can be uniquely determined. That is, the vertical temperature distribution can be traced by a series of different fitting temperatures of each CO emission line (Dartois et al. 2003).

Thirdly, the radial distribution of the surface density over the disk, $\Sigma(r)$, is also assumed to follow a power-law form of the radius with the index of p (Hayashi et al. 1985; Beckwith et al. 1990; Kitamura et al. 2002;

Isella et al. 2007), as described by

$$\Sigma(r) = \Sigma_{100}\left(\frac{r}{100\mathrm{AU}}\right)^{-p} , \tag{2.2}$$

where Σ_{100} is the surface density at $r = 100$ AU. The assumption of the power-law dependency to the surface density is not theoretically proven but most of the disks observed have been explained well even though some discrepancies arise in the disks around AB Aur and HD 163296 (Piétu et al. 2005; Isella et al. 2007). This empirical assumption has been adopted in the model calculation for a long time. Fourthly, it is assumed that the density distribution in the vertical direction can be achieved by hydrostatic equilibrium. The density distribution, $\rho(r, z)$, is therefore expressed by

$$\rho(r, z) = \rho(r, 0)\exp\left[-\left(\frac{z}{H(r)}\right)^2\right] , \tag{2.3}$$

where $\rho(r, 0)$ is the density at the mid-plane of the disk, and $H(r)$ is the scale height and given by

$$H(r) = \sqrt{\frac{2r^3 k_{\mathrm{B}} T(r)}{GM_* m}} , \tag{2.4}$$

where k_{B} is the Boltzmann constant, G is the gravitational constant, M_* is the mass of the central star, and m is the mean mass of gas molecules ($2.34 \times m_{\mathrm{H}}$, where m_{H} is the mass of hydrogen atom). Thus, $\rho(r, 0)$ in equation (2.3) becomes

$$\rho(r, 0) = \frac{\Sigma(r)}{\sqrt{\pi} H(r)} . \tag{2.5}$$

Fifthly, local thermodynamic equilibrium (LTE) is assumed. The number density of H_2 at the position of the photosphere of each CO line can be estimated by equation (2.3). As shown in the fitting results in each object (see chapter 3, 4, and 5), the number density of H_2 at the ^{12}CO (J=3–2) photosphere is calculated to be $\sim 10^7$ cm^{-3} at $r = 100$ AU, and is higher than the typical value of the critical density for ^{12}CO (J=3–2) ($\sim 5 \times 10^4$ cm^{-3} at 60 K, the fitting temperature of this line is discussed in Section 4 in Chapter 3) by more than two orders of magnitude. The LTE assumption is sometimes inadequate for the analysis of protoplanetary disks, since it tends to overestimate the excitation temperature for a higher transition with a high critical density. However, Pavlyuchenkov et al. (2007) evaluated many types of model calculations, and found that the LTE approximation seems to be valid for the cases of J=4–3 or a lower rotational transition of CO. The LTE assumption is, therefore, applicable in our model calculation for the J=1–0 and J=3–2 transitions of ^{12}CO and ^{13}CO. Finally, the abundance ratios of H_2 to ^{12}CO, ^{12}CO to ^{13}CO, ^{12}CO to C^{18}O are assumed to be 10^4, 60, and 350, respectively, which are the typical values in the interstellar medium (Frerking et al. 1982; Wannier et al. 1982). The disk is assumed to be heated only by a stellar radiation, and accretion heating and other heating effects are neglected. This is a reasonable approximation for a protoplanetary disk around pre-main-sequence star with a modest accretion rate, such as the HD 163296 (Garcia Lopez et al. 7.6×10^{-8} $M_\odot$ yr^{-1}, 2006), HD 31648 (Grady et al. a few $\times\ 10^{-8}$ $M_\odot$ yr^{-1}, 2010), and HD 169142 (Dent et al. $\simeq 10^{-8}$ $M_\odot$ yr^{-1}, 2006) cases.

All parameters regarding the object, listed in Table 2.1, should be taken into account in the model calculation for the best accuracy, but some of them rarely affect the disk property. Emission profiles obtained by single-dish telescopes are mostly characterized by three parameters, T_{100}, Σ_{100}, and the outer radius of the disk (r_{out}), and these are regarded as being variables. The other parameters, such as the stellar mass (M_*), the distance (d), the inclination angle (θ), the disk inner radius (r_{in}), the power-law indices (p and q), and the abundance ratio of each CO isotopologues with respect to H_2 are fixed to be constants and adopted values obtained from other observations and model calculations, as listed in Table 2.1.

In actual calculations, Σ_{100} was fixed in each run, and the possible fitting range of T_{100} was searched. Σ_{100} was set to be between 0.001 and 30 g cm^{-2} (ref. Figure 3.12, 4.12, 4.13, and 5.11). The search for T_{100} in upper range of Σ_{100} for each object was stopped at 3 - 30 g cm^{-2}, because T_{100} in each CO line is well confined due to an asymptotic behavior of the fitting temperature with respect to r in a large Σ_{100} region, and the result remains almost the same. The intensity is affected by both T_{100} and Σ_{100} in the case of an optically thin disk, and by only T_{100} in the case of an optically thick disk. Among three variables, $r_{\rm out}$ can be guessed from the separation between two peaks in the profiles obtained from observation, since the Keplerian velocity at $r_{\rm out}$ ($V(r_{\rm out})$) roughly corresponds to half the separation between the two peaks of the profile. For example, $r_{\rm out}$ = 1000 AU is adopted in HD 163296 model calculation as an initial guess, and then adjusted. Figure 2.1 and 2.2 shows the surface density and temperature distributions in the power-law disk model[1]. It is assumed that $r_{\rm out}$ = 550 AU, Σ_{100} = 10 g cm^{-2}, and T_{100} = 30 K in this demonstrative calculation. The full-scale views in two dimension clearly show truncation at the outer edge of the disk, which is remarkable characteristic in the power-law disk model.

Table 2.1. Parameters in the power-law disk model

Variables	Invariables
T_{100}	M_*
Σ_{100}	d
$r_{\rm out}$	θ
	$r_{\rm in}$
	p
	q
	$X(^{12}\rm CO)$
	$X(^{12}\rm CO)/X(^{13}\rm CO)$
	$X(^{12}\rm CO)/X(\rm C^{18}O)$

[1]The two dimensional view to visualize both the surface density and the temperature distributions provided in Figures were calculated, along with the efforts of Kazuya Saigo in National Astronomical Observatory in Japan.

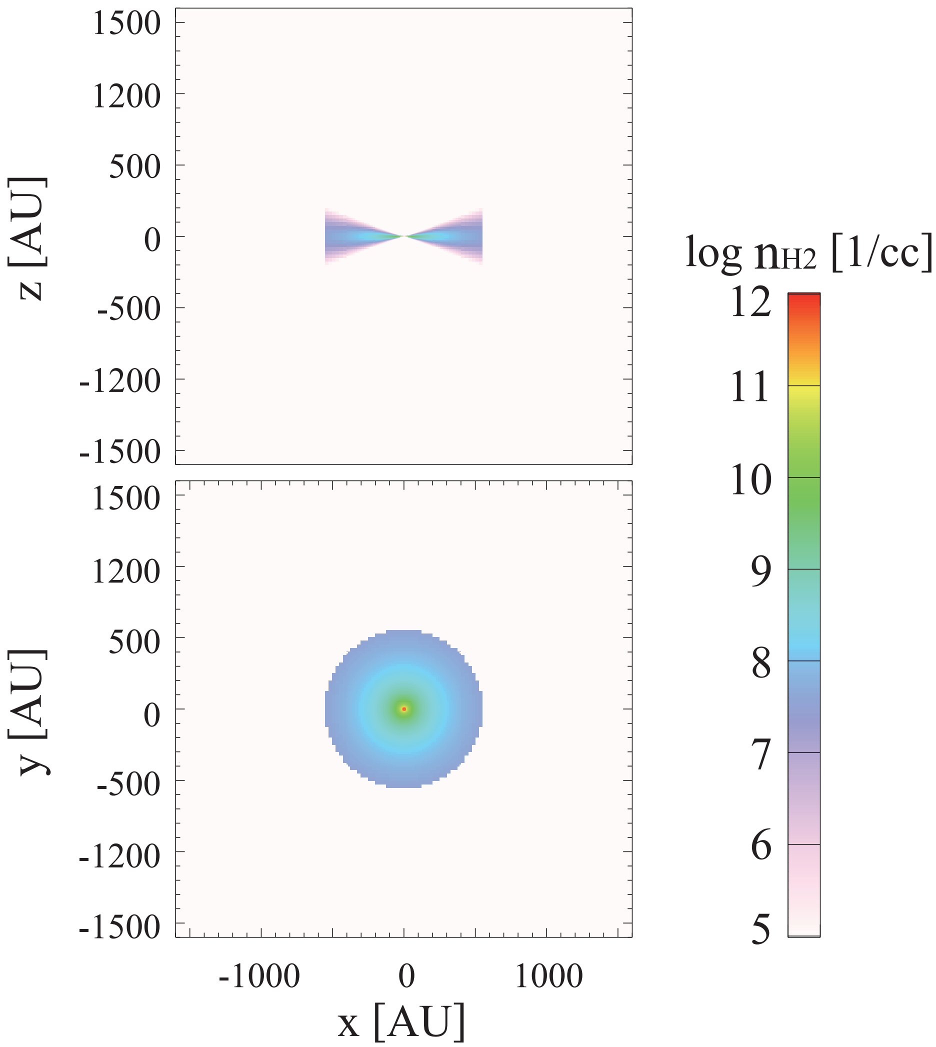

Figure 2.1 Density distribution of power-law model in the edge-on view (Top) and the face-on view at $z = 0$ in the edge-on view (bottom).

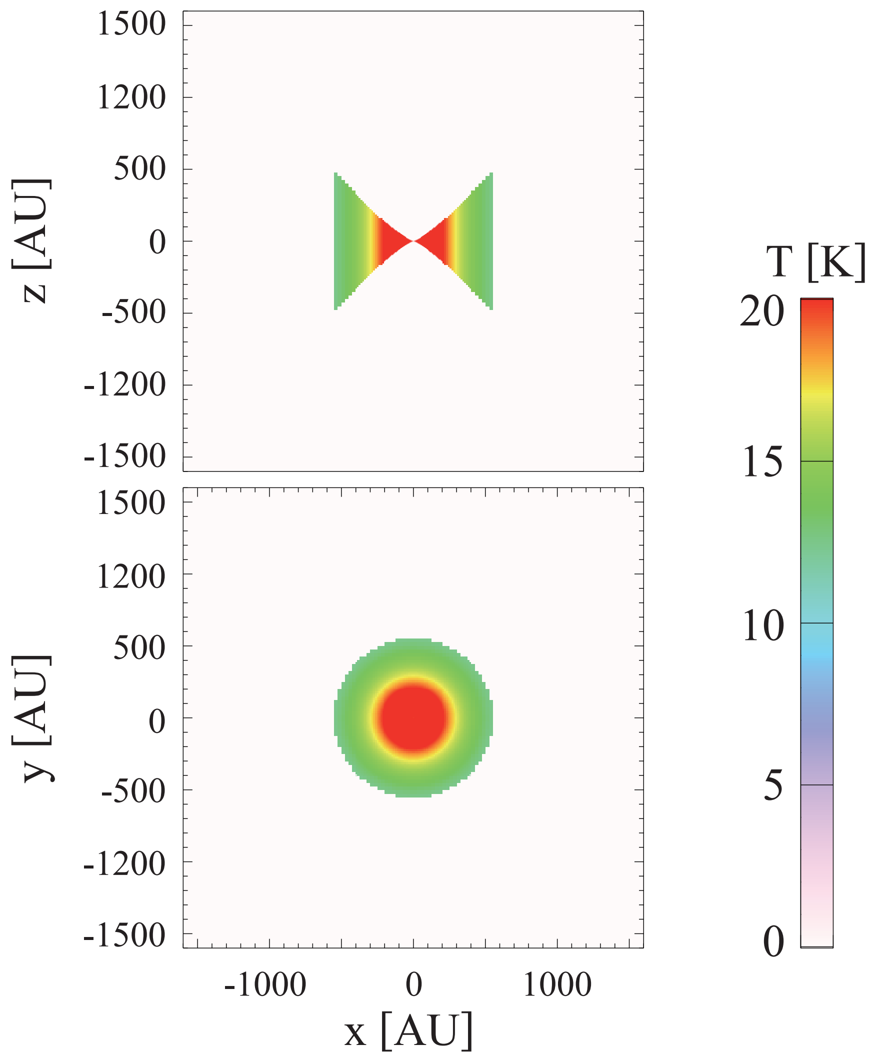

Figure 2.2 Same as Figure 2.1 for temperature distribution.

2.2 Similarity Solution Disk Model

A sudden decrease of density at the outer edge of the disk is created by the artificial truncation in the power-law disk model. This kind of the disk feature is obviously artificial and probably unrealistic. It should be more natural that the gas gradually spreads outward when diffusion kinetics is considered. As observations of dust and gas toward HAe stars had progressed, it became widely known for the study of model fitting that the results from dust continuum and gas emission lines are not simultaneously reproduced by the traditional power-law disk model. In AB Aur., for example, the outer radius of the dust derived from continuum emission is 350 ± 30 AU, whereas the outer radius of the gas derived from ^{12}CO (J=2–1) emission was 1050 ± 10 AU, three times larger than the size derived from dust continuum (Piétu et al. 2005). A HAe star, HD 163296, also shows a similar result: 200 ± 15 AU by the dust continuum observations and 540 ± 40 AU by multi-CO emission observations (Isella et al. 2007). Hughes et al. (2008) use the same HD 163296 data obtained by Isella et al. (2007) and demonstrate that the origin of the discrepancy comes from the truncation caused by the power-law density distribution in the radial direction. They instead introduced the similarity solution disk model, which is similar to the traditional power-law surface density distribution in the inner disk but have an exponential decrease in the outer edge, so-called an exponential tail (Lynden-Bell & Pringle 1974; Hartmann et al. 1998). The model can simultaneously reproduce both continuum and CO emission results of HD 163296 and other protoplanetary disks.

Lynden-Bell & Pringle (1974) studied the disk evolution including viscous dissipation and then a more detail description of steadily accreting disk evolution was developed by Hartmann et al. (1998). The evolution of the surface density by converting gravitational potential energy into radiation due to viscosity (Pringle 1981) is given by

$$\frac{\partial \Sigma(R)}{\partial t} = \frac{3}{R}\frac{\partial}{\partial R}\left[R^{1/2}\frac{\partial}{\partial R}\left(R^{1/2}\nu\Sigma(R)\right)\right] . \tag{2.6}$$

Under the assumption that the viscosity in the disk (ν) has a time-independent power-law dependency ($\nu \propto r^{\gamma}$), then equation (2.6) can be analytically solved. The solution for equation (2.6) is known to have a similarity solution and the disk surface density is expressed by

$$\Sigma(r) = \frac{C}{3\pi\nu_1 r^{\gamma}} T^{-(5/2-\gamma)/(2-\gamma)} \exp\left[-\left(\frac{r}{T}\right)^{2-\gamma}\right] , \tag{2.7}$$

where C is a constant, r is the disk radius normalized by a radial scale factor R_1, $r = R/R_1$, ν_1 is the viscosity at R_1, $\nu_1 = \nu(R_1)$, and T is the non-dimensional time and given by

$$T = \frac{t}{t_{\rm s}} + 1, \tag{2.8}$$

where $t_{\rm s}$ is the timescale of the viscous dissipation in the disk and given by

$$t_{\rm s} = \frac{1}{3(2-\gamma)^2}\frac{R_1^2}{\nu_1}. \tag{2.9}$$

When $t \ll t_{\rm s}$, $T \sim 1$ and therefore the disk hardly evolves. Equation (2.7) is simplified and put several parameters into two constants, C_1 and C_2 in this study as

$$\Sigma(r) = \frac{C_1}{r^{\gamma}} \exp\left[-\left(\frac{r}{C_2}\right)^{2-\gamma}\right] , \tag{2.10}$$

where r is the disk radius in AU and C_1, C_2, and γ are parameters that are adjustable in the model fitting process. The parameter C_1 is the normalized surface density and corresponds to Σ_{100} in the power-law disk model. The parameter C_2 is the radial distance from the central star where the surface density starts decreasing exponentially in a dominant fashion rather than decreasing in power-law. Thus the outer radius ($r_{\rm out}$) is defined as the disk size containing 95 % of total disk mass (Kitamura et al. 2002) and modified equation (2.7) as

$$\Sigma(r) = \Sigma_{100}\left(\frac{r}{r_{\rm out}}\right)^{-p} \exp\left[-3\left(\frac{r}{r_{\rm out}}\right)^{2-\gamma}\right] , \tag{2.11}$$

The parameter γ determines how greatly the surface density decreases exponentially. The radial temperature distribution in the similarity solution disk model is identical to the one in the power-law disk model. The number of free parameters is three (T_{100}, C_1, and C_2) and is the same as that in power-law disk model. The parameters in the similarity solution disk model is summarized in Table 2.1. The fitting temperatures of each CO line at Σ_{100} between 0.0001 and 3 g cm^{-2} are searched as done in the power-law disk model. Figures 2.3 and 2.4 show the surface density and temperature distributions in the similarity solution disk model in the case of $r_{\rm out}$ = 550 AU, Σ_{100} = 10 g cm^{-2}, and T_{100} = 30 K, the same parameter values as applied in the power-law model disk model shown in Figures 2.1 and 2.2. The full-scale views in two dimension shows that both density and temperature distributions fall off gradually. This effect is a remarkable characteristic of the similarity solution disk model and thought to be more realistic feature than the truncation at the edge formed in the power-law disk model. Figure 2.3 and 2.4 shows the surface density and temperature distributions in the similarity solution disk model.

Although Hughes et al. (2008) showed successful fit by similarity solution disk model for four nearby disk systems, the power-law surface density distribution with truncation at the outer edge may be more suitable than the power-law with an exponential tail in some cases. For example, in the case of our solar system, a sudden decrease in the surface density is seen in the density of Kuiper Belt objects that exist beyond a distance of 50 AU from the Sun. Such feature might originate from the primordial solar nebula with sharp outer edge like the case of power-law disk models. The both disk models are compared disk by disk in this thesis (see chapter 3, 4, and 5).

Table 2.2. Parameters in the similarity disk model

Variables	Invariables
C_1	M_*
C_2	d
γ	θ
	$r_{\rm in}$
	p
	$X(^{12}{\rm CO})$
	$X(^{12}{\rm CO})/X(^{13}{\rm CO})$
	$X(^{12}{\rm CO})/X({\rm C}^{18}{\rm O})$

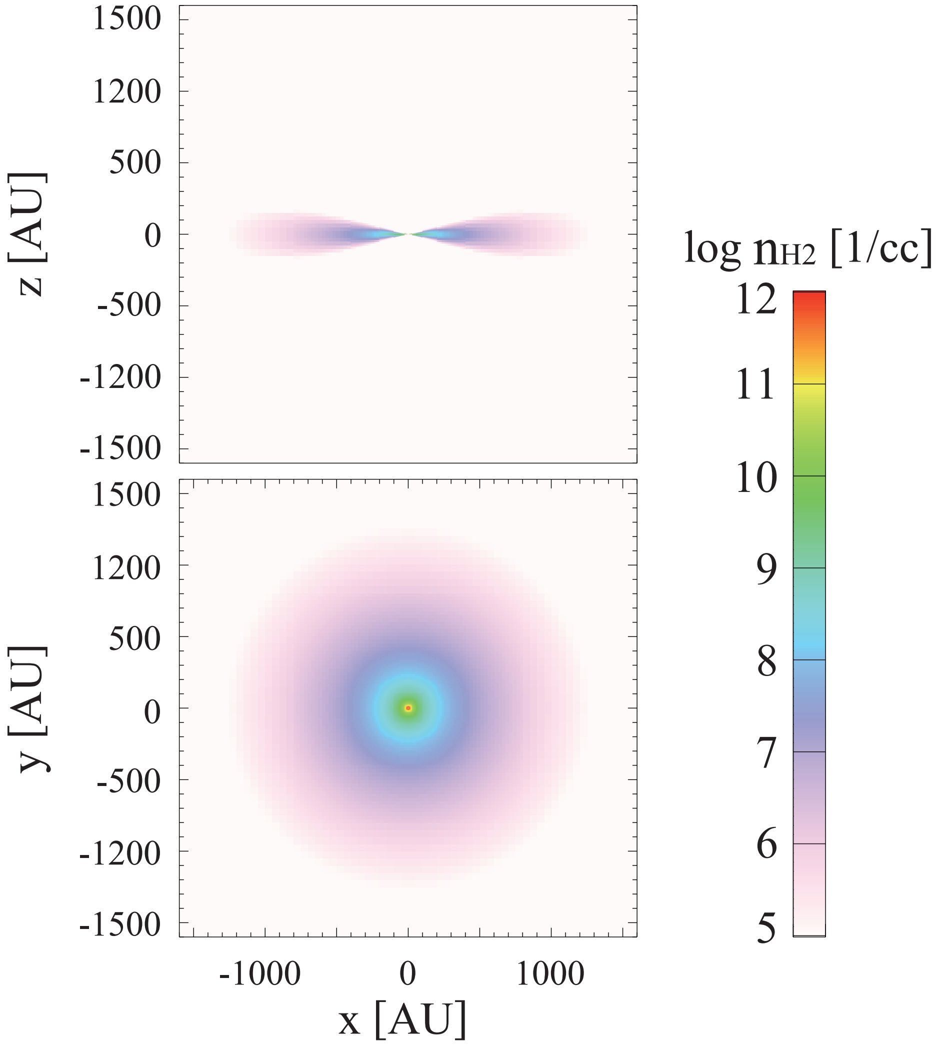

Figure 2.3 Density distribution of similarity solution disk model in the edge-on view (top) and the face-on view at $z = 0$ of the edge-on disk (bottom).

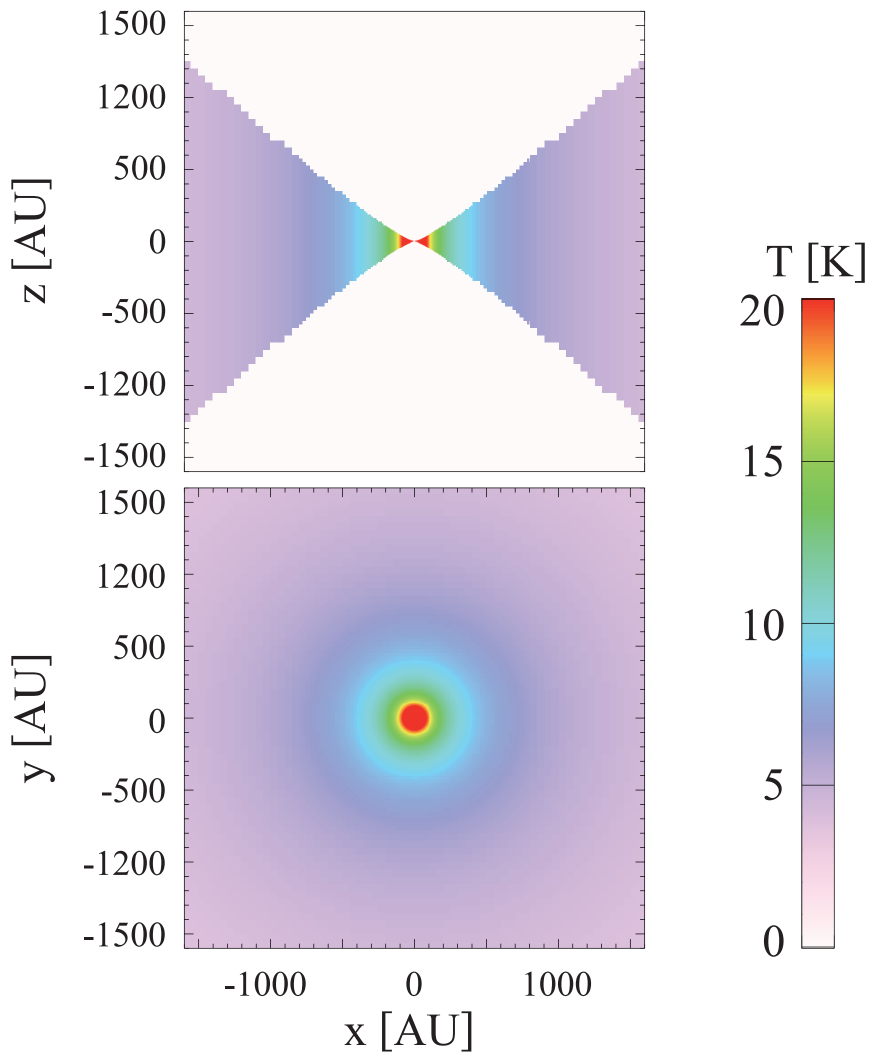

Figure 2.4 Same as Figure 2.3 for temperature distribution.

3 Model Fitting

It is important to establish fitting criteria for judging fitting accuracy and its acceptability. In this study, the fitting results are regarded to be acceptable when the following two conditions were met simultaneously: (i) to exclude the case of a large deviation in amplitude of the profiles, the residual integrated over the range of $T_{\rm mb} \geq 2\ \sigma$ should be less than the uncertainty (1 σ) for the integrated intensity, (ii) to exclude the case of a large deviation in the line shape, more than 80 % of the channels over $T_{\rm mb} > 3\sigma$, should agree with the model calculations within 2 σ. Model fitting results in the following chapter meet the two requirements at the same time mentioned above.

Chapter 3

Disk Structure of HD 163296

1 Introduction

HD 163296 is a pre-main-sequence sungle star with A1V in spectral type. Its luminosity, mass, age, and distance are 30 $L_\odot$, 2.3 $M_\odot$, 4 Myr, and 122 pc, respectively (van den Ancker et al. 1998). A chain of HH objects (HH 409) is discovered and is oriented roughly perpendicular to the disk (Grady et al. 2000). A collimated, bipolar jet with 335 - 380 km s^{-1} in velocity is associated with the star (Devine et al. 2000). HST Space Telescope Imaging Spectrograph (STIS) coronagraphic data indicate that the scattered light from the HD 163296 disk is variable (Wisniewski et al. 2008). Observations at infrared and radio wavelengths revealed the existence of a circumstellar disk with a mass of 0.028 $M_\odot$ and 45° in inclination angle (Mannings & Sargent 1997b; Isella et al. 2007; Hughes et al. 2008). HD 163296 is categorized as belonging to group II by the feature of SED (see Section 2.2 in Chapter 1) as shown in Figure 3.2 (Acke & van den Ancker 2004), and is expected to have a self-shadowed disk (Meeus et al. 2001; Dullemond & Dominik 2004). More recently, imaging studies with IRAM/PdBI, SMA, and VLA both in continuum and in the ^{12}CO, ^{13}CO, and C^{18}O emission lines were performed (Isella et al. 2007), arguing that the disk radius is 550 AU, and that the gas kinematics can be well explained by Keplerian rotation. As a result of the dust opacity, $\kappa \propto \lambda^{-\beta}$ with $\beta = \pm$ 0.1 between 0.87 and 7 mm in wave length, it is very likely that the bulk of the solid material in the HD 163296 disk has coagulated into larger aggregates of millimeter and centimeter size (Natta et al. 2007). Therefore, the HD 163296 system is probably evolving towards a debris disk phase. Hughes et al. (2011) observed the disk by the SMA at a high spectral resolution and detected a $\sim$ 300 m s^{-1} turbulent linewidth. HD 163296 has been extensively observed to unveil the physical and chemical properties and recently structure as well. Thi et al. (2005) probed by many other molecular lines including cyanide carbonate and deuterated molecules and molecular abundance was estimated. HD 163296 is one of the best targets for examining temperature and density structure of the disk in detail, because the basic properties are already known and it exhibits strong emission from the disk in many CO isotopologue lines.

2 Observations

2.1 ^{12}CO (J=1–0) Mapping Observations

Observations of ^{12}CO (J=1–0) emission line were performed in the winter of 2006 by the NRO 45 m telescope shown in Figure 3.3 (left), operated by Nobeyama Radio Observatory (NRO), a branch of National Astronomical

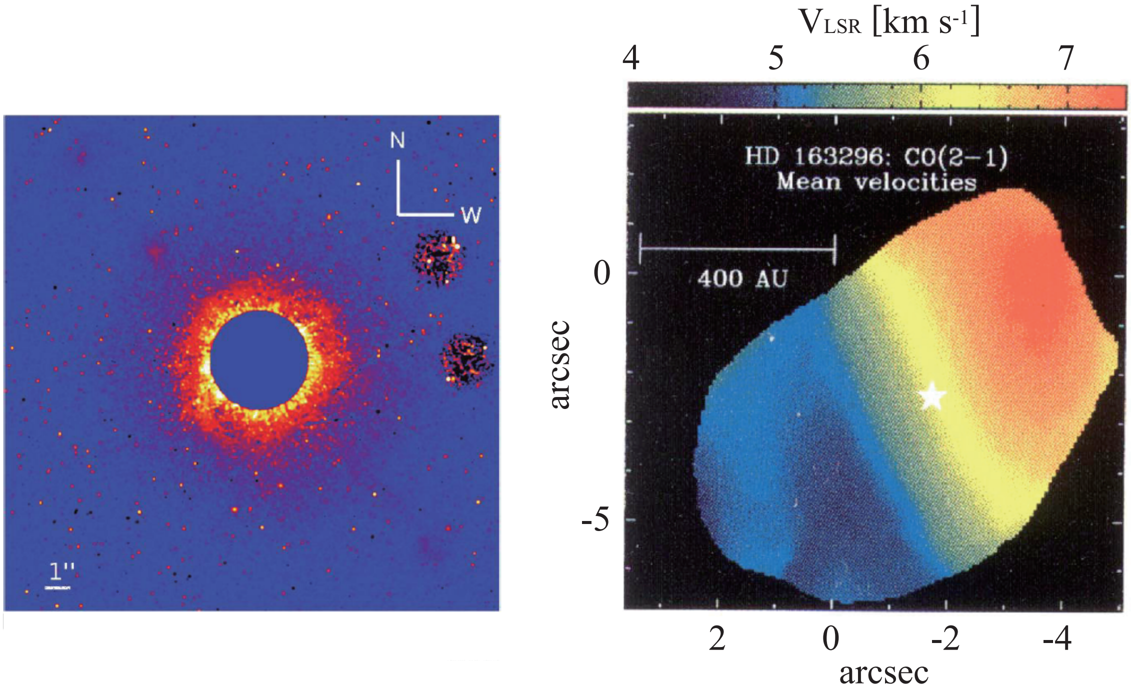

Figure 3.1 (Left): The coronagraphic image of the disk around HD 163296 obtained by HST (Wisniewski et al. 2008). (Right): The intensity-weighted mean velocity map of HD 13296 derived by ^{12}CO (J=1–0) emission line. The star symbol represents the location of the central star (Mannings & Sargent 1997b).

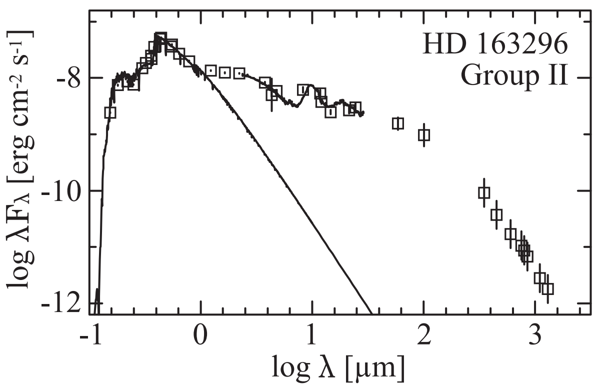

Figure 3.2 SED of HD 163296 (Acke & van den Ancker 2004).

Observatory of Japan (NAOJ). To separate the emission originated from the disk associated with the central star from surrounding components, such as an envelope or a remnant cloud, a profile map including the stellar position and its vicinity with sufficient spatial resolution is decisive in identifying the origin of the emission. To obtain such a map, the multi-beam receiver, 25 Beam Array Receiver System (BEARS: Sunada et al. 2000; Yamaguchi et al. 2000) as shown in Figure 3.3 (right), which is capable of simultaneously detecting 25 different locations in double sideband (DSB) operation, was employed as the frontend and tuned at a rest frequency of ^{12}CO (J=1–0), 115.271 GHz. The half-power beam width (HPBW) is 15″ at this frequency, corresponding to 1800 AU at a distance of 122 pc from the Sun. The beam grid spacing of BEARS is $\sim$ 40″ ($\sim$ 5000 AU) in both R.A. and Dec. directions, but this is much larger than the HPBW, and is therefore insufficient to

Figure 3.3 (Left): NRO 45 m telescope. (Right): BEARS receiver.

Figure 3.4 ASTE telescope.

distinguish the star+disk system from the ambient. To fill these gaps among the beams, the data at positions shifted by 20″ in both R.A. and Dec. directions from the central star is also taken. The integration time for the observation was 7 hours on source. The region of 80″ × 80″ ($\simeq$ 0.05 pc × $\simeq$ 0.05 pc) near the star that covers a typical size of the envelope is provided in the result. A digital spectrometer with 32 MHz in bandwidth and 37.8 kHz ($\simeq$ 0.1 km s^{-1}) in frequency resolution was used as the backend. A correction for atmospheric absorption during the observations was made by the chopper-wheel method (Kutner & Ulich 1981), and the intensities were obtained at the antenna temperature, T_A^*, in Kelvin. A correction by the main beam efficiency (η_mb) was made beforehand when the model calculation results (see Chapter 2) were compared with the brightness temperature, $T_\mathrm{mb} = T_\mathrm{A}^*/\eta_\mathrm{mb}$, where $\eta_\mathrm{mb} = 0.39$ for ^{12}CO (J=1–0) emission line. The DSB system temperature in ^{12}CO (J=1–0) mapping observation was between 250 K and 600 K. The accuracy for telescope pointing was regularly checked against the SiO maser VX Sgr, which was about 3′ away from HD 163296, and the pointing deviation was achieved in less than ±3″ during whole observation period. Data reduction and analysis were made with the NEWSTAR software package developed by NRO, which is a front end of AIPS developed at the National Radio Astronomy Observatory (NRAO).

Observations were made in the position-switching mode. It was found that extended ^{12}CO (J=1–0) emission was present around the region of interest. Hence, a careful search is needed to find an off point as close to HD

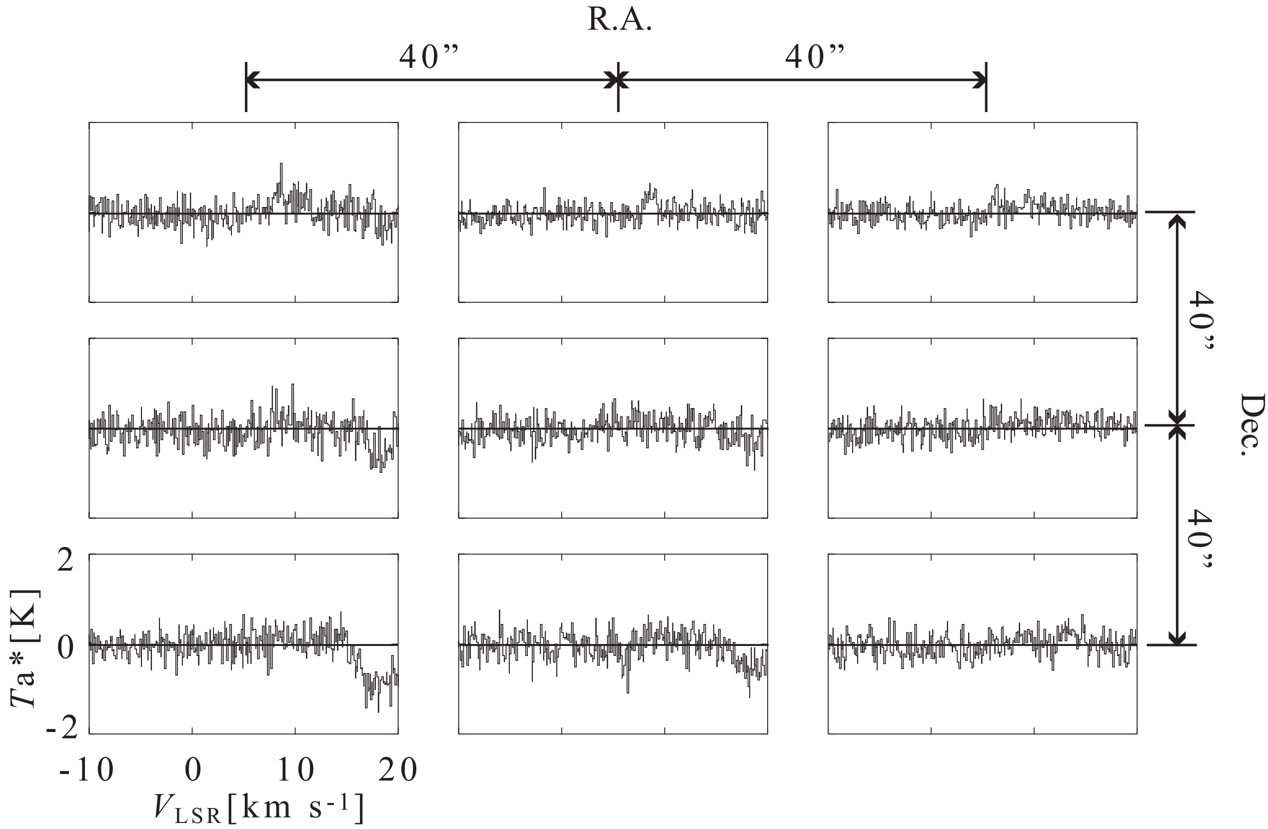

Figure 3.5 Profile map covering 80″ × 80″ (∼ 10000 AU × ∼ 10000 AU) around the off position obtained by the ^{12}CO (J=1–0) observation. The central position is (α, δ) = (17^{h}56^{m}20^s.0, -21°46′23″.2) in J2000, and the angular distance between adjacent points is 40″ in both R.A. and Dec. directions as designated at the upper right corner of each panel.

163296 as possible. The search for off points was conducted with BEARS based on the fact that the systemic velocity of HD 163296 is 6 km s^{-1} (Dent et al. 2005; Isella et al. 2007). An emission-free position applicable as an off point was finally found at about 10′ north from HD 163296. Figure 3.5 is a profile map toward this position, centered at 17^{h}56^{m}20^s.0 and −21°46′23″.2 (J2000) and covering a 80″ × 80″ (∼ 0.05 pc × ∼ 0.05 pc) region, showing that there is no prominent emission detected around 6 km s^{-1} in $V_{\rm LSR}$.

2.2 ^{13}CO (J=1–0) and C^{18}O (J=1–0) Emission Line Observations

Observations of the ^{13}CO (J=1–0) emission line were conducted by the NRO 45 m telescope in the winter of 2008. As will be explained in detail in Section 3.1 in this chapter, the ^{12}CO (J=1–0) emission detected around 6 km s^{-1} in $V_{\rm LSR}$ at the central star is isolated. Therefore, ^{13}CO (J=1–0) observations were made only at the stellar position by a pair of single-beam receivers that enabled us to simultaneously detect both the polarization components in the single sideband (SSB) mode. The receiver was tuned at a ^{13}CO (J=1–0) rest frequency of 110.201 GHz, and the HPBW was 15″ at this frequency. The $\eta_{\rm mb}$ in 2008 at this frequency was 0.4. An Acousto Optical Spectrometer (AOS), whose bandwidth and frequency resolution were 40 MHz and 20 kHz ($\simeq$ 0.055 km s^{-1}), respectively, was used. The system noise temperature during observation was between 300 K and 600 K in the SSB mode. The pointing was regularly checked by the same manner as in ^{12}CO (J=1–0) observations, described in Section 2.1 in this chapter and the pointing accuracy was achieved less than $\pm3''$. The correction for daily intensity variation caused by the small fluctuation in the receivers' sensitivity was made by observing M17SW. The same off point as that in the ^{12}CO (J=1–0) observations was used. All observational data when the wind speed exceeded 5 m s^{-1} were flagged out before obtaining the final profile of ^{13}CO (J=1–0) emission. The resultant total integration time was 8.5 hours on the source. Data reduction and analysis were also made in the same manner as in the ^{12}CO (J=1–0) observation described in Section 2.1 in this chapter.

Subsequently, the follow-up observations by the C^{18}O (J=1–0) emission line were conducted in the spring of 2011. Since HD 163296 system was confirmed to be isolated as will be described in Section in 3.1 and 3.2 in this chapter, C^{18}O (J=1–0) observations were intensively made only toward the stellar position as ^{13}CO (J=1–0) line observations by a pair of sideband-separating new receivers (2SB receivers), T100H/V, which become available in 2009 and enabled us to simultaneously detect both the polarization components. The achieved image rejection ratio (IRR) was 11 - 15 dB. The receivers were tuned at C^{18}O (J=1–0) rest frequency of 109.782 GHz and the HPBW is $15''$ for this line. An AOS, whose bandwidth and frequency resolution were 40 MHz (0.11 km s^{-1}) and 20 kHz (0.05 km s^{-1}) respectively, was used. The system noise temperature during observation was between 250 K and 400 K, relatively higher than the normal in winter season. All observational data when the wind speed exceeded 5 m s^{-1} were flagged out before obtaining the final profile like other line reduction. The windy days in the observation made spectra nosy and the data integrated for only $\sim$ 1.5 hours on the source were available for obtaining the final spectrum. The pointing check and the correction due to atmospheric variation were carried out as the same manner as in ^{12}CO (J=1–0) observations. The daily intensity fluctuation caused by the receivers was corrected by observing W51 main, instead of M17SW in ^{13}CO (J=1–0) observations, every observational day. The receivers was functioning in very stable thus the correction was hardly made. The $\eta_{\rm mb}$ in 2011 at this frequency was 0.42 and applied to convert the raw data of observed antenna temperature to the brightness temperature.

2.3 ^{12}CO and ^{13}CO (J=3–2) Observations

Observations of ^{12}CO and ^{13}CO (J=3–2) lines were carried out in July 2006 with the Atacama Sub-millimeter Telescope Experiment (ASTE), a 10-m sub-millimeter telescope in Chile (Ezawa et al. 2004). HPBWs of the ASTE telescope at 345.79 and 330.59 GHz are $22''$ and $23''$, respectively, which correspond to about 2700 - 2800 AU at the distance to the target, and the $\eta_{\rm mb}$ was 0.6 around these frequencies. An SIS mixer receiver having DSB response was employed. The typical atmospheric opacity at 220 GHz toward the zenith was 0.05 during the observations, and the system noise temperature of the telescope was 250 - 300 K in DSB during observations. The digital auto-correlator with 1024 frequency channels was configured so that the total bandwidth was 128 MHz, resulting in a frequency resolution of 125 kHz, or $\simeq$ 0.11 km s^{-1} at the observed frequencies. Telescope pointing was checked every 1.5 - 2 hours by cross scanning of Jupiter, and the error was proved to be $\leq 3''$. All of the spectra were obtained in a position switching mode: the location of the off-position was $(\Delta\alpha, \Delta\delta) = (-20', +20')$ from the star. In ^{12}CO (J=3–2) observations, the spectra at the stellar position including four adjacent points, 2200 AU apart from the stellar position in R.A. or Dec. direction, were taken to check out whether the emission of the stellar position is really isolated. ^{13}CO (J=3–2) data were taken only toward the stellar position, since the ^{12}CO (J=3–2) at the systemic velocity ($V_{\rm LSR} \sim 6$ km s^{-1}) was proven to be isolated, as explained in Section 2.1 in this chapter. Data reduction and analysis were conducted in the same manner as in ^{12}CO (J=1–0) data reduction.

2.4 HCO$^+$ (J=1–0) Emission Line Observations

Observations of HCO$^+$ (J=1–0) emission line were conducted by the NRO 45 m telescope in May 2011. As shown in Section 2.1 and 2.3 in Chapter 3, the emissions detected in several CO isotopologues around 6 km s^{-1} in $V_{\rm LSR}$ are confirmed to be isolated. Thus, HCO$^+$ (J=1–0) observations were intensively made only toward the stellar position by a pair of new 2SB receivers, T100H/V, whose IRR was achieved to be 11 - 15 dB during the observation. The receivers were tuned at a HCO$^+$ (J=1–0) rest frequency of 89.189 GHz, and the HPBW was about 18$''$ at this frequency. An AOS, whose bandwidth and frequency resolution were 40 MHz and 20 kHz ($\simeq$ 0.05 km s^{-1}) respectively, was used. The system noise temperature during the observation was between 300 K and 350 K, slightly higher than the typical value in winter season. Since it was windy during the observation, all observational data when the wind speed exceeded 5 m s^{-1} were carefully flagged out before obtaining the final profile of HCO$^+$ (J=1–0) emission as the same method as in the reduction of ^{12}CO (J=1–0) data. The resultant total integration time was 1 hour on the source. The pointing check and the atmospheric correction were carried out as the same manner as in ^{12}CO (J=1–0) observations described in Section 2.1 in Chapter 3. The correction for the intensity caused by the small daily fluctuation in the receivers' sensitivities, which were always stable in this observation was made by observing W51 main. The $\eta_{\rm mb}$ in 2011 at this frequency was 0.43 and applied to convert the raw data of the observed antenna temperature to the brightness temperature. The method of data reduction and analysis were also the same as those in the ^{12}CO (J=1–0) observation.

3 Results

3.1 ^{12}CO (J=1–0), ^{13}CO (J=1–0), and C^{18}O (J=1–0) Emissions

Figure 3.6 shows a ^{12}CO (J=1–0) profile map within the 80$''$ × 80$''$ region centered at HD 163296. A clear double-peaked profile with 4.8 σ is seen only at the center panel at 6 km s^{-1} in $V_{\rm LSR}$ that matches with the systemic velocity of HD 163296 (Dent et al. 2005; Isella et al. 2007). The double-peaked profile has a peak intensity of 1.0 K in $T_{\rm mb}$ and 3.2±0.1 km s^{-1} in FWHM velocity width. The achieved mean rms noise level after data reduction was 0.21 K. Figure 3.7a displays the same profile on the center panel in Figure 3.6 in an enlarged view.

Several positions in Figure 3.6, especially 40$''$ away to the west from the center, show an emission feature at $V_{\rm LSR}$ = 6 km s^{-1}, but there seems no emission above the 3σ level at this velocity at four positions adjacent to the star (20$''$ apart from the star). To confirm whether there is no significant emission at 6 km s^{-1} in these regions, these four profiles were averaged into one spectrum (Figure 3.8a). There is no emission above the 3σ level at 6 km s^{-1} in Figure 3.8a. The profile detected at the stellar position (Figure 3.8b, or the central panel in Figure 3.6) is compared with that after subtracting the profile in Figure 3.8a (Figure 3.8c). Although the noise level in Figure 3.8c increases due to subtraction, there is no remarkable difference between these two profiles before and after subtraction. These comparisons strongly suggest that the double-peaked emission component at the star is isolated and originates from the compact circumstellar disk in Keplerian rotation. The components at $V_{\rm LSR}$ = 6 km s^{-1} in south and west regions 40$''$ apart from the star in Figure 3.8 might be emissions from a remnant cloud partially remaining around the star+disk system.

The dip at 8 km s^{-1} around the star+disk system (Figure 3.6) is due to weak emission seen at the off points, especially in the northern region (Figure 3.5); in position switching mode, the emission at the off point appears like an absorption dip. The dip dose not affect further analysis since it does not corrupt the original emission

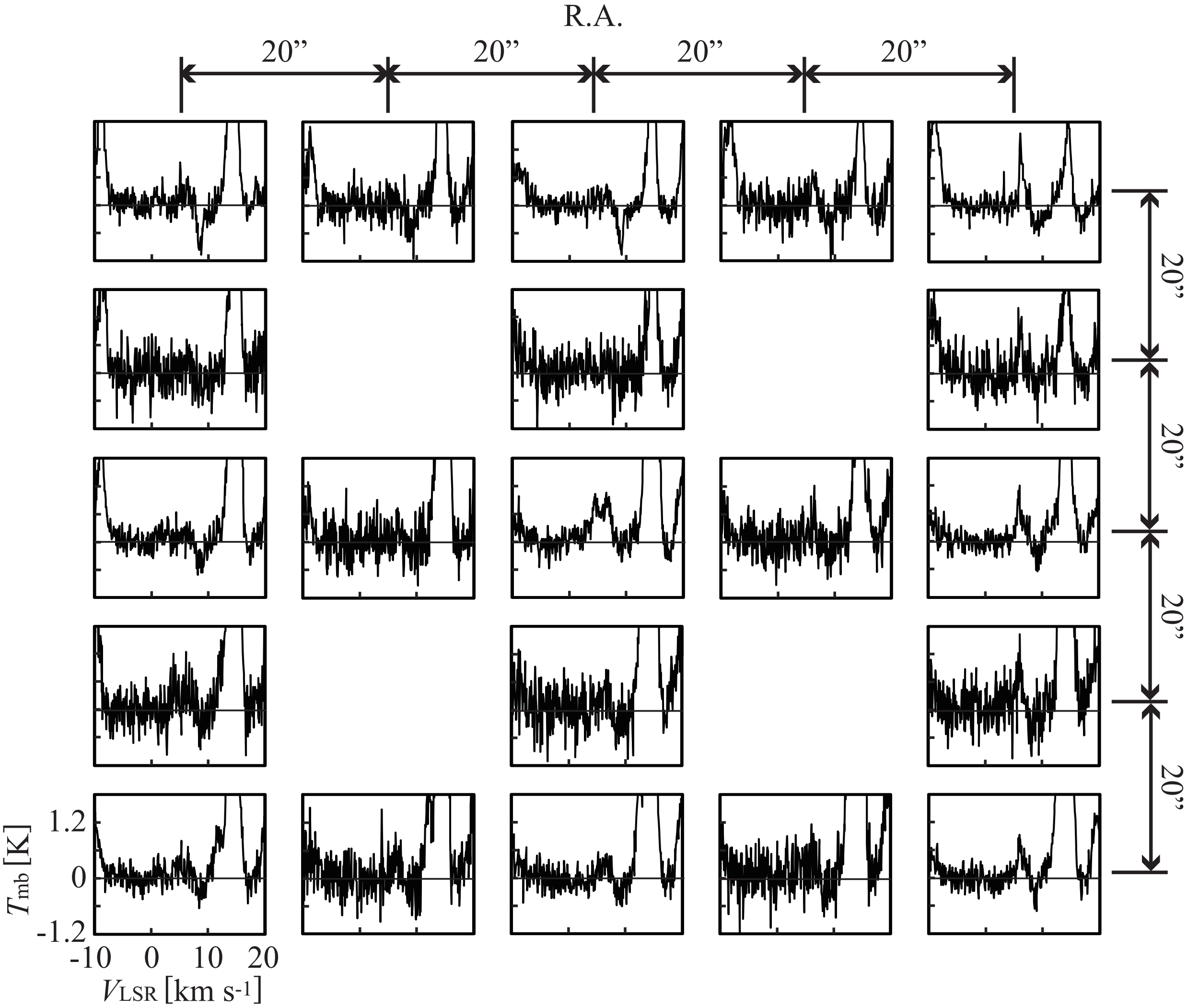

Figure 3.6 Profile map of the ^{12}CO (J=1–0) line around HD 163296. The map center corresponds to the stellar position (α, δ) = ($17^h56^m21^s.29$, -21°57′21″.9) in J2000, and the angular distance between adjacent points is 20″ (≃ 2500 AU) in both R.A. and Dec. directions.

profile at 6 km s^{-1}. In addition, the strong emission components between 10 and 15 km s^{-1} and at 20 km s^{-1} appear regardless of any positions; these two components probably come from foreground or background clouds that exist coincidentally along a line of sight.

Figure 3.7b shows a profile of the ^{13}CO (J=1–0) emission line. Again, a double-peaked profile was clearly detected. The peak intensity and velocity width are 0.36 K in $T_{\rm mb}$ and 3.8±0.2 km s^{-1} at FWHM, respectively. The achieved rms noise level is 0.061 K. Since the ^{12}CO (J=1–0) and ^{13}CO (J=1–0) emissions are detected in the same velocity range, both emissions should have the same origin. The intensity ratio between ^{12}CO (J=1–0) and ^{13}CO (J=1–0) is less than 5, suggesting that the disk is possibly optically thick. Isella et al. (2007) evaluated the optical depth of the CO emission lines by interferometric observations, and concluded that the disk is optically thick. Our model fitting described in Section 4 in this chapter also proves that the disk is optically thick for both of the CO lines. Both of the results obtained from the interferometric and the single-dish telescope observations match and confirmed to be consistent.

The C^{18}O (J=1–0) emission profile with double-peaked feature at the systemic velocity of 6 km s^{-1} in $V_{\rm LSR}$

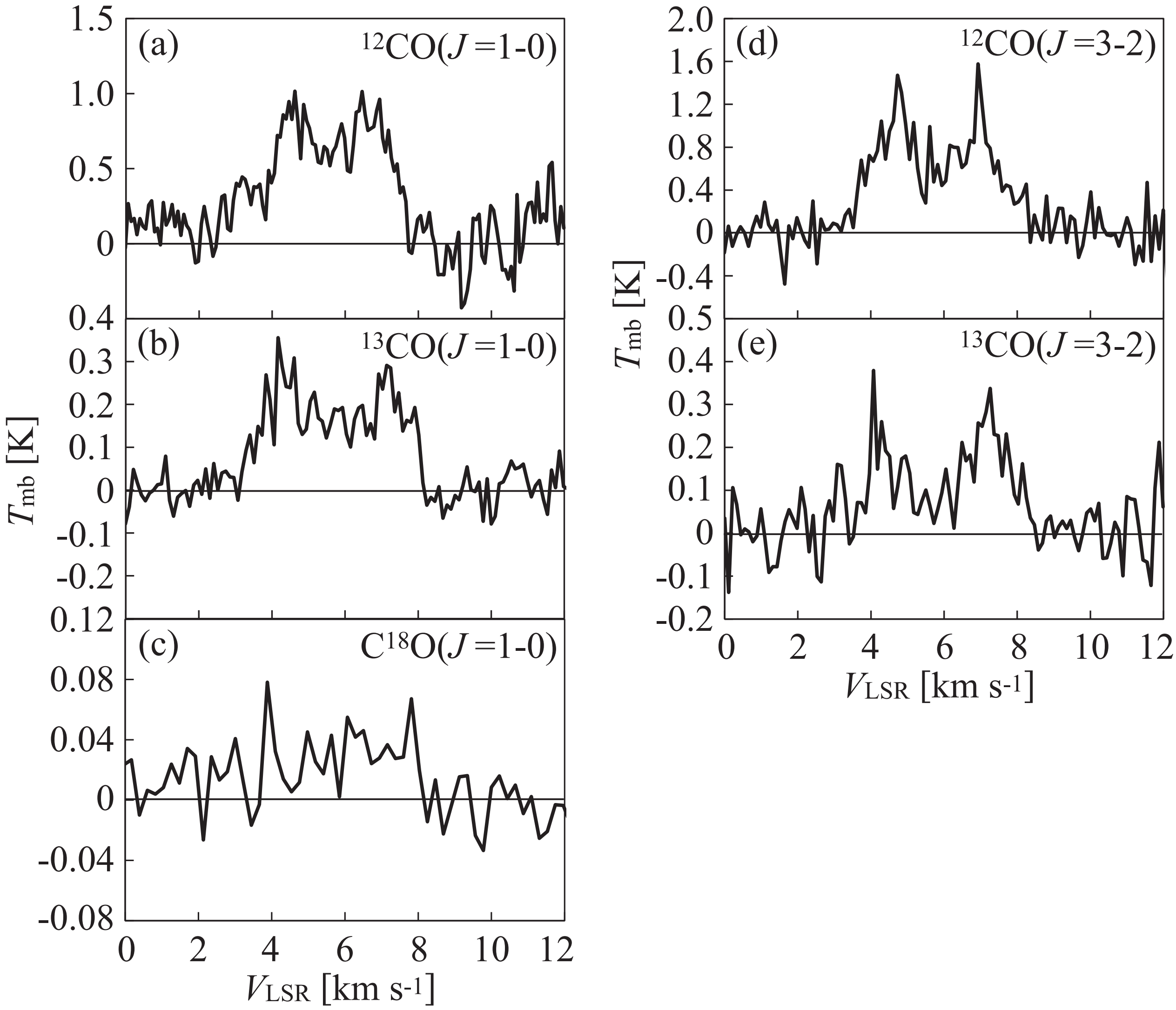

Figure 3.7 Profiles detected in ^{12}CO and ^{13}CO lines toward the stellar position of HD 163296. (a) in ^{12}CO (J=1–0), (b) in ^{13}CO (J=1–0), (c) in C^{18}O (J=1–0), (d) in ^{12}CO (J=3–2), and (e) in ^{13}CO (J=3–2).

is obtained and provided in Figure 3.7c. The rms noise level of 0.0085 K is achieved after 4-channel binning, making 3.9 in the S/N ratio. The peak intensity and velocity width are 0.078 K in $T_{\rm mb}$ and 3.9±0.2 km s^{-1} at FWHM, respectively. Note that the velocity width of the C^{18}O (J=1–0) line is the largest among J=1–0 transition lines (see also Figure 3.17) because C^{18}O (J=1–0) line is the most optically thin line and can trace dense region of the disk, that is the inner region where Keplerian velocity is high.

3.2 ^{12}CO (J=3–2) and ^{13}CO (J=3–2) Emissions

Figure 3.9 shows a ^{12}CO (J=3–2) profile map within the 44″ × 44″ region centered at HD 163296; the central panel of Figure 3.9 is also shown in Figure 3.7d in an enlarged view. The achieved rms level was 0.122 K. A clear double-peaked profile with 11.1 σ at $\sim$ 6 km s^{-1} is seen only in the center panel. The peak intensity and the velocity width are 1.35 K in $T_{\rm mb}$ and 3.1±0.1 km s^{-1} in FWHM, respectively. The emission components between 10 and 15 km s^{-1} and at 20 km s^{-1} in $V_{\rm LSR}$ appear regardless of the positions, as in the case of ^{12}CO

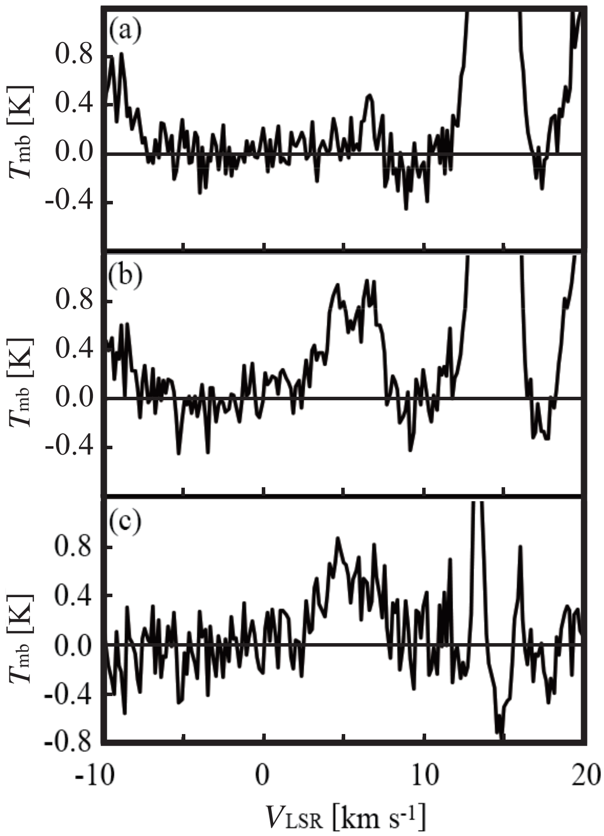

Figure 3.8 Illustrated procedure for validation of emission origin. (a) Averaged ^{12}CO (J=1–0) profile of the four locations 20$''$ away from the central star in Figure 3.6. (b) ^{12}CO (J=1–0) profile toward HD 163296 in Figure 3.6. (c) Profile after subtracting (a) from (b).

(J=1–0) (Figure 3.6). Basically, the ^{12}CO (J=3–2) results show the consistency with the ones obtained in ^{12}CO (J=1–0) line observation.

Figure 3.7e presents the ^{13}CO (J=3–2) spectrum at the stellar position, showing its double-peaked profile. The peak intensity and velocity width are 0.38 K in $T_{\rm mb}$ and 3.85 km s^{-1} in FWHM, respectively. As in the case of the J=1–0 lines, the disk seems to be optically thick for the J=3–2 line because the intensity ratio between ^{12}CO (J=3–2) and ^{13}CO (J=3–2) is 4.2, much smaller than the abundance of 60, which is expected to be in the case of optically thick. Note that the velocity width is larger in ^{13}CO (J=3–2) than ^{12}CO (J=3–2), the same phenomenon is seen in the emissions in the J=1–0 transition (see also Figure 3.18).

3.3 HCO$^+$ (J=1–0) Emission

Figure 3.10 shows an HCO$^+$ (J=1–0) emission originated from the disk around HD 163296. A double-peaked profile with the peak intensity of 0.23 K in $T_{\rm mb}$ is marginally detected at the systemic velocity of $\sim$ 6 km s^{-1} in $V_{\rm LSR}$. The achieved rms level was 0.058 K after 4-channel binning and resulted in 3.8 σ in the S/N ratio. The velocity width is 2.4±0.1 km s^{-1} in FWHM. The noise level of the obtained final spectrum is still too high to apply for model fitting so the estimation of ionization fraction was made by the empirical equation (1.22) and the number density of gas derived from model fitting.

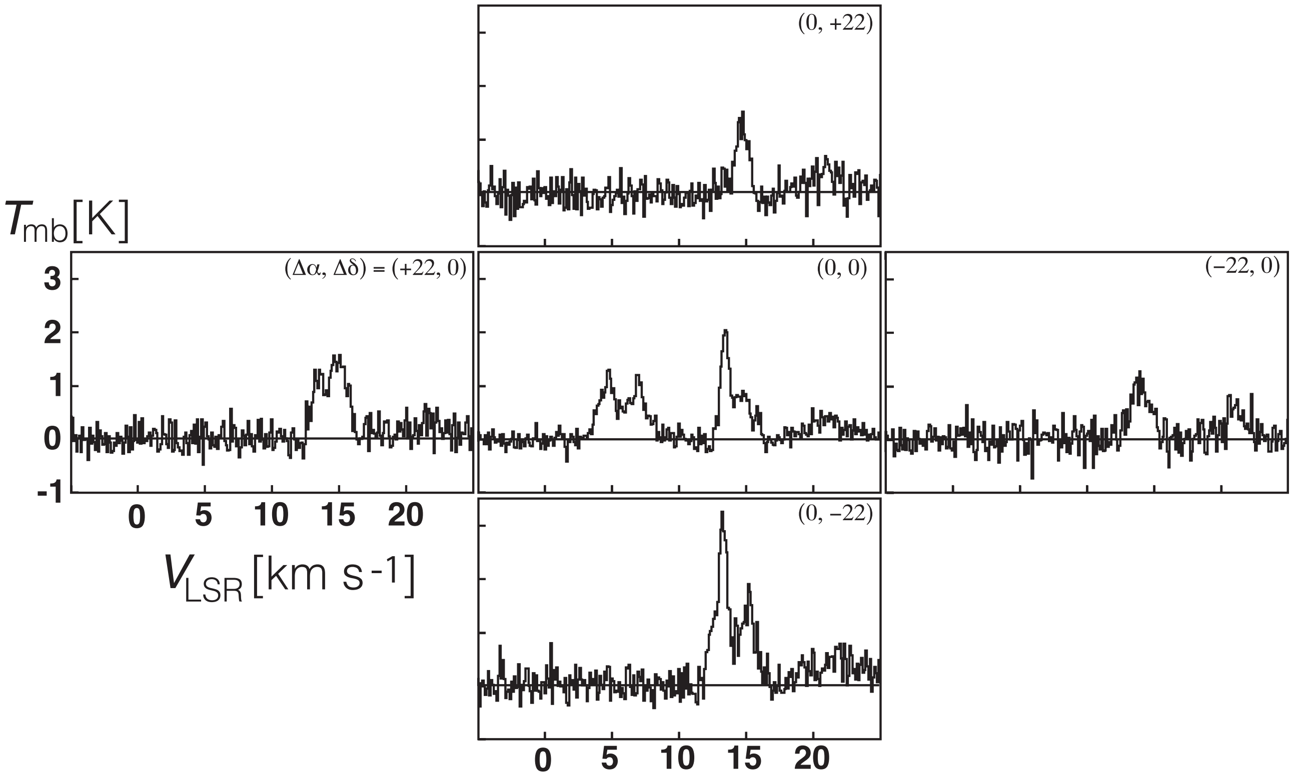

Figure 3.9 Emission profile map of ^{12}CO (J=3–2) around HD 163296. The center panel indicates the direction of the star;disk system.The offset (in arc-second) from the stellar position is shown in the top right corner of each panel.

4 Model Fitting

Model fitting is one of the effective methods to estimate the physical properties of disks around HAeBe stars (Dullemond et al. 2001; Dullemond 2002; Testi et al. 2003; Natta et al. 2004). All of the observational profiles were fitted, which are three CO isotopologues' emission lines with two different rotational transitions, with those calculated by the disk models described in Chapter 2. Two kinds of disk models were adopted in the model fitting; a classical disk model that includes power-law forms of the temperature and surface density distributions in the radial direction with inner and outer cutoffs developed by Kitamura et al. (1993) described in Section 2.1 in Chapter 2 and a similarity solution disk model that is refurbished based on the Kitamura et al. (1993) disk model described in Section 2.2 in Chapter 2. The results are compared with these obtained by millimeter and sub-millimeter interferometers in detail in Section 5 in this chapter (Isella et al. 2007). Although interferometric observations can provide detailed geometrical structure with high spatial resolution, it might be unable to detect emission from the diffuse gas uniformly extending away due to the spatial filtering effect. Single-dish telescopes with a large diameter, on the other hand, have higher sensitivity to the weak extended emission, which interferometers can not detect well. Interferometric and single dish observations are, therefore, complementary to each other, and comparing their results is a fruitful way to gain a better understanding of the disk nature.

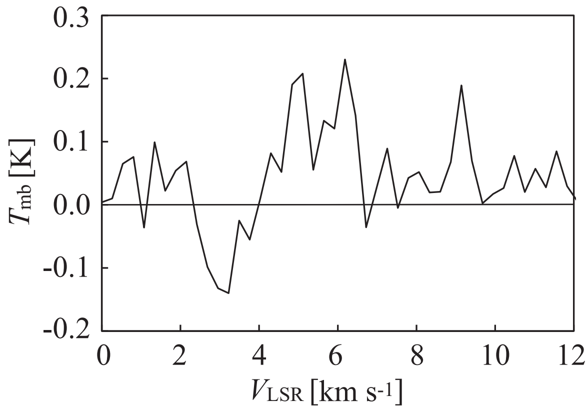

Figure 3.10 HCO^+ (J=1–0) spectrum for HD163296.

4.1 Fitting Results of Power-Law Disk Model

The best-fit temperatures and the outer radius at 0.1, 0.3, 1, and 3 g cm^{-2} in Σ_{100} where the fitting solution for all of the CO lines simultaneously exists are provided in Table 3.1. The best fitting results when Σ_{100} = 1 g cm^{-2} are shown in Figure 3.11 and the corresponding disk temperature, intensity, and density distributions in two dimensional views are provided in Appendix C1. Note that the observed profiles shown in Figure 3.11 were re-sampled with a velocity resolution of 0.08 km s^{-1} for ^{12}CO (J=1–0) line, 0.05 km s^{-1} for C^{18}O (J=1–0) line, and 0.11 km s^{-1} for the others to directly compare with the model calculations. As shown in Table 3.1, the fitting temperature of ^{12}CO (J=3–2) shows the highest value among all of the CO lines. It is essential to ascertain the goodness of the solution obtained in the model fitting. Figure 3.12 shows the fitting temperature at several specific Σ_{100} between 0.003 and 3 g cm^{-2}.

The best-fit T_{100} values for the ^{12}CO (J=3–2) line given in Table 3.1 are between 58.5 ± 9.5 K, and this range is significantly higher than those estimated for the other CO lines, 31 ± 15 K when Σ_{100} is greater than 0.1 g cm^{-2}. This difference in the best-fit T_{100} implies that the disk is composed of at least two layers with distinct temperatures. The uncertainty of the fitting temperature is smaller for a higher surface density, or large optical depth in the disk. For a lower surface density, the fitting temperature range becomes drastically larger, or no solution exists; the ^{13}CO (J=1–0) emission line, for instance, dose not have any fitting temperature at Σ_{100} less than 0.1 g cm^{-2}. The fitting errors in temperature at 0.1 g cm^{-2} in Σ_{100} are more than 30 % for ^{13}CO (J=1–0) line and more than 20 % for ^{13}CO (J=3–2) line, respectively. Those at Σ_{100} greater than 0.3 g cm^{-2}, on the other hand, are less than 20 % for all of the CO lines, and the fitting temperatures are gradually confined as Σ_{100} becomes larger. Σ_{100} greater than 0.1 g cm^{-2} obtained by model fitting corresponds to 10 $\lesssim$ (∼ 5 even at r_{out} = 550 AU) in optical depth, and therefore the disk is surely optically thick for all CO lines.

Table 3.1 Best Fit Parameters at r_{out} = 550 AU in the power-law disk model

	T_{100} [K]				
Σ_{100} [g cm^{-2}]	^{12}CO(J=3–2)	^{13}CO(J=3–2)	^{12}CO (J=1–0)	^{13}CO(J=1–0)	C^{18}O(J=1–0)
0.1	63^{+5}_{-5}	38^{+8}_{-8}	35^{+3}_{-4}	26^{+8}_{-6}	20^{+10}_{-4}
0.3	59^{+4}_{-3}	33^{+2}_{-6}	32^{+4}_{-3}	21^{+4}_{-3}	10^{+3}_{-2}
1	55^{+5}_{-3}	30^{+5}_{-5}	30^{+3}_{-3}	19^{+3}_{-3}	9^{+2}_{-2}
3	53^{+4}_{-4}	28^{+5}_{-4}	29^{+3}_{-3}	18^{+3}_{-2}	9^{+2}_{-2}

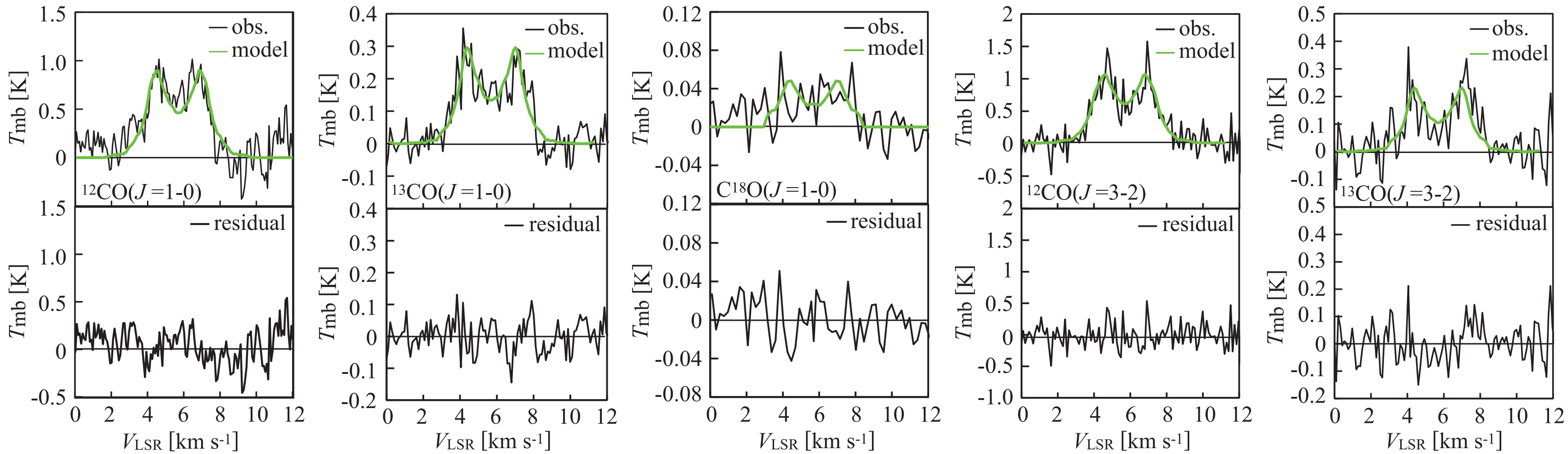

Figure 3.11 Fitting results in power-law disk model. (Upper panels): Comparisons between the line profiles obtained by our observations (solid line) and best-fit model calculations when $\Sigma_{100} = 1$ g cm^{-2} (green lines). Best-fit values for T_{100} and r_{out} in the model calculations are listed in Table 3.1. (Lower panels): Difference between the observed and calculated profiles shown in the upper panels.

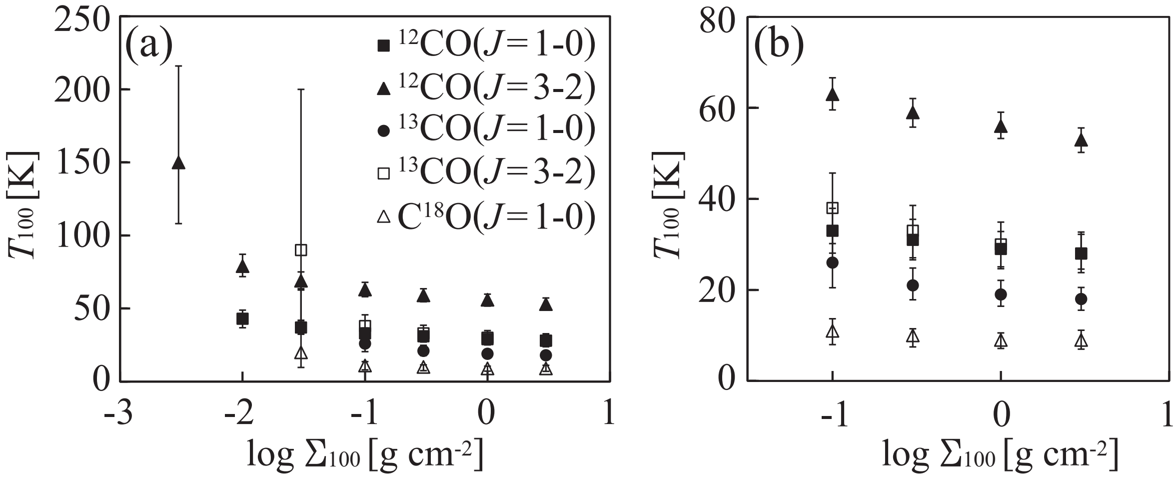

Figure 3.12 Best-fit values of T_{100} with uncertainties for the acceptable fit in the power-law disk model calculations as a function of Σ_{100}. Panel (a) shows the cases of $\Sigma_{100} = 0.003 - 3$ g cm^{-2}, and panel (b) magnifies the lower-right part of the panel (a).

4.2 Fitting Results of Similarity Solution Disk Model

Model fitting by the similarity solution disk model likewise is done for comparison with the results by power-law disk model. The best-fit temperatures and the outer radius at 0.001, 0.01, 0.1, and 1 g cm^{-2} in Σ_{100} where the fitting solution for all of the CO lines simultaneously exist are provided in Table 3.2. The best fitting results when $\Sigma_{100} = 1$ g cm^{-2} are shown in Figure 3.13 and the corresponding disk temperature, intensity, and density distributions in two dimensional views are provided in Appendix C2. Figure 3.14 shows the fitting temperature at several specific Σ_{100}. Note that the solution in the lower range of Σ_{100} is not reliable even though fitting solution exists. Since the surface density tapers off gradually and the mass still remains in the outer region of the disk in the similarity solution disk model, not like a truncation structure seen in the power-law disk model, model fitting can be achieved by adjusting T_{100} in low Σ_{100}. Although it is difficult to determine the surface density in similarity solution disk model, the surface density might be determined by merging fitting parameters obtained by other models, such as SED. As in the case of the results from the power-law disk model, the fitting temperature of ^{12}CO (J=3–2) shows the highest among all of the CO lines (ref. Table 3.2).

Table 3.2 Best-fit parameters at r_{out} = 900 AU in the similarity solution disk model

	T_{100} [K]				
Σ_{100} [g cm^{-2}]	^{12}CO(J=3–2)	^{13}CO(J=3–2)	^{12}CO (J=1–0)	^{13}CO(J=1–0)	C^{18}O(J=1–0)
0.1	63^{+5}_{-5}	38^{+8}_{-8}	35^{+3}_{-4}	26^{+8}_{-6}	20^{+10}_{-4}
0.3	59^{+4}_{-3}	33^{+2}_{-6}	32^{+4}_{-3}	21^{+4}_{-3}	10^{+3}_{-2}
1	55^{+5}_{-3}	30^{+5}_{-5}	30^{+3}_{-3}	19^{+3}_{-3}	9^{+2}_{-2}
3	53^{+4}_{-4}	28^{+5}_{-4}	29^{+3}_{-3}	18^{+3}_{-2}	9^{+2}_{-2}

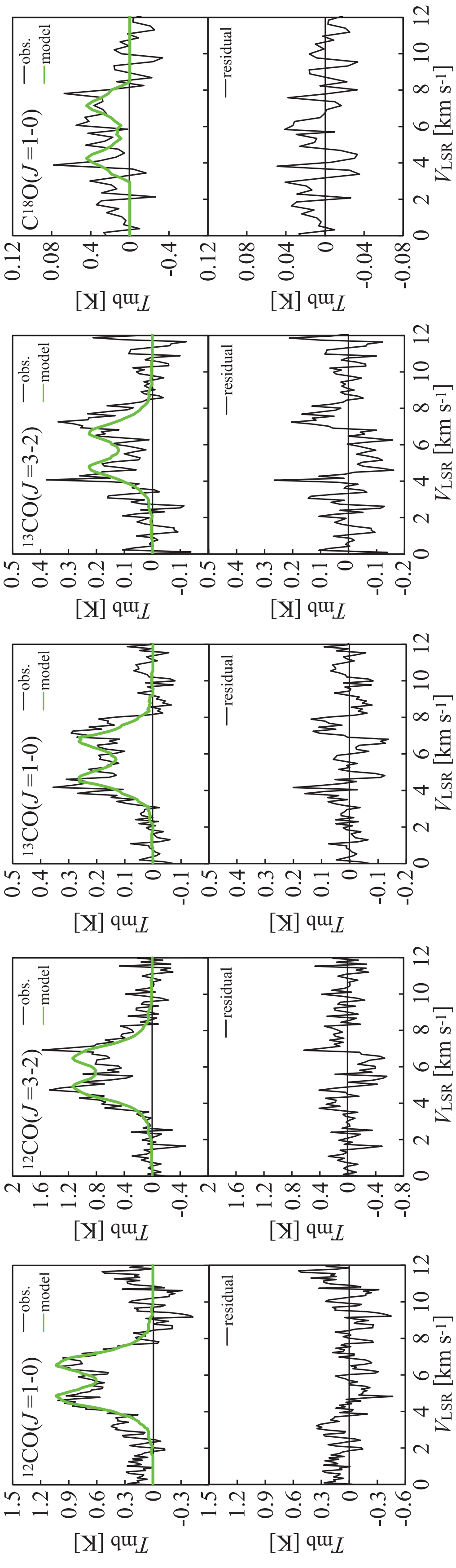

Figure 3.13 Fitting results in the similarity solution disk model. (Upper panels): Comparisons between the line profiles obtained by our observations (solid line) and best-fit model calculations when $\Sigma_{100} = 1$ g cm^{-2} (green lines). Best-fit values for T_{100} and $r_{\rm out}$ in the model calculations are listed in Table 3.2. (Lower panels): Difference between the observed and calculated profiles shown in the upper panels.

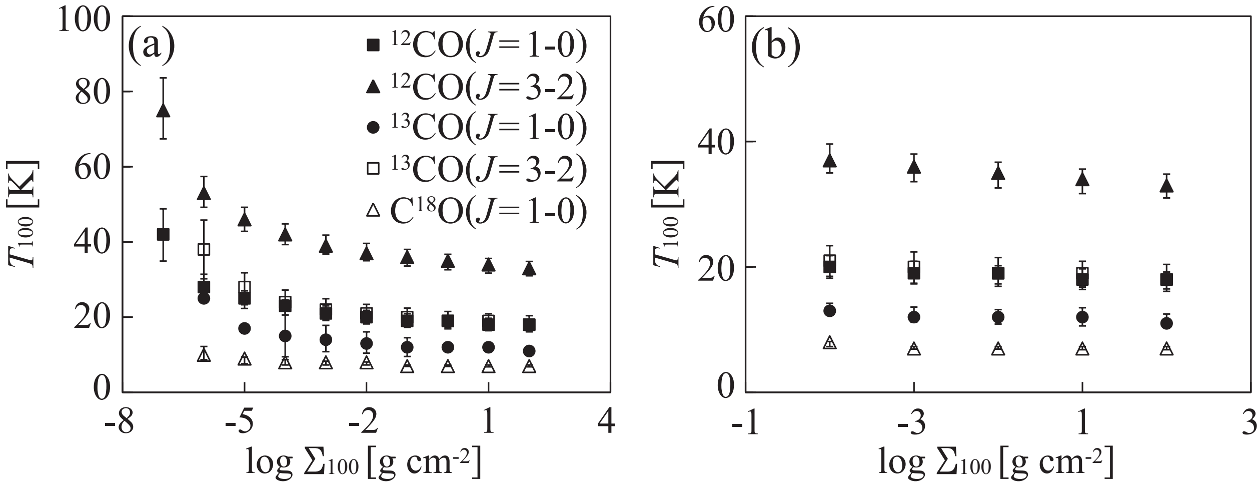

Figure 3.14 Best-fit values of T_{100} with uncertainities for the acceptable fit in the similarity solution disk model calculations as function of Σ_{100}. Panel (a) shows the cases of $\Sigma_{100} = 10^{-7} - 10^{2}$ g cm^{-2}, and panel (b) magnifies the lower-right part of the panel (a).

5 Discussion

5.1 Comparison with the Results by Interferometric Observation

High-resolution images of HD 163296 were taken with interferometers at multi-wavelengths (the IRAM/PdBI, SMA, and VLA) both in continuum and in the emission lines of ^{12}CO, ^{13}CO, and C^{18}O (Isella et al. 2007). They compared the observational results of the CO emissions with those predicted by the self-consistent disk model to estimate the physical disk properties. Although the assumptions in the model calculations were slightly different from each other, the temperature and the minimum surface density of the disk derived in Section 4 in this chapter showed a reasonable agreement with the values obtained by Isella et al. (2007); the temperature at 100 AU and the minimum surface density at 10 AU from the central star were estimated to be 26^{+8}_{-6} K and 1 g cm^{-2} from our ^{13}CO (J=1–0) observations, and they were within the possible fitting range obtained by Isella et al. (2007): 30±10 K and 4^{+12}_{-3} g cm^{-2}, respectively. The radius derived by the power-law disk model from single-dish observations, which generally have higher sensitivity to weaker emission, is 550±100 AU, and was consistent with the one derived by interferometric observations. As it will be discussed in detail in Section 5.3 in Chapter 3, the radius derived by the similarity solution disk model is 900±100 AU, which is consistent with the radius of 800 AU derived from the same disk model by Hughes et al. (2008).

Table 3.3 Summary of best-fit parameters for the continuum and the CO emissions obtained by interferometers (Isella et al. 2007)

Parameters	Continuum	^{12}CO(J=2–1)	^{12}CO (J=3–2)	^{13}CO(J=1–0)
M_* [$M_\odot$]	2.6^a	$2.6^{+0.3}_{-0.5}$	2.4±0.8	2.6±0.6
inclination [deg.]	40±12	45±5	45±10	50±8
$r_{\rm out}$ [AU]	200±15	550±50	550±100	500±80
Σ_{10} [g cm^{-2}]	46±4	90±70	90^a	4^{+12}_{-3}
p	0.8±0.1	$0.6^{+0.3}_{-0.1}$	0.6^a	1.0±0.5
q	-	$0.5^{+0.2}_{-0.1}$	0.8±0.4	0.8±0.4

5.2 Vertical Temperature Distribution

As fitting results of Σ_{100} shown in Table 3.1 and 3.2, and intensity ratio between different isotopologues with the same rotational transition, the disk is arguably optically thick in CO emissions. Taking advantage of different mass opacity of CO isotopologues whose emission lines reflect the temperature at each photosphere[1] located at different altitude from the mid-plane of the disk, the vertical thermal structure of the disk can be analyzed. Figure 3.12 is the best-fit T_{100} as a function of Σ_{100} and shows that model fittings in the case of ^{12}CO (J=1–0), ^{13}CO (J=1–0), ^{13}CO (J=3–2), and C^{18}O (J=1–0) emission lines succeeded at almost the same temperature when $\Sigma_{100} \gtrsim 0.1$ g cm^{-2}, but the ^{12}CO (J=3–2) results require almost double of the fitting temperature of the other three lines to reproduce the emission profile obtained from the observation. These different temperatures can be explained by the temperature distribution along the vertical direction, as theoretically predicted in the passive disk structure model (Chiang & Goldreich e.g. 1997).

To examine the vertical temperature distribution in detail, the computation of the column densities of H_2 that satisfy the optical depth for each CO emission line to be unity ($N_{\tau_{\nu_0}=1}$) was made by

$$N_{\tau_{\nu_0}=1} = \frac{3k_B T_{\rm ex} \Delta V_{\rm gas}}{8\pi^3 B\mu^2 \cos\theta} \frac{1}{(J+1)} \exp\left[\frac{hBJ(J+1)}{k_B T_{\rm ex}}\right] \left[1 - \exp\left(\frac{h\nu_0}{k_B T_{\rm ex}}\right)\right]^{-1}, \quad (3.1)$$

where B is the rotational constant of a molecule, μ is the permanent dipole moment, $T_{\rm ex}$ is the excitation temperature, $\Delta V_{\rm gas}$ is the velocity width of a gas molecule, θ is the inclination angle, h is the Planck constant, J is the rotational quantum number, and ν_0 is the frequency of the transition (Scoville et al. 1986). Note that $N_{\tau_{\nu_0}=1}$ is the column density obtained by integrating the number density from the disk surface to the disk interior along a line of sight.

In this thesis, the assumption $\Delta V_{\rm gas} = \Delta V_{\rm th}$ was adopted for simplicity, where $\Delta V_{\rm th}$ is the thermal velocity width of gas molecules, and expressed by

$$\Delta V_{\rm gas} \equiv \Delta V_{\rm th} = \sqrt{\frac{8\ln 2 k_{\rm B} T(r)}{m_{\rm CO}}}. \quad (3.2)$$

Turbulent velocity ($V_{\rm turb}$) can also contribute to $\Delta V_{\rm gas}$. Hughes et al. (2011) derived a turbulent line width of ~ 0.3 km s^{-1} for the disk around HD 163296 from fitting the observed line profile with high spectral resolution (44 m s^{-1}) by SMA with the disk model in which $V_{\rm turb}$ is parameterized. Previous observations also revealed that $V_{\rm turb}$ in disks around TTS or HAe star is comparable to $\Delta V_{\rm th}$: 0.07 - 0.15 km s^{-1} in DM Tau (Dartois et al. 2003; Simon et al. 2000) and 0.38 km s^{-1} in AB Aur (Piétu et al. 2005). In such cases, however, the line profile calculated by the model is not altered significantly by $\Delta V_{\rm turb}$ because the line shape is mainly determined by the Keplerian rotation velocity. This assumption probably produces a factor of uncertainty for the estimation of $N_{\tau_{\nu_0}=1}$, but does not significantly affect the following discussion.

$N_{\tau_{\nu_0}=1}$ for each CO emission line provides the information about the vertical location of the photosphere of each CO emission line in the disk. Figure 3.15 shows $N_{\tau_{\nu_0}=1}$ and vertical locations of photospheres of each CO emission line. The results are provided in the case of $T_{100} = 30$ K and 60 K, which are the representative values of the low-temperature interior and the high-temperature surface, respectively, as described in Section 4.1 in Chapter 3. To derive the location of each photosphere the fitting result of $\Sigma_{100} = 0.1$ g cm^{-2} is selected as a representative case, since this value is consistent with the results by Isella et al. (2007). In both cases shown by Figure 3.15, $N_{\tau_{\nu_0}=1}$ results in the descending order of ^{12}CO (J=3–2), ^{12}CO (J=1–0), ^{13}CO (J=3–2),

[1]In fact, a photosphere is where the optical depth (τ) becomes 2/3. However, the surface where $\tau = 1$ is regarded as a photosphere in this thesis.

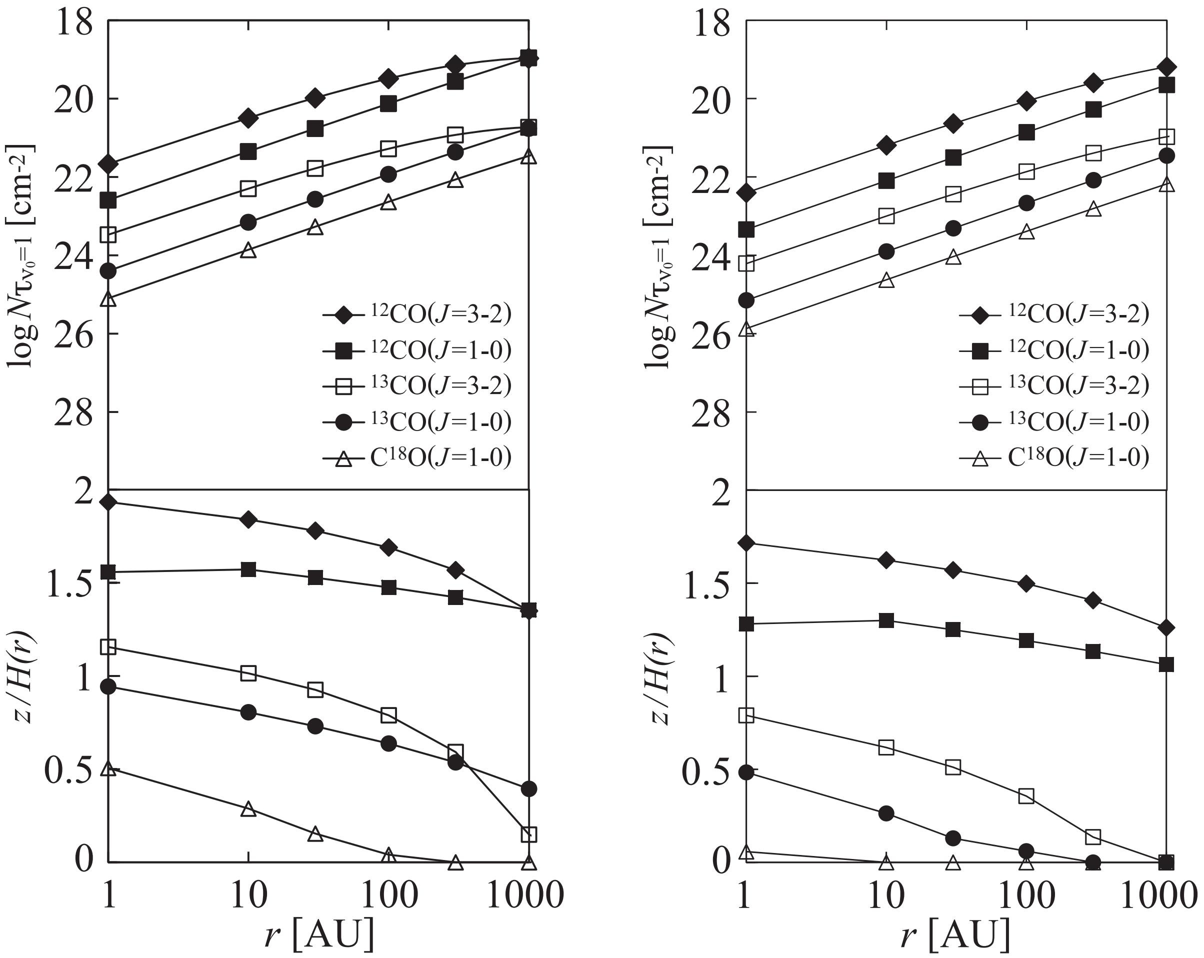

Figure 3.15 Vertical locations of the photospheres of each CO isotopologue line. (upper panels): Column densities in $N(H_2)$ that are required to become $\tau_{\nu_0} = 1$ for each CO emission line are provided. The radial temperature dependence is set to be $T(r) = 30(r/100\text{AU})^{-0.5}$ [K] (left) and $T(r) = 60(r/100\text{AU})^{-0.5}$ [K] (right), respectively. Note that the vertical axises are reversed. (lower panels): The vertical distance of the photospheres for all CO emissions from the mid-plane of the disk normalized by the scale height at the local temperature in the case of $\Sigma_{100} = 1$ g cm^{-2} is provided. Note that these vertical locations of each CO line are equivalent to the location corresponding to $N_{\tau_\nu 0}$ =1 shown in the upper panel.

^{13}CO (J=1–0), and C^{18}O (J=1–0) implying that the photosphere of ^{12}CO (J=3–2) emission layer is located uppermost among the five CO lines. The total geometric cross Section of grains per hydrogen atom (σ_d) in interstellar medium is $\sim 10^{-21}$ cm^2 at visible wavelength (Stahler & Palla 2004), hence the column density that makes the optical depth for the stellar radiation unity is 10^{21} cm^{-2}. The grazing angle is assumed to be 0.05 in the Inoue et al. (2009) calculation; hence, the column density of the upper layer should be about 5×10^{19} cm^{-2}. This column density is consistent with the one above the photosphere of ^{12}CO (J=3–2) at $r \gtrsim$ 100 AU, as shown in Figure 3.15. $N_{\tau_{\nu_0}=1}$ of ^{12}CO (J=1–0) decreases faster than that of ^{12}CO (J=3–2) at $r > 300$ AU in the case of $T_{100} = 30$ K because CO molecules is not sufficiently excited to the $J = 3$ level due to lower temperatures. The same phenomenon is seen in ^{13}CO as well. From comparisons between the fitting temperature and the vertical locations of the photosphere of each CO line, the general trend is that the farther away the layer is from the mid-plane of the disk, the warmer it reaches. This is quite reasonable because the gas around the disk surface should be easily heated by the direct radiation from the central star, whilethe gas in the disk interior remains at low temperature due to little radiation reached from the central star.

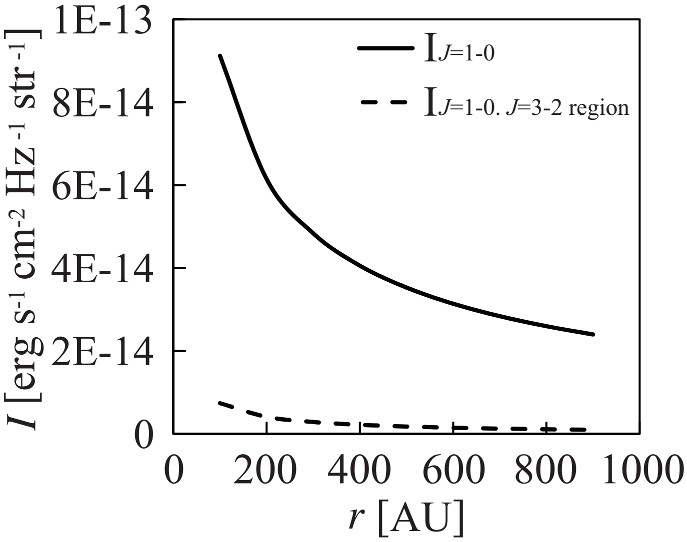

Figure 3.16 Influence of the higher temperature layer on the ^{12}CO (J=1–0) emission by higher temperature layer. The solid line represents the intensity of ^{12}CO (J=1–0) emission at the fitting temperature and surface density (T_{100} = 30 K and Σ_{100} = 1 g cm^{-2}). The dashed line represents the intensity of the ^{12}CO (J=1–0) emission line from the region where the optical depth of ^{12}CO (J=3–2) is less than unity when T_{100} = 60 K.

When the $N_{\tau_{\nu_0}=1}$ shown in Figure 3.15 was derived, it was assumed that the disk temperature is uniform in the vertical direction. These considerations, however, might be invalid as a consequence of the vertical temperature distribution; the ^{12}CO (J=3–2) emission line originates from an upper layer of the disk, but this could also contribute significantly to the other CO lines. Therefore, it was evaluated how strongly such an upper layer affects the other CO emissions. Figure 3.16 shows how strongly the ^{12}CO (J=1–0) is emitted from above the photosphere of ^{12}CO (J=3–2). In this figure, the optical depth of the ^{12}CO (J=1–0) emission line in the region above the photosphere of ^{12}CO (J=3–2) was first calculated, and then the intensity of ^{12}CO (J=1–0) at the fitting temperature, which was compared with that originated from the region, was calculated. The contribution of the high-temperature layer is less than 10 % of the ^{12}CO (J=1–0) intensity, and can be safely neglected. Therefore, the estimated vertical location of each CO emission layer in Figure 3.15 is validated.

As shown in Figure 3.12, the temperatures of the ^{12}CO (J=1–0) and ^{13}CO (J=3–2) layers are almost the same when $\Sigma_{100} > 0.1$ g cm^{-2}. The temperature of the ^{13}CO (J=1–0) and C^{18}O (J=1–0) layers seems to be even lower. Such a vertical thermal structure of irradiated accretion disks around TTS has been theoretically predicted. D'Alessio et al. (1999) constructed detailed vertical structure models of irradiated accretion disks, and extensively explored the dependence of the structure and the emission properties on the mass accretion rate, viscosity parameter, and disk radius. Inoue et al. (2009) also proposed a 3-layer disk model. The middle layer can form where the optical depth for the radiation reprocessed by the upper layer is less than unity. The above fitting results suggest the existence of such a 3-layer structure.

5.3 Radial Density Distribution

As explained in Chapter 1 regarding the planetary system formation, planet mass at different orbital radii or timescale of planet formation can be predicted if the radial surface density distribution is determined.

In addition, the radial surface density distribution is of great interest because it is decisive in identifying the presence of exponential tail in the radial surface density distribution near outer edge. Power-law distribution in the surface density has been widely accepted until recently but the outermost region now needs to be examined more quantitatively as well. A series of the CO isotopologue observations manifests that the velocity widths of each CO emission profile are different in HD163296. Figure 3.17 is a comparison among CO isotopologue emission profiles with the same J=1–0 rotational transition. The profile obtained by the most optically thick line such as ^{12}CO (J=1–0) is the narrowest and the profile obtained by the most optically thin line such as C^{18}O (J=1–0) is the widest. The same phenomenon is seen in the spectra of ^{12}CO (J=3–2) and ^{13}CO (J=3–2) ; narrower in ^{12}CO (J=3–2) line and wider in ^{13}CO (J=3–2) line as shown in Figure 3.18. Since the different velocity width reflects different size of a Keplerian disk, each CO emission line also traces different radial location. The fact that the outer radius derived by dust continuum is different from the one derived by line emission is well explained by the similarity solution disk model with an exponential tail which makes the surface density tapers off gradually at the outer edge. Figure 3.19 shows the radial surface density distribution and mid-plane density profiles for the power-law and the similarity solution disk models. The solid lines indicate the distributions in the power-law disk model, while the dashed lines indicate distributions in the similarity solution disk model. The distribution curves for both disks show similar profiles in inner disk since the same parameters are used in the index of $\Sigma(r)$ (ref. equation (2.2) and (2.10)).

As results of comparison of model fitting in both of the models, the power-law disk model shows better fitting than the similarity solution disk model. The residuals for both models are provided in Figure 3.20. The residual after fitting in power-law disk model is smaller than in the similarity solution disk model. The fitting result seems to be supportive of a truncation structure at the outer edge of the disk. However the disk is thought to be rather evolved and even close to a debris disk (Isella et al. 2007), and therefore a large amount of gas could already be lost. The exponential tail is believed to be present in the low density region near outer edge of the disk, and thus is not detected simply because of the low density of the disk and the sensitivity limit of the present observations. The exponential tail may be detected in the future work by observation instruments with higher sensitivity.

5.4 Ionization Fraction of the Disk

The ionization fraction of the gas disk is one of the important factors for inducing MRI. The ionization fraction of the disk can be estimated by equation (1.22). Since the observed emission is mainly originated from the outer disk when spatially unresolved, the both simulation and observation data at r = 100 AU from the central star were applied. For numerical evaluation, the CO abundance with respect to HCO$^+$ ([CO]/[HCO$^+$]) calculated by Walsh et al. (2010) is $\sim 10^5$ and the number density of hydrogen based on the observational results as described in Figure 3.19 is $\sim 10^8$. Equation (1.22) produces [e$^-$] $\sim 10^{-9}$ but this could be overestimated for protoplanetary disk since $n_{\rm H}$ in protoplanetary disks should be larger than that in dense cores. It is expected that higher density of $n_{\rm H}$ promotes recombination and as a result [e$^-$] will decrease as $n_{\rm H}$ rises. Therefore, [e$^-$] is thought to be even lower probably by 2 - 3 order of magnitude. However, MRI can be invoked even when [e$^-$] $\sim 10^{-10}$ - 10^{-12}. Although it is necessary to investigate more the ionization fraction, our observational results have supported so far that MRI can be driven in the disk around HD 163296. [CO]/[HCO$^+$] can be estimated by calculating the surface density of HCO$^+$ through model fitting and the results obtained based on observations should be evaluated for their consistency. The disk is optically thick in HCO$^+$ (J=1–0) line, thus H^{13}CO$^+$ (J=1–0) line is more suitable for determining the HCO$^+$ density of the disk. It is thought to be capable of detecting H^{13}CO$^+$ (J=1–0) emission which have hardly been detected in protoplanetary disks

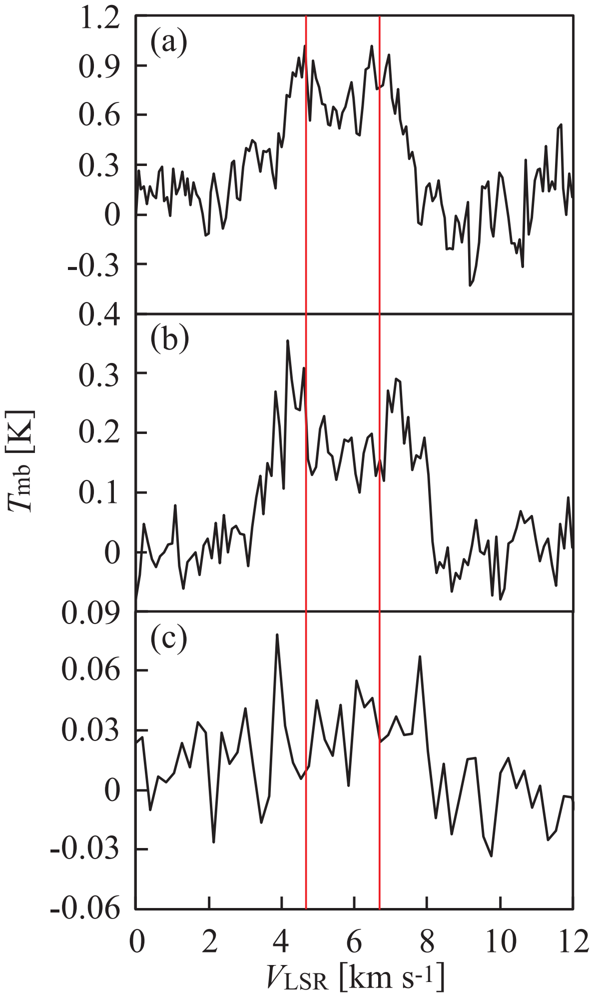

Figure 3.17 Comparison of peak-to-peak velocity width among CO isotopologue emission profiles. The observational profiles are ^{12}CO (J=1–0) (a), ^{13}CO (J=1–0) (b), and C^{18}O (J=1–0) (c), respectively. The red lines indicate the velocities of each peak in ^{12}CO (J=1–0) profile.

so far by recent advanced receivers with high sensitivity.

6 Chapter Summary

This paper presents observational results of the disk around HD 163296 in the ^{12}CO (J=1–0), ^{12}CO (J=3–2), ^{13}CO (J=1–0), ^{13}CO (J=3–2), and C^{18}O (J=1–0) emission lines. Double-peaked profiles originating from a rotating circumstellar disk were successfully detected in all of the CO lines. The physical parameters of the disk, such as the temperature distribution, the surface density distribution and the outer radius, were estimated by model fitting by utilizing a disk model. These physical values obtained by single dish observation were confirmed to be consistent with the results of interferometric observations (Isella et al. 2007).

The disk must be optically thick for all of the CO lines. Taking advantage of the difference in the position of the photosphere among the CO lines, the temperature distribution in the vertical direction was revealed . It has been proven that there are at least two distinct temperature layers, possibly three layers, from model fittings. The temperature in the uppermost ^{12}CO (J=3–2) emitting layer is estimated to be 58.5 ± 9.5 K at

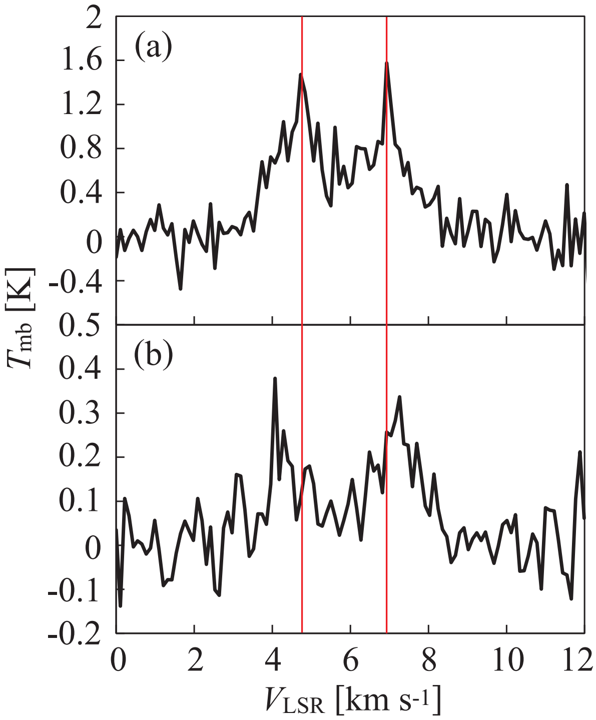

Figure 3.18 The same as Figure 3.17 in the case of (a), ^{12}CO (J=3–2) and (b), ^{13}CO (J=3–2) emission.

100 AU from the central star, and it is about twice higher than that in the inner regions emitting the other CO lines, 31 ± 15 K at 100 AU. Since the vertical temperature distribution inside of a disk is commonly suggested for both TTS and HAe stars (DM Tau, AB Aur, and HD 31648), such a temperature distribution may be ubiquitous in protoplanetary disks (Piétu et al. 2007).

The radial surface density distribution is investigated by comparing the classical power-law disk model with a truncation at the outer edge and the similarity solution disk model with an exponential tail. As a result of the comparison, the power-law disk model fits the observed profiles better than the similarity solution disk model does. The exponential tail occurred at low density in the outer disk region is not detected in the well-evolved HD 163296 disk probably because of sensitivity limit and needs further investigation to make a conclusion. HCO^+ (J=1–0) observation provides the order estimation about the ionization fraction of the disk. The result indicates that ionization fraction is of order 10^{-9}, which is capable of driving MRI in th disk. The HCO^+ abundance is not based on the observational results but theoretical prediction based on the computation through chemical reaction network in the estimation of the ionization fraction. The ionization fraction derived from observation is desired. The derivation of HCO^+ abundance can be greatly improved if the optically thin $H^{13}CO^+$ (J=1–0) line is utilized as a means to trace the disk mass.

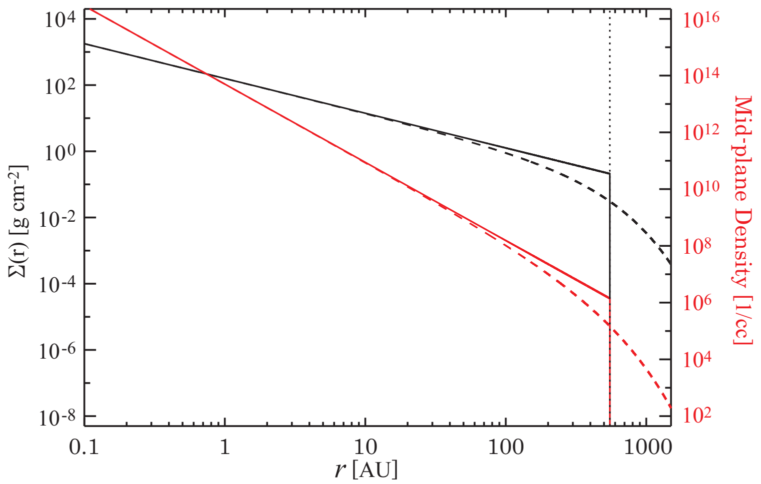

Figure 3.19 Comparison of radial surface density distribution (black) and mid-plane density distribution (red) between the power-law disk model (solid lines) and the similarity solution disk model (dashed lines) when $\Sigma_{100} = 1$ g cm^{-2} as a representative fitting value.

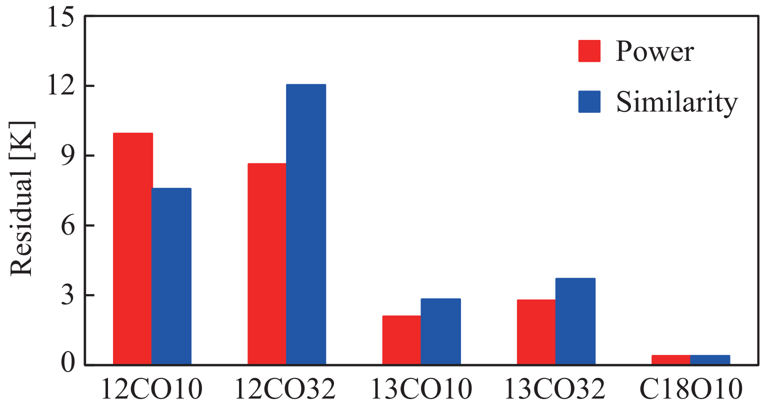

Figure 3.20 Residuals resulting from subtraction of the profile calculated by the disk models from the observed emissions. The red bar indicates the residual generated by the power-law disk model and the blue bar is the same as the red by the similarity solution disk model. The residuals of each CO isotopologue line are provided and indicated in the abscissa and the difference between channels over the range of the emission profile is provided in the ordinate.

Chapter 4

Disk Structure of HD 31648

1 Introduction

HD 31648 (MWC 480) is one of the well-known HAe stars with A2/3e + sh in spectral type (Thé et al. 1994) and the strong Hα emission line from the star was first discovered by Merril et al. (1942). HD31648 is located in the Taurus - Auriga star-forming region at a distance of 140 pc, where a local group of TTSs and HAeBe stars exist, and van den Ancker et al. (1998) identified the distance is 131^{+24}_{-18} pc by Hipparcos measurement. Mannings et al. (1997a) detected a disk with a mass of 0.024 $M_\odot$ in Keplerian rotation associated with a star with thermal dust continuum emission at wavelength λ = 1.3 mm and ^{12}CO (J=2–1) emission line as shown in Figure 4.1. They also determined the stellar mass, inclination, and size of the disk to be $2.3^{+0.1}_{-0.3}$ $M_\odot$, 30°, and 695 AU, respectively by fitting spectral-line maps of ^{12}CO (J=2–1) with a Keplerian rotation disk model developed by Koerner (1997). They estimated the stellar age of $\sim$ 6 Myr by adapting the evolutionary track developed by D'Antona & Mazzitelli (1994) and Simon et al. (2000) estimated the age of $\sim$ 7 Myr based on other three theoretical evolutionary tracks. Thus, HD31648 is well evolved. HD 31648 is categorized as a group II object by the feature of its SED (see Section 2.2 in Chapter 1) as shown in Figure 4.2 (Acke & van den Ancker 2004), and is expected to have a self-shadowed disk (Meeus et al. 2001; Dullemond & Dominik 2004). HD 31648 is observed by many other molecular lines including cyanide carbonate and deuterated molecules and molecular abundance was estimated (Thi et al. 2005). HD31648 is also the star+disk system that disk chemistry study has extensively conducted in detail (Simon et al. 2000; Piétu et al. 2007).

2 Observations

2.1 ^{12}CO (J=1–0) Mapping Observations

Observations of ^{12}CO (J=1–0) emission line were performed in the winter of 2007 by the NRO 45 m telescope. The emission originated from the disk is confirmed by mapping the neighbor including HD 31648 as the same method as the observation of HD 163296 described in Section 2.1 in Chapter 3. The beam grid spacing of BEARS is $\sim 40''$, corresponding to $\sim$ 5600 AU, and twice larger than that in HD 163296 observation since it was previously checked that the emission of the HD 31648 system was originated from the compact region by the ^{12}CO (J=3–2) observation, details in Section 2.3 in this chapter. The HPBW is $15''$ at this frequency, corresponding to 2100 AU at a distance of 140 pc from the Sun. The DSB system temperature in ^{12}CO (J=1–0) mapping observation was between 300 K and 700 K and the integration time for the observation was about

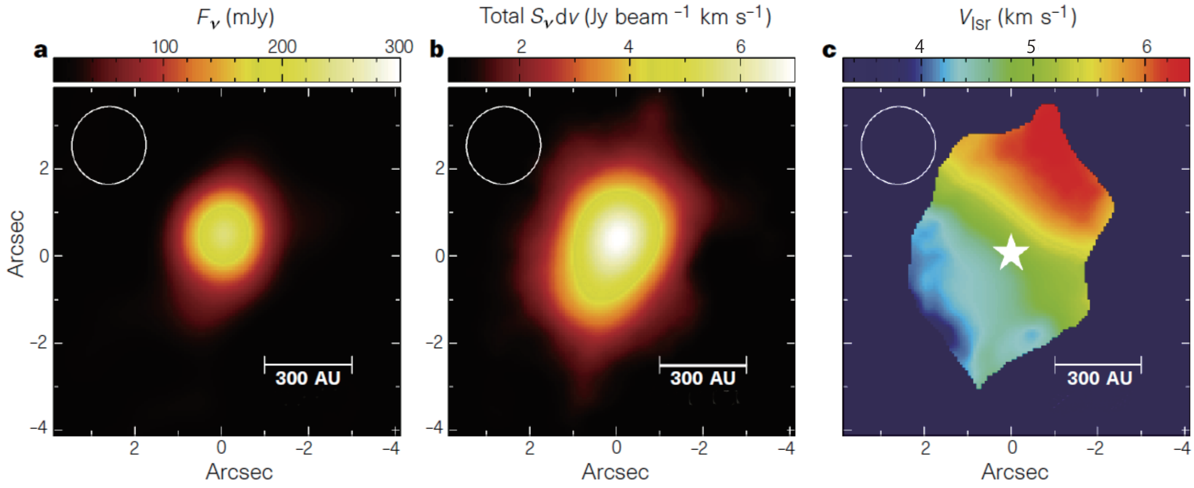

Figure 4.1 Images of millimeter-wave emission from HD 31648 (Mannings et al. 1997a). The full-width-half-maximum of the synthesized beam is shown at the top left corner in each panel. (Left): Flux density of thermal continuum emission from dust grains at λ = 1.3 mm. The scale is designated by the color bar at the top of the panel. (Center): Integrated intensity of ^{12}CO (J=2–1) emission above the 3 σ level in the velocity range between +2.4 and +7.6 km s^{-1}. The scale is designated by the color bar at the top of the panel as the integrated flux density scale. (Right): Intensity-weighted mean gas velocity map. The systemic velocity, $V_{\rm LSR} \sim 5.1$ km s^{-1}, corresponds to the green area and the star symbol indicates the position of the central star. Blue-shifted (approaching) and red-shifted (receding) velocity components are shown as blue and red, respectively.

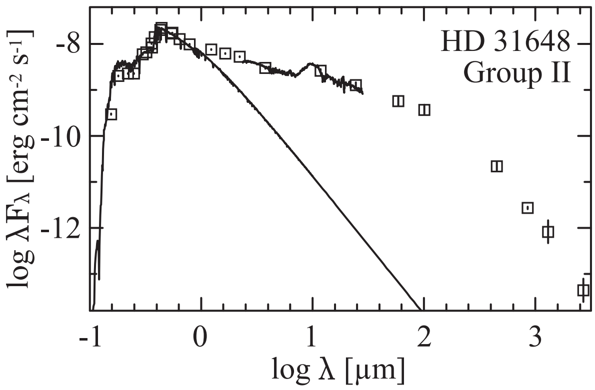

Figure 4.2 SED of HD 31648 (Acke & van den Ancker 2004).

9 hours on the source in double sideband (DSB) mode. A digital spectrometer with 16 MHz (corresponding to 42 km s^{-1}) in bandwidth and 46 kHz (corresponding to 0.12 km s^{-1}) in frequency resolution was selected as the backend. The intensity of the emission was obtained in the antenna temperature, $T^*_{\rm A}$, in Kelvin and converted into the brightness temperature by applying $\eta_{\rm mb}$ = 0.45 for ^{12}CO (J=1–0) line, an average value among 25 detectors of BEARS receiver provided in the NRO status report. The accuracy for telescope pointing was regularly checked against the SiO maser NML Tau and the pointing accuracy was achieved in less than $\pm 5''$ during the whole observation period. The intensity was calibrated by observing Orion KL every once a observational day. Data reduction and analysis were made with the NEWSTAR package as HD 163296 data reduction.

2.2 ^{13}CO (J=1–0) and C^{18}O (J=1–0) Emission Line Observations

Observations of the ^{13}CO (J=1–0) emission line were conducted by the NRO 45 m telescope in the winter of 2009 and C^{18}O (J=1–0) line observation subsequently in the winter 2010. As shown in Section 3.1 and 3.2 in this Chapter, the ^{12}CO (J=1–0) emission detected around 5 km s^{-1} in $V_{\rm LSR}$ at the central star is isolated. Thus, ^{13}CO (J=1–0) observations were intensively made only toward the stellar position by a pair of sideband-separating receivers (2SB receivers), T100H/V, which enabled us to simultaneously detect both the polarization components. The receivers were tuned at ^{13}CO (J=1–0) and C^{18}O (J=1–0) rest frequency of 110.201 GHz and 109.782 GHz, and the HPBW was about 15$''$ around these frequencies. An AOS, whose bandwidth and frequency resolution were 40 MHz (0.11 km s^{-1}) and 20 kHz (0.05 km s^{-1}) respectively, was used. The system noise temperature during observation was between 150 K and 300 K[1]. The IRR was 11 - 15 dB during observation. All observational data when the wind speed exceeded 5 m s^{-1} were flagged out before obtaining the final profile of ^{13}CO (J=1–0) emission. The resultant total integration time was 6 hours on the source. The pointing check and the correction due to atmospheric variation were carried out as the same manner as in ^{12}CO (J=1–0) observations described in Section 2.1 in this chapter. Although the receivers was functioning in very stable, the correction for daily intensity fluctuation caused by the receivers was made by observing Orin KL every observational day. The $\eta_{\rm mb}$ in 2009 at this frequency was 0.42 and applied to convert the raw data of observed antenna temperature to the brightness temperature. The method of data reduction and analysis were also the same as those in the ^{12}CO (J=1–0) observation described in Section 2.1 in this chapter.

2.3 Five Point Observation in ^{12}CO (J=3–2) Line

Observations of ^{12}CO (J=3–2) line were carried out in August 2005 with the ASTE 10-m diameter telescope. HPBW of the ASTE telescope at 345.79 GHz is 22$''$, which corresponds to $\sim$ 3000 AU at a distance of 140 pc away from the Sun, and the $\eta_{\rm mb}$ was 0.6 at this frequency. An SIS mixer receiver having DSB response was employed. The typical atmospheric opacity at 220 GHz toward the zenith was 0.05 during the observations, and the system noise temperature was 250 - 300 K during the observations. The same digital auto-correlator with 1024 frequency channels and 128 MHz in bandwidth was used in HD 163296 observation and thus have a frequency resolution of 125 kHz, corresponding to $\sim$ 0.11 km s^{-1} at the observation frequency. Telescope pointing was checked every 1.5 - 2 hours by cross scanning of Jupiter and as a result it was achieved less than 3$''$ in pointing accuracy. The observation was conducted in a position switching mode and the location of the off-position was $(\Delta\alpha, \Delta\delta) = (+20', +20')$ from the stellar position. It was carefully checked that the star+disk system was surely isolated as well as ^{12}CO (J=1–0) observations by taking spectra not only at the stellar position, but also at four adjacent points, 22$''$ apart from the stellar position in R.A. and Dec. directions as shown in Figure 4.7. Data reduction and analysis were conducted in the same manner as in ^{12}CO (J=1–0) observations, described in Section 2.1 in this chapter.

2.4 HCO^{+} (J=1–0) Emission Line Observations

Observations of HCO^{+} (J=1–0) emission line were conducted by the NRO 45 m telescope in May 2011, the same season the HCO^{+} (J=1–0) observation of HD 163296 was done. As shown in Section 3.1 and 3.2 in this chapter, the emissions detected in several CO isotopologues at the systemic velocity of 5 km s^{-1} in $V_{\rm LSR}$ (Mannings et al. 1997a; Mannings & Sargent 1997b; Thi et al. 2005) are confirmed to be isolated. Thus, HCO^{+}

[1]The system noise temperature was drastically improved when 2SB receivers, T100H/V, were newly installed in NRO 45 m telescope. The typical noise temperature was used to be 250 - 500 K in the former receivers, S80/100.

(J=1–0) observations were intensively made only toward the stellar position by a pair of new 2SB receivers, T100H/V. The settings for the receivers and the AOS are the same with those in the HCO^+ (J=1–0) line observation of HD 163296: 40 MHz in the bandwidth, 20 kHz ($\simeq$ 0.05 km s^{-1}) in the frequency resolution. The IRR was 12 -17 dB. The system noise temperature during observation was between 280 K and 350 K, almost the same as the HD163296 observation and still slightly higher than the typical value in winter season. The accuracy for telescope pointing was regularly checked against the SiO maser NML Tau. Since it was again intermittently windy during the observation, the pointing deviation was relatively large, $\sim \pm 5''$, and all observed spectra were carefully flagged out when the wind speed exceeded 5 m s^{-1} to obtain a final profile of HCO^+ (J=1–0) emission by the same method as in the reduction of ^{12}CO (J=1–0). The resultant total integration time was about 2 hours on the source. The pointing check and the atmospheric correction were carried out as the same manner as in the ^{12}CO (J=1–0) observations. The correction for the intensity variation caused by the small daily fluctuation in the receivers' sensitivities was made by observing W51 main. Since the receiver system was working in very stable in this observation and there was no need to correct the observed intensity. The $\eta_{\rm mb}$ in 2011 at this frequency was 0.43 and applied to convert the raw data of the observed antenna temperature to the brightness temperature. The method of data reduction and analysis were also the same as those in the ^{12}CO (J=1–0) observation.

3 Results

3.1 ^{12}CO (J=1–0), ^{13}CO (J=1–0), and C^{18}O (J=1–0) Emissions

Since it is essential for the observations in the position-switching mode to establish a proper off point, a careful search for an emission free point was conducted in the beginning of the observation by ^{12}CO (J=1–0) line, the most optically thick line. The BEARS receiver was used based on the fact that the systemic velocity of HD 31648 is 5 km s^{-1} (Mannings et al. 1997a; Mannings & Sargent 1997b; Thi et al. 2005). An emission-free position applicable as an off point was finally determined at about $25'$ north from HD 31648 based on the result of the search and A_V map (Dobashi et al. 2005). Figure 4.3 is a profile map around the off point of which the integration time is 1 hour on the source and covers an $80'' \times 80''$ ($\sim$ 0.05 pc $\times \sim$ 0.05 pc) region. It is confirmed that there is no prominent emission detected around 5 km s^{-1} in $V_{\rm LSR}$. The absorption component seen at -2 km s^{-1} in $V_{\rm LSR}$ is formed as a result of subtracting the emission component of the other off-point from the original off-point. Since the systemic velocity of HD 31648 is 5 km s^{-1}, this absorption component does not affect any data reduction and is applicable as an off-point in the position-switching observation.

A $80'' \times 80''$ profile map centered at star+disk system obtained by ^{12}CO (J=1–0) line is provided in Figure 4.4. As in the case of HD 163296 observation, a clear double-peaked profile at 5 km s^{-1} in $V_{\rm LSR}$ is detected only at the center panel and therefore the ^{12}CO (J=1–0) emission originated from the star+disk system (see also Figure 4.7 in the case of ^{12}CO (J=3–2) line observation). The emission feature has a peak intensity of 0.36 K in $T_{\rm mb}$, 2.4$\pm$0.2 km s^{-1} in FWHM velocity width, and 0.083 K in the mean rms noise level after $\sim$ 9 hour integration time on the source, resulting in 4.3 σ in S/N ratio. Several panels in Figure 4.4, especially north-west direction from the center, show an absorption feature at $V_{\rm LSR} = -2$ km s^{-1} as the profile map of off-point shown in Figure 4.3. In order to confirm whether there is no significant emission at 5 km s^{-1} around the star+disk system, the same method is used as in HD 163296 observation as explained in Section 3.1 in Chapter 3. The observed ^{12}CO (J=1–0) emission profile, as indicated in the center panel in Figure 4.4 (Figure 4.5a), the four profiles at north, south, east, and west positions $\sim 40''$ away from the system were averaged into one spectrum (Figure 4.5b), and the resultant profile after subtracting Figure 4.5a from Figure

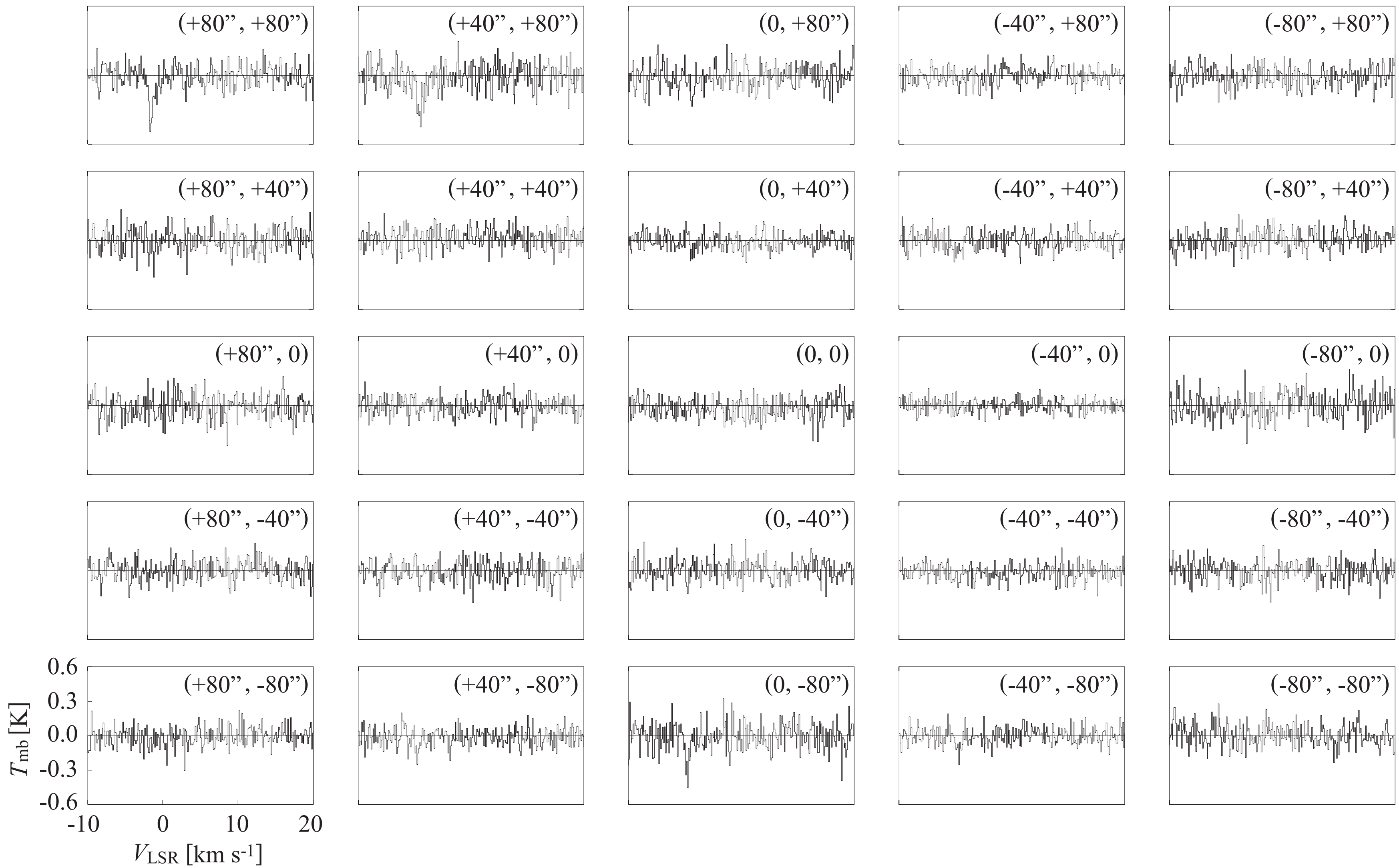

Figure 4.3 Profile map around the off point. The central position is $(\alpha, \delta) = (04^h58^m46^s.27, +30°15'37''.0)$ in J2000, and the angular distance between adjacent points is $40''$ (corresponding to 5600 AU) in both R.A. and Dec. directions as designated at the upper right corner of each panel.

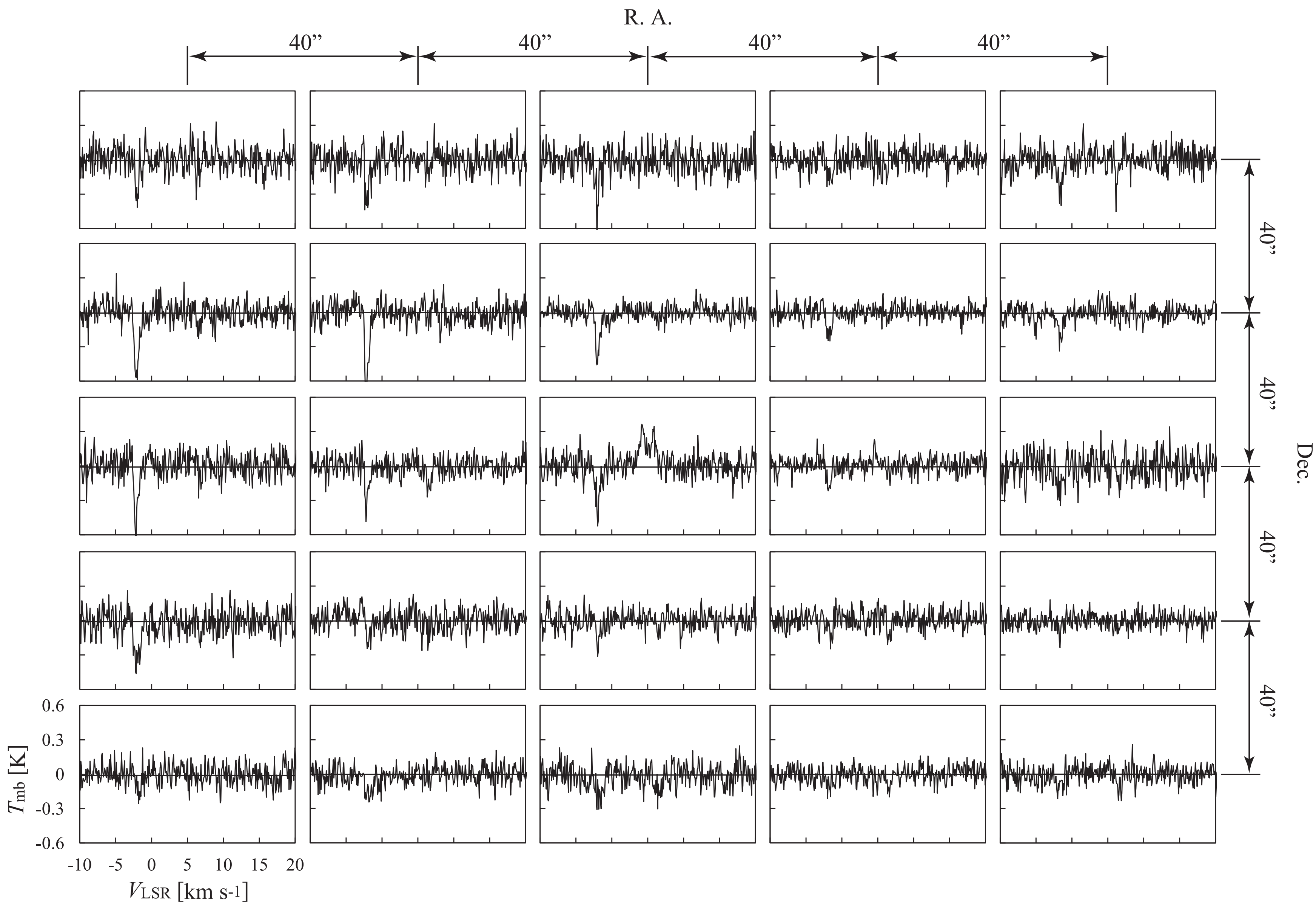

Figure 4.4 ^{12}CO (J=1–0) profile map covering $120'' \times 120''$ ($\simeq$ 0.08 pc $\times \simeq$ 0.08 pc) of the ^{12}CO (J=1–0) line around HD 31648. The map center corresponds to the stellar position $(\alpha, \delta) = (04^h58^m46^s.27, +29°50'37''.0)$ in J2000, and the angular distance between adjacent points is $\sim 40''$ (corresponding to 5600 AU) in both R.A. and Dec. directions.

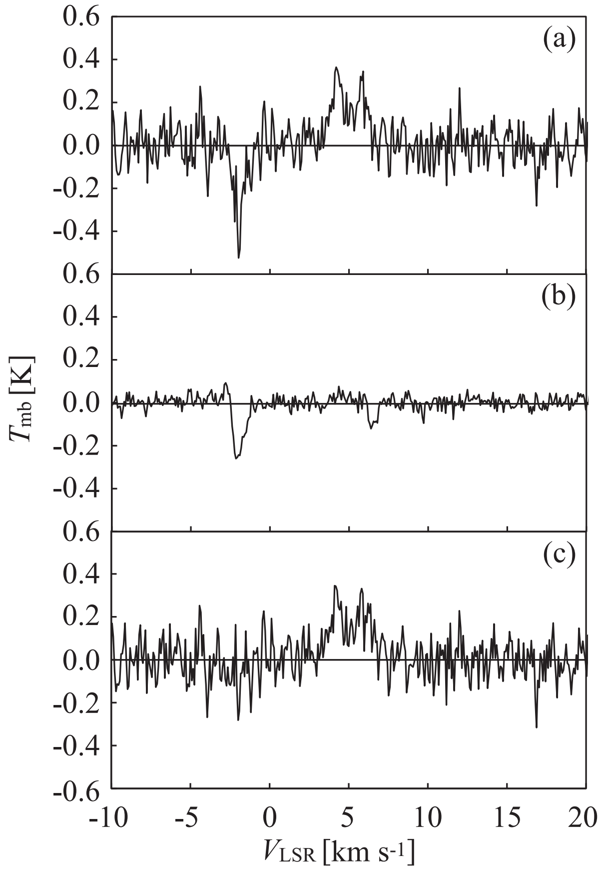

Figure 4.5 Verification that the disk is isolated from an ambient. (a) Observed ^{12}CO (J=1–0) emission profile toward HD 31648 in Figure 4.5. (b) Averaged ^{12}CO (J=1–0) profile of the four locations around HD 31648 $\sim$ 40$''$ away from the central star in Figure 4.4. (c) Resultant profile after subtracting (a) from (b).

4.5b (Figure 4.5c) are provided. The resultant emission profile in Figure 4.5c remains almost the same original profile feature shown in Figure 4.5a in spite of the increased noise level due to the subtraction process. Thus, the double-peaked emission component at the star is isolated and originates from the compact circumstellar disk in rotation.

A double-peaked profile with peak intensity of 0.13 K in $T_{\rm mb}$ and low rms noise level of 0.013 K in $\sim$ 6 hour integration time on source after data reduction is obtained in ^{13}CO (J=1–0) line observation. The FWHM velocity width is 4.46$\pm$0.15 km s^{-1}, which is nearly twice as greater as that of ^{12}CO (J=1–0) emission profile. A weak emission in C^{18}O (J=1–0) line is detected by 2 σ intensity. Although the S/N ratio of the C^{18}O (J=1–0) emission is insufficient to accept the observed emission as an official result, the line width seems to be wider than that of ^{13}CO (J=1–0) line profile. The peak-to-peak separation of the double-peaked profile in optically thin line becomes wider, whereas narrower in optically thick line. The similar trend is also seen in the HD 163296 profiles and this phenomenon is well characterized by Keplerian rotational disk. As will be discussed in Section 5 in this chapter, the differences in the velocity width at different lines shows a clue regarding the outer disk structure and even provides the information of the angular momentum transport in the disk.

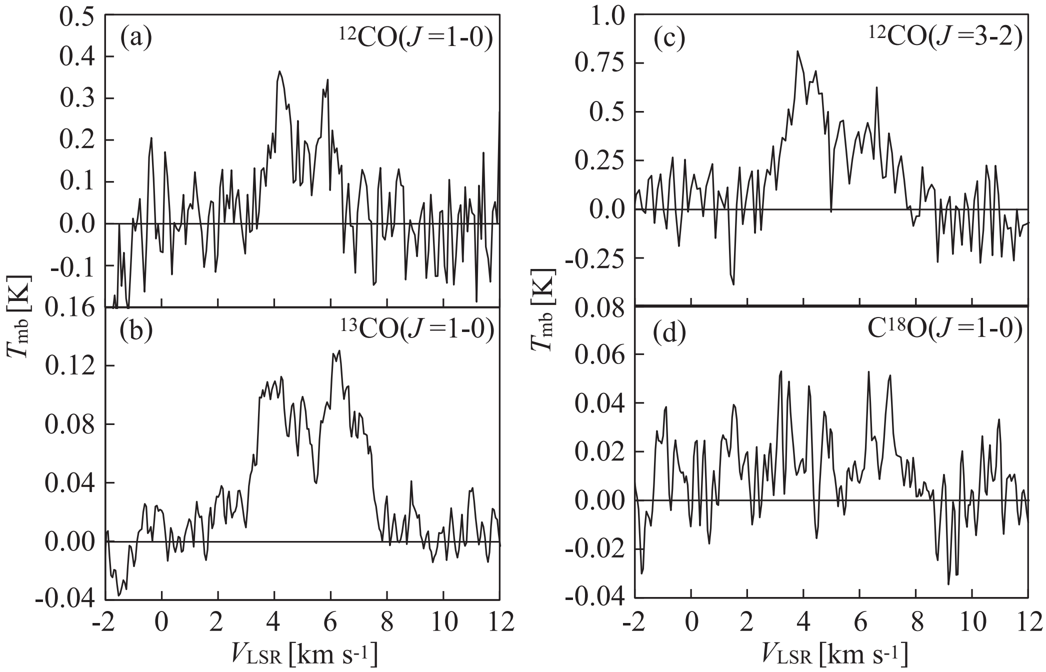

Figure 4.6 Emission profiles detected toward the stellar position of HD 31648. The each CO isotopologue line is designated in upper-right corner of each panel. The $C^{18}O$ (J=1–0) emission profile is provided just for reference due to insufficient S/N ratio less than 3 σ.

3.2 ^{12}CO (J=3–2) Emission

A profile map of ^{12}CO (J=3–2) spectra that covers the 44″ × 44″, corresponding to ≃ 6200 AU × ≃ 6200 AU, region around HD 31648 as shown in Figure 4.7. The center panel of Figure 4.7 is identical to Figure 4.6c. A double-peaked profile including defect emission in the red-shifted range at ∼ 5 km s^{-1} in $V_{\rm LSR}$ is seen only in the center panel. The peak intensity and the velocity width are 0.81 K in $T_{\rm mb}$ and 4.5±0.25 km s^{-1} in FWHM, respectively. The achieved rms level was 0.158 K after ∼ 2 hours in integration time on the source. The deficiency seen in thein the red-shift component is caused by an operational malfunction in observation and thus, a new observation by the same line was made in November 2011 by ASTE. A clear double-peaked spectra with 0.59 K in antenna temperature with 9 σ in S/N ratio. The new result is provided in the appendix A.

In addition to the analysis to confirm the origin of the emission by ^{12}CO (J=1–0) spectra (ref. Figure 4.5), the ^{12}CO (J=3–2) spectra were also analyzed so that the observed double-peaked emission can be examined more quantitatively. The analytical methodology is the same applied to ^{12}CO (J=1–0) spectra and details are described in Section 3.1 in this chapter. The resultant emission profile after subtraction shown in Figure 4.8c remains almost the same as the original profile feature before subtraction shown in Figure 4.5a in spite of the increased noise level due to the subtraction process.Thus, the double-peaked emission component at the star is surely originates from the compact circumstellar disk in rotation. The results of both ^{12}CO (J=1–0) and ^{12}CO (J=3–2) spectral analysis are consistent with each other and support that HD 31648 is the expected isolated star+disk system.

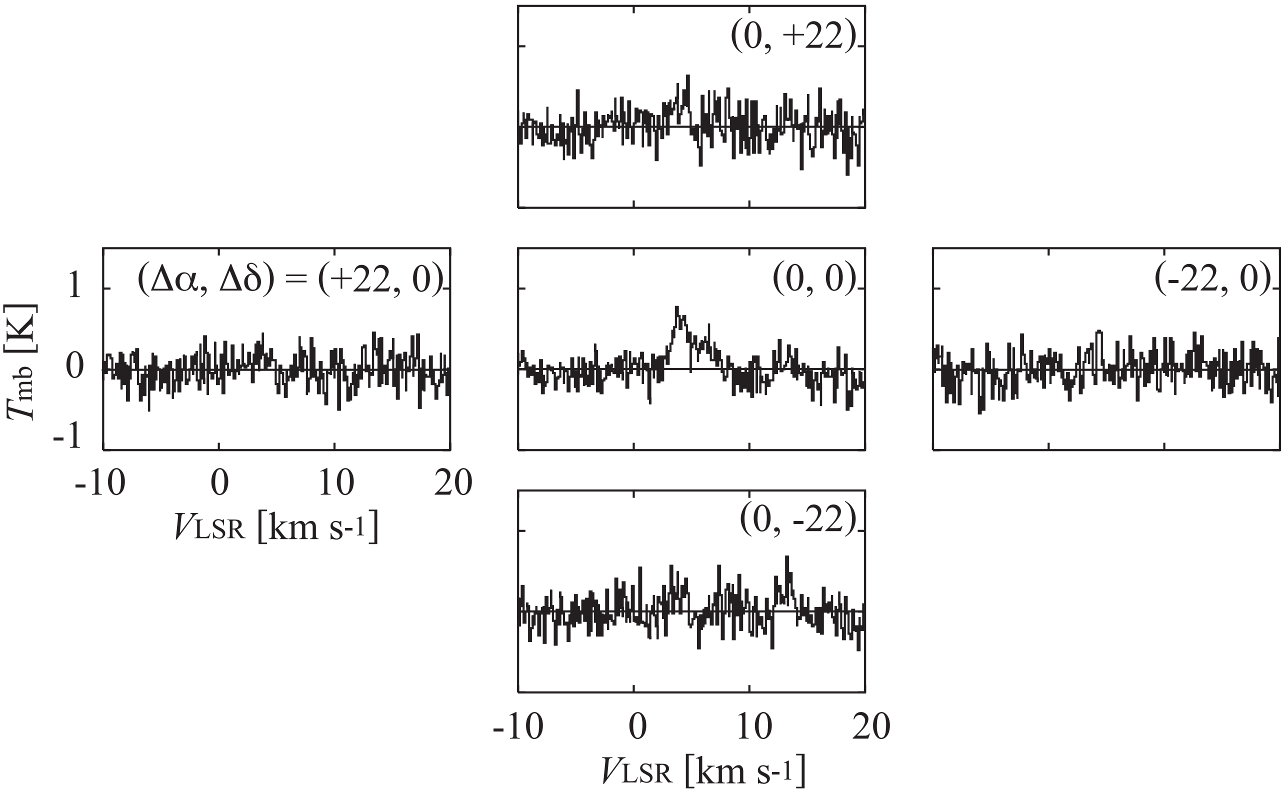

Figure 4.7 Profile map of the ^{12}CO (J=3–2) spectra for HD 31648. The map center corresponds to the stellar position, (α, δ)=($04^h58^m46^s.27$, $+29°50'37''.0$) in J2000, and the angular distance between adjacent points is 22″ (~ 3000 AU) in both R.A. and Dec. directions.

3.3 HCO$^+$ (J=1–0) Emission

Figure 4.9 shows an HCO$^+$ (J=1–0) emission originated from the disk around HD 31648. An emission close to double peak profile with the peak intensity of 0.1 K in $T_{\rm mb}$ and 2.7±0.1 km s^{-1} in the FWHM velocity width is detected at the systemic velocity of ~ 5 km s^{-1} in $V_{\rm LSR}$. The achieved rms level was 0.028 K. The observed spectrum dose not show a clear double-peaked profile probably because the noise level is still high or pointing deviation is still large due to windy condition. Therefore, it is not preferable to apply for model fitting to determine the ionization fraction of the disk and the empirical equation (1.22) is used to estimate the ionization fraction instead. However, the detection of an HCO$^+$ (J=1–0) emission with decent noise level even in undesirable bad weather indicates the capability of the detection of an H^{13}CO$^+$ (J=1–0) emission.

4 Model Fitting

4.1 Fitting Results of Power-Law Disk Model

The disk properties, $r_{\rm out}$, T_{100}, and Σ_{100} are estimated through model fitting by the power-law disk models. HD 31648 shows large difference in peak-to-peak velocity width in multi-CO line observations as shown in Figure 4.6 (see also Figure 4.16 for details). Thus, it can not fit all of the CO line profiles simultaneously by a single value of $r_{\rm out}$ in the power-law disk model: the derived $r_{\rm out}$ in ^{12}CO (J=1–0) line profile is 500±100 AU, whereas $r_{\rm out}$ in the other lines is 1000±100 AU. Figure 4.10 and 4.11 show the fitting results by the power-law

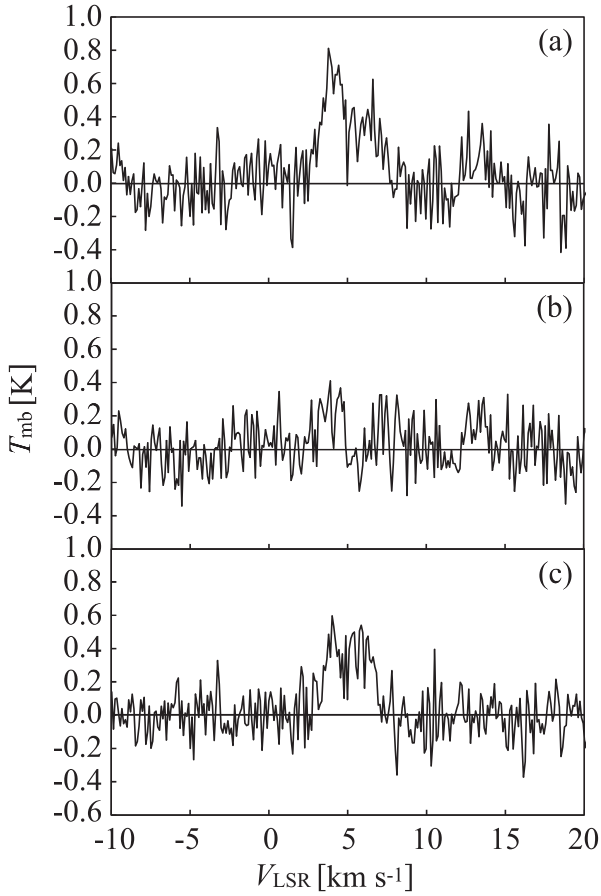

Figure 4.8 Same as Figure 4.5 but in ^{12}CO (J=3–2) line observation.

disk model when Σ_{100} = 0.1 g cm^{-2} in the case of $r_{\rm out}$ = 500 and 1000 AU, respectively. The corresponding disk temperature, intensity, and density distributions in two dimensional views are provided in Appendix C3. Figure 4.10 and 4.11 demonstrate that all CO line profiles are not fitted by a single set of parameters at the same time. In Figure 4.10, for example, the fitting in ^{12}CO (J=1–0) line is not successful while the others achieve acceptable fitting. When the improvement in ^{12}CO (J=1–0) line fitting is attempted, the other lines become unacceptable fitting as shown in Figure 4.11. Parameter search for simultaneous fit was cautiously made and it was found that no solution to satisfy fitting in all of the CO lines exists. These imply that the power-law disk model bears potential improvements and the model fitting is further examined by the similarity solution disk model in Section 4.2 in this chapter.

The best-fit temperatures for each $r_{\rm out}$ at Σ_{100} between 0.001 and 10 g cm^{-2} that all of the CO lines simultaneously fit by a single set of parameters are provided in Table 4.1 when $r_{\rm out}$ = 500 AU and Table 4.2 when $r_{\rm out}$ = 1000 AU. The fitting temperature of ^{12}CO (J=3–2) shows the highest value among all of the CO lines, for example 52^{+8}_{-9} K in $r_{\rm out}$ = 500 AU and 35±5 K in $r_{\rm out}$ = 1000 AU when Σ_{100} = 1 g cm^{-2} whereas the fitting temperatures of the other lines are 3 - 5 time lower than the ^{12}CO (J=3–2) fitting temperature. This difference in the best-fit T_{100} implies that the disk is composed of at least two layers with distinct temperatures. The result of fitting temperature shows the same tendency of the result derived in HD 163296.

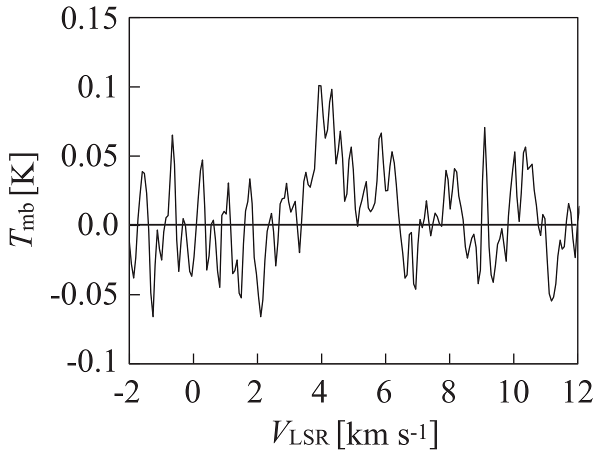

Figure 4.9 HCO^+ (J=1–0) spectrum for HD 31648.

Table 4.1 Best Fit Parameters at r_{out} = 500 AU

	T_{100} [K]			
Σ_{100} [g cm^{-2}]	^{12}CO (J=3–2)	^{12}CO (J=1–0)	^{13}CO (J=1–0)	C^{18}O (J=1–0)
0.1	59^{+10}_{-11}	20±5	20±1	11±2
0.3	55^{+9}_{-10}	19^{+5}_{-4}	17±1	9^{+2}_{-1}
1	52^{+8}_{-9}	18^{+4}_{-5}	16±1	9^{+1}_{-2}
3	49±8	18^{+4}_{-5}	15±1	8±1

4.2 Fitting Results of Similarity Solution Disk Model

Model fitting by the similarity solution disk model is examined since the fitting by the power-law disk model is not successful. Different velocity width in each CO line shown in Figure 4.6 (see also Figure 4.16) probably causes unsuccessful fitting by the power-law disk model. The emission with the widest velocity width is the one by optically thin line, C^{18}O (J=1–0) line, which traces the dense gas rotating with high Keplerian velocity in the inner disk, while the narrowest velocity width is seen in the optically thick line, ^{12}CO (J=1–0) line, which traces low density gas rotating with high Keplerian velocity in the outer disk. Similarity solution disk model is more suitable for describing low density component making narrow velocity width feature because low density gas is well considered as an exponential tail in the model (details in Chapter 2).

The best-fit temperatures and the outer radius at 0.001, 0.01, 0.1, and 1 g cm^{-2} in Σ_{100} where the solution to satisfy model fitting by a single set of parameters in all of the CO lines exist are provided in Table 4.3. The best fitting results when Σ_{100} = 0.1 g cm^{-2} are shown in Figure 4.14 and the corresponding disk temperature,

Table 4.2 Best Fit Parameters at r_{out} = 1000 AU

	T_{100} [K]			
Σ_{100} [g cm^{-2}]	^{12}CO (J=3–2)	^{12}CO (J=1–0)	^{13}CO (J=1–0)	C^{18}O (J=1–0)
0.03	44^{+6}_{-8}	14^{+3}_{-2}	35^{+7}_{-15}	17^{+2}_{-7}
0.1	40±6	14^{+2}_{-3}	14±1	9±1
0.3	38^{+6}_{-5}	13±2	13^{+3}_{-2}	9±1
1	35±5	13±2	12^{+1}_{-2}	8±1

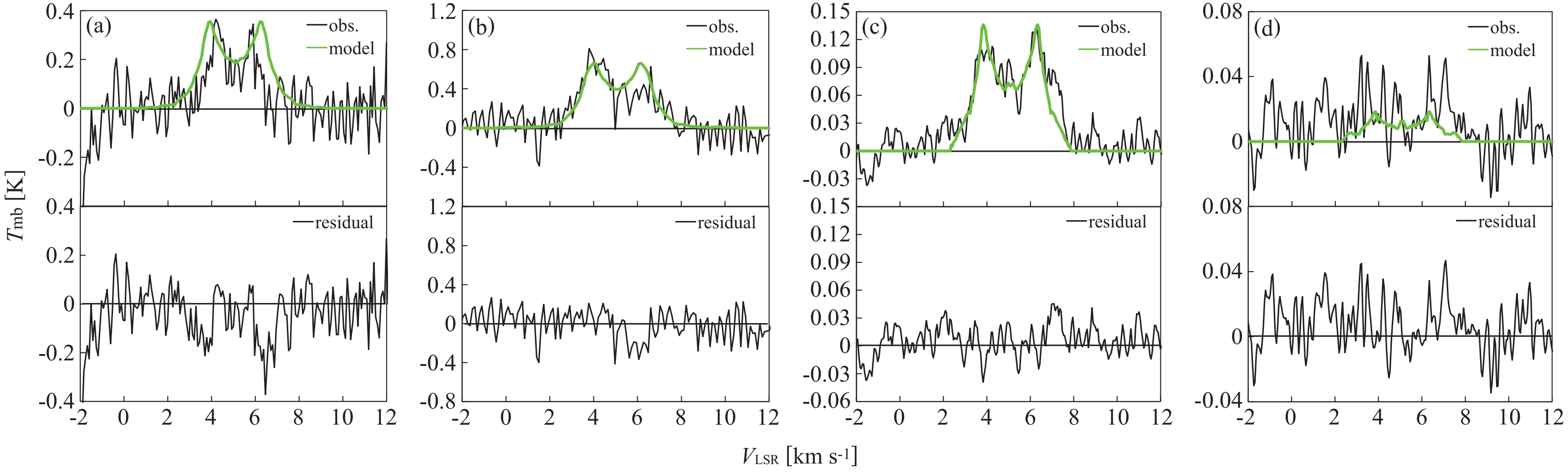

Figure 4.10 Fitting results of (a): ^{12}CO (J=1–0), (b): ^{12}CO (J=3–2), (c): ^{13}CO (J=1–0), and (d): C^{18}O (J=1–0) spectrum in the power-law disk model. (Upper panels): Comparisons between the line profiles obtained by the observations (dark line) and best-fit model calculations when $r_{\rm out}$ = 500 AU and Σ_{100} = 0.1 g cm^{-2} are provided (green lines). The corresponding T_{100} to these $r_{\rm out}$ and Σ_{100} parameters for each line profile is given as listed in Table 4.1. (Lower panels): Difference between the observed and calculated profiles shown in the upper panels.

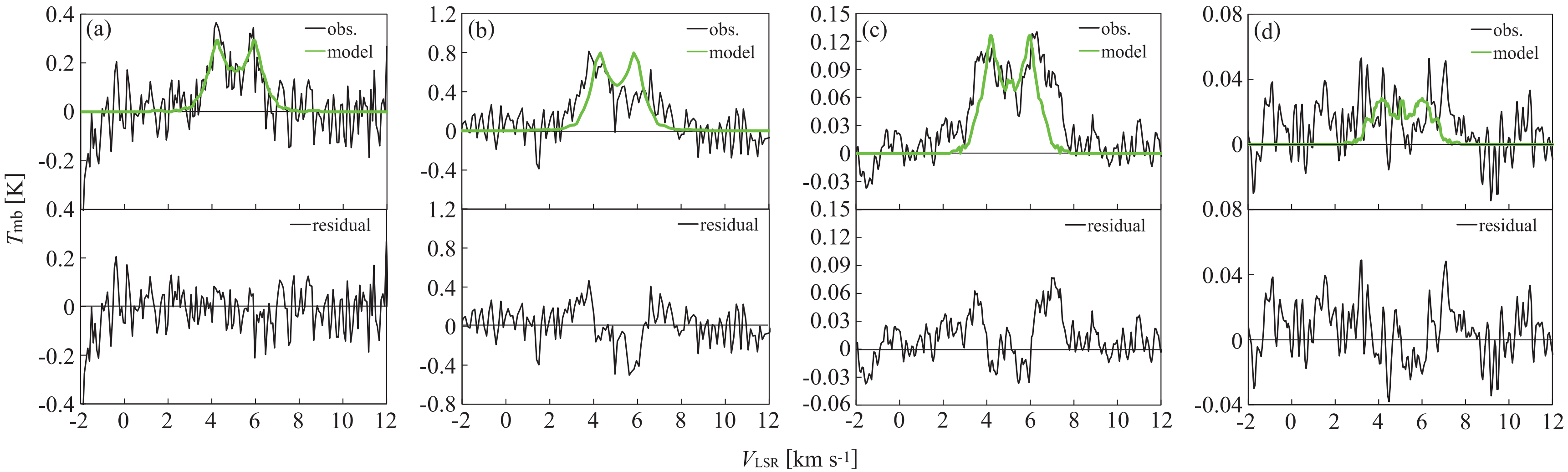

Figure 4.11 The same as Figure 4.10 in the case of $r_{\rm out}$ = 1000 AU and Σ_{100} = 0.1 g cm^{-2}. T_{100} is given in Table 4.2

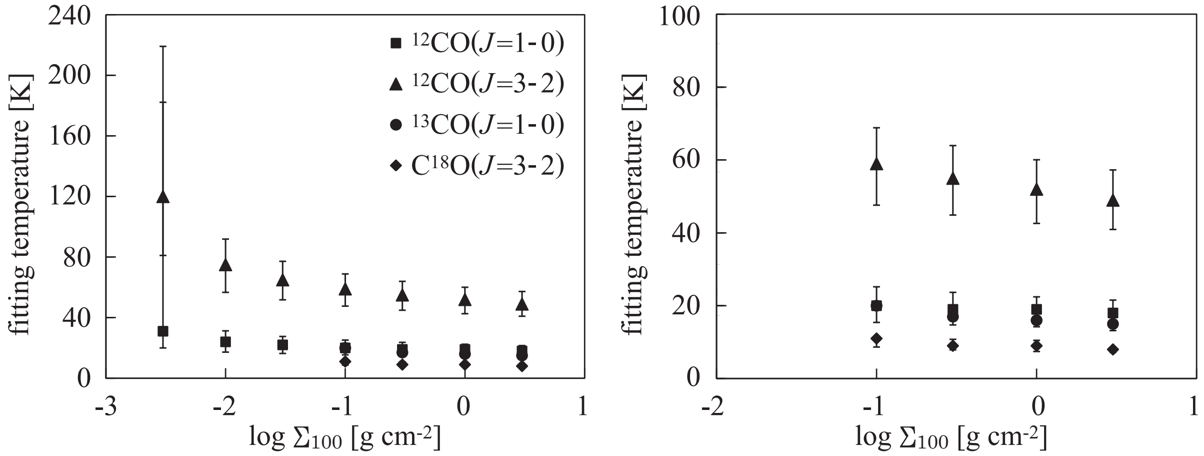

Figure 4.12 Best-fit T_{100} parameter with uncertainties for the acceptable fit when r = 500 AU as a function of Σ_{100} in the power-law disk model. (Left): The panel shows the best-fit T_{100} between 0.003 and 3 g cm^{-2} in Σ_{100}, (Right): It is the same panel as the one on the left in an enlarged view of the lower-right part.

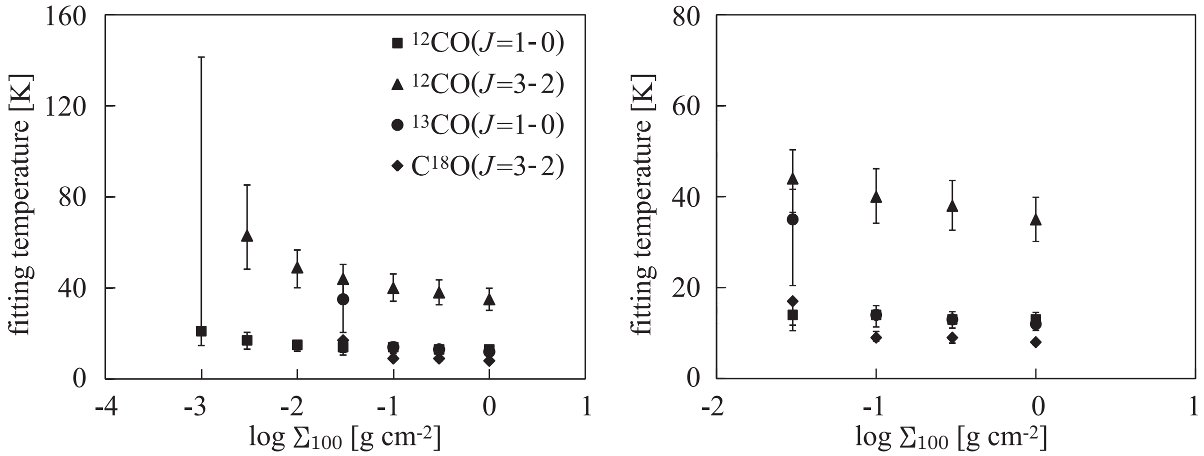

Figure 4.13 The same as Figure 4.12 in the case of $r_{\rm out}$ = 1000 AU.

intensity, and density distributions in two dimensional views are provided in Appendix C4. Figure 4.15 shows the fitting temperature at several specific Σ_{100}. Note that the fitting solution in the lower range of Σ_{100} might be incorrect even though fitting solution exists because the disk mass becomes too low to keep a consistency with the results derived from dust continuum and other CO line observations. Since the surface density tapers off gradually and the mass still remains in the outer region of the disk in the similarity solution disk model, not like a truncation structure seen in the power-law disk model, model fitting can be achieved by adjusting T_{100} in low Σ_{100} range. Although it is difficult to determine the surface density only by similarity solution disk model, supplemental assessment such as SED fitting helps confine parameters by merging SED's fitting parameter range with the one in the similarity solution disk model. Hence, it will contribute the improvement in determining the disk mass. As in the case of the results from the power-law disk model, the fitting temperature of ^{12}CO (J=3–2) shows the highest among all of the CO lines (ref. Table 3.2). Although fitting temperature of all CO lines derived by the similarity solution disk model result in lower temperatures in the power-law disk model because $r_{\rm out}$, both results show the same temperature distributions and therefore hold consistency each other.

Table 4.3 Best-fit parameters at $r_{\rm out}$ = 800 AU in the similarity solution disk model

	T_{100} [K]			
Σ_{100} [g cm^{-2}]	^{12}CO(J=3–2)	^{12}CO (J=1–0)	^{13}CO(J=1–0)	C^{18}O(J=1–0)
0.001	38^{+5}_{-6}	12^{+2}_{-2}	12^{+1}_{-1}	7^{+1}_{-1}
0.01	35^{+5}_{-5}	11^{+2}_{-1}	11^{+2}_{-1}	7^{+1}_{-1}
0.1	34^{+4}_{-5}	11^{+2}_{-2}	11^{+1}_{-1}	7^{+1}_{-1}
1	33^{+4}_{-5}	11^{+2}_{-2}	11^{+1}_{-1}	7^{+1}_{-1}

5 Discussion

5.1 Vertical Temperature Distribution

The disk is arguably optically thick in CO emissions as results of intensity ratio between CO isotopologues with the same rotational transition. The results of fitting temperature derived by any disk models shows the temperature of the ^{12}CO (J=3–2) is the highest among the CO isotopologue lines even taking account of uncertainties designated by the error bars that attributes to observations (ref. Figure 4.12 and 4.13). The same method introduced to HD 163296 disk to examine the vertical temperature distribution is applied as described in Section 5.2 in Chapter 3. The vertical location of photosphere of each CO emission line is already calculated and the result is provided in Figure 3.15 with the representative T_{100} of the low-temperature interior and the high-temperature surface for HD 31648; 40 - 100 K in the ^{12}CO (J=3–2) line and 15 - 40 K in the other lines. The relation between the fitting temperature and the vertical locations of the photosphere of each CO line indicates that the temperature of the upper-most layer is 2 to 3 times higher than the that of the mid-plane of the disk as the HD 163296 disk. Therefore, it concludes that the disk around HD 31648 is comprised of at least two different temperature layers beyond $\sim$ 100 AU from the central star.

5.2 Radial Density Distribution

As explained in Chapter 1 regarding the planetary system formation, the variety of extrasolar planetary systems may stem from those of protoplanetary disk structure. It should therefore be comprehensively examined from the dense inner part near the central star to the outer edge of the disk. The combination of multi-line observations and model fitting can unveil the disk structure. As results of careful evaluations of model fitting through test calculations in all physical cases, it concludes that the power-law disk model is not suitable for model fitting toward HD 31648 and a single set of parameters does not exist to simultaneously fit all of the lines. The similarity solution disk instead shows apparently better fitting result and achieves reasonable fitting for any CO lines. These comparative results suggest that the radial surface density of the disk around HD 31648 probably falls off gradually rather than a sharp outer edge.

Figure 4.16 is a comparison of the velocity width among CO isotopologue emission profiles in the same J=1–0 rotational transition. The velocity width of optically thicker emission is wider while the one of optically thinner emission is narrower. Since the different velocity width reflects a different radial size of the disk and thus each CO emission line traces different radial location: the outer radius can be traced by an optically

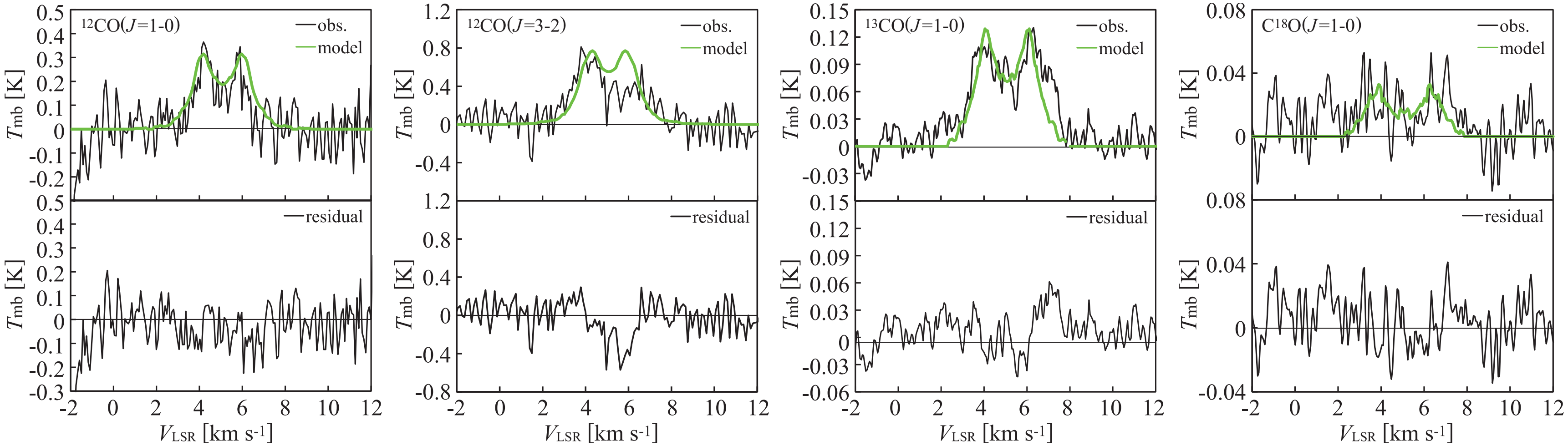

Figure 4.14 Fitting results of each CO isotopologue spectrum in the similarity solution disk model. (Upper panels) Comparisons between the line profiles obtained by our observations (solid line) and best-fit model calculations when $\Sigma_{100} = 0.1$ g cm^{-2} (green lines). Best-fit values for T_{100} and $r_{\rm out}$ in the model calculations are listed in Table 4.3. (Lower panels) Difference between the observed and calculated profiles shown in the upper panels.

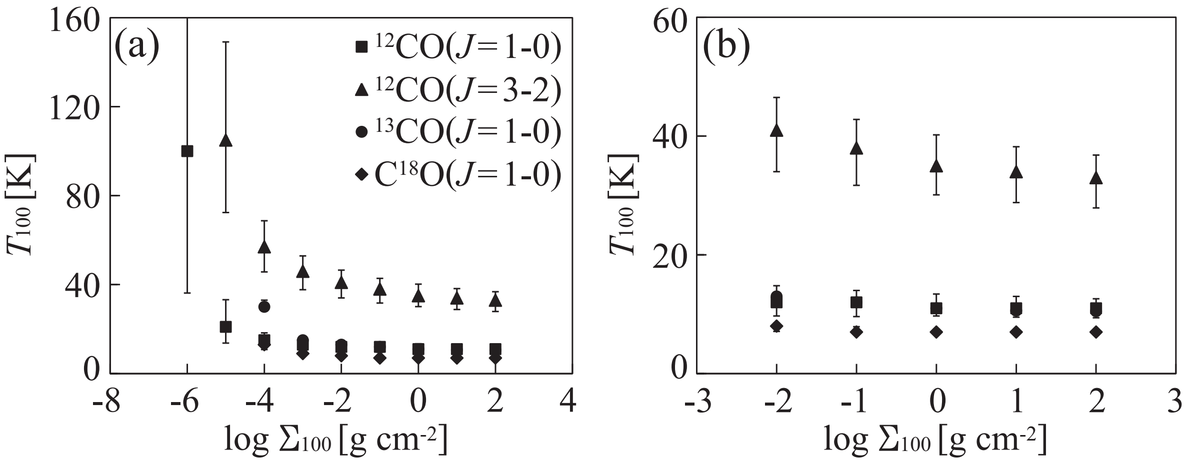

Figure 4.15 Best-fit T_{100}.

thicker line whereas the inner radius can be traced by an optically thinner line. The fact that the outer radius derived by dust continuum and line emission is contradicted: 350±30 AU in $\lambda = 1.4$ and 2.8 mm continuum and 1050±10 AU in ^{12}CO (J=2–1) in AB Aur (Piétu et al. 2005), and 200±15 AU in $\lambda = 0.87$ - 7 mm continuum and 500 - 550±100 AU in ^{12}CO (J=2–1), ^{12}CO (J=3–2), and ^{13}CO (J=1–0) lines (Isella et al. 2007). These discrepancies are re-solved by introducing the similarity solution disk model with an exponential tail which makes the surface density tapers off gradually at the outer edge. Figure 4.17 shows the radial surface density distribution and mid-plane density profiles based on model fitting results in the power-law and the similarity solution disk models. The solid lines indicate the distributions in the power-law disk model, while the dashed lines indicate distributions in the similarity solution disk model. The distribution curves for both disks show similar profiles in inner disk since the same numerical values are applied in the index of $\Sigma(r)$ (ref. equation (2.2) and (2.10)), while the curves show different in the outer disk.

The different results in $r_{\rm out}$ derived from the emissions of CO isotopologues by the power-law disk model can be explained by the similarity solution disk model as Hughes et al. 2008 did in the case of discrepancy arising from dust continuum and gas emission. This is the first case to show that the different velocity width occurred in gas emissions is fitted by the similarity solution disk model. Figure 4.18 shows the sum of residuals in absolute value for both models. The residual after fitting in the similarity solution disk model is smaller than in power-law disk model in the case of HD 31648. This result manifests that a dense gas disk is associated with the central star and the gas probably extends a few hundreds AU away.

A further improvement in fitting by the similarity solution disk model is expected because the calculated profiles are still slightly off. If the other line broadening factors such as turbulence are considered in the model, the better fitting with high accuracy will be achieved. The theoretical idea to take the turbulent component into account in the model was present since long time ago. The turbulent broadening effect is usually included in the thermal linewidth as expressed below.

$$\Delta v(r) = \sqrt{\frac{2k_{\rm B}T(r)}{m} + \xi^2}, \qquad (4.1)$$

where $\Delta v(r)$ is the total linewidth, ξ is the linewidth due to turbulence, $\sqrt{2k_{\rm B}T(r)/m}$ is the thermal linewidth, where $k_{\rm B}$ is Boltzmann's constant, $T(r)$ is the temperature at distance r from the central star, and m is the mean mass of gas molecules. The attempt to estimate turbulent velocity through this method was implemented by

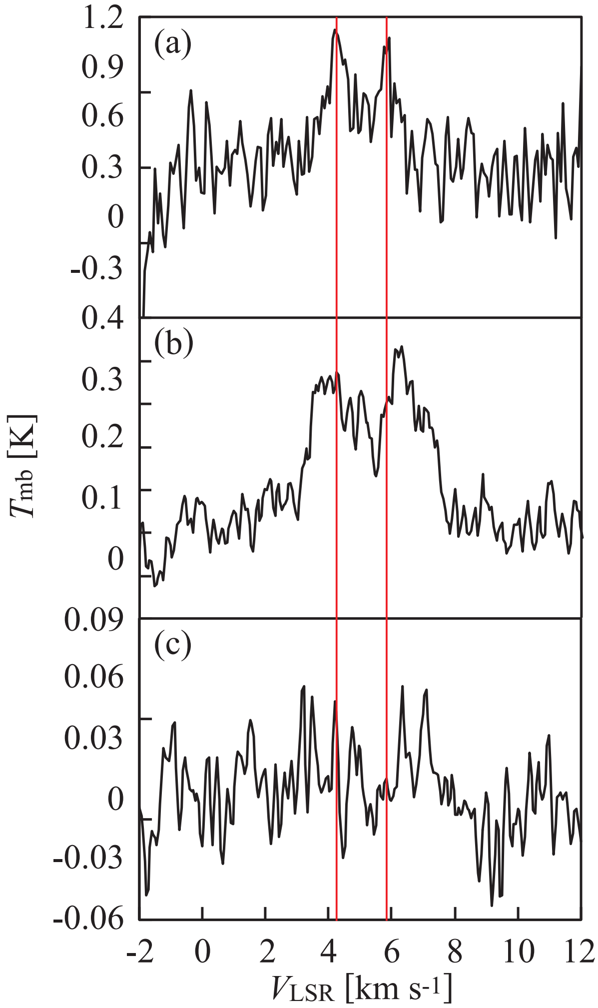

Figure 4.16 The same as Figure 3.17 and 3.18 for HD 31648.

Hughes et al. (2011) (see section 5.2 in Chapter 3). If the presence of turbulence is confirmed in protoplanetary disks, it will be a strong observational evidence to support MRI in the outer disk. Confirming turbulence and deriving the ionization fraction in the disk, which will be discussed in the next Section in this chapter, are important factors to verify MRI based on observations.

5.3 Ionization Fraction of the Disk

The ionization fraction of the gas disk is definitely an important factor for determining MRI existence and can be estimated by equation (1.22). Since the observed emission is mainly originated from the outer disk when spatially unresolved, the both simulation and observation data at r = 100 AU from the central star, such as Σ_{100} and [HCO^+], were considered. Furthermore, all reaction rates at the outer disk is assumed to be almost identical to the dense core's. For numerical evaluation, the CO abundance with respect to HCO^+ calculated by Walsh et al. (2010) is 10^5 and the number density of hydrogen based on the observational results as described in Figure 4.17 is $\sim 10^6$. As a result of substituting all numerical values into equation (1.22), it produces $[e^-] = \sim 10^{-7}$. Note that this could be overestimated for protoplanetary disk since $n_{\rm H}$ in protoplanetary disks should be larger than that in dense cores. It is expected that recombination reaction is promoted by higher density

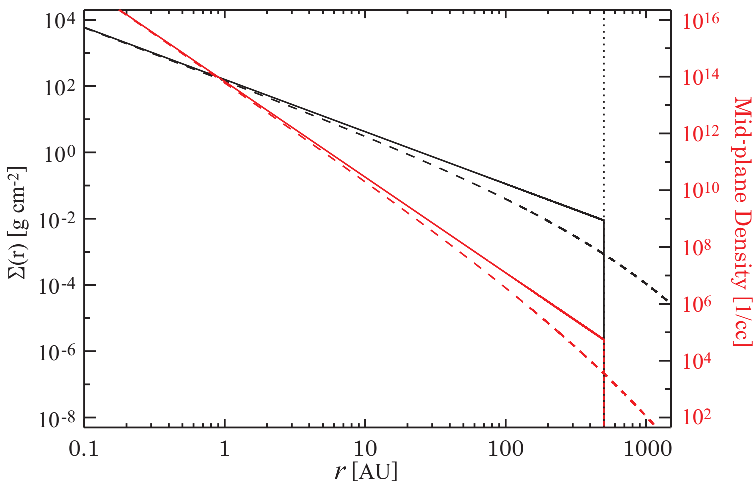

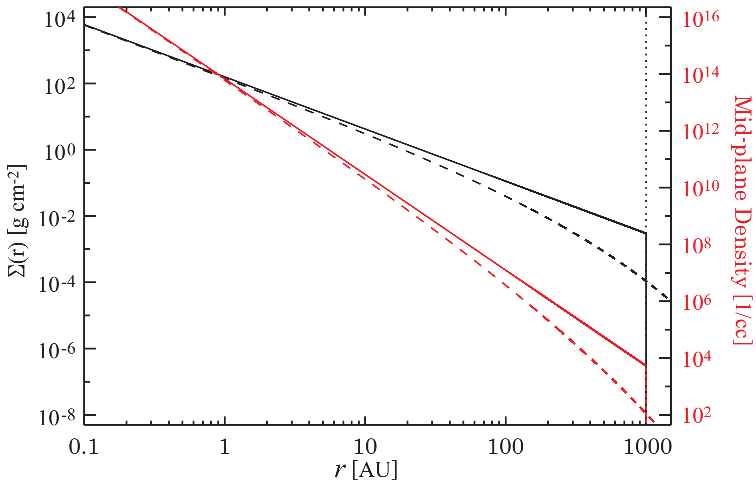

Figure 4.17 Comparison of the radial surface density distribution ($\Sigma(r)$) designated by black-colored lines and the number density distribution at mid-plane ($n_{z=0}$) designated by red-colored lines between the power-law disk model (solid lines) and the similarity solution disk model (dashed lines) when $\Sigma_{100} = 1$ g cm^{-2} applied as a representative fitting value. (top): $\Sigma(r)$ and $n_{z=0}$ distributions are shown when r = 500 AU. (bottom): $\Sigma(r)$ and $n_{z=0}$ distributions are shown when r = 1000 AU.

of $n_{\rm H}$ and as a result [e$^-$] will decrease as $n_{\rm H}$ rises. Therefore, [e$^-$] can be even lower probably by 2 - 3 order of magnitude. However, MRI can still be invoked even when [e$^-$] $\sim 10^{-10}$ - 10^{-12}. Although it is necessary to investigate more the ionization fraction, our observational results have supported so far that MRI can be driven in the disk around HD 31648.

The [CO]/[HCO^+] is not estimated from model fitting since the noise level is still high and the double-peaked profile seems to contain a defect in red-shift component. However, it is better to use the surface density of HCO^+ obtained by observations and should be evaluated for the consistency between results from calculation through chemical network and model fitting of the observed emission. The disk is usually optically thick in HCO^+ (J=1–0) line, thus $H^{13}CO^+$ (J=1–0) line is more suitable and can provide HCO^+ density of the disk more accurately. It is thought to be capable of detecting $H^{13}CO^+$ (J=1–0) emission which have hardly been detected in protoplanetary disks so far by recent advanced receivers with high sensitivity.

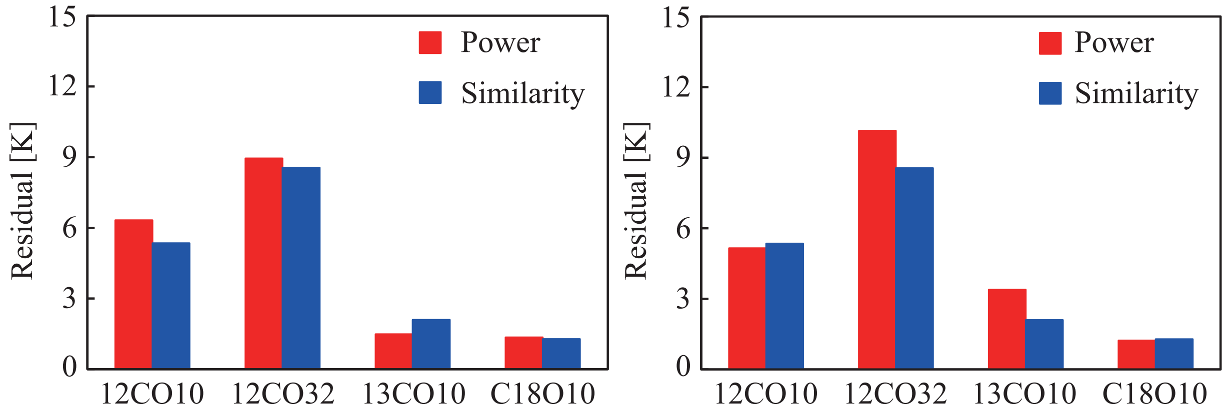

Figure 4.18 Residuals resulting from subtraction of the profile calculated by the disk models from the observed emissions. The red bar indicates the residual generated by the power-law disk model and the blue bar is the same as the red by the similarity solution disk model. The residuals of each CO isotopologue line indicated in the abscissa are provided when r = 500 AU (left) and when r = 1000 AU (right). The sum of residuals at each channel over the emission profile range is provided in the ordinate.

6 Chapter Summary

This chapter presents emissions of the disk around HD 31648 in the ^{12}CO (J=1–0), ^{12}CO (J=3–2), ^{13}CO (J=1–0), and C^{18}C (J=1–0) lines. Double-peaked profiles originating from a rotating circumstellar disk were successfully detected in all of the CO lines. Surface density and temperature distributions both in radial and vertical directions and outer radius were estimated by model fitting. The intensity ratio between J=1–0 and J=3–2 rotational transitions with the same CO isotopologue and the results of model fitting suggest that the disk is optically thick in all of the CO lines although C^{18}C (J=1–0) is optically thin because a weak emission was obtained. The temperature distribution in the vertical direction was revealed by comparing and cross-referring the position of the photosphere and fitting temperature of each CO isotopologue line. As a result, at least two distinct temperature layers must exist in the disk: 35 - 50 K in the uppermost ^{12}CO (J=3–2) emitting layer and 15 - 20 K near the mid-plane of the disk. Since the vertical temperature distribution inside of a disk is commonly suggested for both TTSs and HAe stars (DM Tau, AB Aur, and HD 31648), such a temperature distribution may be ubiquitous in protoplanetary disks (Piétu et al. 2007).

It is also found that all CO isotopologue lines are not fitted by the power-law disk model and the fitting can be improved by the similarity solution disk model. The surface density distribution in the outer disk can therefore be characterized by the fact that the surface density fall off gradually in the radial direction. The radial surface density with a truncation at the outer edge of the disk brought by the power-law disk model is unlikely. This implies that the gas extend several hundreds away from the central star, which can be described as an exponential tail in the similarity solution disk model.

HCO$^+$ (J=1–0) observation provides the order estimation about the ionization fraction of the disk. The result indicates that ionization fraction is of order 10^{-8}, which is capable of driving MRI in th disk. If the ionization fraction and turbulence in the disk are confirmed in the disk, MRI is strongly supported and can be a good candidate for disk gas dissipation.

Chapter 5

Disk Structure of HD169142

1 Introduction

HD 169142 (MWC 925, SAO 186777) is a Herbig Ae star with 2.5 $M_\odot$ in stellar mass (Dominik et al. 2003), A8Ve in spectral type, and 6^{+6}_{-3} Myr in age (Grady et al. 2007). It is located 145 pc away from the sun (Sylvester et al. 1996) in Ophiuchus direction and the circumstellar material around the central star was first identified by Walker & Wolstencroft (1988). Unlike most of the HAeBe stars, it shows no evidence of proximity to a cloud or extended molecular gas (Meeus et al. 2001). Observations of molecular gas in this disk are therefore easier to interpret. HD 31648 is categorized as a group I object by the feature of its SED (see Section 2.2 in Chapter 1) as shown in Figure 5.2 (Acke & van den Ancker 2004), and is expected to have a self-shadowed disk (Meeus et al. 2001; Dullemond & Dominik 2004).

Dent et al. (2005) have shown that the disk contains intermediate amount of CO gas between those of the typical HAe stars and debris disks, while sufficient CO gas and dust still remain in the outer disk (Raman et al. 2006; Panić et al. 2008). Subsequently, they showed infrared excess with lack of silicate features at 10 μm (Dent et al. 2006). Dominik et al. (2003) derived a disk mass of 0.1 $M_\odot$ by adopting the outer radius of 100 AU, a low inclination of 8°, and steep reduction ($p = 2$, ref. equation 2.2) in the radial surface density, Σ(r), in the power-law distribution for a self-consistent disk model including both the emission from the flaring part of the disk and from the inner rim (Dullemond et al. 2001). Furthermore, Dent et al. (2006) derived a disk mass of 4×10^{-2} $M_\odot$ by fitting both the observed SED and the resolved 7 mm continuum emission. They adopted the outer radius of 300 AU and inclination of 30° to an accretion disk model (D'Alessio et al. 2005). Near-IR polarization images show that the dust in the disk extends to at least 217 AU (Kuhn et al. 2001). More recent sub-millimeter observations show bright and narrow CO lines (Dent et al. 2005; Raman et al. 2006). Raman et al. (2006) spatially resolve the disk and find a fit to the CO J=2–1 line and 1.3 mm continuum observations by adopting a flared accretion disk model with a 235 AU in radius and a 13° inclination from face on.

Sylvester et al. (1996) obtained mid-IR spectra in the 10 - 20 μm bands by the 3.8-m United Kingdom Infra-Red Telescope (UKIRT) and showed that the circumstellar environment of HD 169142 has hot material concentrated within a radius of 140 AU from the central star. Grady et al. (2007) fit the SED and the Near Infrared Camera and Multi-Object Spectrometer (NICMOS) on the HST image at 1.1 μm (Figure 5.1) with a model consisting of two distinct disk components: the inner disk from 0.15 to 5 AU radius and the outer disk extending from 44 to 230 AU. It suggests that the disk should contain an internal cavity (Calvet et al. ref. 2004) where the near stellar dust has grown and settled to the mid-plane, and where the stellar radiation field has subsequently photo-dissociated the gas. HD 169142 is a good candidate of a so-called "transitional disk",

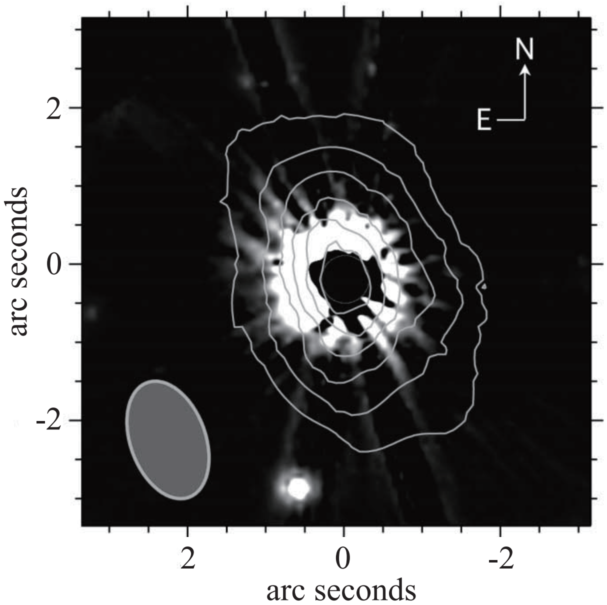

Figure 5.1 HST NICMOS coronagraphic image of the disk around HD 169142. ^{12}CO (J=2–1) emission at 230 GHz with contour scale imaged by the SMA (Raman et al. see 2006, for detail) is superimposed onto the disk image in λ = 1.1 μm scattered light (Grady et al. 2007). The contour increment is 0.4 Jy km s^{-1} and the beam size of 1.6″ × 1.0″ is provided at the lower-left corner.

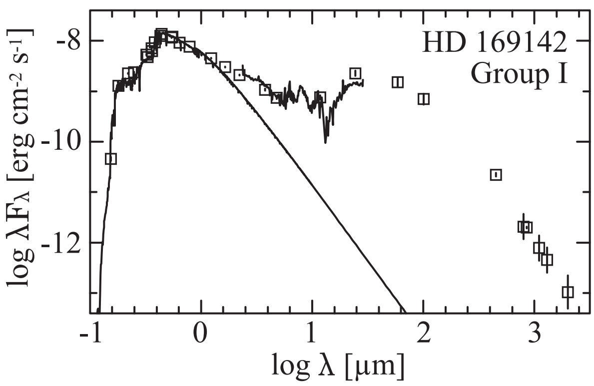

Figure 5.2 SED of HD 169142 (Acke & van den Ancker 2004).

which deficient in warm, near-stellar dust and gas but harboring abundant material at larger radii (Strom & Najita 2005).

2 Observations

2.1 ^{12}CO (J=1–0) Mapping Observations

Observations of ^{12}CO (J=1–0) emission line were performed in the winter 2009 by the NRO 45 m telescope. Since it is necessary to confirm the emission originated from the disk such as HD 163296 and HD 31648 cases (ref. Section 2.1 in Chapter 3 and 4), a close mapping observation covering the stellar position and its vicinity with sufficient spacial resolution was first conducted to separate the disk emission from surrounding components, such as an envelope or a remnant cloud. Mapping observations including the stellar position and the adjacent 4 positions 20″ (≃ 2900 AU) away from the central star in north, south, east, and west directions were conducted by moving antenna, rather than just a 5 × 5 grid mapping observation with 40″ separation at the stationary position. A pair of new two sideband (2SB) separating SIS recievers, T100H and T100V (T100H/V), which can simultaneously observe in both sidebands, lower sideband (LSB) and upper sideband (USB) (Takahashi et al. 2010), rather than BEARS used in HD 163296 and HD 31648 observations were used for the mapping observation because the sensitivity of T100H/V is improved so greatly that T100H/V need less on source time than the BEARS. The 2SB reciever system temperature in ^{12}CO (J=1–0) mapping observation was between 180 K and 300 K and the integration time for the observation was 2.5 hours on the source. The image rejection ratio (IRR) of the T100H/V in this observation was 11 -15 dB. An AOS with 40 MHz (109 km s^{-1}) in bandwidth and 20 kHz (0.05 km s^{-1}) in frequency resolution was used in the backend. The half-power beam width (HPBW) is 15″ at this frequency, corresponding to 2200 AU. The telescope pointing adjustment was carried out every an hour by observing the SiO maser VX Sgr and the pointing accuracy was achieved ±5″ during observation. The calibration for daily variation in intensity caused by the receivers' sensitivity fluctuation was done by checking a standard reference object, W51 main, before observation and the correction for the atmospheric variation was performed by chopper wheel method. The observed $T_{\rm A}^*$ is converted into $T_{\rm mb}$ in Kelvin by applying 0.36 in the $\eta_{\rm mb}$ for ^{12}CO (J=1–0) line provided in the NRO status report. Data reduction and analysis of HD 169142 were made with the NEWSTAR package as in the HD 163296 and HD 31648 data reductions.

2.2 ^{13}CO (J=1–0) Emission Line Observations

Observations of the ^{13}CO (J=1–0) emission line were conducted by the NRO 45 m telescope in the winter of 2010 and 2011. As shown in the profile maps of Figure 5.4 and 5.6 in the following Section 2.3 in this chapter, covering 20″ × 20″ and 22″ × 22″ compact region observed emission at 7 km s^{-1} in $V_{\rm LSR}$ is confirmed to be originated from the star+disk system. Therefore, ^{13}CO (J=1–0) observations were intensively made only toward the stellar position. A pair of sideband-separating SIS (2SB) receivers, T100H/V, are used and tuned at a ^{13}CO (J=1–0) rest frequency of 110.201 GHz. The achieved IRR was 11 - 15 dB in the whole observation. The HPBW was 15″, corresponding to 2200 AU at this frequency. The same AOS and frequency configuration in the backend were adopted as the ^{12}CO (J=1–0) 5 point observation. The system noise temperature during observation was between 130 K and 350 K. Since there were some windy days, some data have large noise and possibly contain no stellar emission due to a large pointing deviation. Therefore, all spectral data were carefully checked one by one and the data with wind speed exceeded 5 m s^{-1} were flagged out before obtaining the final spectrum in ^{13}CO (J=1–0) line. The resultant total integration time was ∼ 1 hour on the source. The pointing check and the correction due to atmospheric variation were carried out as the same manner as in ^{12}CO (J=1–0) observations. The correction for the intensity caused by the small daily fluctuation in the receivers' sensitivities that were always stable in this observation was made by observing standard reference object W51 main, which is prepared in NRO. As provided in the NRO status report, the $\eta_{\rm mb}$ in 2009 at this frequency was 0.42 and applied to convert the raw data of the observed $T_{\rm A}^*$ to $T_{\rm mb}$. The data reduction and analysis were took the same way as those in the ^{12}CO (J=1–0) observation mentioned above.

2.3 ^{12}CO (J=3–2) Mapping Observations

The mapping observation by ^{12}CO (J=3–2) line were carried out in August 2005 with the ASTE telescope. The HPBW of the ASTE telescope at the rest frequency of 345.79 GHz is 22″, which correspond to ∼ 3200 AU at a distance of 145 pc away from the Sun, and the $\eta_{\rm mb}$ was 0.6 at this frequency. An SIS mixer receiver having DSB response was employed. The typical atmospheric opacity at 220 GHz toward the zenith was 0.05 during the observations, and the system noise temperature was 250 - 300 K during the observations. The same digital auto-correlator with 1024 frequency channels and 128 MHz in bandwidth as used in HD 163296 observation and thus have a frequency resolution of 125 kHz, corresponding to ~ 0.11 km s^{-1} at the observation frequency. Telescope pointing was checked every 1.5 - 2 hours by cross scanning of Jupiter and as a result it was achieved $\leq 3''$ in pointing accuracy. The observation was conducted in a position switching mode and the location of the off-position was $(\Delta\alpha, \Delta\delta) = (+20', 0')$ from the stellar position. It was carefully checked that the star+disk system was surely isolated as well as ^{12}CO (J=1–0) observations by taking spectra not only at the stellar position, but also at four adjacent points, $22''$ apart from the stellar position in R.A. and Dec. directions as shown in Figure 4.7. Data reduction and analysis were conducted in the same manner as in ^{12}CO (J=1–0) observations, described in Section 2.1.

2.4 HCO$^+$ (J=1–0) Emission Line Observations

Observations of HCO$^+$ (J=1–0) emission line (89.188526 GHz in the rest frequency) were conducted by the NRO 45 m telescope in May 2011. As results of the profile maps around the star+disk system obtained, it is found that the emission around 7 km s^{-1} in $V_{\rm LSR}$ is not significantly contaminated by surroundings and therefore HD 169142 is isolated (see profile maps shown in Figure 5.4 and 5.6). Thus, the antenna was just focused on only stellar position in the whole HCO$^+$ (J=1–0) observations. The same 2SB receivers, T100H/V, are selected and the spectrometer used in this observation is in the same settings as HCO$^+$ (J=1–0) observations of HD 163296 and HD 31648. The IRR was 11 - 15 dB in this frequency. The system noise temperature during observation was between 300 K and 400 K and the $\eta_{\rm mb}$ in 2011 at this frequency was 0.43. The pointing accuracy was $\pm 6''$ and rather deteriorated due to strong wind. All observational data less than 5 m s^{-1} in the wind speed are extracted to maximize the S/N ratio in the data reduction. The resultant total integration time was about 1.5 hours on the source after flagging out. The pointing check and the atmospheric correction were carried out as the same manner as in ^{12}CO (J=1–0) observations as described in Section 2.1 in this chapter. W51 main, a well-studied massive star-forming regions, applied as a standard reference object for correcting daily fluctuation in intensity due to the small fluctuation in the receivers' sensitivity. The correction was almost unnecessary because the system as a whole was stable while the observation was going on.

3 Results

3.1 ^{12}CO (J=1–0) and ^{13}CO (J=1–0) Emissions

Since a proper off point is essential for the position-switching observation, a search for an emission free point was conducted by ^{12}CO (J=1–0) line, the most optically thick line, before observing HD 169142. Figure 5.3 is a spectrum at off-point position with 1 σ = 0.054 K after $\sim$ 1 hour integration. No emission nor absorption is detected at the systemic velocity of 7 km s^{-1} and it is applicable for an off-point.

A $44'' \times 44''$ ($\simeq$ 6400 AU $\times \simeq$ 6400 AU) profile map obtained centered at the star+disk system by ^{12}CO (J=1–0) line shown in Figure 5.4. As in the case of HD 163296 and HD 31648 observations, a clear double-peaked profile at the systemic velocity of 7 km s^{-1} in $V_{\rm LSR}$ (Panić et al. 2008) is detected only at the center panel and therefore the ^{12}CO (J=1–0) emission originated from the star+disk system (see also Figure 5.6 in the case of ^{12}CO (J=3–2) line observation). The emission feature has a peak intensity of 0.44 K in $T_{\rm mb}$, 1.7±0.2

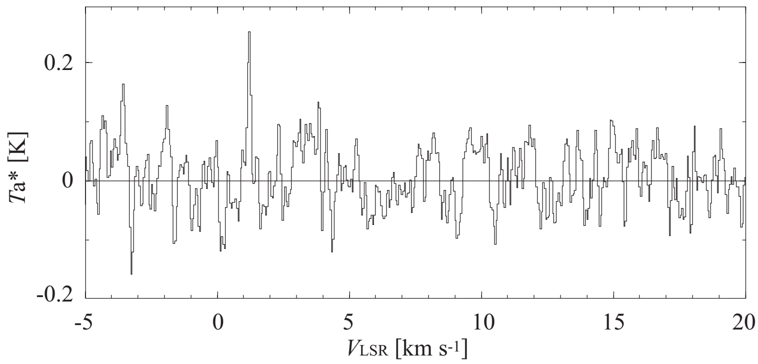

Figure 5.3 Spectrum at off point applied in HD 169142 observation. The off point position is (α, δ) = ($18^h28^m34^s.68$, -$29^\circ34'44''.3$) in J2000.

km s^{-1} in FWHM velocity width, and 0.076 K in the mean rms noise level after $\sim$ 2.5 hours integration time on source, resulting in 5.8 σ in S/N ratio.

Figure 5.8b shows a profile of the ^{13}CO (J=1–0) emission. The single-peaked profile due to the in face-on configuration was detected. The peak intensity with 1 σ = 0.061 K and velocity width are 0.37 K in $T_{\rm mb}$ and 1.52$\pm$0.15 km s^{-1} at FWHM, respectively. Both of the ^{12}CO (J=1–0) and ^{13}CO (J=1–0) emissions should have the same origin because they are detected in the same systemic velocity. The intensity ratio between ^{12}CO (J=1–0) and ^{13}CO (J=1–0) is $\sim$ 1, suggesting that the disk is possibly optically thick.

3.2 ^{12}CO (J=3–2) Emission

A 5-point profile map of ^{12}CO (J=3–2) spectra that consists of 4 profiles 22$''$ ($\sim$ 3200 AU) away from the central star in north, south, east, and west directions and a profile at the central star is shown in Figure 5.6.Since a strong 9 σ emission with 1.1 K in $T_{\rm mb}$ at 7 km s^{-1} in $V_{\rm LSR}$ after 2.5 hours integration time on the source is seen only at the central panel, the origin of the emission likely to be star+disk system. As confirmed in the analysis of the disks around HD 163296 and HD 31648, the origin of the observed emission was checked for making sure by means of making subtraction of the emission profile from the averaged 4 profiles around the central star as done in the other two disks (see Figure 3.8 and 4.8) . The central panel of Figure 5.6 is identical to Figure 5.8a. The profile after subtracting the averaged profile of 4 ambient spectra in the adjacent panels from the profile of the star+disk system in the central panel as shown in Figure 5.8c still remains a strong emission feature. Thus, it conclude that the observed emission is originated from the star+disk system and is hardly contaminated by foreground and background emissions. The velocity width of the ^{12}CO (J=3–2) profile is 1.3$\pm$0.1 km s^{-1} in FWHM and does not change from the one of ^{12}CO (J=1–0) profile due to face-on disk configuration.

3.3 HCO^+ Emission

Figure 5.9 shows an HCO^+ (J=1–0) emission originated from the disk around HD 31648. An emission profile with the peak intensity of 0.1 K in $T_{\rm mb}$ and 3.3$\pm$0.2 km s^{-1} in the FWHM velocity width is detected at the systemic velocity of $\sim$ 5 km s^{-1} in $V_{\rm LSR}$. The integration time is about 1.5 hours on the source. Since the elevation of the object is low from the site of NRO 45 m telescope, less than 30°, and the noise level is still rather high and produces barely 3.0 in the S/N ratio after 4 channel binning. The observed HCO^+ (J=1–0) data is treated as a reference and used for rough estimation of ionization fraction as will be seen in Section 5.3

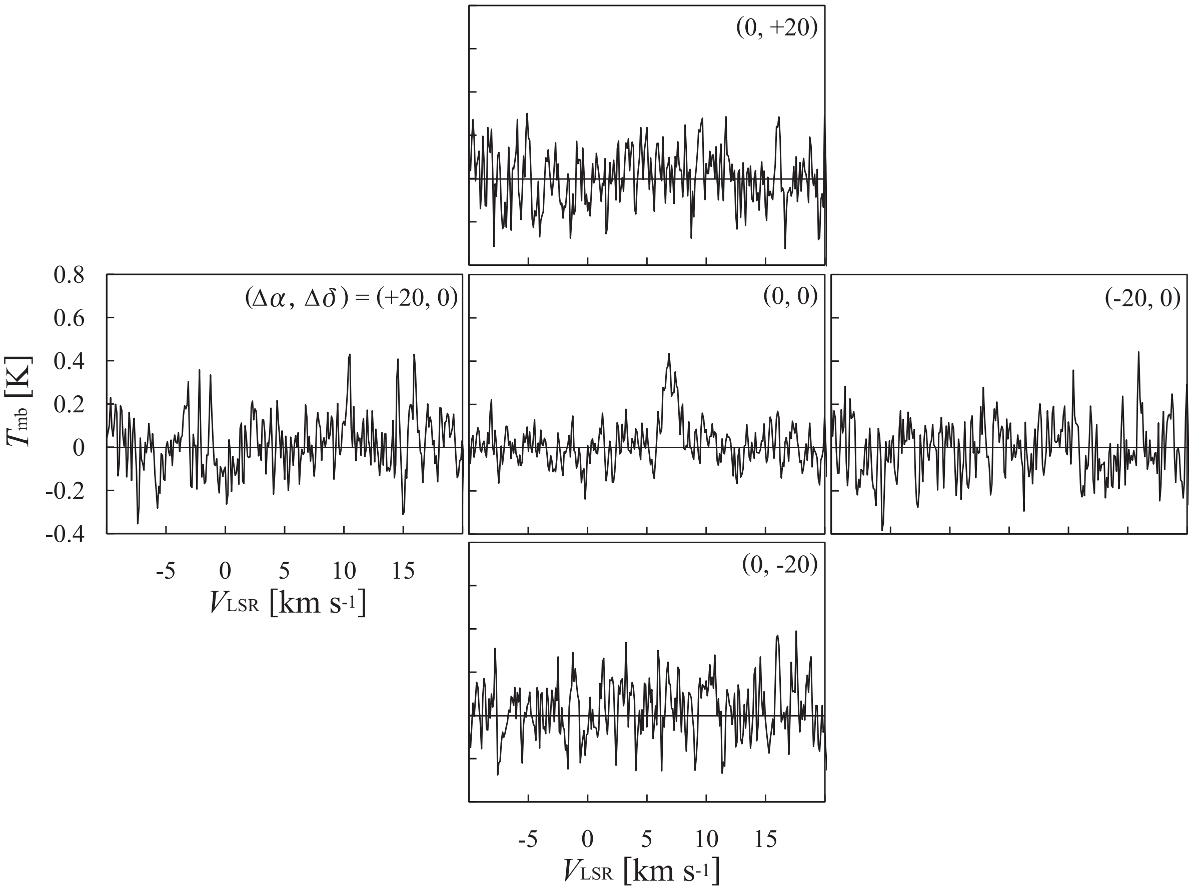

Figure 5.4 A five-point profile map of the ^{12}CO (J=1–0) line around HD 169142. The map center corresponds to the stellar position (α, δ)=($18^h 24^m 29^s.78$, -29°46′49″.37) in J2000, and the angular distance between adjacent points is 20″ (∼ 2900 AU) in both R.A. and Dec. directions as designated at the upper right corner of each panel.

in this chapter.

4 Model Fitting

4.1 Fitting Results of Power-Law Disk Model

The observed emission were reproduced by using two physical models of disk structure; power-law disk model with cut-off at the outer edge and similarity solution disk model with an exponential tail in radial surface density distribution, to estimate the disk properties, $r_{\rm out}$, T_{100}, and Σ_{100}. HD 169142 shows almost the same spectral width in all CO isotopologue profiles due to its face-on disk configuration as shown in Figure 5.8 (see also Figure 5.14). Therefore, it is hard to trace the disk size by CO isotopologue lines with different optical depth. Figure 5.10 shows the best-fit results for each CO line by power-law disk model when Σ_{100} = 0.1 g cm^{-2} and the corresponding disk temperature, intensity, and density distributions in two dimensional views are provided in Appendix C5. Figure 5.11 shows the best-fit temperatures at each $r_{\rm out}$ at Σ_{100} between 0.001 and 3 g cm^{-2} that all of the CO lines simultaneously fit by a single set of parameters and corresponding fitting values are provided in Table 5.1. As seen in Figure 5.11, T_{100} in each CO line is well converged to a specific value of temperature in an asymptotic behavior at large Σ_{100} so that the disk becomes optically thick for all of

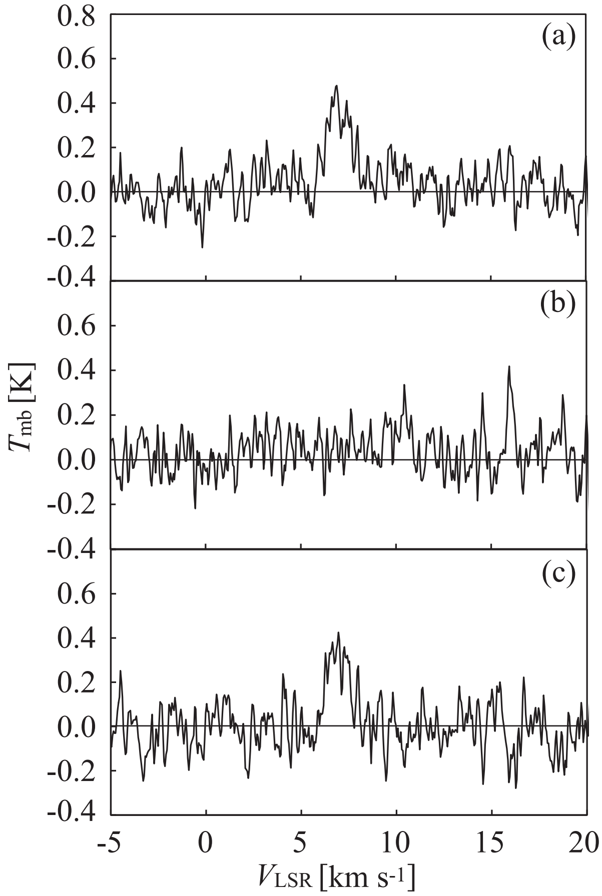

Figure 5.5 Verification of the emission from the star+disk system. (a) Observed ^{12}CO (J=1–0) emission profile toward HD 169142 in Figure 5.4. (b) ^{12}CO (J=1–0) profile generated by averaging the profiles at four locations around HD 169142 20″ away in north, south, east, and west directions from the central star in Figure 5.4. (c) Resultant profile after subtracting (a) from (b).

the CO line emissions, and therefore the calculation is stopped at 3 g cm^{-2}. The lower limit of Σ_{100} or lower limit of the disk mass can be estimated. Note that the observational data by optically thin line, such as C^{18}O (J=1–0) or H^{13}CO^{+} (J=1–0), need to constrain the upper-limit of surface density. The fitting temperature of ^{12}CO (J=3–2) shows the highest value among all of the CO lines; $\sim$ 45 K in ^{12}CO (J=3–2) and $\sim$ 20 K in the other CO lines.

Table 5.1 Best Fit Parameters at $r_{\rm out}$ = 500 AU

	T_0 [K]		
Σ_{100} [g cm^{-2}]	^{12}CO (J=3–2)	^{12}CO (J=1–0)	^{13}CO (J=1–0)
0.3	53^{+13}_{-14}	18±6	28^{+5}_{-15}
1	50^{+8}_{-9}	17^{+5}_{-6}	26^{+23}_{-15}
3	47^{+11}_{-11}	16±5	21±10
10	45^{+10}_{-11}	16^{+4}_{-5}	19^{+7}_{-9}

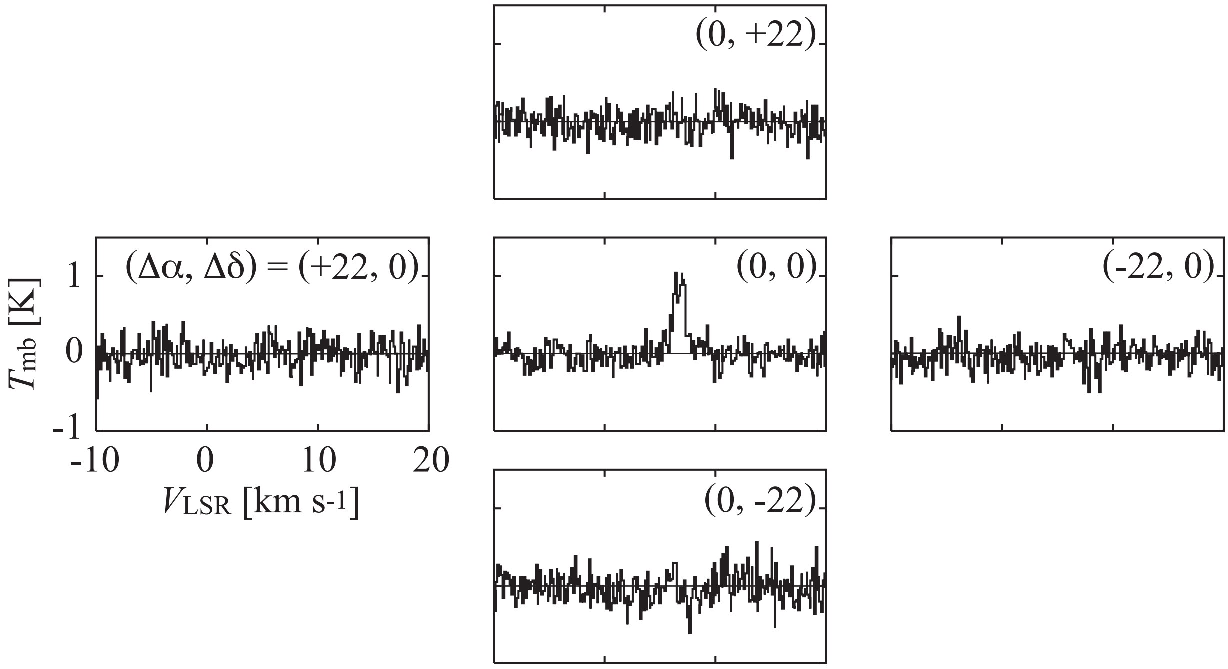

Figure 5.6 The same profile map shown in Figure 5.4 in ^{12}CO (J=3–2) line.

4.2 Fitting Results of Similarity Solution Disk Model

The model fitting was conducted by the similarity solution disk model as well for describing the disk temperature and surface density structure through comparing fitting results obtained from both disk models. The best-fit temperatures and the outer radius at 0.001, 0.01, 0.1, and 1 g cm^{-2} in Σ_{100} where the fitting solution for all of the CO lines simultaneously exist are provided in Table 5.2. The best fitting results when Σ_{100} = 0.1 g cm^{-2} are shown in Figure 5.12 and the corresponding disk temperature, intensity, and density distributions in two dimensional views are provided in Appendix C6. Figure 5.13 shows the fitting temperature at several specific Σ_{100}. Note that the solution in the lower range of Σ_{100} range is not reliable even though fitting solution exists since the consistency with the disk mass from dust continuum observation no longer be maintained. The disk mass of HD 169142 is derived to be 4 × 10^{-2} - 0.1 $M_\odot$ by SED fitting applying steep power-law with p = 2 in $\Sigma(r)$ (Dominik et al. 2003) and by fitting resolved 7 mm continuum emission (Dent et al. 2006). The fitting can be achieved by adjusting T_{100} in low Σ_{100} in the similarity solution disk model because the surface density tapers off gradually and the mass still remains in the outer region of the disk. Figure 5.15 describes the distribution of the surface density and the number density at mid-plane of the disk in both models when Σ_{100} = 1 g cm^{-2}. The disk radius is truncated at r_{out} while it extends up to more than 1000 AU from the central star. Although it is difficult to confine the surface density in similarity solution disk model, the surface density might be confined by merging fitting parameters obtained by other data, such as SED. As in the case of the results from the power-law disk model, the fitting temperature of ^{12}CO (J=3–2) shows the highest among all of the CO lines (ref. Table 5.2).

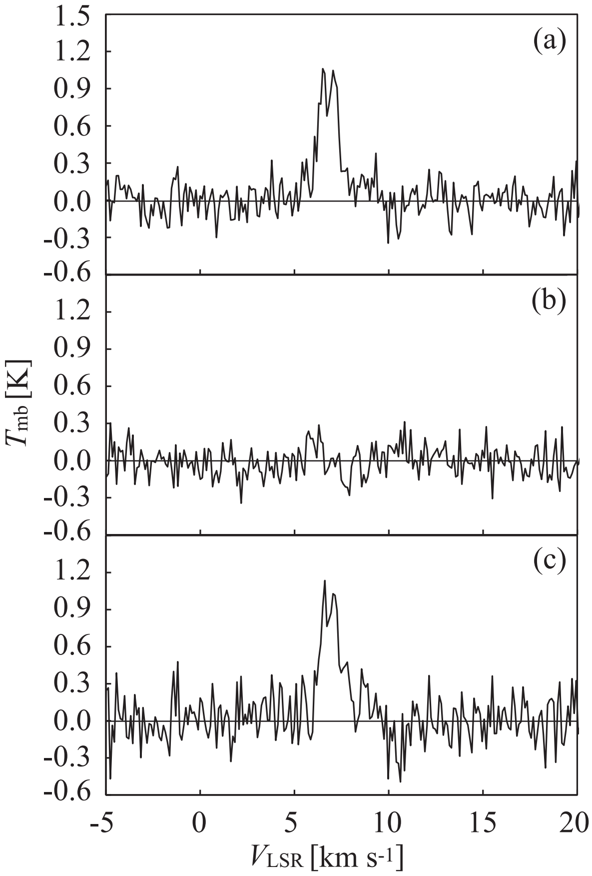

Figure 5.7 The same as Figure 5.5 for ^{12}CO (J=3–2) line.

Table 5.2 Best Fit Parameters at $r_{\rm out}$ = 800 AU

	T_0 [K]		
Σ_{100} [g cm^{-2}]	^{12}CO (J=3–2)	^{12}CO (J=1–0)	^{13}CO (J=1–0)
0.001	36±7	15^{+3}_{-4}	15^{+4}_{-10}
0.01	35^{+5}_{-7}	14±3	14^{+4}_{-9}
0.1	33^{+6}_{-6}	14^{+2}_{-3}	13±4
1	33^{+5}_{-6}	14^{+2}_{-3}	13^{+3}_{-4}

5 Discussion

5.1 Vertical Temperature Distribution

The result from the ratio between observed line intensities with the same rotational transition and the surface density estimated from the model fitting are consistent and both supports that the disk is optically thick for all CO lines. Thus it is natural to think that all CO emissions originate from their own photosphere. Taking with the derived vertical location of each CO emission photosphere through equation (3.1) as shown in Figure 3.15, it is holistically interpreted to credit the HD 169142 disk with vertical temperature distribution inside of the gas disk like the disks around HD 163296 and HD 31648. Both disk models describing the disk temperature and surface density structure can be applied for the analysis of the disk temperature structure.

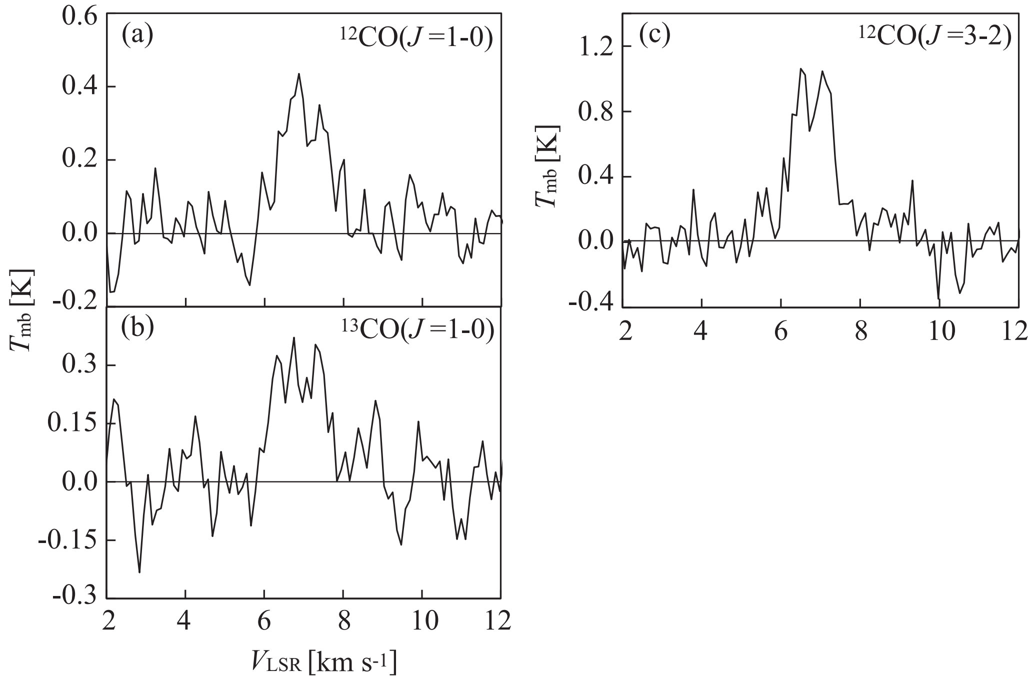

Figure 5.8 Emission profiles detected toward the stellar position of HD 169142. The each CO isotopologue line is designated in upper-right corner of each panel.

The results of fitting temperature derived by any disk models shows the temperature of the ^{12}CO (J=3–2) is the highest among the CO isotopologue lines even uncertainties designated by the error are considered (see Figure 5.11 and 5.13): $\sim$ 40 K in the ^{12}CO (J=3–2) line and $\sim$ 20 K in the other lines. The same method to examine the vertical temperature distribution is applied as that described in Section 5.2 in Chapter 3 and Section 5.1 in Chapter chap:HD31648. The vertical location of photosphere of each CO emission line is provided in Figure 3.15 with the representative T_{100} of the low-temperature interior and the high-temperature surface. The relation between the fitting temperature and the vertical location of the photosphere of each CO line indicates that the temperature of the upper-most layer is nearly twice as high as that of the mid-plane of the disk as the vertical temperature structure seen in the HD 163296 and HD 31648 disks.

5.2 Radial Density Distribution

As introduced in Chapter 1 regarding the planetary system formation, the variety of planetary systems depends on initial condition of the temperature and density structure of the protoplanetary disks. The radial density structure can be examined by comparing the two disk models, the power-law disk model with truncation at the outer disk and the similarity solution disk model with tapering off at the outer disk. However, it is difficult to detect the exponential tail component near the outer edge of the disk even though it exists because HD 169142 is a face-on object, which Kepler rotation is hardly reflected to the profile width. Figure 5.14 shows a comparison of ^{12}CO (J=1–0) spectrum with ^{13}CO (J=1–0) one. The both lines are supposed to trace the emission from different radial location, as well as vertical depth. ^{13}CO (J=1–0) line is optically thin relative to ^{12}CO (J=1–0) line and thus ^{13}CO (J=1–0) emission should mainly come from denser region, that is inner and higher Keplerian velocity of the disk than ^{12}CO (J=1–0) emission. However, their velocity widths are almost the same and different Keplerian velocity is not reflected to these profiles. Therefore, HD 169142 can

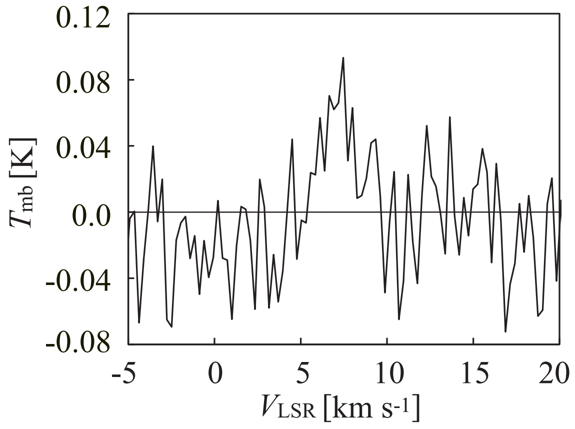

Figure 5.9 HCO^+ (J=1–0) spectrum for HD169142.

be well fitted by both disk models as shown in the fitting results provided in Figure 5.10 and 5.12. Figure 5.15 shows the radial surface density distribution and mid-plane density profiles for the power-law and the similarity solution disk models. The solid lines indicate the distributions in the power-law disk model, while the dashed lines indicate distributions in the similarity solution disk model. The distribution curves for both disks show similar profiles in inner disk since the same parameters are used in the index of $\Sigma(r)$ (ref. equation (2.2) and (2.10)).

5.3 Ionization Fraction of the Disk

As Sano & Stone (2002) points out regarding MRI induction, the ionization fraction of the gas disk determines the possibility to invoke the instability. Equation (1.22) provides an estimation of ionization fraction and is applicable for the disk beyond 100 AU; it is not suitable for applying it to high temperature region in the disk such as a inner disk near the central star or upper disk surface where the stellar UV can reach because the reaction rate will be significantly changed. Since the observed emission is mainly originated from the outer disk when spatially unresolved, the both simulation and observation data at r = 100 AU from the central star were applied. Furthermore, all reaction rates at the outer disk is assumed to be almost identical to the dense core's. For numerical evaluation, the CO abundance with respect to HCO^+ calculated by Walsh et al. (2010) is 10^5 and the number density of hydrogen based on the observational results as described in Figure 5.15 is $\sim 10^7$. As a result of substituting all numerical values into equation (1.22), it produces $[e^-] = \sim 10^{-7}$ for HD 169142 disk. Even if the $[e^-]$ contains large amount of uncertainty, it is still sufficient to invoke MRI occurred when $[e^-] \geq\sim 10^{-10}$. Although the CO abundance with respect to HCO^+ in equation (1.22) is available in some materials, the value based on the observation is wanted. However, the $[CO]/[HCO^+]$ is not estimated from model fitting since the noise level is still high. It is better to use the surface density of HCO^+ obtained by observations and should be evaluated for the consistency between results from calculation through chemical network and model fitting of the observed emission. The estimation of the ratio can be improved when density of HCO^+ is directly derived by observation. $H^{13}CO^+$ (J=1–0) line is more suitable because of optically thin and traces the disk mass more accurately than HCO^+ (J=1–0) line. $H^{13}CO^+$ (J=1–0) emission is thought to be detected which have hardly been detected in protoplanetary disks so far by recent advanced receivers with high sensitivity.In spite of many factors that can be improved, our observational results have supported so far that MRI can be invoked in the disk around HD 169142.

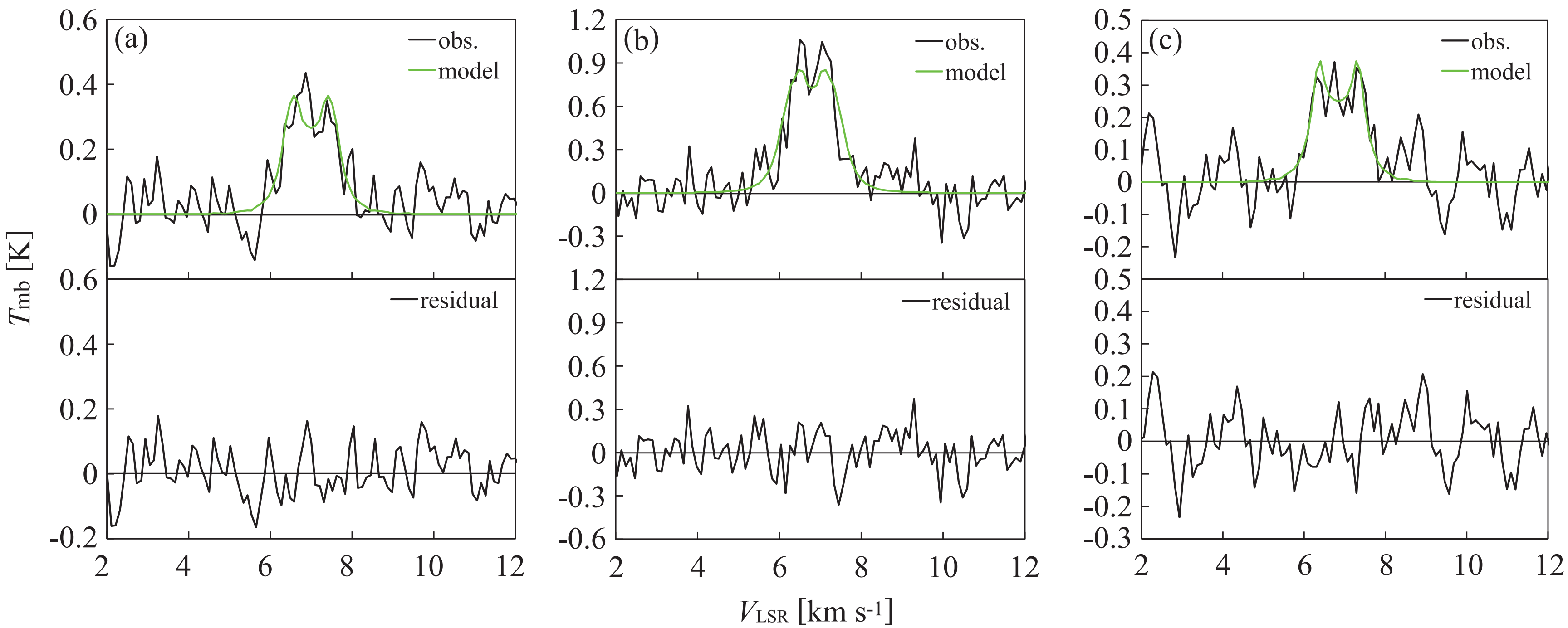

Figure 5.10 Fitting results by the power-law disk model in the case of ^{12}CO (J=1–0) (a), ^{12}CO (J=3–2) (b), and ^{13}CO (J=1–0) (c). (Upper panels): Comparisons between the line profiles obtained by the observations (dark line) and best-fit model calculations when $r_{\rm out}$ = 500 AU and Σ_{100} = 0.1 g cm^{-2} are provided (green lines). The corresponding T_{100} to these r_{out} and Σ_{100} parameters for each line profile is given as listed in Table 5.1. (Lower panels): Difference between the observed and calculated profiles shown in the upper panels.

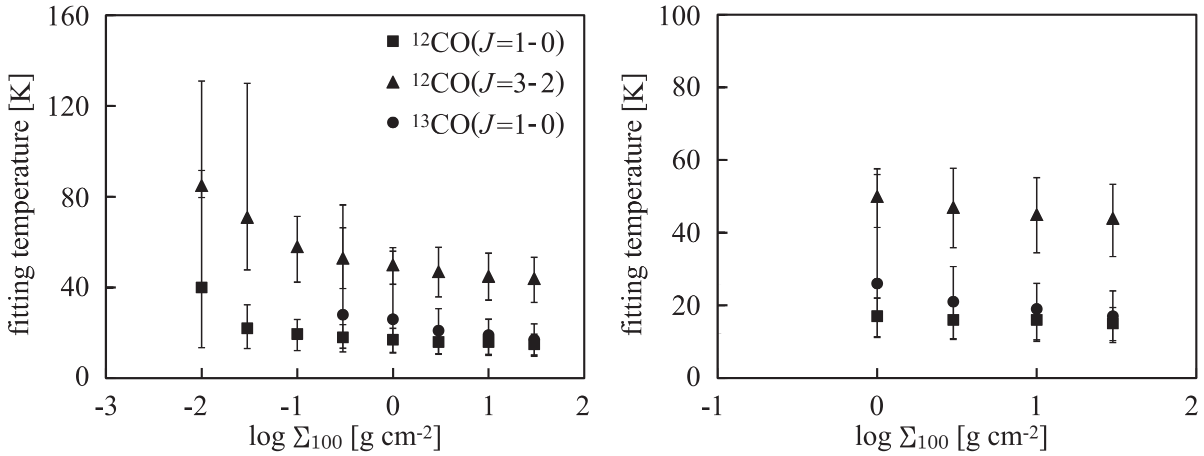

Figure 5.11 Best-fit T_{100} parameter with uncertainties for the acceptable fit in model calculations as a function of Σ_{100} in the power-law disk model. (Left): The panel shows the best-fit T_{100} between 0.003 and 3 g cm^{-2} in Σ_{100}, (Right): It is the same panel as the one on the left in an enlarged view of the lower-right part.

6 Chapter Summary

The observation toward the HD 169142 star+disk system in the ^{12}CO (J=1–0), ^{12}CO (J=3–2), and ^{13}CO (J=1–0) emission lines were conducted and the disk emissions were detected by ^{12}CO (J=1–0) and ^{12}CO (J=3–2) lines. Single peak profile formed by face on disk configuration are obtained in all CO lines. The physical properties and structure of the disk were examined by two disk models describing temperature and surface density distributions: the power-law disk model and the similarity solution disk model. As a result of model fitting and intensity ratio between emission lines with the same rotational transition, the disk is optically thick. Different fitting temperature of each CO isotopologue line that originated from the photosphere in different depth suggests that at least two distinct temperature layers exist inside of the disk and the temperature in the uppermost ^{12}CO (J=3–2) emitting layer is about twice as high as the lower temperature around the mid-plane of the disk. The radial surface density distribution was also investigated by comparing the two disk models. There are no difference in fitting results and accuracy between the two disk models. Since HD 169142 is a face-on object and disk emission is hardly reflected to the profile width, it is difficult to detect the exponential tail component near the outer edge of the disk even though it exists.

HCO^+ (J=1–0) emission with barely 3σ is detected and used to make an oder estimation of the ionization fraction of the disk. The disk probably reaches to 10^{-8} in the ionization fraction which sufficiently enough to drive MRI. $H^{13}CO^+$ (J=1–0) line is more suitable because of optically thin and traces the disk mass more accurately than HCO^+ (J=1–0) line. $H^{13}CO^+$ (J=1–0) emission has hardly been detected in protoplanetary disks so far but it is now thought to be quite capable by recent advanced receivers with high sensitivity. HD 169142 could be a good object to examine MRI because the disk is face-on whose emission profile is hardly affected by Kepler rotation and it might be easier to detect velocity component other than Keplerian velocity through model fitting.

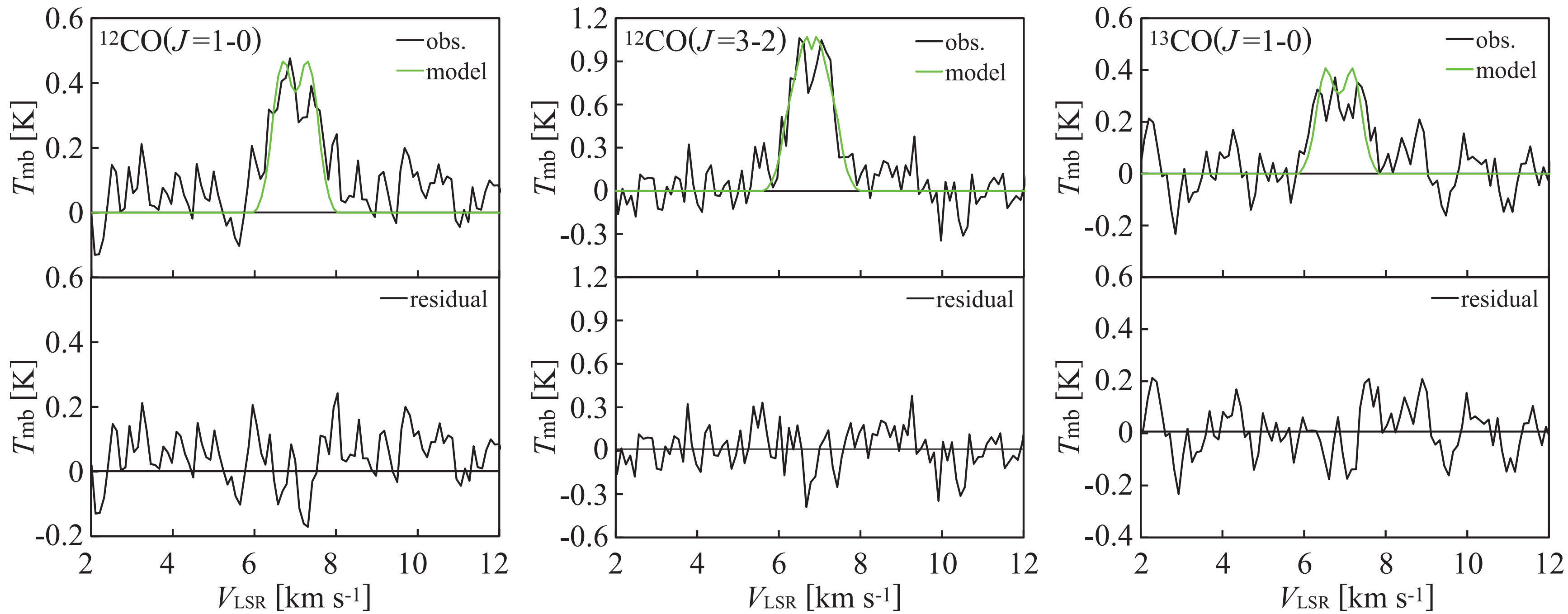

Figure 5.12 Fitting results by the power-law disk model in the case of ^{12}CO (J=1–0) (a), ^{12}CO (J=3–2) (b), and ^{13}CO (J=1–0) (c). (Upper panels) Comparisons between the line profiles obtained by our observations (solid line) and best-fit model calculations when $\Sigma_{100} = 0.1$ g cm^{-2} (green lines). Best-fit values for T_{100} and $r_{\rm out}$ in the model calculations are listed in Table 5.2. (Lower panels) Difference between the observed and calculated profiles shown in the upper panels.

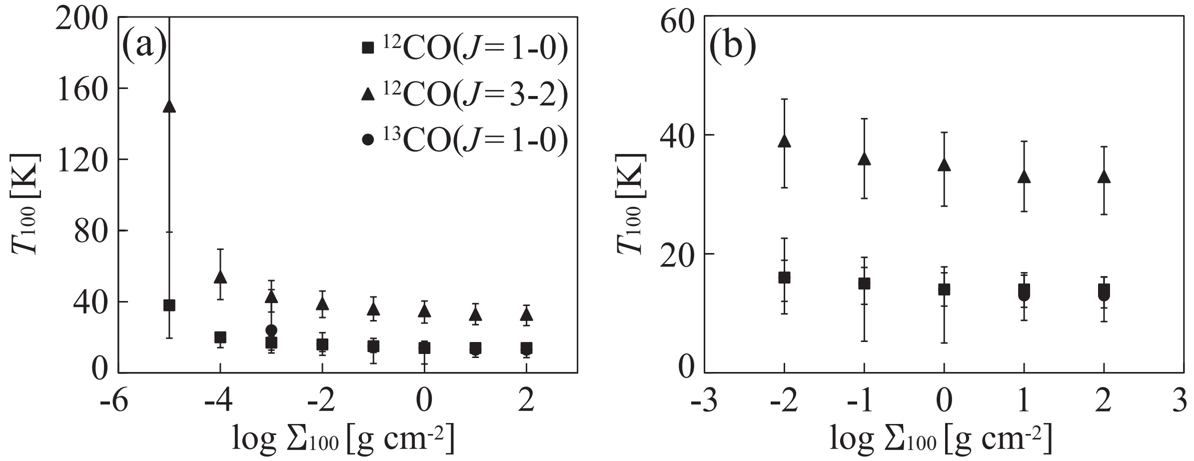

Figure 5.13 The same as Figure 5.11 for the model fitting by the similarity solution disk model.

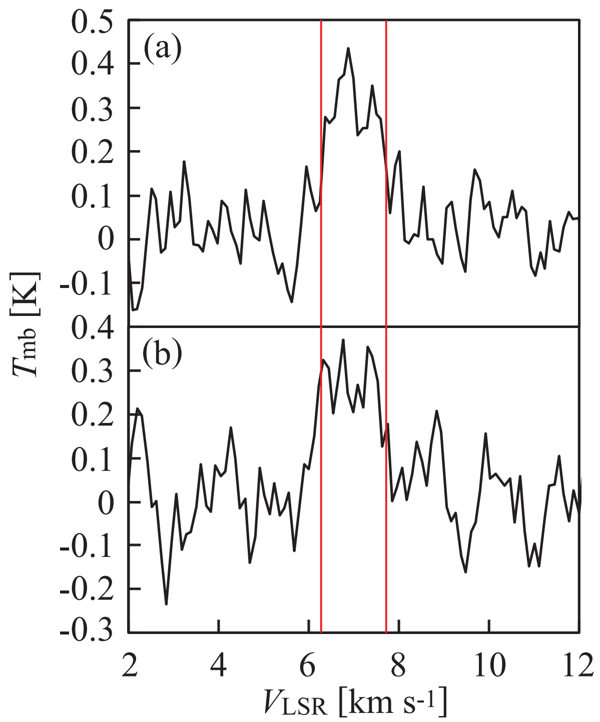

Figure 5.14 The same as Figure 3.17, 3.18, and 4.16 for HD 169142.

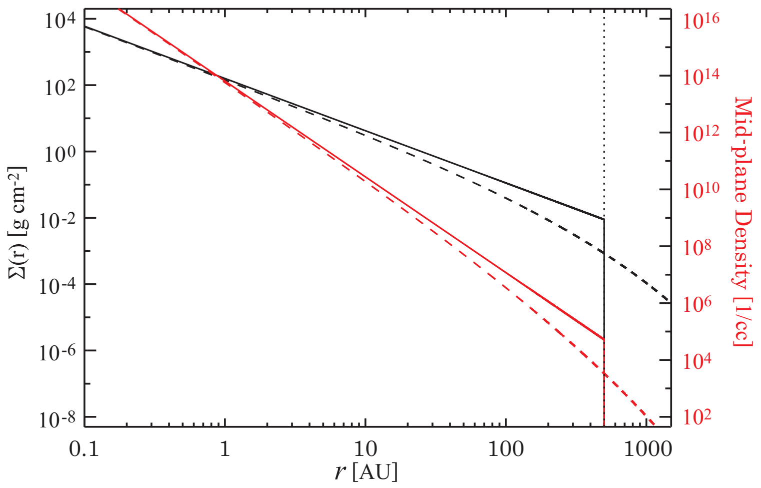

Figure 5.15 The same as Figure 3.19 for HD 169142. $\Sigma_{100} = 1$ g cm^{-2} is applied for the calculation.

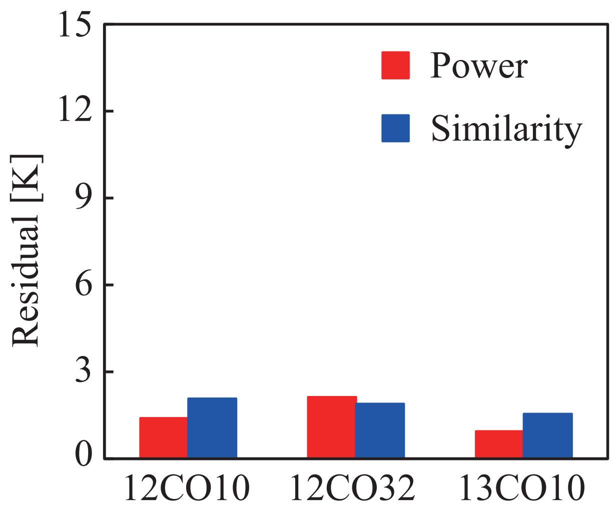

Figure 5.16 The same Figure as 3.20 for HD 169142 model fitting.

Chapter 6

Conclusion

The results discussed in this work can provide several clues for understanding general idea of the protoplanetary disk structure of HAe stars. Line observation strategies aimed at analyzing vertical temperature distribution and radial density distribution functioned adequately as a starting point for understanding planet formation. As results of multi-CO isotopologue line data and the vertical location of each photosphere analytically-computed, it concludes that the protoplanetary disk have temperature distribution in vertical direction inside of the disk at nearly 100 AU from the central star and beyond. The results also show that the farther away the layer is from the mid-plane of the disk, the warmer it reaches: 30 - 60 K in ^{12}CO (J=3–2) upper photosphere and 10 - 30 K around mid-plane of the disk. Figure 6.1 illustrates temperature distribution in a schematic cross-sectional view of the disk. The temperature distribution is detected at the outer region of the disk, the right side on the figure, by our single-dish observations. Since all of the observed protoplanetary disks around HD 163296, HD 31648, and HD 169142 shows the same results, such a vertical thermal structure of irradiated accretion disks is ubiquitous in protoplanetary disks.

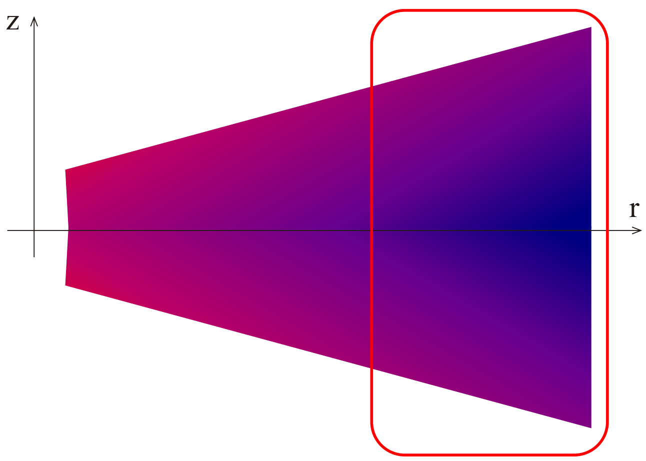

Figure 6.1 Schematic view of temperature distribution in the protoplanetary disks. High temperature represents in red and low temperature represents in blue. Vertical temperature distributions derived by our observations is located at the outer region of the disk represented by red box. Note that the scale is not true in this diagram.

A remarkable characteristic of the radial density distribution is discovered by our observation. The similarity solution disk model apparently performs better in model fitting of HD 31648 disk whereas there is no good fitting solution to satisfy all CO emissions simultaneously in a single set of parameters of the power-law disk model. The power-law disk model shows similar or better fitting result than the similarity solution disk model does in the HD 163296 case simply because HD 163296 is an evolved system in between a class II pre-main sequence disk and a debris disk which is more evolved. The density where it starts falling off gradually as representing by an exponential tail is too low to detect due to the sensitivity limit of instrumental capability. If the sensitivity is improved, the exponential tail might be detected in the HD 163296 star+system. There is no significant difference in model fitting results in the case of HD 169142 star+disk system due to its face-on configuration. This result suggests that the similarity solution is still applicable even for face-on system. Hence, based on the all observational facts, protoplanetary disks generally have density structure tapering off gradually at the outer edge as shown in Figure 6.2 (left).

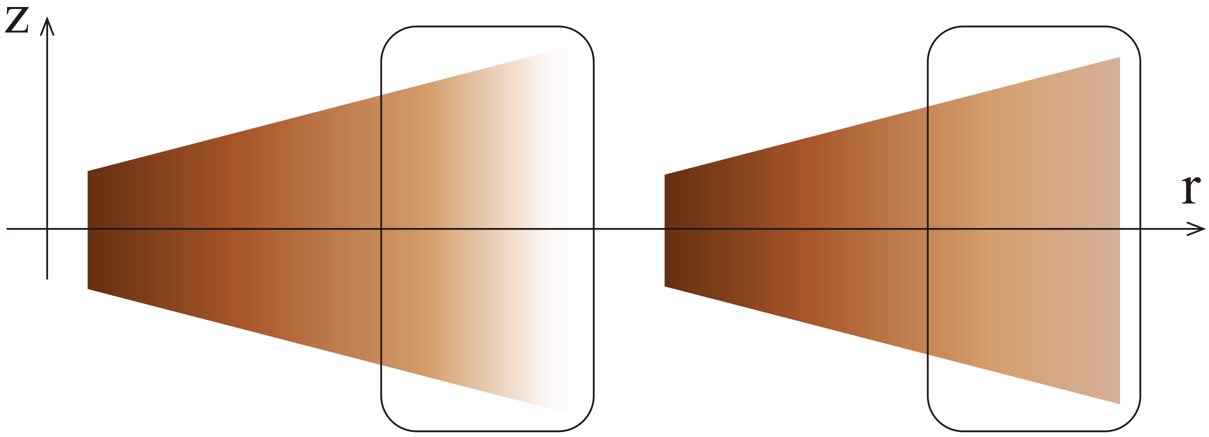

Figure 6.2 Schematic view of density distribution in the protoplanetary disks. High density represents in dark color and vice versa. (Left): Density structure is described by the similarity solution disk model and is supported by our observations. (Right): Density structure is described by the power-law disk model and provided as a reference. Remarkable difference is seen at the outer region including the outer edge of the disk indicated by the black boxes: fading out in density structure in the similarity solution disk model and truncation in the power-law disk model. The vertical density distribution, which is not shown in the diagram, is considered in the assumption of hydrostatic equilibrium and the density should become smaller towards the upper surface of the disk. Note that the scale is not true in this diagram.

Although it is necessary for estimating the ionization fraction, which determine the presence of the MRI, by fitting the observational profile, the results of HD 16326, HD 31648, and HD 169142 support that MRI can occur in protoplanetary disks. The ionization fraction was found to be nearly 10^{-8} - 10^{-9} and sufficiently high enough to drive MRI (10^{-10} - 10^{-12}). HCO^+ is a good ion tracer and $H^{13}CO^+$ (J=1–0) line is more suitable for estimating the ionization fraction because it is more optically thin line than HCO^+ (J=1–0) line and thus capable of tracing mass more accurately. In spite of a plenty of unknown factors for gas dispersion mechanism, our observational results suggest that the MRI may occur at a distance of 100 AU from the central star. MRI can also be indirectly confirmed by detecting turbulence invoked by MRI by observation with high spectral resolution. The line broadening due to turbulence can be estimated by model fitting and parameterizing the turbulent linewidth. The MRI is one of the strong candidate that triggers gas dispersion of the disk as it induces turbulence in the disk. HCN is not detected in all of the disk. The freezing temperature of HCN is nearly 100 K and probably it is frozen even in the disks around HAe stars.

The temperature and density structure of protoplanetary disks are still open questions. Better knowledge, such as the radial and vertical density distributions, will be provided by high-resolution observations in the upcoming ALMA era.

Appendix A

New Spectral Result of ^{12}CO (J=3–2) for HD 31648

Since the ^{12}CO (J=3–2) spectrum obtained in 2005 shows a deficiency in the red-shift component in the emission profile probably caused by an operational malfunction in the observation, a new observation in the same line was conducted in 2011. A side-band separating (2SB) mixer receiver, CATS345, and an XF-type digital spectro-correlator, MAC, are used. The MAC spectrometer was set in 128 MHz in bandwidth and 125 kHz ($\simeq$ 0.11 km s^{-1} in Velocity resolution at 350 GHz) in spectral resolution. The system noise temperature was 330 - 380 K during the observations. $\eta_{\rm mb}$ was 0.6 at 345.79 GHz. Telescope pointing was checked every an hour by observing the nml-Tau SiO maser and achieved less than 3$''$ in the pointing deviation. The observation was conducted in a position switching mode and the off-position was (α, δ) = (04^{h}58^{m}46^s.27, +30°15′37″.0) in J2000. Data reduction and analysis were made by NEWSTAR, a front end of AIPS, in the same manner as in ^{12}CO (J=1–0) observations, described in section 2.1 in chapter 4. A clear double-peaked spectra with a peak intensity of 0.59 K in antenna temperature with 7 σ in S/N ratio is obtained. The old spectrum shown in Figure 4.6c will be replaced by this new spectrum and the model fitting with this will be re-evaluated.

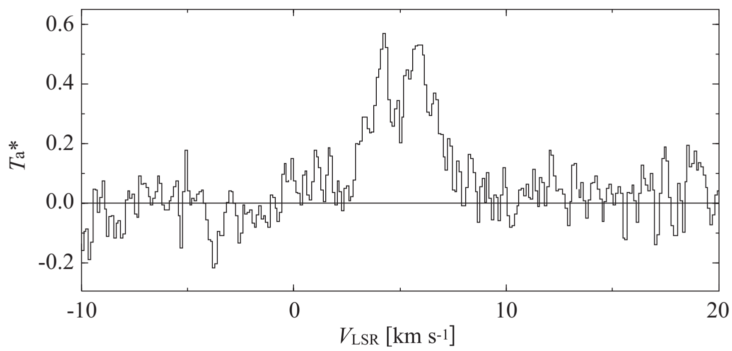

Figure A.1 A new ^{12}CO (J=3–2) spectrum.

Appendix B

Empirical Derivation of Ionization Fraction by HCO^+

The reaction and destruction for HCO^+ are realized in the course of several chemical processes and the individual chemical reaction pathway is provided below (Stahler & Palla 2004). The process described below is chemical reactions in dark clouds or dense cores but it is still applicable for the regions sufficiently far away from the central star and relatively near the mid-plane in protoplanetary disks where the stellar UV does not reach. The environment of the region in the disk is thought to be similar to that of dark clouds or dense cores. The first process is the generation of H_3^+ through cosmic-ray striking H_2.

$$H_2^+ + H_2 \rightarrow H_3^+ + H. \tag{B.1}$$

The H_3^+ generally undergoes dissociative recombination and expressed by

$$H_3^+ + e^- \rightarrow H_2 + H. \tag{B.2}$$

The reaction rates in equation (B.1) and equation (B.3) are k_1 and k_2, respectively, with units of cm^3 s^{-1}. HCO^+ is created as product of chemical reaction between H_3^+ and CO:

$$H_3^+ + CO \rightarrow HCO^+ + H_2. \tag{B.3}$$

The HCO^+ can also be destroyed by dissociative recombination and expressed by

$$HCO^+ + e^- \rightarrow CO + H. \tag{B.4}$$

By letting $k_{\rm dr}(HCO^+)$ be the recombination rate in equation (B.4), the number density of HCO^+ is

$$[HCO^+] = \frac{k_2[H_3^+][CO]}{k_{\rm dr}(HCO^+)[e^-]}. \tag{B.5}$$

Similarly, $[H_3^+]$ can be determined by letting $k_{\rm dr}(H_3^+)$ be the recombination rate in equation (B.3) as

$$[H_3^+] = \frac{k_1[H_2^+]}{k_{\rm dr}(H_3^+)[e^-]}. \tag{B.6}$$

Finally, $[H_2^+]$ can be obtained by balancing cosmic ray ionization with destruction by H_2:

$$[H_2^+] = \frac{\zeta(H_2)}{k_1 n_H}, \tag{B.7}$$

where $\zeta(H_2)$ is the volumetric impact rate with cosmic ray. By combining equation (B.5), (B.6), and (B.7), then

$$[e^-]^2 = \frac{k_2 \zeta(H_2)}{k_{dr}(H_3^+) k_{dr}(HCO^+)} \frac{[CO]}{[HCO^+]} \frac{1}{n_H}. \tag{B.8}$$

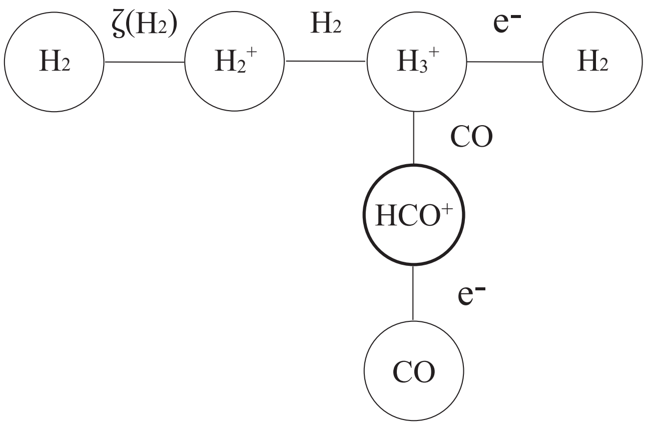

Figure B.1 Diagram of chemical reactions creating and destroying HCO^+ molecules in dark clouds or dense cores.

Appendix C

Temperature and Density Distributions in Two Dimensional View

1 2D View of the Protoplanetary Disk around HD 163296: Power Law Disk Model

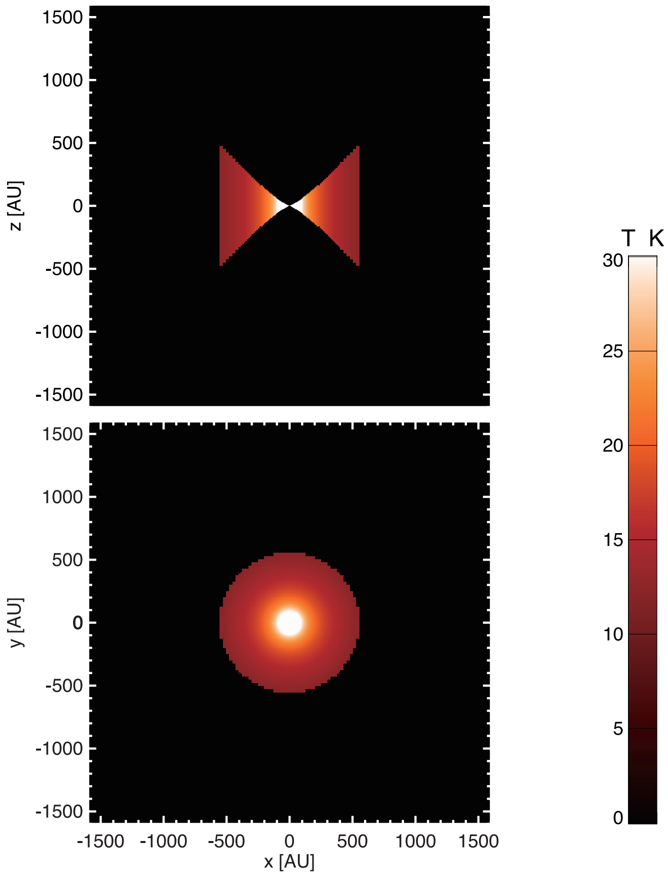

Figure C.1 Temperature distribution as a function of the disk radius in a two dimensional view. It is based on the result of fitting temperature of ^{12}CO (J=1–0) emission in power law model. (Top) Edge-on view of the disk is shown. (Bottom) Face-on view of the disk at z = 0 of the edge-on view is shown.

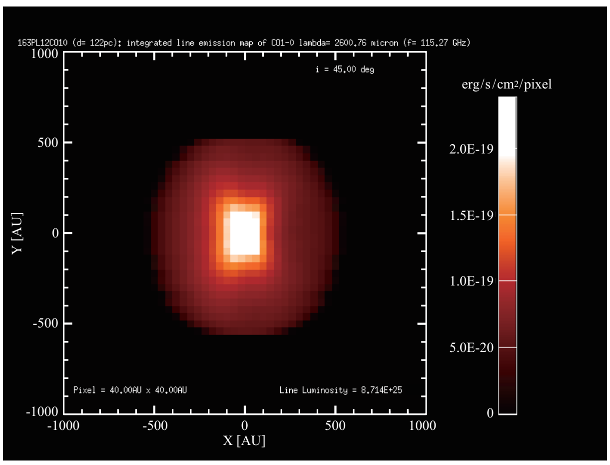

Figure C.2 ^{12}CO (J=1–0) intensity in two dimensional view. The rotational axis of the disk is horizontally oriented at an inclination angle with respect to the paper. Left side of the disk indicates near side and right side of the disk indicates far side.

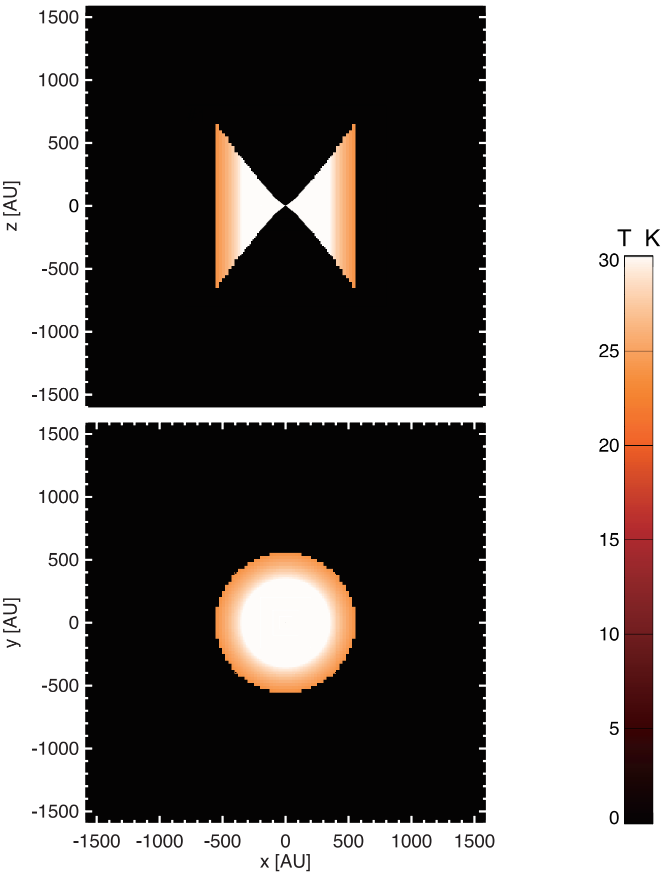

Figure C.3 The same temperature distribution as Figure C.1 based on fitting temperature of ^{12}CO (J=3–2) emission.

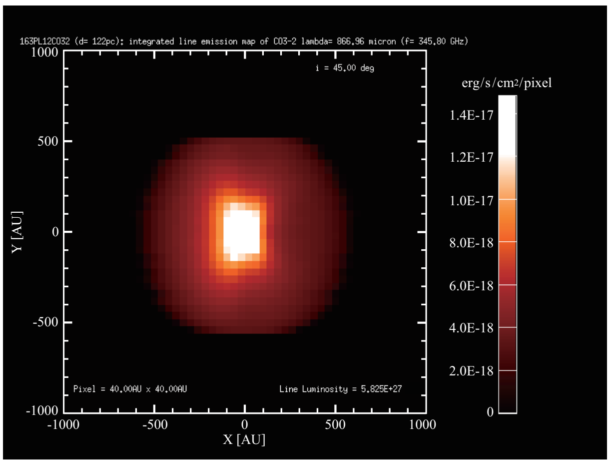

Figure C.4 ^{12}CO (J=3–2) intensity in two dimensional view. The disk orientation is the same as Figure C.2.

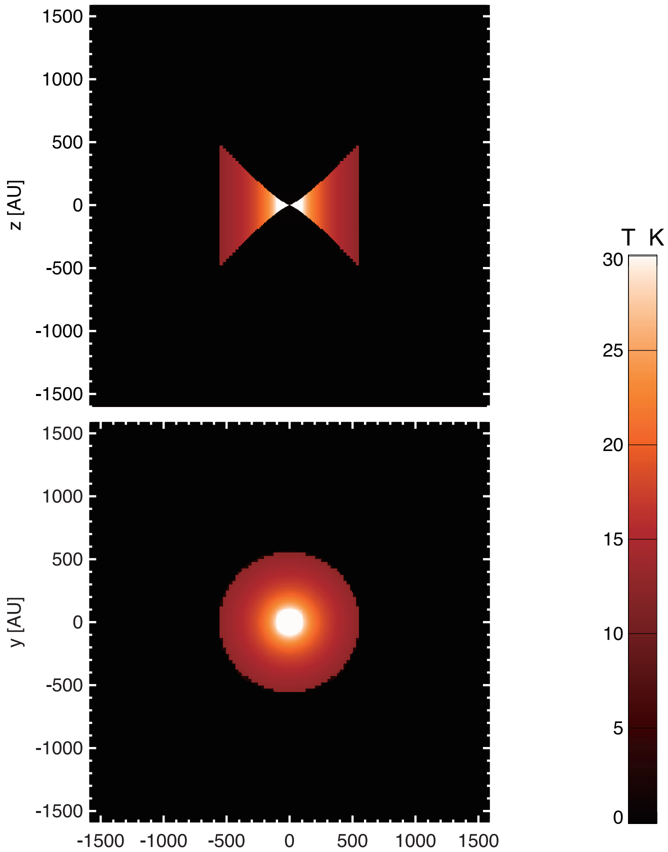

Figure C.5 The same temperature distribution as Figure C.1 based on fitting temperature of ^{13}CO (J=1–0) emission.

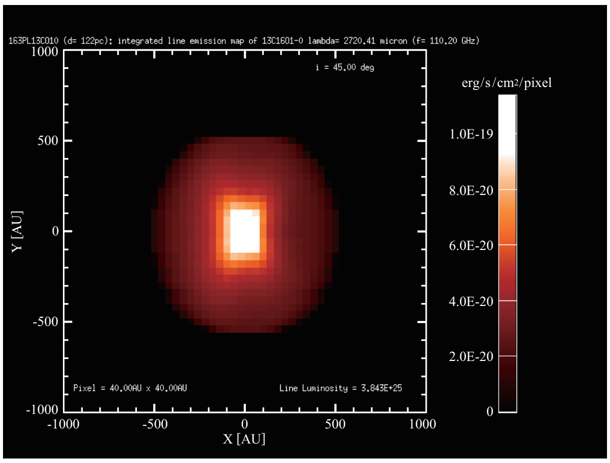

Figure C.6 ^{13}CO (J=1–0) intensity in two dimensional view. The disk orientation is the same as Figure C.2.

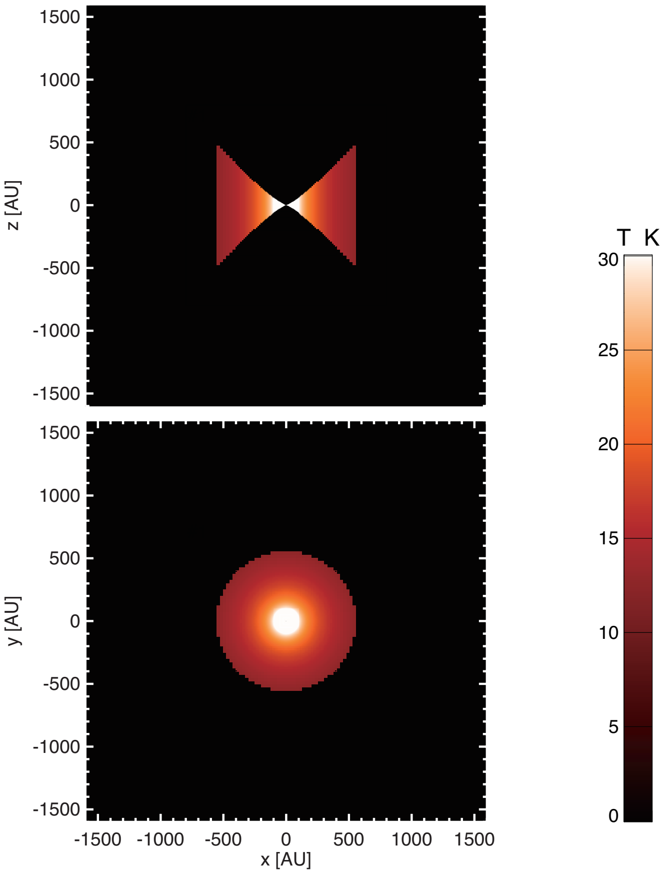

Figure C.7 The same temperature distribution as Figure C.1 based on fitting temperature of ^{13}CO (J=3–2) emission.

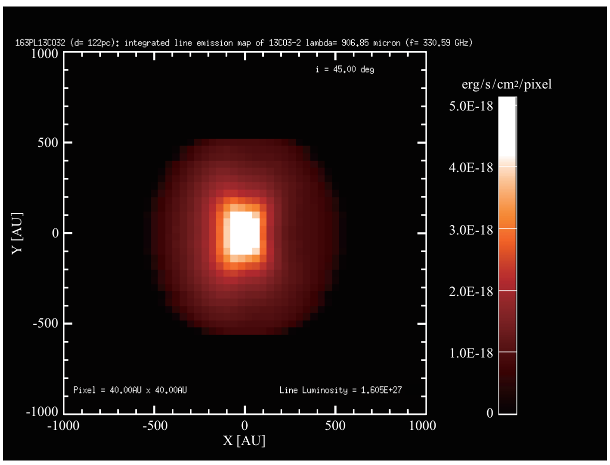

Figure C.8 ^{13}CO (J=3–2) intensity in two dimensional view. The disk orientation is the same as Figure C.2.

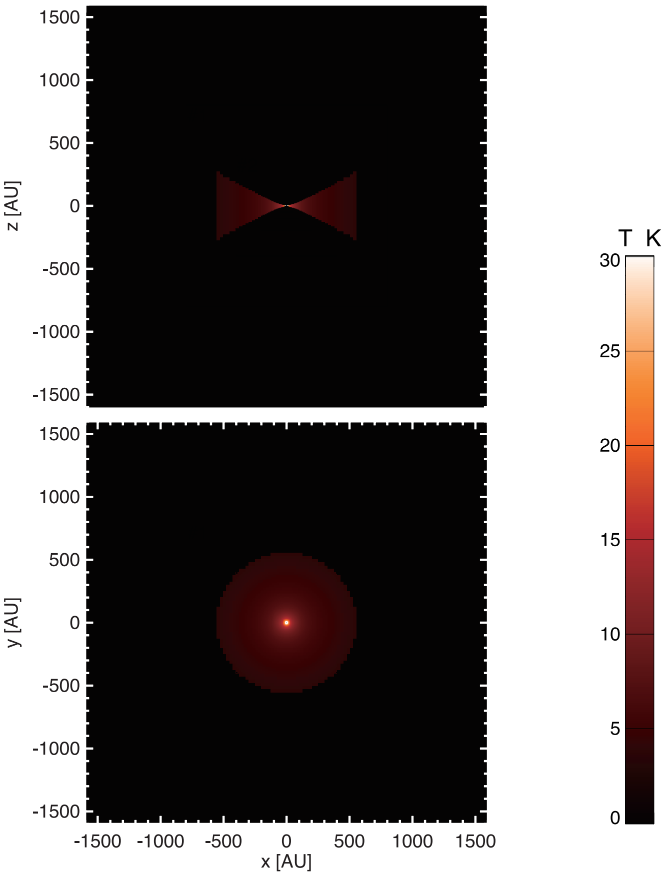

Figure C.9 The same temperature distribution as Figure C.1 based on fitting temperature of $C^{18}O$ (J=1–0) emission.

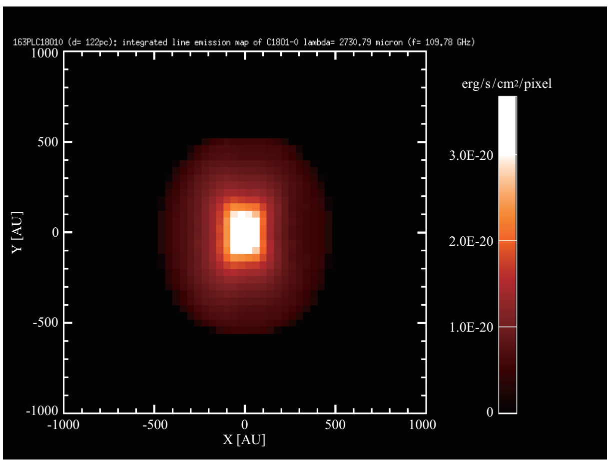

Figure C.10 $C^{18}O$ (J=1–0) intensity in two dimensional view. The disk orientation is the same as Figure C.2.

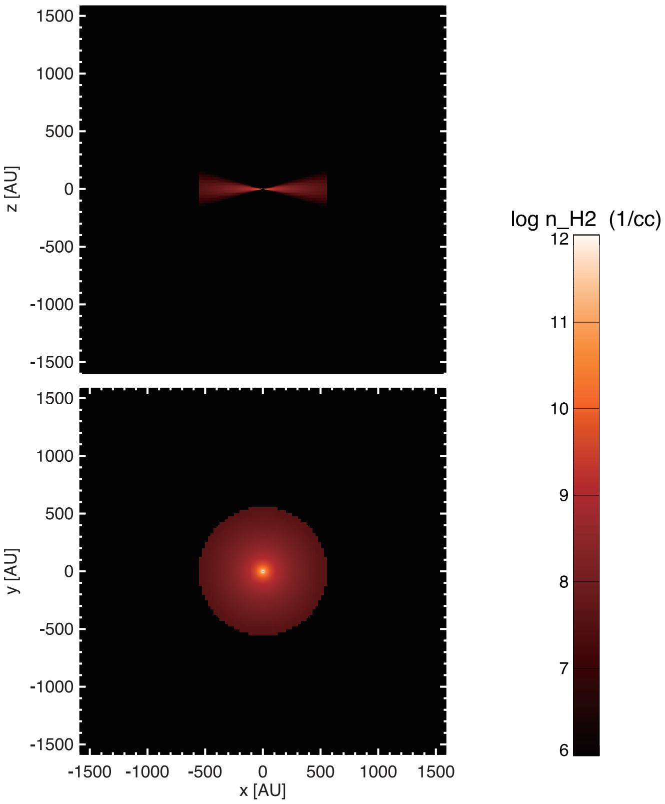

Figure C.11 Density distribution as a function of the disk radius in a two dimensional view. It is applied that $\Sigma_{100} = 10$ g cm^{-2} in the density distribution as a representative value.

2 2D View of the Protoplanetary Disk around HD 163296: Similarity Solution Disk Model

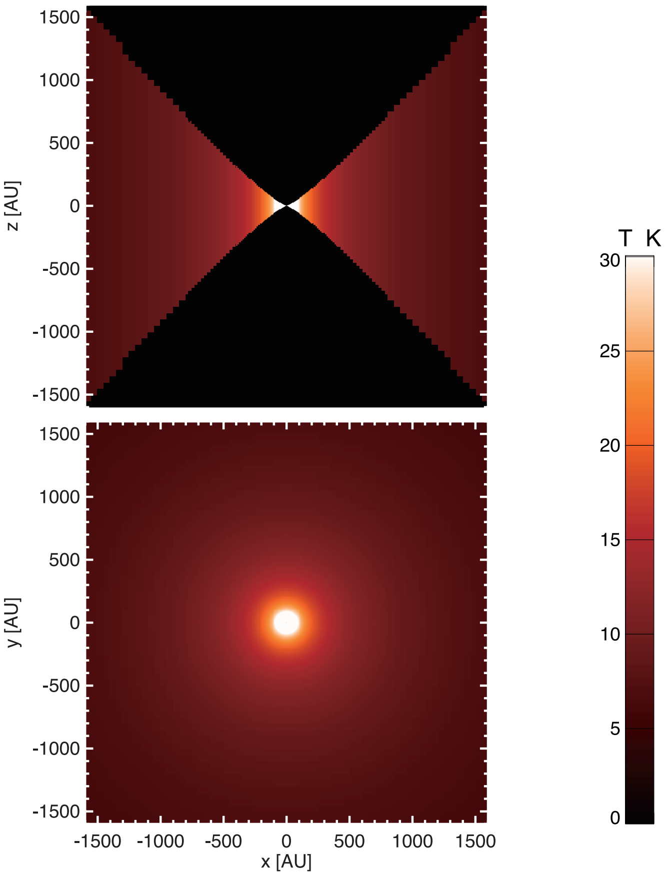

Figure C.12 Temperature distribution as a function of the disk radius in a two dimensional view. It is based on the result of fitting temperature of ^{12}CO (J=1–0) emission in similarity solution model. (Top) Edge-on view of the disk is shown. (Bottom) Face-on view of the disk at z = 0 of the edge-on view is shown.

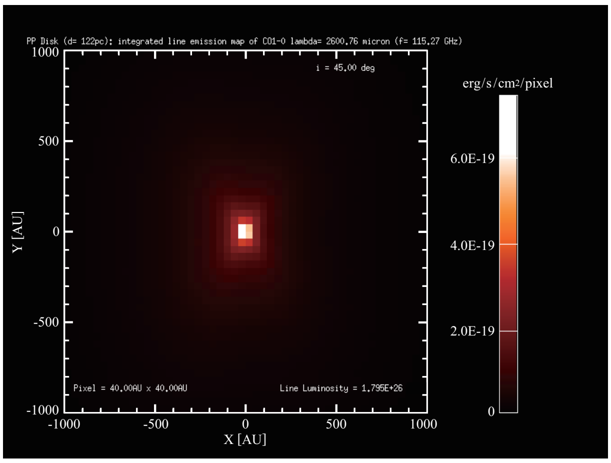

Figure C.13 ^{12}CO (J=1–0) intensity in two dimensional view. The rotational axis of the disk is horizontally oriented at an inclination angle with respect to the paper. Left side of the disk indicates near side and right side of the disk indicates far side.

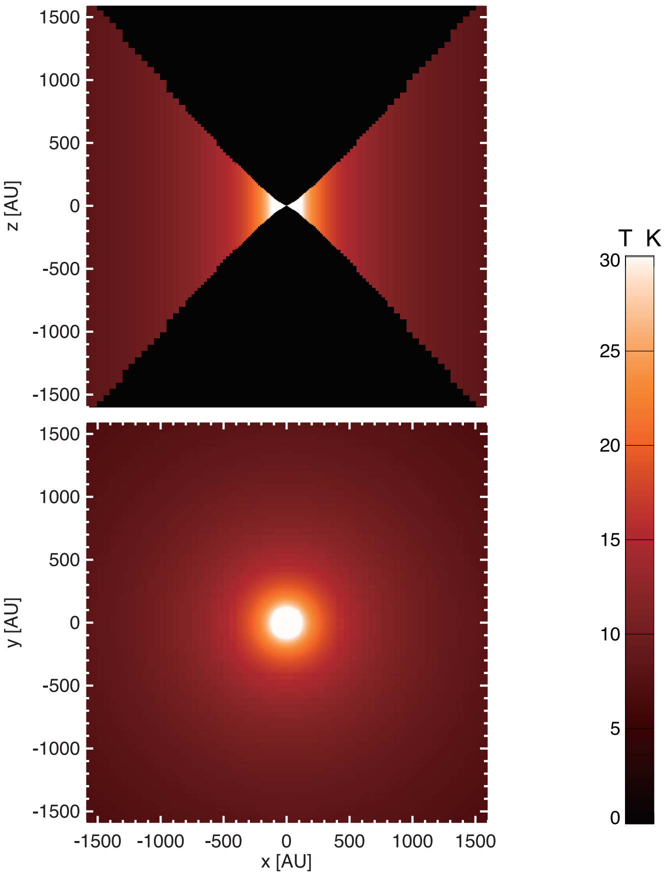

Figure C.14 The same temperature distribution as Figure C.12 based on fitting temperature of ^{12}CO (J=3–2) emission.

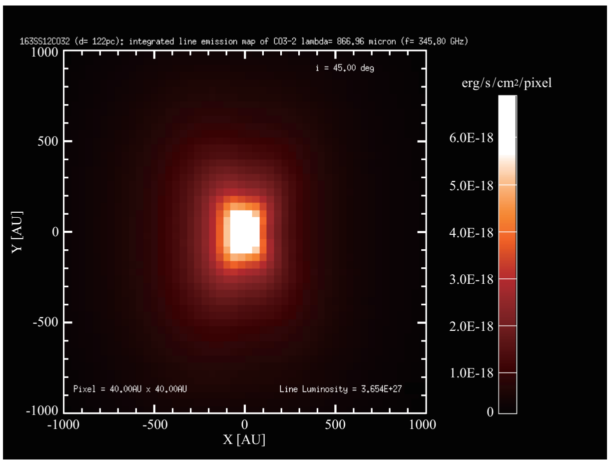

Figure C.15 ^{12}CO (J=3–2) intensity in two dimensional view. The disk orientation is the same as Figure C.13.

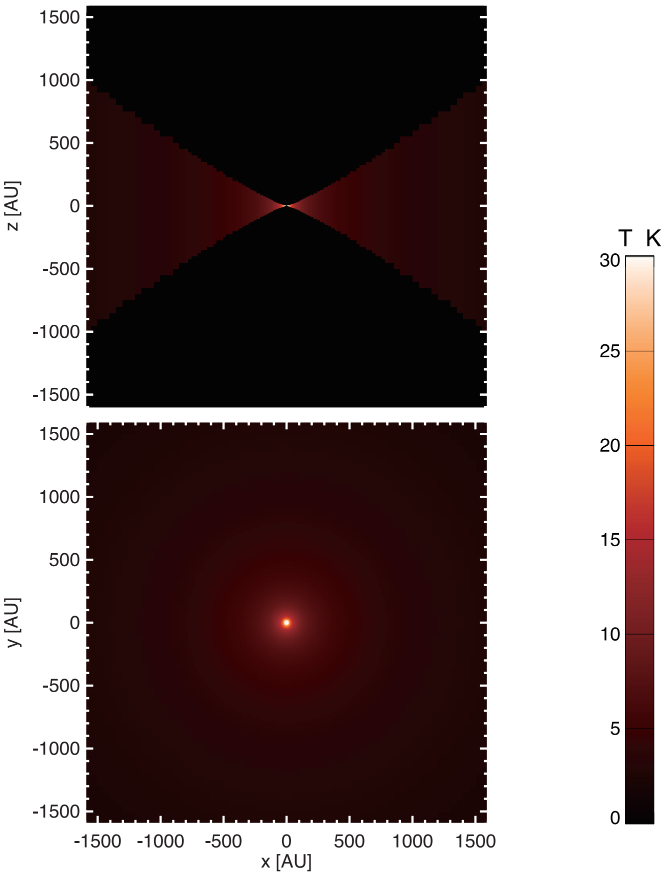

Figure C.16 The same temperature distribution as Figure C.16 based on fitting temperature of ^{13}CO (J=1–0) emission.

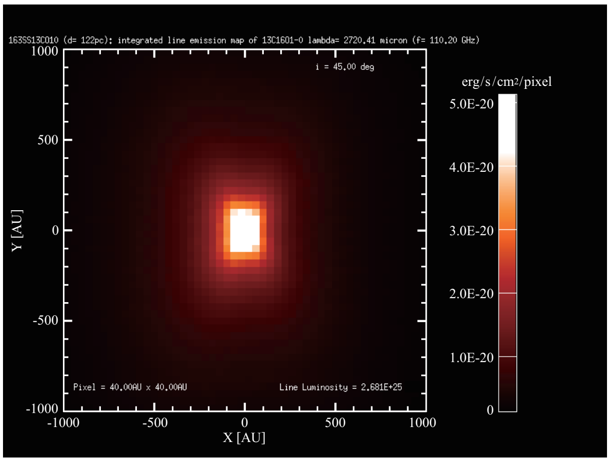

Figure C.17 ^{13}CO (J=1–0) intensity in two dimensional view. The disk orientation is the same as Figure C.13.

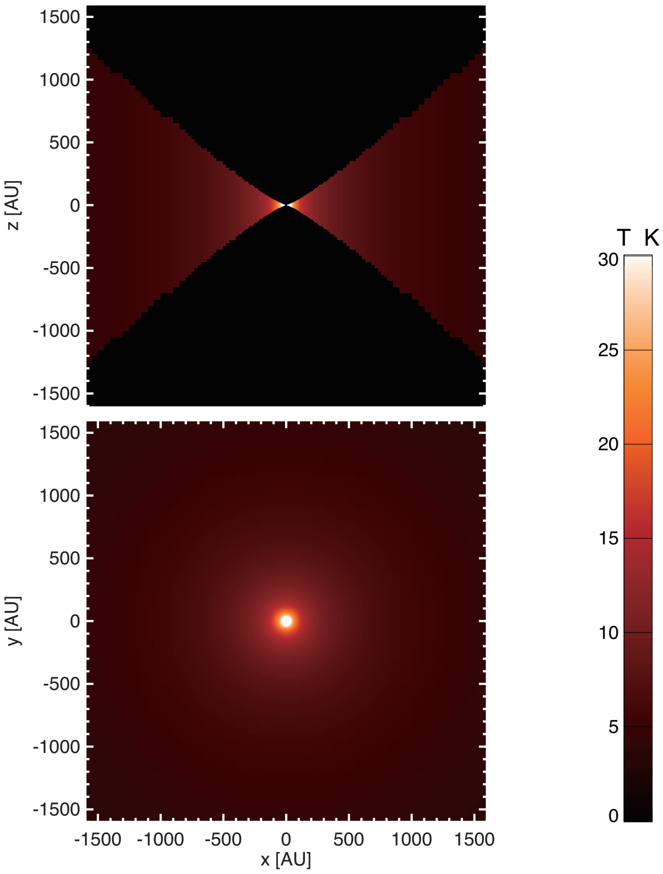

Figure C.18 The same temperature distribution as Figure C.16 based on fitting temperature of ^{13}CO (J=3–2) emission.

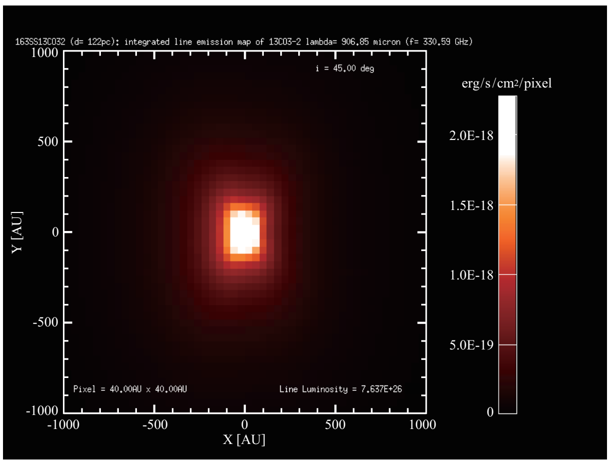

Figure C.19 ^{13}CO (J=3–2) intensity in two dimensional view. The disk orientation is the same as Figure C.13.

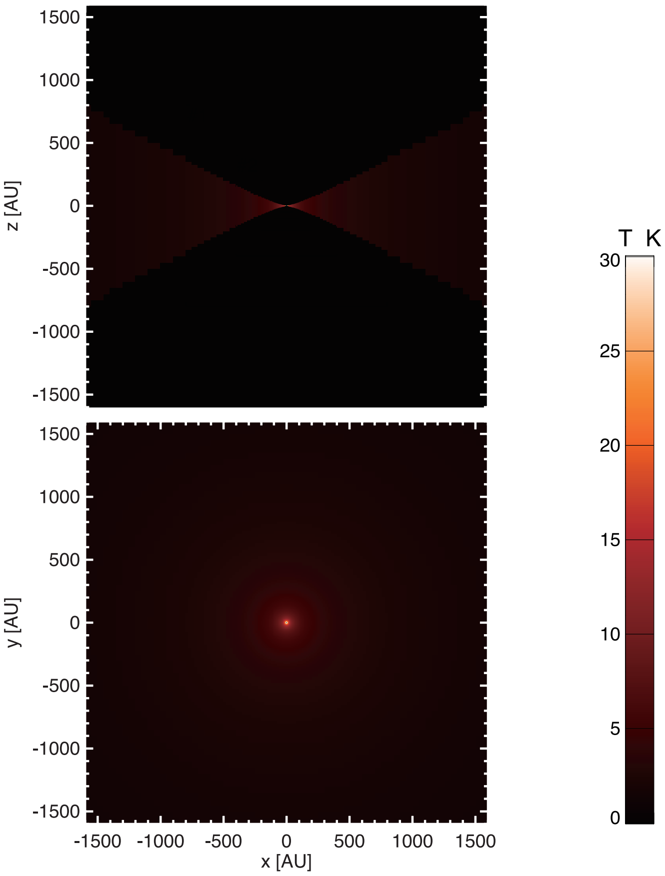

Figure C.20 The same temperature distribution as Figure C.16 based on fitting temperature of $C^{18}O$ (J=1–0) emission.

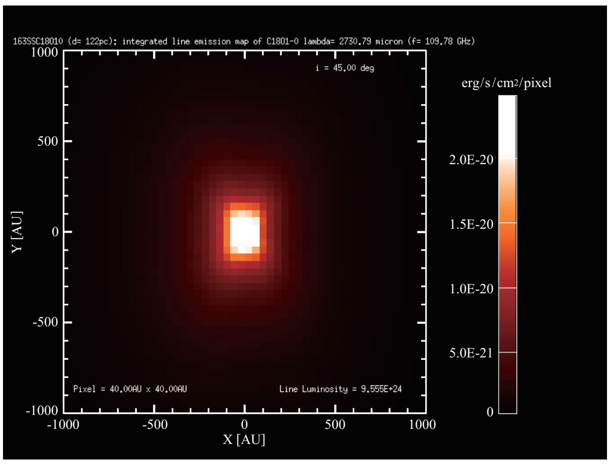

Figure C.21 $C^{18}O$ (J=1–0) intensity in two dimensional view. The disk orientation is the same as Figure C.13.

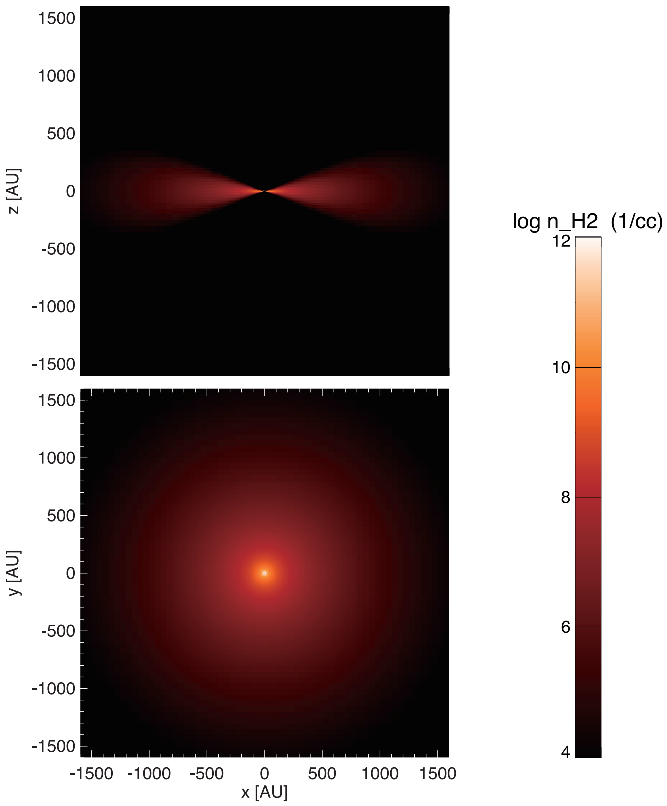

Figure C.22 The same figure as C.11 in similarity solution model.

3 2D View of the Protoplanetary Disk around HD 31648: Power Law Disk Model

In the case of $r = 500$ AU

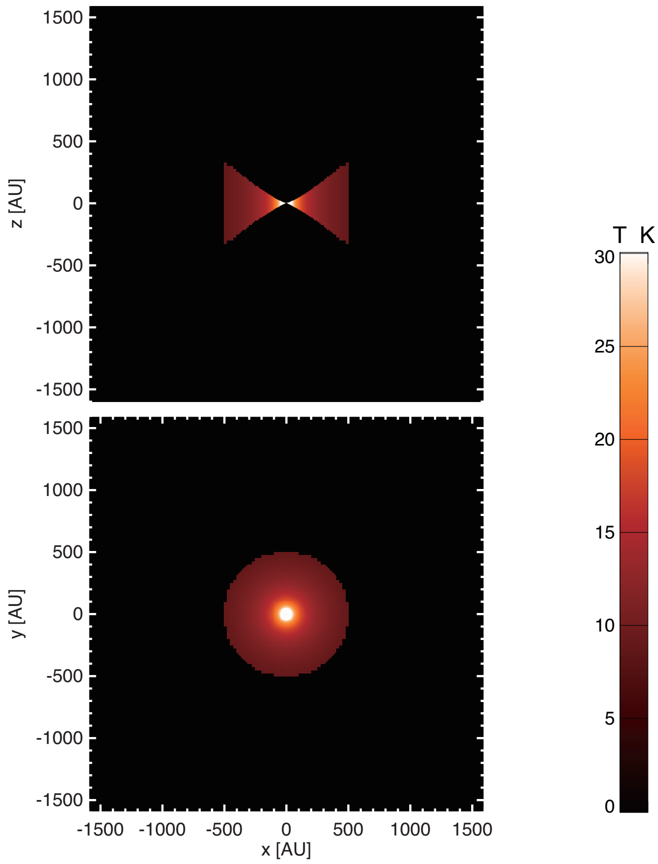

Figure C.23 Temperature distribution as a function of the disk radius in a two dimensional view. It is based on the result of fitting temperature of ^{12}CO (J=1–0) emission in power law model. (Top) Edge-on view of the disk is shown. (Bottom) Face-on view of the disk at $z = 0$ of the edge-on view is shown.

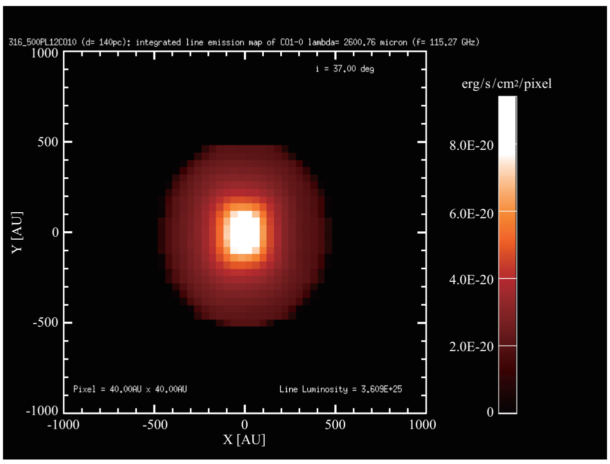

Figure C.24 ^{12}CO (J=1–0) intensity in two dimensional view. The rotational axis of the disk is horizontally oriented at an inclination angle with respect to the paper. Left side of the disk indicates near side and right side of the disk indicates far side.

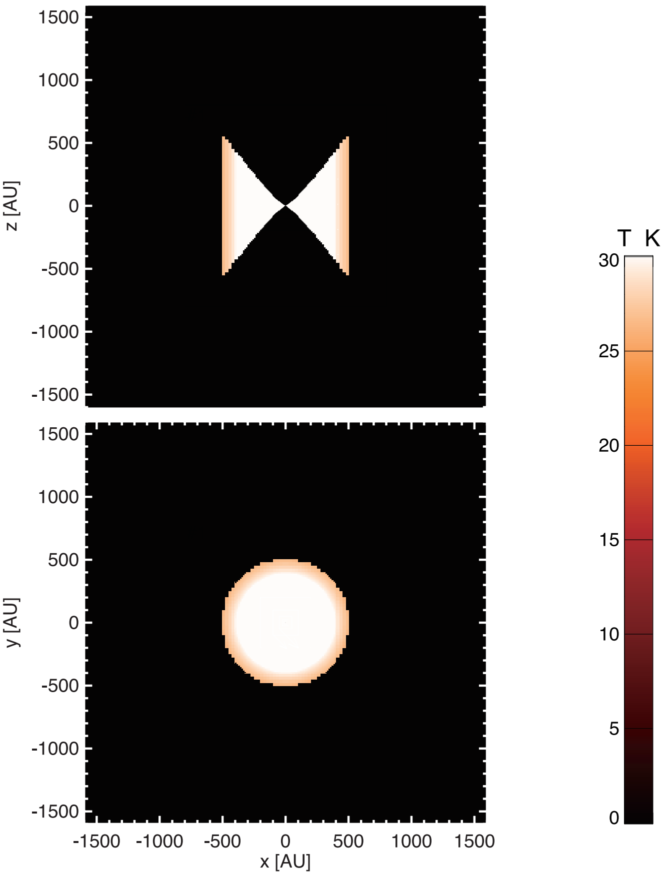

Figure C.25 The same temperature distribution as Figure C.23 based on fitting temperature of ^{12}CO (J=3–2) emission.

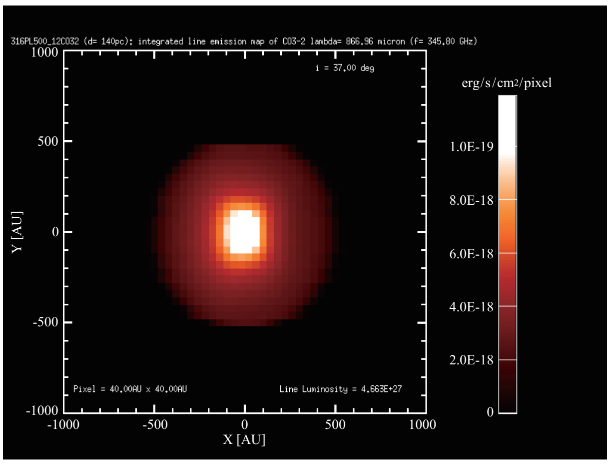

Figure C.26 ^{12}CO (J=3–2) intensity in two dimensional view. The disk orientation is the same as Figure C.24.

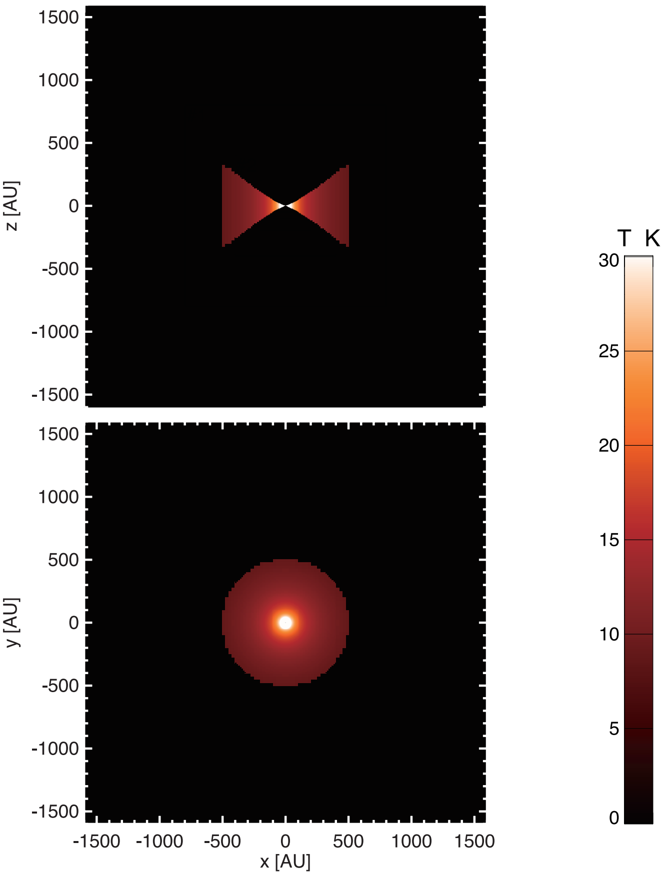

Figure C.27 The same temperature distribution as Figure C.23 based on fitting temperature of ^{13}CO (J=1–0) emission.

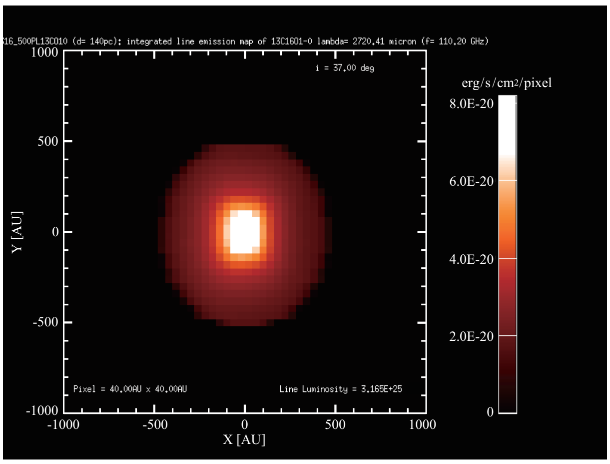

Figure C.28 ^{13}CO (J=1–0) intensity in two dimensional view. The disk orientation is the same as Figure C.24.

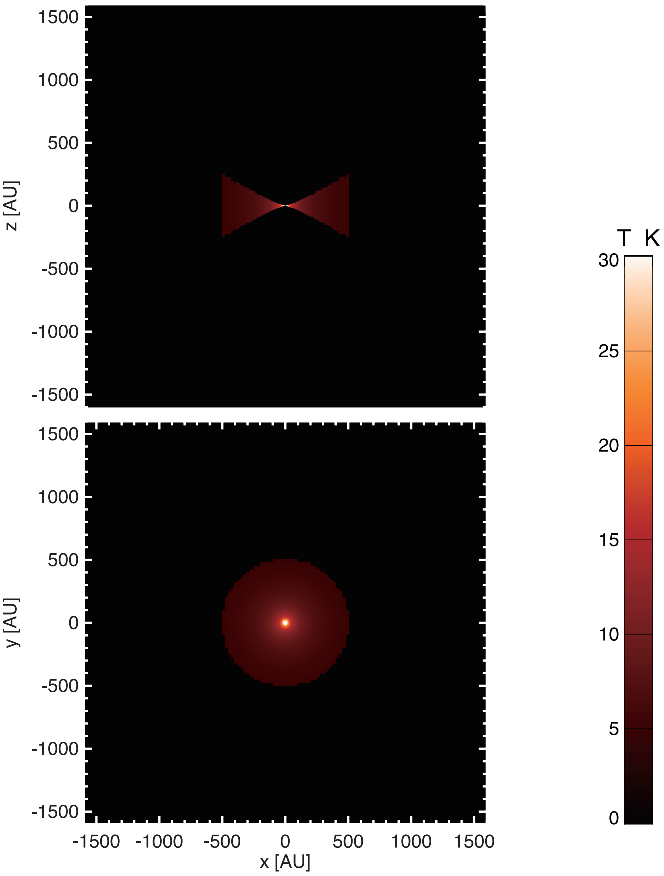

Figure C.29 The same temperature distribution as Figure C.23 based on fitting temperature of $C^{18}O$ (J=1–0) emission.

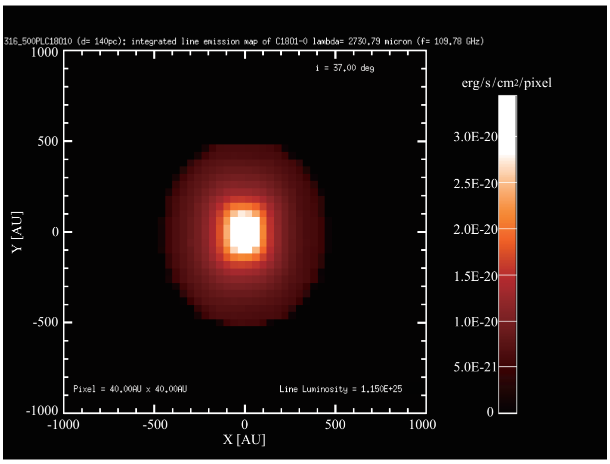

Figure C.30 $C^{18}O$ (J=1–0) intensity in two dimensional view. The disk orientation is the same as Figure C.24.

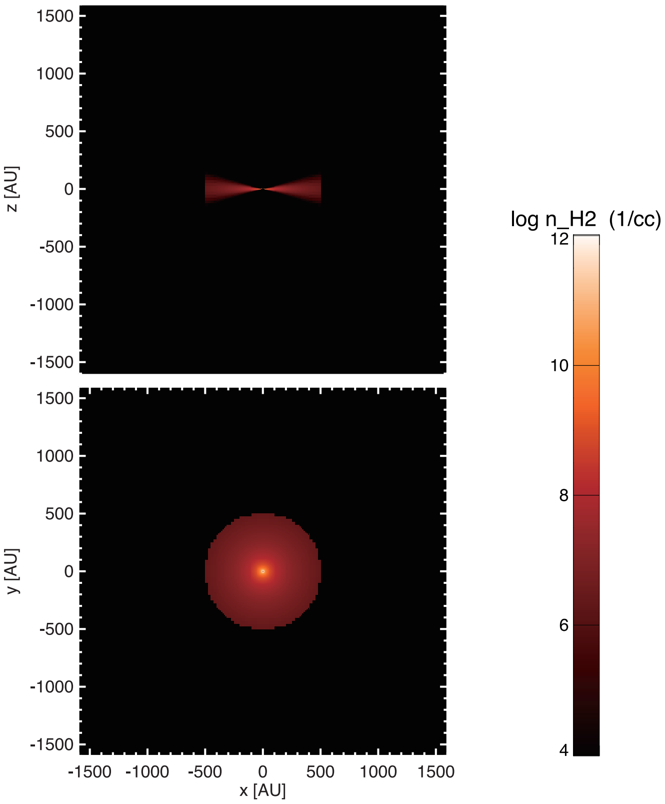

Figure C.31 The same Figure as C.11 in HD 31648.

In the case of r = 1000 AU

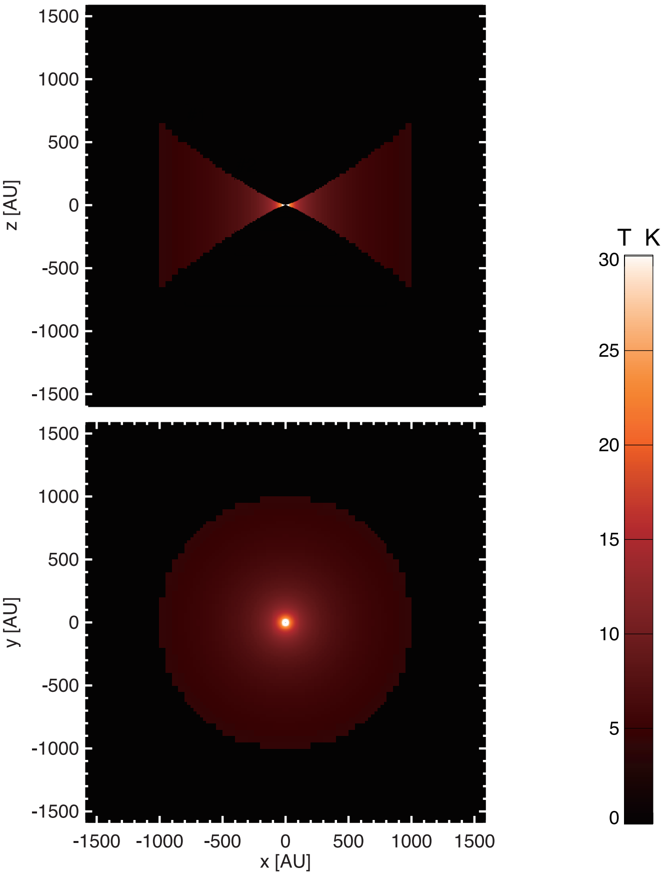

Figure C.32 Temperature distribution as a function of the disk radius in a two dimensional view. It is based on the result of fitting temperature of ^{12}CO (J=1–0) emission in power law model. (Top) Edge-on view of the disk is shown. (Bottom) Face-on view of the disk at z = 0 of the edge-on view is shown.

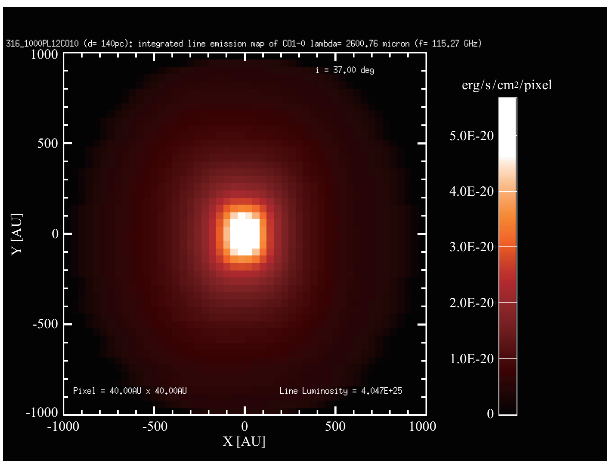

Figure C.33 ^{12}CO (J=1–0) intensity in two dimensional view. The rotational axis of the disk is horizontally oriented at an inclination angle with respect to the paper. Left side of the disk indicates near side and right side of the disk indicates far side.

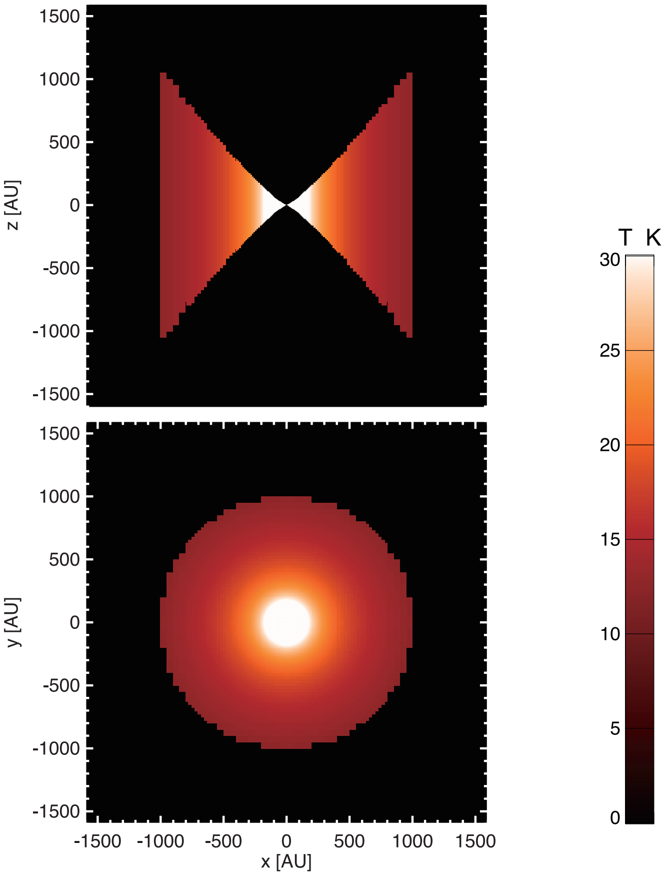

Figure C.34 The same temperature distribution as Figure C.32 based on fitting temperature of ^{12}CO (J=3–2) emission.

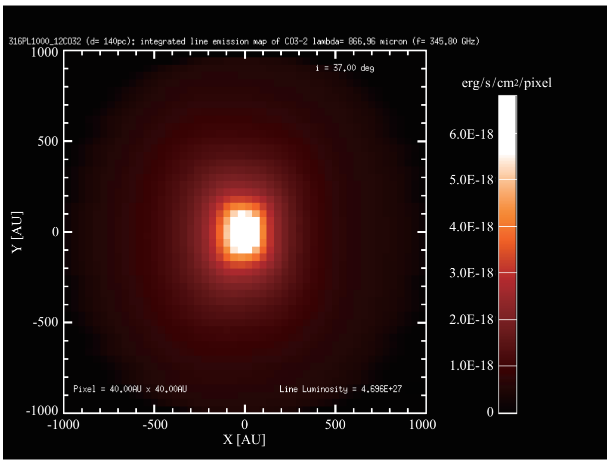

Figure C.35 ^{12}CO (J=3–2) intensity in two dimensional view. The disk orientation is the same as Figure C.33.

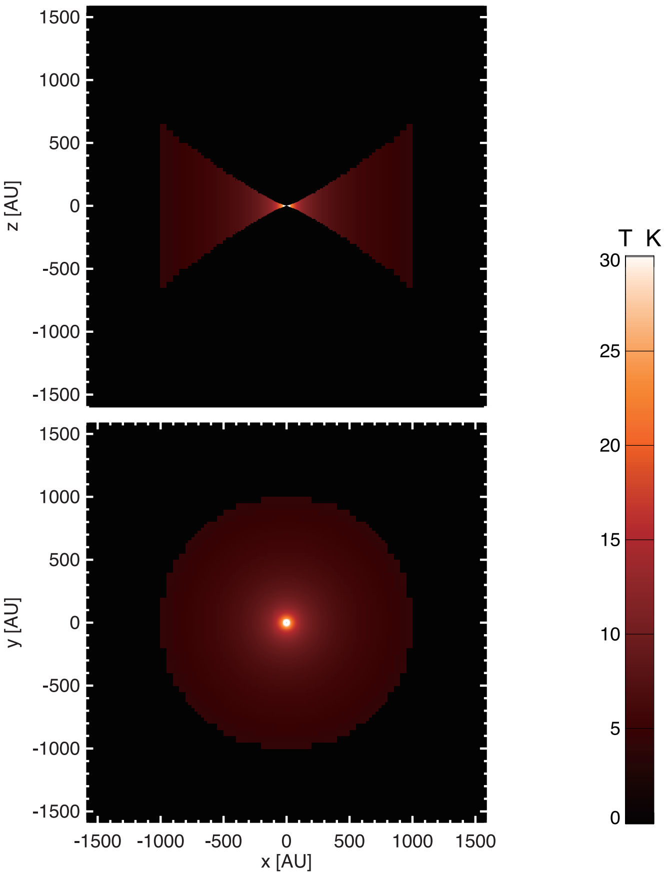

Figure C.36 The same temperature distribution as Figure C.32 based on fitting temperature of ^{13}CO (J=1–0) emission.

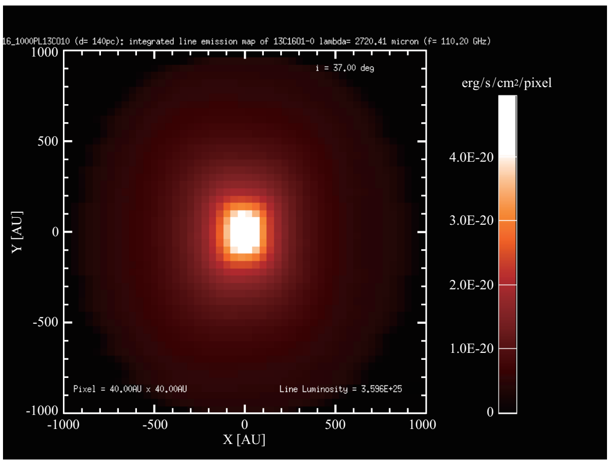

Figure C.37 ^{13}CO (J=1–0) intensity in two dimensional view. The disk orientation is the same as Figure C.33.

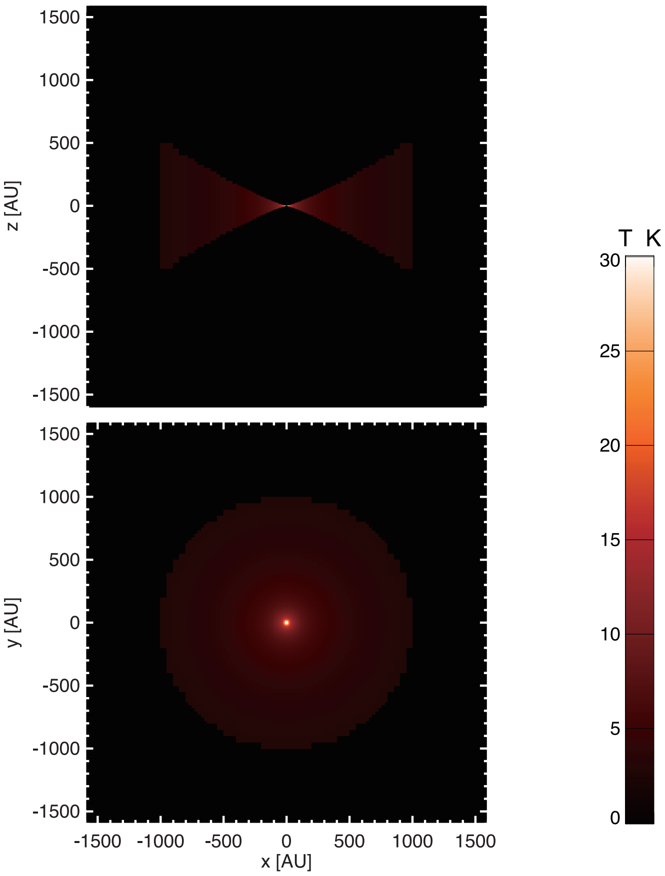

Figure C.38 The same temperature distribution as Figure C.32 based on fitting temperature of C^{18}O (J=1–0) emission.

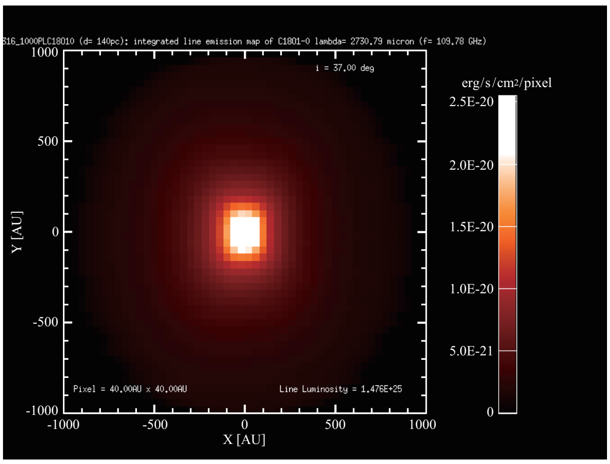

Figure C.39 C^{18}O (J=1–0) intensity in two dimensional view. The disk orientation is the same as Figure C.33.

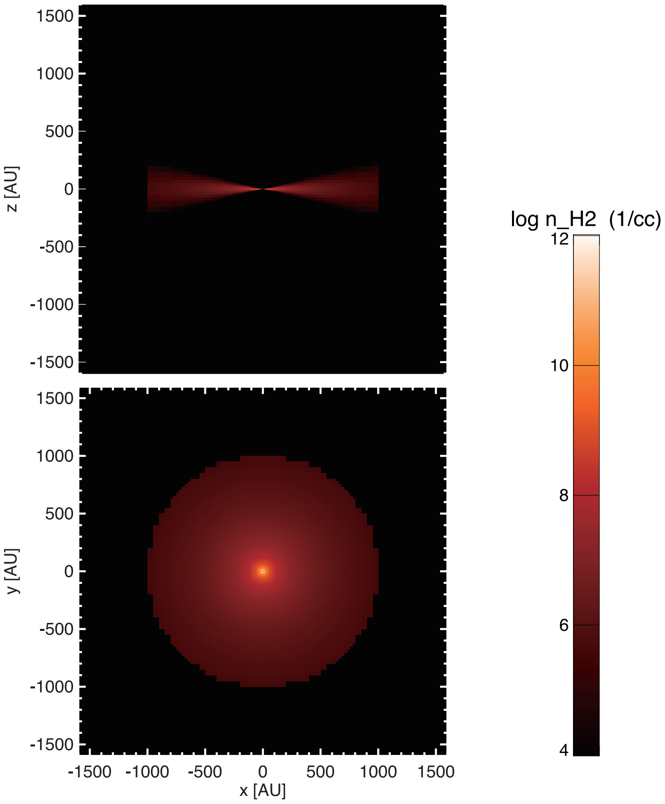

Figure C.40 The same figure as C.11 in HD 31648.

4 2D View of the Protoplanetary Disk around HD 31648: Similarity Solution Disk Model

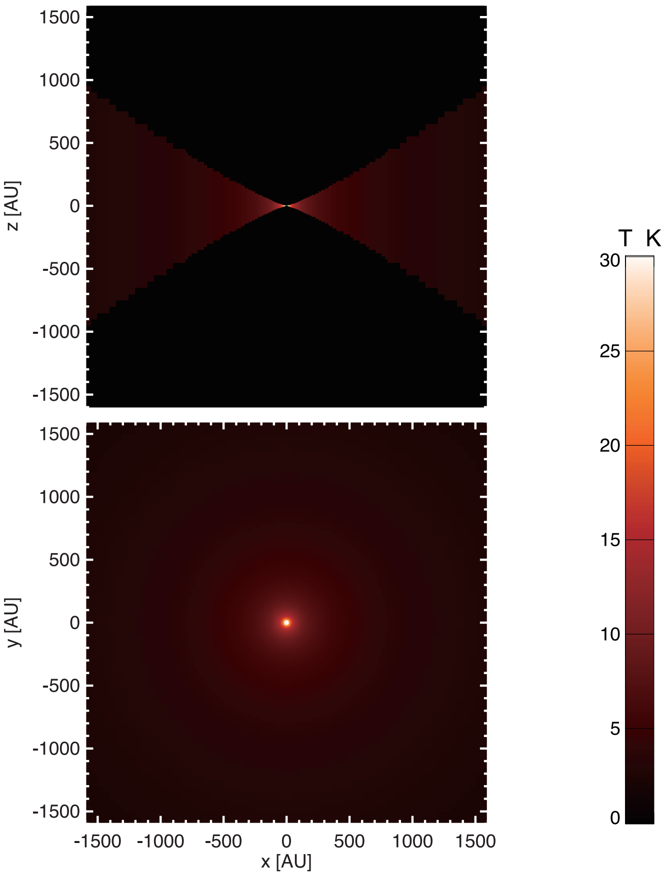

Figure C.41 Temperature distribution as a function of the disk radius in a two dimensional view. It is based on the result of fitting temperature of ^{12}CO (J=1–0) emission in similarity solution model. (Top) Edge-on view of the disk is shown. (Bottom) Face-on view of the disk at z = 0 of the edge-on view is shown.

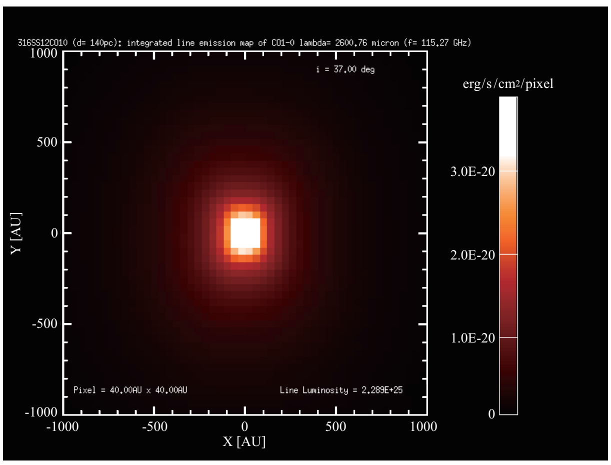

Figure C.42 ^{12}CO (J=1–0) intensity in two dimensional view. The rotational axis of the disk is horizontally oriented at an inclination angle with respect to the paper. Left side of the disk indicates near side and right side of the disk indicates far side.

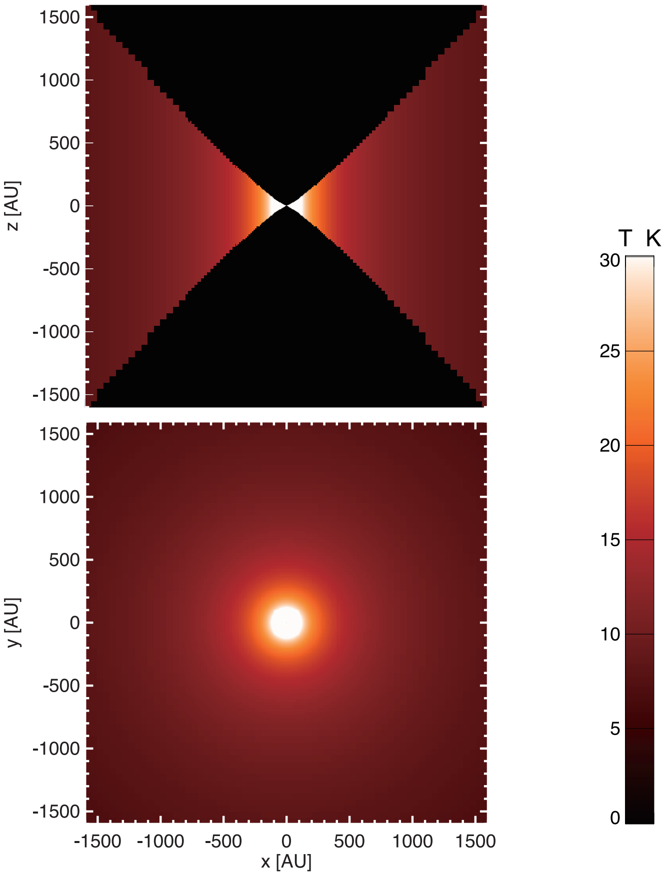

Figure C.43 The same temperature distribution as Figure C.41 based on fitting temperature of ^{12}CO (J=3–2) emission.

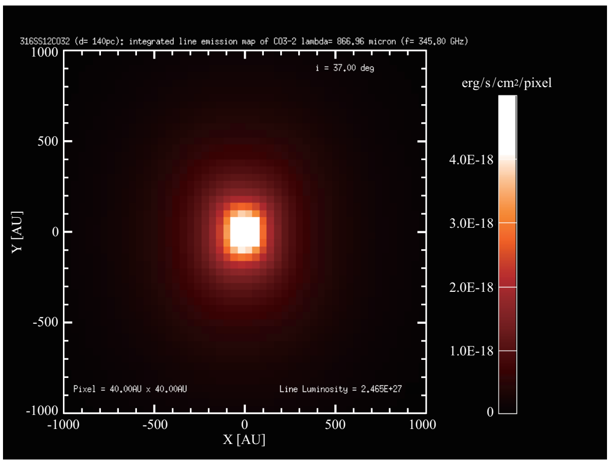

Figure C.44 ^{12}CO (J=3–2) intensity in two dimensional view. The disk orientation is the same as Figure C.42.

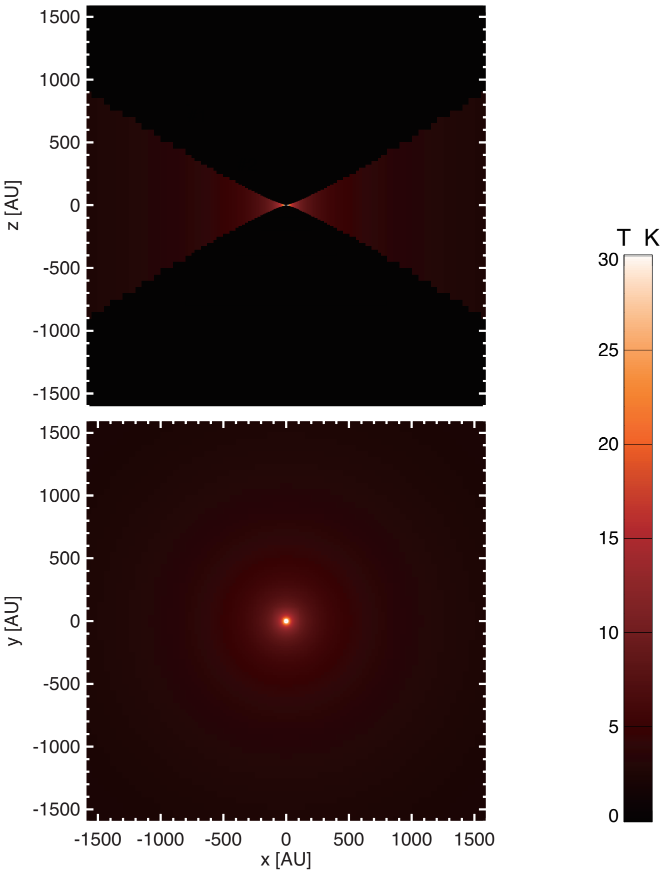

Figure C.45 The same temperature distribution as Figure C.41 based on fitting temperature of ^{13}CO (J=1–0) emission.

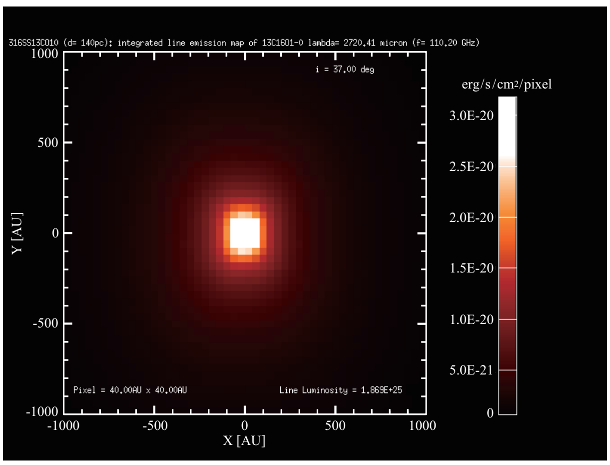

Figure C.46 ^{13}CO (J=1–0) intensity in two dimensional view. The disk orientation is the same as Figure C.42.

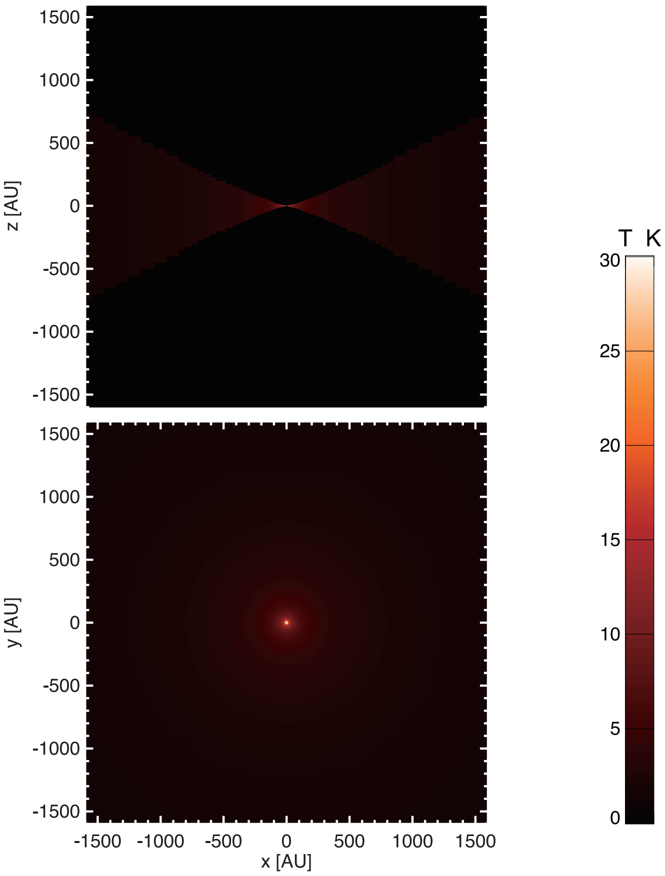

Figure C.47 The same temperature distribution as Figure C.41 based on fitting temperature of $C^{18}O$ (J=1–0) emission.

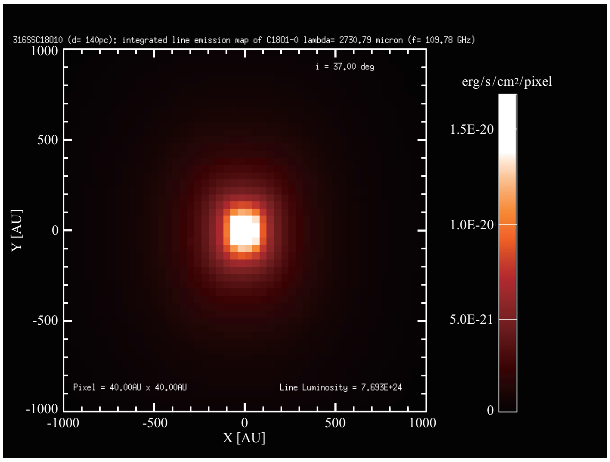

Figure C.48 $C^{13}O$ (J=1–0) intensity in two dimensional view. The disk orientation is the same as Figure C.42.

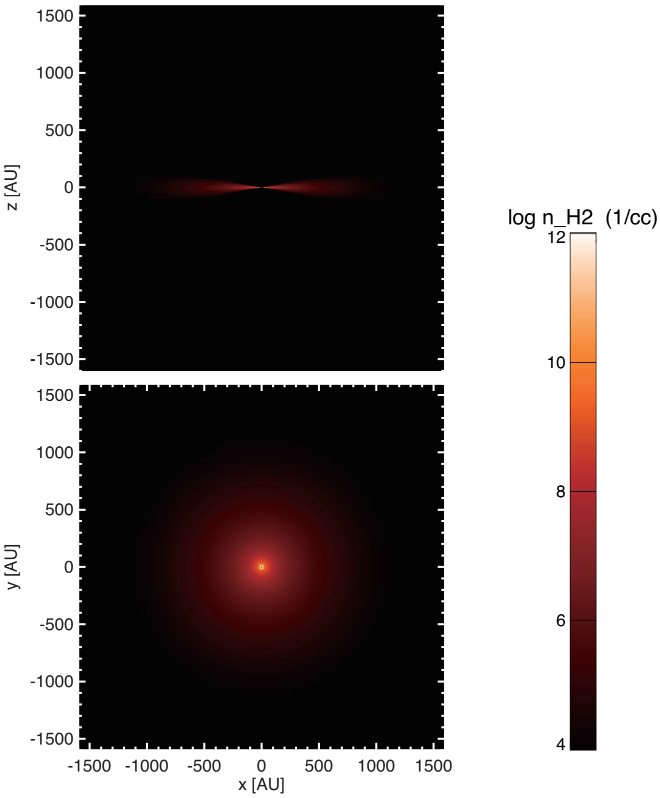

Figure C.49 The same figure as C.22 in HD 31648.

5 2D View of the Protoplanetary Disk around HD 169142: Power Law Disk Model

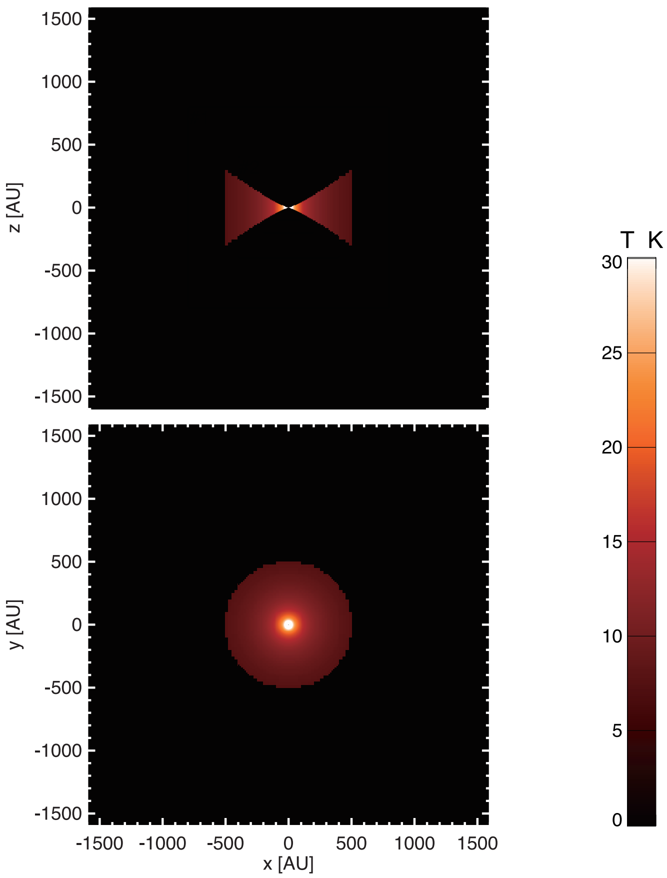

Figure C.50 Temperature distribution as a function of the disk radius in a two dimensional view. It is based on the result of fitting temperature of ^{12}CO (J=1–0) emission in power law model. (Top) Edge-on view of the disk is shown. (Bottom) Face-on view of the disk at $z = 0$ of the edge-on view is shown.

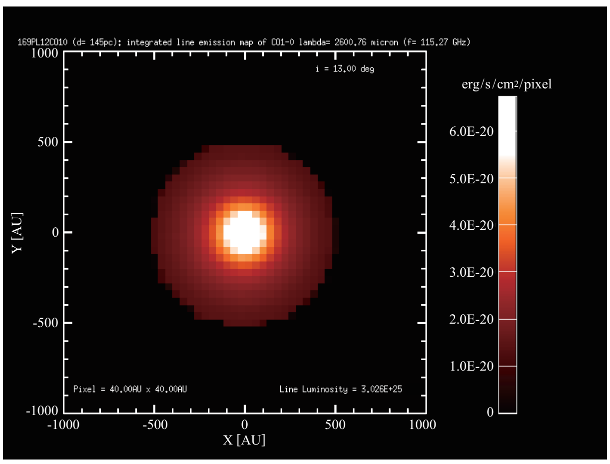

Figure C.51 ^{12}CO (J=1–0) intensity in two dimensional view. The rotational axis of the disk is horizontally oriented at an inclination angle with respect to the paper. Left side of the disk indicates near side and right side of the disk indicates far side.

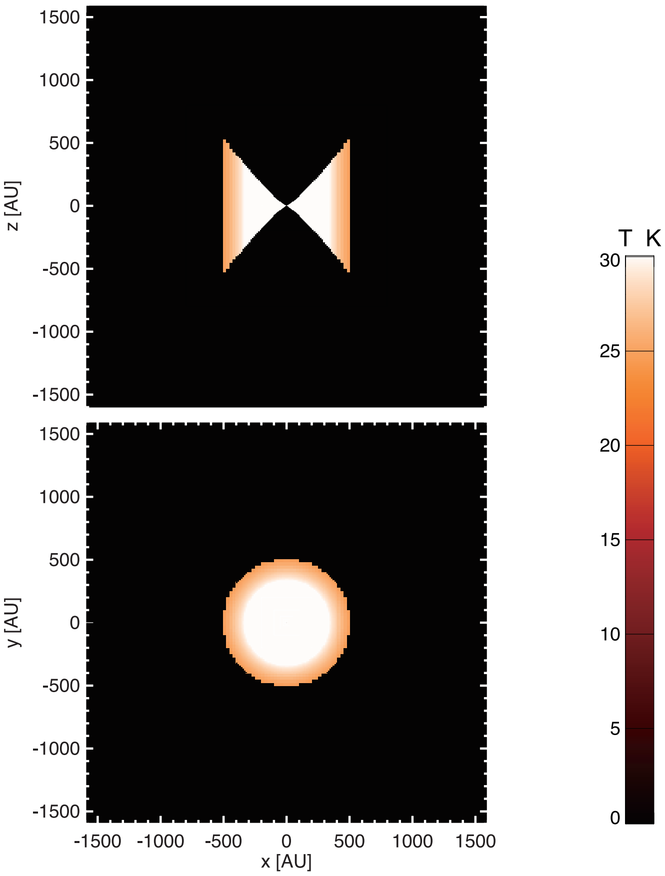

Figure C.52 The same temperature distribution as Figure C.50 based on fitting temperature of ^{12}CO (J=3–2) emission.

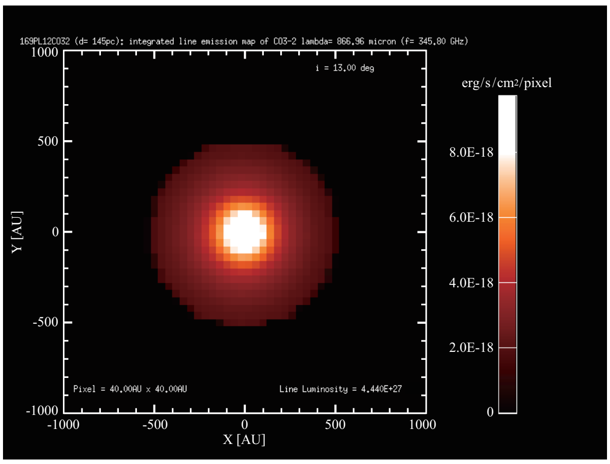

Figure C.53 ^{12}CO (J=3–2) intensity in two dimensional view. The disk orientation is the same as Figure C.51.

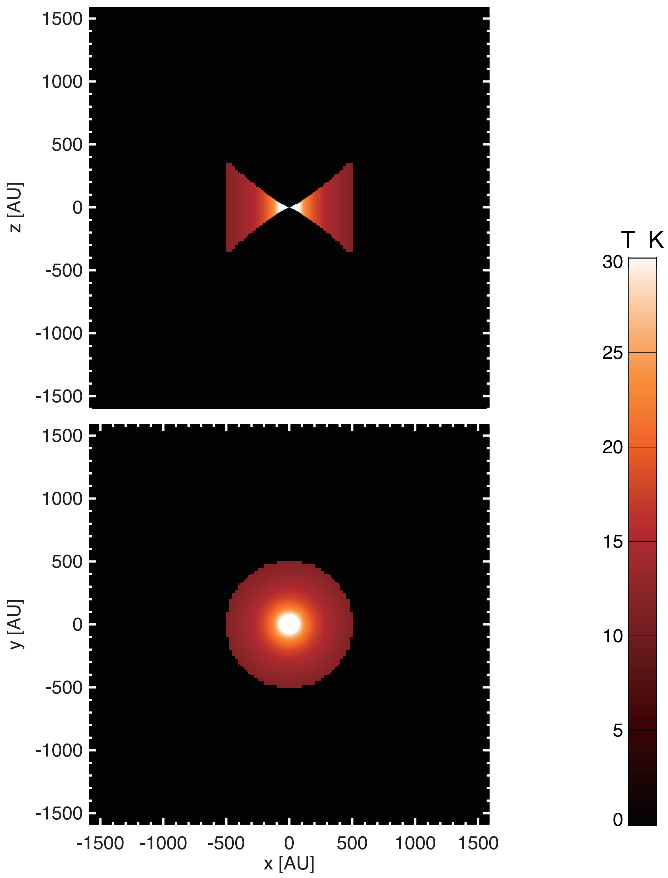

Figure C.54 The same temperature distribution as Figure C.50 based on fitting temperature of ^{13}CO (J=1–0) emission.

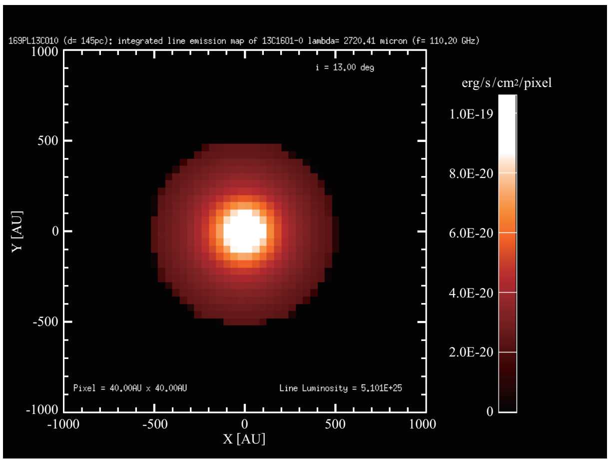

Figure C.55 ^{13}CO (J=1–0) intensity in two dimensional view. The disk orientation is the same as Figure C.51.

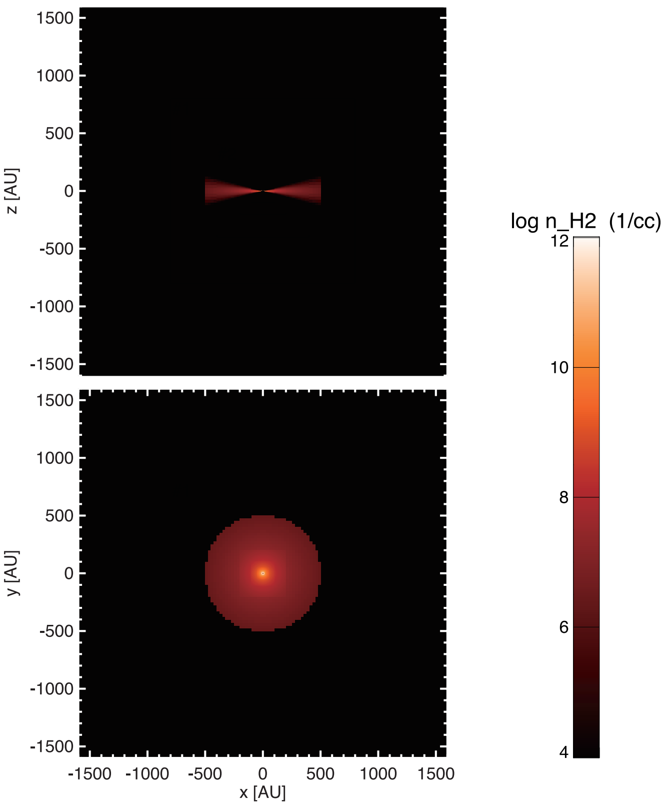

Figure C.56 The same figure as C.11 in HD 169142.

6 2D View of the Protoplanetary Disk around HD 169142: Similarity Solution Disk Model

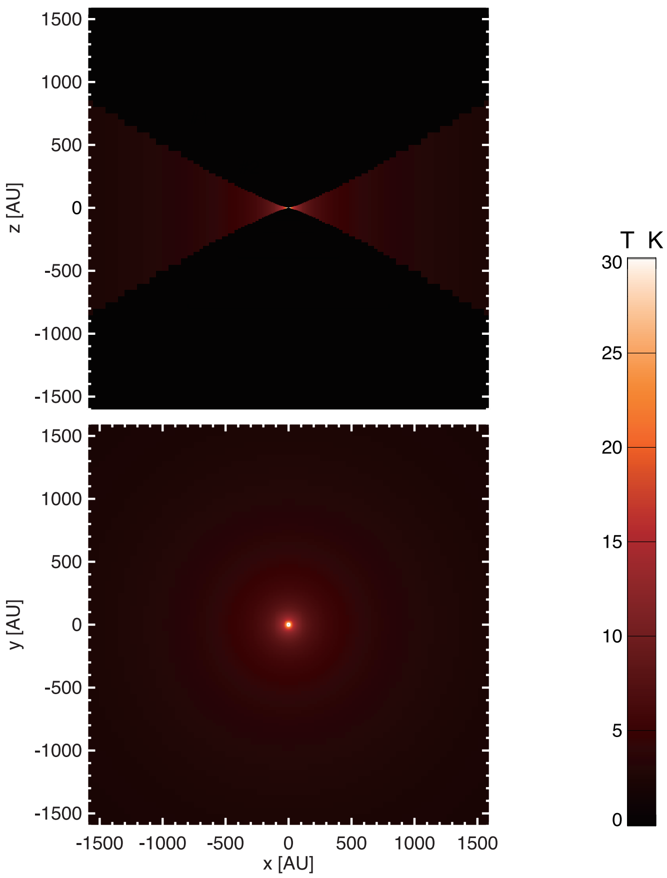

Figure C.57 Temperature distribution as a function of the disk radius in a two dimensional view. It is based on the result of fitting temperature of ^{12}CO (J=1–0) emission in similarity solution model. (Top) Edge-on view of the disk is shown. (Bottom) Face-on view of the disk at $z = 0$ of the edge-on view is shown.

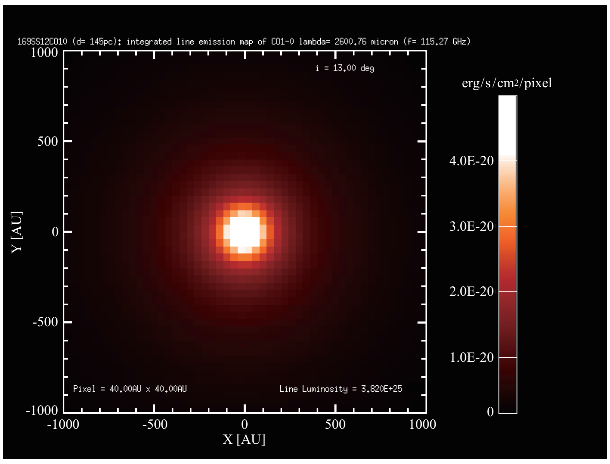

Figure C.58 ^{12}CO (J=1–0) intensity in two dimensional view. The rotational axis of the disk is horizontally oriented at an inclination angle with respect to the paper. Left side of the disk indicates near side and right side of the disk indicates far side.

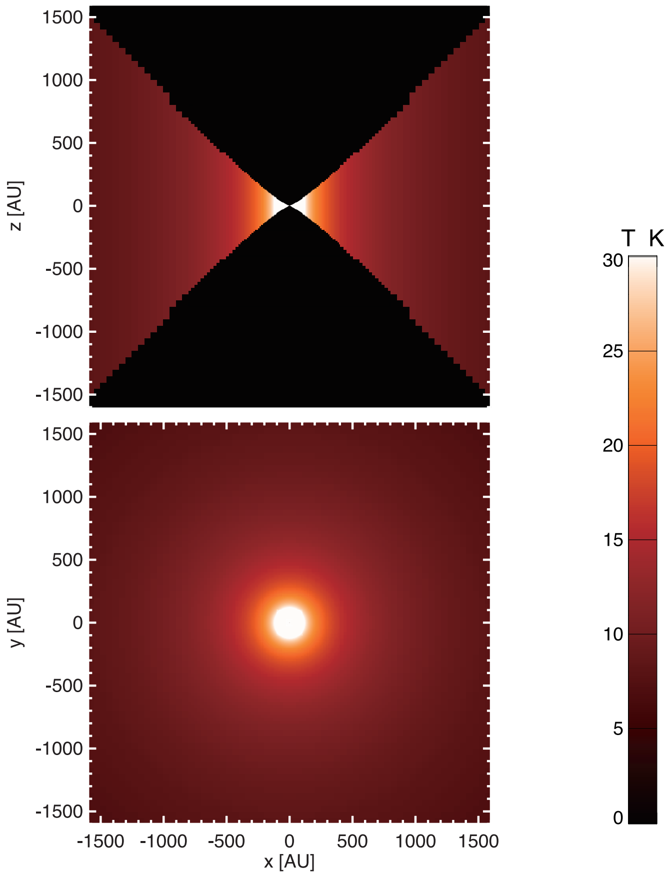

Figure C.59 The same temperature distribution as Figure C.57 based on fitting temperature of ^{12}CO (J=3–2) emission.

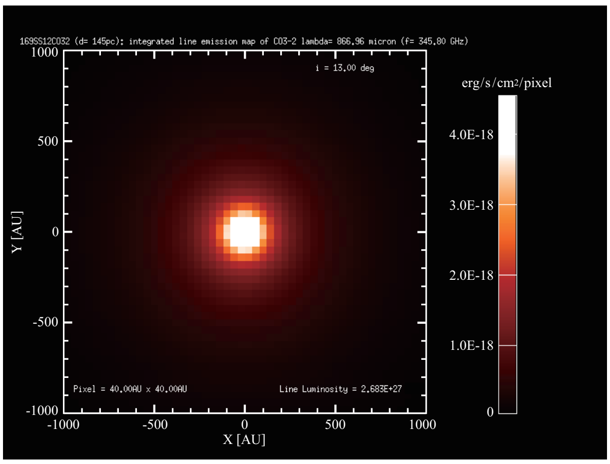

Figure C.60 ^{12}CO (J=3–2) intensity in two dimensional view. The disk orientation is the same as Figure C.58.

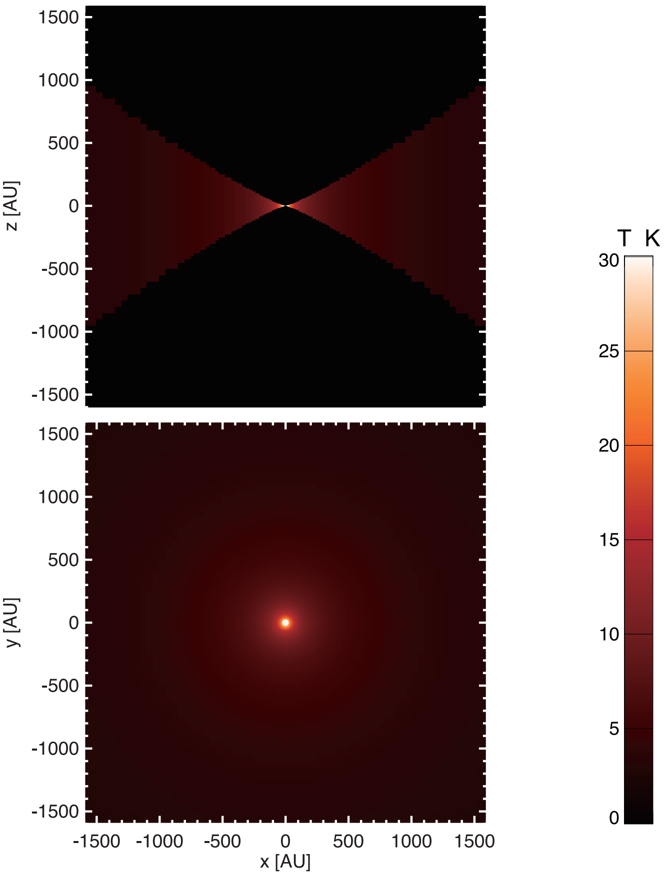

Figure C.61 The same temperature distribution as Figure C.61 based on fitting temperature of ^{13}CO (J=1–0) emission.

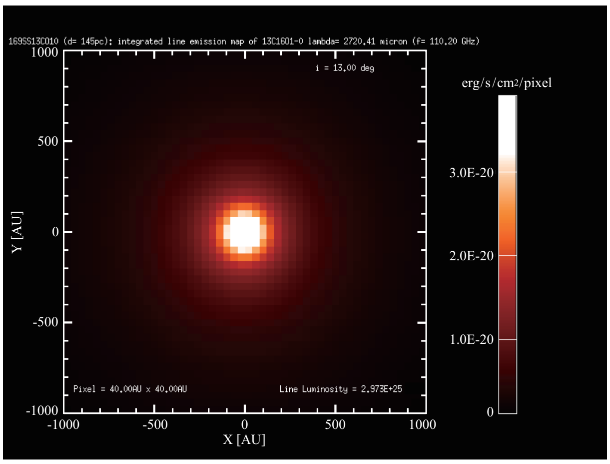

Figure C.62 ^{13}CO (J=1–0) intensity in two dimensional view. The disk orientation is the same as Figure C.62.

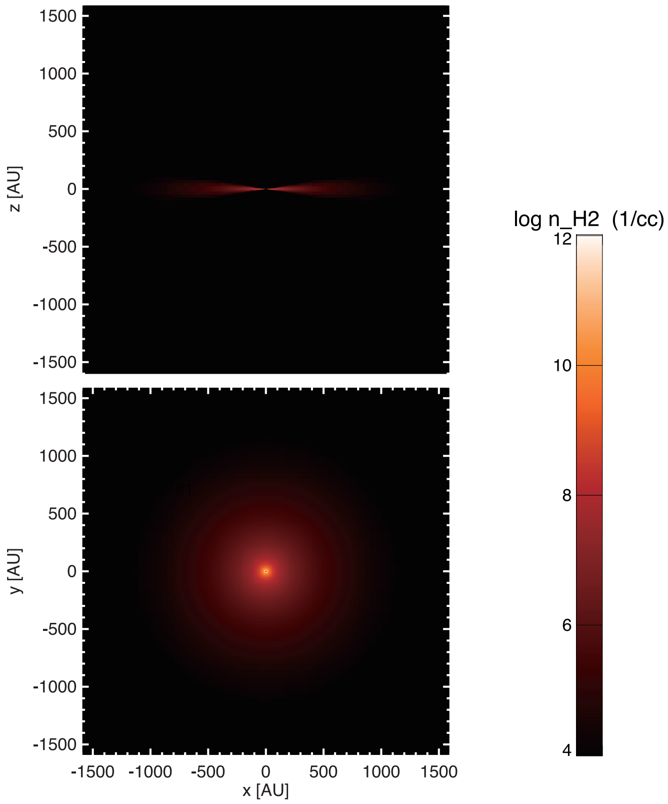

Figure C.63 The same figure as C.22 in HD 169142.

References

Acke, B. & van den Ancker, M. E. 2004, A&A, 426, 151

Adams, F. C., Emerson, J. P., & Fuller, G. A. 1990, ApJ, 357, 606

Akiyama, E., Momose, M., Hayashi, H., & Kitamura, Y. 2011, PASJ, 63, 1059

André, P., Ward-Thompson, D., & Barsony, M. 1993, ApJ, 406, 122

André, P. 1994, The Cold Universe, 179

Appenzeller, I. 1994, ASPC, 62, 12

Armitage, P. J. 2010, Astrophysics of Planet Formation, Cambridge University Press

Balbus, S. A., & Hawley, J. F. 1991, ApJ, 376, 214

Barrado y Navascués, D., Stauffer, J. R., Song, I., & Caillault, J. -P. 1993, ApJ, 520, 123

Beckwith, S. V. W., Sargent, A. I., Chini, R. S., & Güesten, R. 1990, AJ, 99, 924

Beckwith, S. V. W. & Sargent, A. I. 1993, ApJ, 402, 280

Böhm, T. & Catala, C. 1995, A&A, 155, 169

Böhm, T., Catala, C., Donati, J. -F., Welty, A., Baudrand, J., Butler, C. J., Carter, B., Collier-Cameron, A., Czarny, J., Foing, B., Ghosh, K., Hao, J., Houdebine, E., Huang, L., Jiang, S., Neff, J. E., Rees, D., Semel, M., Simon, T., Talavera, A., Zhai, D., & Zhao, F. 1996, A&AS, 120, 431

Brooke, T. Y., Tokunaga, A. T., & Strom, S. E. 1993, AJ, 106, 656

Bruhweiler, F. C., Freire Ferrero, R., Bourdin M. O., & Gull, T. R. 2010, ApJ, 719, 1872

Cabot, W., Canuto, V. M., Hubickyj, O. 1987, Icarus, 69, 423

Calvet, N., D'Alessio, P., Hartmann, L., Wilner, D., Walsh, A., & Sitko, M. 2002, ApJ, 568, 1008

Calvet, N., Muzerolle, J., Briceño, C., Hernández, J., Hartmann, L., Saucedo, J. L., & Gordon, K. D. 2004, AJ, 128, 1294

Calvet, N., D'Alessio, P., Watson, D. M., Franco-Hernández, R., Furlan, E., Green, J., Sutter, P. M., Forrest, W. J., Hartmann, L., Uchida, K. I., Keller, L. D., Sargent, B., Najita, J., Herter, T. L., Barry, D. J., & Hall, P. 2005, ApJ, 630, L185

Cantó, J., Rodríguez, L. F., Calvet, N., & Levreault, R. M. 1984, ApJ, 282, 631

Caselli, P., Benson, P. J., Myers, P. C., & Tafalla, M. 2002, ApJ, 572, 238

Chiang, E. I. & Goldreich, P. 1997, ApJ, 490, 368

Chiang, E. I., Joung, M. K., Creech-Eakman, M. J., Qi, C., Kessler, J. E., Blake, G. A., & van Dishoeck, E. F. 2001, ApJ, 547, 1077

Crifo, F., Vidal-Madjar, A., Lallement, R., Ferlet, R., & Gerbaldi, M. 1997, A&A, 320, 29

D'Alessio, P., Calvet, N., Hartmann, L., Lizano, S., & Cantó, J. 1999, ApJ, 527, 893

D'Alessio, P., Hartmann, L., Calvet, N., Franco-Hernández, R., Forrest, W. J., Sargent, B., Furlan, E., Uchida, K., Green, J. D., Watson, D. M., Chen, C. H., Kemper, F., Sloan, G. C., & Najita, J. 2005, ApJ, 621, 461

D'Alessio, P., Merín, B., Calvet, N., Hartmann, L., & Montesinos, B. 2005, Rev. Mex. Astron. Astrofis., 41, 61

D'Antona, F. & Mazzitelli, B. 1994, ApJS, 90, 476

Dartois, E., Dutrey, A., & Guilloteau, S. 2003, A&A, 399, 773

Davies, J. K., Evans, A., Bode, M. F., & Whittet, D. C. B. 1990, MNRAS, 274, 517

Dent, W. R. F,, Greaves, J. S., & Coulson, I. M. 2005, MNRAS, 359, 663

Dent, W. R. F., Torrelles, J. M., Osorio, M., Calvet, N., & Anglada, G. 2006, MNRAS, 365, 1283

Devine, D., Grady, C. A., Kimble, R. A, Woodgate, B., Bruhweiler, F. C., Boggess, A., Linsky, J. L., & Clampin, M. 2000, ApJ, 542, L115

Dobashi, K., Uehara, H., Kandori, R., Sakurai, T., Kaiden, M., Umemoto, T., & Sato, F. 2005, PASJ, 57, 1

Dominik, C., Dullemond, C. P., Waters, L. B. F. M., & Walch, S. 2003, A&A, 398, 607

Dullemond, C. P., Dominik, C., & Natta, A. 2001, ApJ, 560, 957

Dullemond, C. P. 2002, A&A, 395, 853

Dullemond, C. P., & Dominik, C. 2004, A&A, 417, 159

Edwards, S., Ray, T. P., & Mundt, R. 1993, in Protostars & planets II, ed. E. H. Levy & J. I. Lunine Tucson: (THE UNIVERSITY OF ARIZONA PRESS) 567

Espaillat, C., Calvet, N., D'Alessio, P., Bergin, E., Hartmann, L., Watson, D., Furlan, E., Najita, J., Forrest, W., McClure, M., Sargent, B., Bohac, C., & Harrold, S. T. 2007, ApJ, 664, L111

Espaillat, C., Calvet, N., D'Alessio, P., Hernández, J., Qi, C., Hartmann, L., Furlan, E., & Watson, D. M. 2007, ApJ, 670, L135

Ezawa, H., Kawabe, R., Kohno, K., & Yamamoto, S. 2004, Proc. SPIE, 5489, 763

Frerking, M. A., Langer, W. D., & Wilson, R. W. 1982, ApJ, 262, 590

Fuente, A., Martín-Pintado, J., Rodríguez-Franco, A., & Moriarty-Schieven, G. D. 1998, A&A, 339, 575

Fukagawa, M., Hayashi, M., Tamura, M., Itoh, Y., Hayashi, S. S., Oasa, Y., Takeuchi, T., Morino, J., Murakawa, K., Oya, S., Yamashita, T., Suto, H., Mayama, S., Naoi, T., Ishii, M., Pyo, T., Nishikawa, T., Takato, N., Usuda, T., Ando, H., Iye, M., Miyama, S. M., & Kaifu, N. 2004, ApJ, 605, L53

Fukagawa, M., Tamura, M., Itoh, Y., Kudo, Y., Imaeda, Y., Oasa, Y., Hayashi, S. S., & Hayashi, M. 2006, ApJ, 636, L153

Gammie, C. F. 1996, ApJ, 457, 355

Gammie, C. F. 2001, ApJ, 553, 174

Garcia Lopez, R., Natta, A., Testi, L., & Habart, E. 2006, A&A, 459, 837

Goodmann, A. A., Benson, P. J., Fuller, G. A., & Myers, P. C. 1993, ApJ, 406, 528

Grady, C. A., Devine, D., Woodgate, B., Kimble, R., Bruhweiler, F. C., Boggess, A., Linsky, J. L., Plait, P., Clampin, M., & Kalas, P. 2000, A&A, 544, 895

Grady, C. A., Schneider, G., Hamaguchi, K., Sitko, M. L., Carpenter, W. J., Hines, D., Collins, K. A., Williger, G. M., Woodgate, B. E., Henning, Th., Ménard, F., Wilner, D., Petre, R., Palunas, P., Quirrenbach, A., Nuth, J. A. III, Silverstone, M. D., & Kim, J. S. 2007, ApJ, 665, 1391

Grady, C. A., Hamaguchi, K., Schneider, G., Stecklum, B., Woodgate, B. E., McCleary, J. E., Williger, G. M., Sitko, M. L., Menard, F., Henning, Th., Brittain, S., Troutmann, M., Donehew, B., Hines, D., Wisniewski, J. P., Lynch, D. K., Russell, R. W., Rudy, R. J., Day, A. N., Shenoy, A., Wilner, D., Silverstone, M., Bouret, J.-C., Meusinger, H., Clampin, M., Kim, S., Petre, R., Sahu, M., Endres, M., & Collins, K. A. 2010, ApJ, 719, 1565

Hartmann, L., Calvet, N., Gullbring, E., & D'Alessio, P. 1998, ApJ, 495, 385

Hayashi, C. 1981, Prog. Theor. Phys. Suppl., vol. 70, 35

Hayashi, C., Nakazawa, K., & Nakagawa, Y. 1985, in Protostars & planets II, ed. D. C. Black & M. S. Matthews Tucson: (THE UNIVERSITY OF ARIZONA PRESS) 1100

Hensberge, H., Pavlovski, K., & Verschueren, W. 2000, ESASP, 445, 395

Herbig, G. H. 1960, ApJS, 4, 337

Hillenbrand, L. A., Strom, S. E., Vrba, F. J., & Keene, J. 1992, ApJ, 397, 613

Hillenbrand, L. A. 1997, AJ, 113, 1733

Hughes, A. M., Wilner, D. J., Andrews, S. M., Qi, C., & Hogerheijde, M. R. 2011, ApJ, 727, 85

Hughes, A. M., Wilner, D. J., Qi, C., & Hogerheijde, M. R. 2008, ApJ, 678, 1119

Inoue, A., Oka, A., & Nakamoto, T. 2009, MNRAS, 393, 1377

Isella, A., Testi, L., Natta, A., Neri, R., Wilner, D., & Qi, C. 2007, A&A, 469, 213

Ishitsu, N. & Sekiya, M. 2003, Icarus, 165, 181

Kenyon, S. J. & Hartmann, L. 1987, ApJ, 323, 714

Kitamura, Y., Omodaka, T., Kawabe, R., Yamashita, T., & Handa, T. 1993, PASJ, 45, L27

Kitamura, Y., Momose, M., Yokogawa, S., Kawabe, R., Tamura, M., & Ida, S. 2002, ApJ, 581, 357

Kuhn, J. R., Potter, D., & Parise, B. 2001, ApJ, 553, L189

Kokubo, E., & Ida, S. 2002, ApJ, 581, 666

Koerner, D. W. 1997, ApJ, IAUS, 170, 162

Kutner, M. L., & Ulich, B. L. 1981, ApJ, 250, 341

Lada, C. 1988, IAUS, 115, 1L

Lada, C. J., Alves, J., & Lada, E. A. 1996, AJ, 111, 1964

Lagrange, A. -M., Bonnefoy, M., Chauvin, G., Apai, D., Ehrenreich, D., Boccaletti, A., Gratadour, D., Rouan, D., Mouillet, D., Lacour, S., & Kasper, M. 2010, Science, 329, 57

Lin, D. N. C, & Papaloizou, J. 1980, MNRAS, 191, 37

Lynden-Bell, D., & Pringle, J. E. 1974, MNRAS, 168, 603

Mann, I., Nakamura, A. M., & Mukai, T. 2009, Small Bodies in Planetary Science, Springer

Mannings, V., Koerner, D. W. & Sargent, A. I. 1997, Nature, 388, 555

Mannings, V. & Sargent, A. I. 1997, ApJ, 490, 792

Mayor, M. & Queloz, D. 1995, Nature, 378, 355

McCaughrean, M. J. & O'dell, C. R. 1996, AJ, 111, 1977

Meeus, G., Waelkens, C., & Malfait, K. 1998, A&A, 329, 131

Meeus, G., Waters, L.B.F.M., Bouwman, J., van den Ancker, M. E., Waelkens, C., & Malfait, K. 2001, A&A, 365, 476

Merril, P. W., Burwell, C. G., & Miller, W. C. 1942, ApJ, 96, 15

Mundt, R. & Ray, T. P. 1994, ASPC, 62, 237

Natta, A., Palla, F., Butner, H. M., Evans, N. J. II, & Harvey, P. M. 1993, ApJ, 406, 674

Natta, A., Testi, L., Muzerolle, J., Randich, S., Comerón, F., & Persi, P. 2004, A&A, 424, 603

Natta, A., Testi, L., Calvet, N., et al., 2007, in Protostars & planets V, ed. B. Reipurth, D. Jewitt, % K. Keil Tucson: (THE UNIVERSITY OF ARIZONA PRESS), 767

Nisini, B., Milillo, A., Saraceno, P., & Vitali, F. 1995, A&A, 302, 169

Nomura, H. 2002, ApJ, 567, 587

Okamoto, Y. K., Kataza, H., Honda, M., Yamashita, T., Onaka, T., Watanabe, J., Miyata, T., Sako, S., Fujiyoshi, T., & Sakon, I. 2004, Nature, 431, 660

Omodaka, T., Kitamura, Y., & Kawazoe, E. 1992, ApJ, 396, 87

Palla, F. & Stahler, S. W. 1990, ApJ, 360, 47

Palla, F. & Stahler, S. W. 1993, ApJ, 418, 414

Pavlyuchenkov, Ya., Semenov, D, Henning, Th., Guilloteau, S., Piétu, V., Launhardt, R., Dutrey, A. 2007, ApJ, 669, 1262

Panić, O., Hogerheijde, M. R., Wilner, D., & Qi, C. 2008, A&A, 491, 219

Pérez, M. R., THé, P. S., Westerlund, B. E. 1987, PASP, 99, 1050

Piétu, V., Dutrey, A., & Guilloteau, S. 2007, A&A, 467, 163

Piétu, V., Dutrey, A., & Kahane, C. 2003, A&A, 398, 565

Piétu, V., Guilloteau, S., & Dutrey, A. 2005, A&A, 443, 945

Pringle, J. E. 1981, ARA&A, 19, 137

Raman, A., Lisanti, M., Wilner, D. J., Qi, C., & Hogerheijde, M. 2006, ApJ, 131, 2290

Safronov, V. 1969, Evolution of the protoplanetary cloud and formation of the earth and planets. Nauka Press.

Sano, T., Miyama, S. M., Umebayashi, T., & Nakano, T. 2000, ApJ, 543, 486

Sano, T. & Stone, J. M. 2002, ApJ, 570, 314

Scoville, N. Z., Sargent, A. I., Sanders, D. B., Claussen, M. J., Masson, C. R., Lo, K. Y., & Phillips, T. G. 1986, ApJ, 303, 416

Shakura, N. I., & Sunyaev, R. A. 1973, A&A, 24, 337

Simon, M., Dutrey, A., & Guilloteau, S. 2001, ApJ, 545, 1034

Smith, B. A. & Terrile, R. J. 1984, Science, 226, 1421

Stahler, S. W. & Palla, F. 2004, The formation of stars (New York: WILEY-VCH)

Sunada, K., Yamaguchi, C., Kuno, N., Okumura, S., Nakai, N., & Ukita, N. 2000, ASPC, 217, 19

Strom, S. E., & Najita, J. 2005, in Protostars and Planets V (LPI Contrib. 1286; Houston: LPI), 8078

Sylvester, R. J., Skinner, C. J., Barlow, M. J., & Mannings, V. 1996, MNRAS, 279, 915

Takahashi, S., Takano, S., Iono, D., Kuno, N., Sakai, T, Horigome, O., & Yanagisawa, K. 2010, ASPC, 434, 425

Tamura, M., Gatley, I., Joyce, R. R., Ueno, M., Suto, H., & Sekiguchi, M. 1991, ApJ, 378, 611

Tanaka, H., Himeno, Y., & Ida, S. 2005, ApJ, 625, 414

Testi, L., Natta, A., Shepherd, D.S., & Wilner, D. J. 2003, A&A, 403, 323

Thé, P. S., Winter, D., & Pérez, M. R. 1994, A&A, 104, 315

Thi, W. -F, van Zadelhoff, G. -J, & van Dishoeck, E. F. 2004, A&A, 425, 995 van den Ancker, M. E., The, P. S., Feinstein, A., Vazquez, R. A., de Winter, D., & Perez, M. R. 1997, A&AS, 123, 63

van den Ancker, M. E., de Winter, D., & Tjin A Djie, H.R.E. 1998, A&A, 330, 145

Walker, H. J. & Wolstencroft, R. D. 1988, PASP, 100, 1509

Walsh, C., Millar, T. J., & Nomura, H. 2010, ApJ, 722, 1607

Walsh, C., Nomura, H., Millar, T. J., & Aikawa, Y. 2012, ApJ, in press [arXive:astro-ph/1201.2613v1]

Wannier, P. G., Penzias, A. A., & Jenkins, E. B. 1982, ApJ, 254, 100

Waters, L. B. F. M., & Waelkens, C. 1998, ARA&A, 36, 233

Weidenschilling, S. J. 1977, Ap&SS, 51, 153

Weintraub, D. A., Sandell, G., & Duncan, W. D. 1989, ApJ, 340, 69

Wisniewski, M., Clampin, M., Grady, C. A., Ardila, D. R., Ford, H. C., Golimowski, D. A., Illingworth, G. D., Krist, J. E. 2008, ApJ, 682, 548

Whitney, B. A., Wood, K., Bjorkman, J. E., & Cohen, M. 2003, ApJ, 598, 1079

Yamaguchi, C., Sunada, K., Iizuka, Y., Iwashita, H., & Noguchi, T. 2000, SPIE, 4015, 614

Youdin, A. N, & Shu, F. H. 2002, ApJ, 580, 494

Zickgraf, F. -J., C., Wolf, B., Leitherer, C., Appenzeller, I., & Stahl, O. 1986, A&A, 163, 119

Zuckerman. B. & Matthew A. M. 1996, The origin and evolution of the universe (Jones & Bartlett Pub.)